HARNESSING THE OPTICAL PROPERTIES OF GOLD NANORODS: FLUORESCENCE ENHANCEMENT, BIOSENSING AND PHOTOTHERMAL THERAPY

BY

NARDINE S. ABADEER

DISSERTATION

Submitted in partial fulfillment of the requirements
for the degree of Doctor of Philosophy in Chemistry
in the Graduate College of the
University of Illinois at Urbana-Champaign, 2016

Urbana, Illinois

Doctoral Committee:

Professor Catherine J. Murphy, Committee Chair and Director of Research
Professor Ryan C. Bailey
Professor Wen-Tso Liu
Assistant Professor Prashant K. Jain

ABSTRACT

In recent years, there has been great interest in the synthesis, characterization, and application of gold nanomaterials, especially gold nanorods. Due to their small size, ease of functionalization, and uniquely tunable optical properties, gold nanorods have potential application in solar cells, sensing, bioimaging, drug delivery, and cancer therapy. Excitation of a gold nanorod localized surface plasmon resonance (LSPR) can result in the enhancement of many photophysical processes such as light absorption, Rayleigh (Mie) scattering, and fluorescence. The presence of a strong electromagnetic field has been observed to enhance spectroscopic molecular signals from fluorophores, Raman-active molecules, and two-photon chromophores bound to or near the metal surface. Additionally, strong light absorption and nonradiative dissipation of absorbed energy allows for the use of gold nanorods in photothermal heating applications. Optical applications such as these may be realized by carefully engineering the size, shape, surface chemistry of gold nanorods.

The focus of this dissertation is in exploring how gold nanorod surface properties can be modified for various optical applications. In each chapter, gold nanorods are prepared, the surface coating is modified, and the materials are characterized by a variety of methods. This thesis seeks to demonstrate how these materials may be useful, with a focus on three particular applications: fluorescence enhancement, biosensing and photothermal therapy.

Chapter 1 is an introduction to gold nanorods and contains a thesis overview. The unique optical properties, which are the basis for most applications, are discussed. This is followed by a general overview of the possible optical applications of gold nanorods. The history of advancements in gold nanorod synthesis and techniques for surface modification are described. There is a particular focus on the surface modification techniques most often used in this thesis, including thiol functionalization, silica coating and layer-by-layer wrapping of polyelectrolytes. Methods for characterization of gold nanorods, and their surface coatings are described, and the chapter ends with a dissertation overview.

Plasmonic nanoparticles can strongly interact with adjacent fluorophores, resulting in plasmon-enhanced fluorescence or fluorescence quenching. Chapter 2 explores how fluorescence behavior is altered near a gold nanorod surface. Fluorescence coupling is dependent upon nanoparticle composition, the distance between the fluorophore and the plasmonic surface, the transition dipole orientation, and the degree of spectral overlap between the fluorophore's absorbance/emission and the surface plasmon band of the nanoparticles. We examine the distance and plasmon wavelength dependent fluorescence of an infrared dye ("IRDye") bound to silica-coated gold nanorods. Nanorods with plasmon band maxima ranging from 530 to 850 nm are synthesized and then coated with mesoporous silica shells 11–26 nm thick. IRDye is covalently attached to the nanoparticle surface *via* a click reaction. Steady-state fluorescence measurements demonstrate plasmon wavelength and silica shell thickness dependent fluorescence emission. Maximum fluorescence intensity, with approximately 10-fold enhancement, is observed with 17 nm shells when the nanorod plasmon maximum is resonant with IRDye absorption. Time-resolved

photoluminescence reveals multi-exponential decay and a sharp reduction in fluorescence lifetime with decreasing silica shell thickness, and when the plasmon maximum is closer to IRDye absorption/emission. Control experiments are carried out to confirm that the observed changes in fluorescence are due to plasmonic interactions, not simply surface attachment. There is no change in fluorescence intensity or lifetime when IRDye is bound to mesoporous silica nanoparticles. In addition, IRDye loading is limited to maintain a distance between dye molecules on the surface to more than 9 nm, well above the Förster radius. This assures minimal dye–dye interactions on the surface of the nanoparticles.

The interface between nanoparticles and bacterial surfaces is of great interest for applications in nanomedicine and food safety. In Chapter 3, we investigate how nanoparticles might interact with bacteria by monitoring the binding of bacterial lipopolysaccharides to gold nanorods. We demonstrate that interactions between gold nanorods and lipopolysaccharides are governed by the nanoparticle surface coating. Polymer-coated gold nanorod substrates are exposed to lipopolysaccharides extracted from *Pseudomonas aeruginosa*, *Salmonella enterica* and *Escherichia coli*, and attachment is monitored using localized surface plasmon resonance refractometric sensing. The number of lipopolysaccharide molecules attached per nanorod is calculated from the shift in the plasmon maximum, which results from the change in refractive index after analyte binding. Colloidal gold nanorods in water are also incubated with lipopolysaccharides to demonstrate the effect of lipopolysaccharide concentration on plasmon shift, ζ-potential, and association constant. Both gold nanorod surface charge and surface chemistry affect gold nanorod–lipopolysaccharide interactions. In general, anionic lipopolysaccharides are found to attach more effectively to cationic gold nanorods than to neutral or anionic gold nanorods. Some variation in lipopolysaccharide attachment is also observed between the three strains studied, demonstrating the potential complexity of bacteria–nanoparticle interactions.

In recent years, there has been a great deal of interest in the preparation and application of nanoparticles for cancer therapy. Chapter 4 reviews the progress in thermal cancer treatments using gold nanoparticles. Gold nanoparticles are especially suited to thermal destruction of cancer due to their ease of surface functionalization and photothermal heating ability. We begin with an introduction to the properties of gold nanoparticles and heat-generating mechanisms which have been established. The pioneering work in photothermal therapy is discussed along with the effects of photothermal heating on cells *in vitro*. Additionally, radiofrequency-mediated thermal therapy is reviewed. We focus the discussion on the developments and progress in nanoparticle design for photothermal cancer therapy since 2010. This includes *in vitro* and *in vivo* studies, and the recent progression of gold nanoparticle photothermal therapy toward clinical cancer treatment. The chapter concludes with a perspective on the prospects of commercial application of photothermal-mediated cancer therapy with gold nanoparticles

Chapter 5 expands the range of photothermal therapy applications to inactivation of vegetative cells and endospores of the bacterium *Geobacillus stearothermophilus.* Gold nanorods are prepared and characterized and are coated with four different neutral or charged polymers to investigate the impact of surface charge on cell attachment and inactivation. The effects of gold nanorod exposure and photothermal

heating using a 785 nm laser on colony growth of spores and vegetative cells reveal greater reductions in colony formation with charged nanorods. Additionally, spore morphology is examined before and after treatment. There are small changes in morphology observed as increasing area per spore and decreased spore aspect ratio which might be correlated with inactivation. Although the inactivation of endospores is not as great as traditional sterilization techniques, these results demonstrate that there is potential in the application of photothermal heating with gold nanorods to inactivate heat-resistant bacterial endospores.

In Chapter 6 we consider how gold nanorod surface chemistry may be modified by silica coating and silane functionalization to maintain optical stability and therefore increase the effectiveness of gold nanorods in optical applications. Heating in an oven to 150°C, and charging due to electron beam exposure cause shortening and widening of gold nanorods and result in decreased in aspect ratio. However, these changes in morphology and optical properties are greatly reduced by silica coating and silane functionalization. Pulsed laser irradiation also is found to alter gold nanorod optical properties, and interesting changes in gold nanorod morphology are observed. Together, these results suggest that silica coating and silane functionalization improve the shape stability of gold nanorods and therefore may help to preserve the optical properties, especially compared to CTAB gold nanorods.

The increased prevalence of functionalized nanomaterials in a range of applications will inevitably lead to nanomaterial contamination of soil and groundwater. Chapter 7 moves past nanotechnology applications to consider the environmental fate of gold nanomaterials. We investigate how nanoparticle shape and surface chemistry influences their stability and transport within environmental systems. A library of spherical and rod-shaped gold nanoparticles is prepared with different surface chemistries. Nanoparticle stability against aggregation in simulated groundwater is investigated. The stability of gold nanoparticle probes in simulated groundwater depends on both the surface charge imparted by the capping agent, and the nature of the interaction between the nanoparticle surface and the capping agent. However, in the presence of natural organic matter, gold nanoparticles are found to form heteroaggregates, regardless of the initial surface coating. In addition, nanoparticle retention in columns of soil and alginate is quantified. The surface charge and capping agent interaction also influence retention of functionalized nanoparticles. Negatively-charged gold nanoparticles are only weakly retained in soil and alginate, and hence, are potentially much more mobile in environmental matrices than nanoparticles carrying positive surface charges. Together, these data suggest that the environmental fate of nanoparticles is strongly influenced by their surface chemistry, as well as core material and size.

ACKNOWLEDGEMENTS

I am now at the end of my time as a PhD student in Materials Chemistry at the University of Illinois at Urbana-Champaign. In the past five years I have learned a great deal about science, life, and my role in the world. I have become much more of an academic, a thinker and have grown intellectually in ways I would never have expected. Some of the most challenging and most rewarding and exciting experiences in my life have occurred during my time in graduate school. This education I have received is a wonderful privilege and of course this journey has not been made alone. There are many who I would like to thank who have been beside me during the process.

I would like to thank my PhD advisor Professor Catherine J. Murphy for excellent direction. You have given me the freedom to explore interesting and exciting paths in my research projects. Your direction has helped me become an independent thinker about science and I am excited to take what I have learned from you into my future scientific career.

Great work cannot be done without great coworkers. I would like to thank all of the members of the Murphy Research Group, past and present, especially those with whom I have collaborated, discussed science with, and learned from. Alaaldin Alkilany, Davin Chernak, Meredith Walker, Sean Sivapalan, Stefano Boulos, Jie An Yang, Jingyu Huang, Bethany Grillo, Samuel Lohse, Ran Liu, Jonathan Eller, Ariane Vartanian, Elissa Grzincic, Wayne Lin, Lisa Jacob, Nathan Burrows, Jordan Dennison, Joshua Hinman, JI (Ricky) Li, Priscila Falagan-Lotsch, Huei-Huei Chang, Meng Wu, Xi (Cassie) Zhang, Daniel Hofmann, and Fred Idesis, thank you. I also thank the contribution of undergraduate researchers Andrei Andreev, Frances Venable, Junheng Li and Andrew Wang to various projects. I am especially appreciative to current and former office mates (Stefano, Jonathan, Wayne, Ariane and Elissa). I have greatly enjoyed the debates about science, religion, and ethics and have learned so much. I will miss you all!

There are many collaborators who have contributed to work in this thesis. I especially thank Marshall Brennan and William (Bill) Wilson, who I collaborated with at UIUC to explore plasmon-enhanced fluorescence. The magnificent facilities and helpful staff at the Materials Research Laboratory allowed me to collect beautiful data. I thank Wacek Sweich, Julio Soares, Honghui Zhou, and Lou Ann Miller at the Materials Research Laboratory for their help and assistance in materials characterization.

The experience of doing research abroad in the Spring of 2014 was exciting and I learned a great deal about physics and the benefits of collaborative research. I also made some wonderful friends who I am very grateful to know both in the Bionanophotonics research group (Inès, Gülis, Gergő, Anni and Gustav) and those at New Life Church in Gothenburg. I also thank my collaborators Professor Mikael Käll, Gergő Fülöp, Si Chen, as well as everyone in the Bionanophotonics group in Applied Physics at Chalmers University of Technology in Gothenburg, Sweden. It was amazing to be part of such a diverse group of researchers!

There are many others within the University of Illinois who have been helpful in this journey. I thank all of the faculty and administrative staff in the Chemistry Department, especially Connie Knight, Beth Myler, Karen Watson, Stacy Dudzinski, and Theresa Struss. The IMP office staff are wonderful and encouraging

and always seem to have a constant supply of coffee and sweet treats available. I also thank my faculty committee members Professor Ryan Bailey, Professor Prashant Jain, and Professor Wen-Tso Liu for their helpful discussion and direction throughout my PhD.

I thank my parents Said and Yvone Abadeer for always supporting me in my pursuit of higher education. You taught me about love, responsibility, sacrifice, hard work, and faith. I know that I would not have been inspired to go this far in my education without your support and encouragement. I thank my brother Samer for always being willing to help me out or give career advice. I especially thank my sister, best friend and travel buddy Caroline for always being willing to listen when I was frustrated, happy, sad or excited and for never doubting my ability to succeed, even when I did. I could not have made it without you!

I also thank all the friends and extended family in Illinois, Wisconsin, Minnesota, and around the world who have encouraged and supported me during my time in graduate school. I especially thank all the wonderful friends I have made in the Champaign-Urbana community as part of 312 House, the Baptist Housing Ministry, the East Central Illinois Women Chemists Committee, PANDA House, the Intensive English Institute, Intervarsity Graduate Christian Fellowship, Bridges International, and Christ Community Church. You all, who are too numerous to count or name, have kept me sane and grounded me while in graduate school. Many of you have helped me to remember that while education and hard work are important, my life is centered in my Christian faith. I know I have truly been blessed with the resources and unique opportunity to learn and study. I do not know what the future holds, but it is indeed exciting!

I end my acknowledgements with the following passage from Philippians 3:12-14. "*Not that I have already obtained all this or have already arrived at my goal, but I press on to take hold of that for which Christ Jesus took hold of me. Brothers and sisters, I do not consider myself yet to have taken hold of it. But one thing I do: Forgetting what is behind and straining toward what is ahead, I press on toward the goal to win the prize for which God has called me heavenward in Christ Jesus*."

Nardine S. Abadeer

University of Illinois at Urbana-Champaign

April 26, 2016

TABLE OF CONTENTS

CHAPTER 1:
INTRODUCTION AND DISSERTATION OVERVIEW

1.1 OPTICAL PROPERTIES OF GOLD NANORODS

The ancient Roman glass chalice the Lycurgus cup (Figure 1.1), is well-known for its brilliant colors. When light is reflected from the surface, the Lycurgus cup is jade green, but light transmitted through it turns the cup ruby red. The presence of trace amounts of tiny gold and silver particles impregnated in the glass is the reason for these intense colors.

Figure 1.1 The Lycurgus Cup from 4th century Rome, which is currently on display at the British Museum in London. Photograph reprinted with permission from Ran Liu (2013).

These small metal particles are ~50-100 nm in diameter, and at the nanoscale, interactions between visible light and a metal nanoparticle can become quite interesting.[1] In nano size regimes, electron motion is confined and new material properties can appear which are not present in bulk materials. This is because the mean free path of an electron in gold is around 50 nm, and when particle size is comparable to the electron mean free path in a metal, surface effects dominate material properties and optical responses.[2,3]

In his 1908 paper, Gustav Mie used Maxwell's equations to develop a mathematical solution to the problem of extinction (scattering + absorption) of electromagnetic radiation incident on a small conducting sphere surrounded by a medium with a known dielectric constant. Mie found that optical properties in gold nanoparticles are dependent on several factors including nanoparticle size, medium refractive index, and the dielectric constant of the metal. Increases in particle size from 20 to 100 nm resulted in a small red-shift in the extinction maximum.[4] Mie also predicted that extinction spectra would change if nanoparticles were non-spherical in shape, such as ellipsoids.[5] Richard Gans later extended Mie's solution to spheroidal gold nanoparticles and he indeed found the wavelength of light absorption was highly dependent on gold nanoparticle aspect ratio (length/width).[6]

Gold nanoparticles confine resonant photons, which in-turn generates strong electromagnetic fields at the nanoparticle surface. The field strength decays exponentially as function of distance, and the distance is comparable to nanoparticle size/diameter. This feature of strong absorption and scattering of light by gold nanoparticles is known as the localized surface plasmon resonance (LSPR). Upon illumination at resonant wavelengths, free conduction band (6s) electrons in a gold nanoparticle are delocalized and undergo collective oscillation.[7] Oscillation of electrons generates a charge separation between the free electrons and the metal nanoparticle core.[3] In gold nanospheres, this electron oscillation induces strong light absorption and an LSPR peak around 520 nm. As Mie and Gans predicted, this effect is also dependent on nanoparticle shape and size. In anisotropic (non-spherical) nanoparticles, there can be electron oscillation along multiple axes.[8] The discussion here is focused on the properties of gold nanorods, which are rod-shaped gold nanoparticles, and can be prepared having varying aspect ratios. In gold nanorods there is oscillation along the shorter (transverse) axis and longer (longitudinal) axis (Figure 1.2). Therefore, the surface plasmon resonance splits into two bands with two observable absorbance peaks.

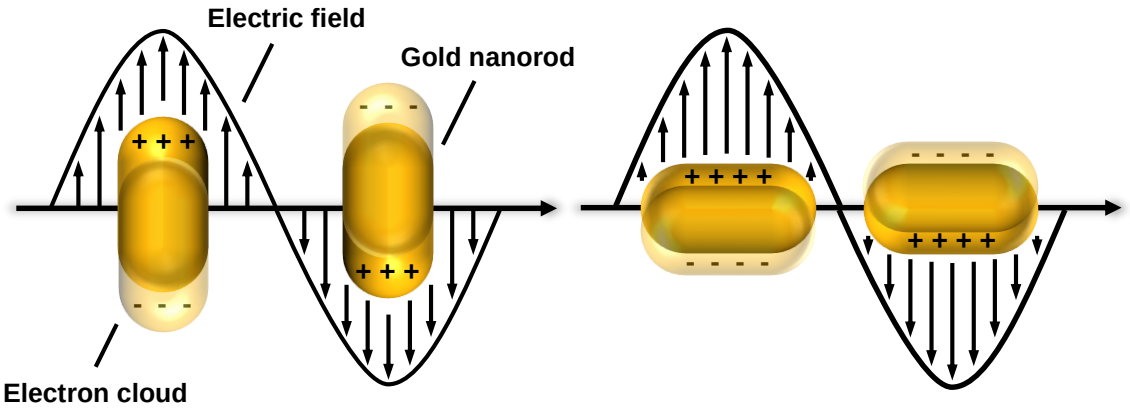

Figure 1.2 Schematic of the localized surface plasmon resonance on gold nanorods. Upon illumination at resonant wavelengths, conduction band electrons in the gold nanorod are delocalized and undergo collective oscillation along the longitudinal and transverse axes. This generates an electromagnetic field at the gold nanorod surface.

Because the aspect ratio of gold nanorods can be synthetically controlled, the longitudinal absorption maximum can be tuned from the visible to the near infrared. In aqueous solutions of gold nanorods, the LSPR wavelength maximum (λ_{max}) is approximately linearly proportional to aspect ratio (AR) and generally follows the trend in Equation 1.1.[3,9] This tunability can be easily seen in Figure 1.3 where gold nanorod aspect ratio increases from 1 to 4, as seen by transmission electron microscopy (TEM). In the corresponding UV-vis spectra for these gold nanorods, the LSPR maxima for the longitudinal peaks shift from 520 to 820 nm as aspect ratio is increased.

$$\lambda_{max} = 95*AR + 420 \text{ nm} \quad (1.1)$$

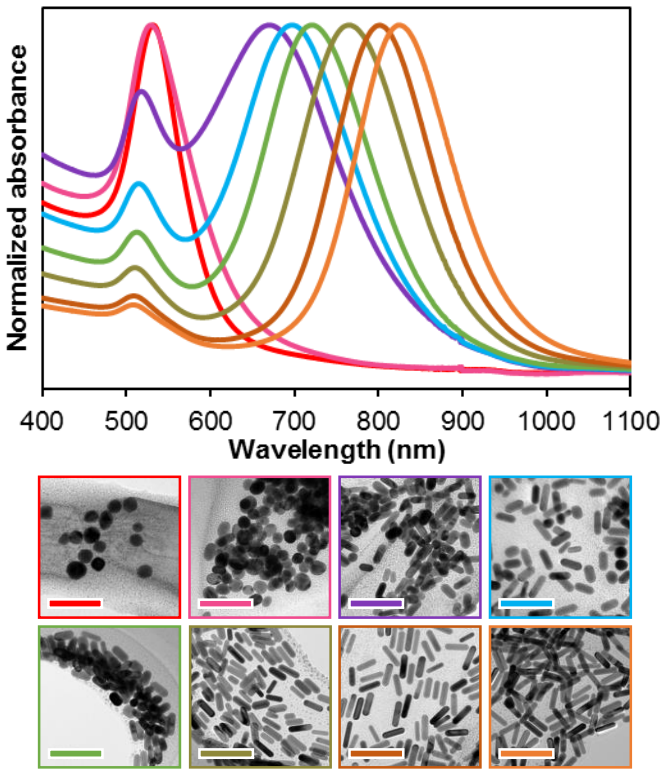

Figure 1.3 UV-vis absorbance spectra and TEM images of gold nanorods with increasing aspect ratio from 1 to 4, left to right. Color of TEM outlines and scale bars correspond to UV-vis traces. Scale bars = 50 nm.

Excitation of a gold nanorod LSPR can result in the enhancement of many photophysical processes such as light absorption, Rayleigh (Mie) scattering, and fluorescence.[10] The presence of a strong electromagnetic field (Figure 1.4) has been observed to enhance spectroscopic molecular signals from various chromophores in a distance dependent manner. This has been observed with fluorescent dyes,[11] Raman-active molecules,[12] and two-photon chromophores[13] which are bound to or near the metal surface. Additionally, strong light absorption and nonradiative dissipation of that absorbed energy allows for the use of gold nanorods in photothermal heating applications.

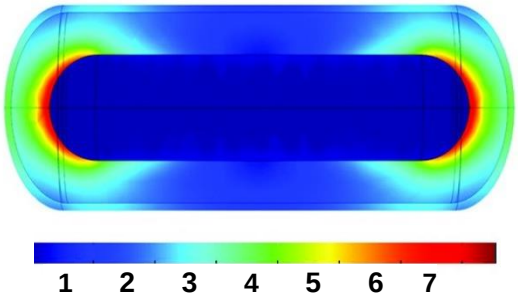

Figure 1.4 Calculated electric field enhancement on a gold nanorod (7.5 by 50 nm) using COMSOL Multiphysics. The electric field is strongest at the nanorod ends and decays exponentially as a function of distance. Adapted with permission from Reference 13. Copyright (2012) American Chemical Society.

1.2 APPLICATIONS OF GOLD NANORODS

Because of their unique optical properties, gold nanorods have potential use in a variety of biomedical, electronics, and energy-related applications. Biomedical applications include imaging of tumors *in vivo*, sensing of disease biomarkers, delivery of chemotherapeutic drugs and antibiotics, and photothermal killing of cancer cells and bacteria.[3] Other applications include single molecule sensing,[14] optical data storage,[15,16] and enhancement of absorption or photochemical reactions in solar cells.[17-19] These applications are realized by investigating the photophysical processes (Figure 1.5) which occur when a gold nanorod is irradiated at resonant wavelengths, and by engineering the gold nanorod structure and surface coating for a particular application.

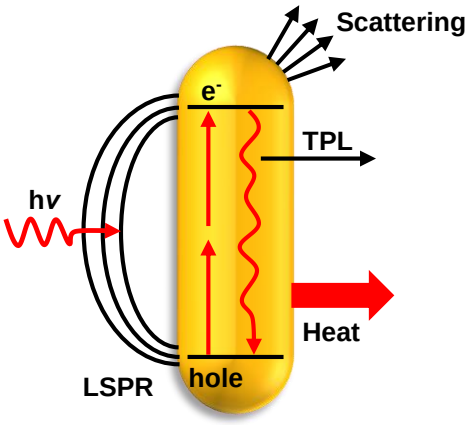

Figure 1.5 Examples of photophysical processes within a gold nanorod. Near-infrared irradiation induces excitation of the longitudinal LSPR, resulting in absorption and resonant light scattering. An electronic transition from the *d*-band to the *sp*-band occurs with two-photon absorption, generating an electron-hole pair. Recombination of the separated charges results in two-photon luminescence (TPL) emission. Heat is also generated as a consequence of electron-phonon collisions. Adapted with permission from Reference 20. Copyright (2009) John Wiley & Sons.

Imaging of cells and/or tumors with gold nanorods has been performed using a variety of techniques.[19] In a typical darkfield imaging system, a white light source is irradiated on a biological sample and only light scattered from the sample is collected by the detector. Because gold nanorods can scatter light in the near-infrared region, they can be detected under darkfield microscopy. For example, Hu *et al.*[21] prepared gold nanorods functionalized with transferrin to target the surface of cancer cells which overexpressed transferrin receptors. After incubation, darkfield imaging of Panc-1 and MiaPaCa human pancreatic cancer cells revealed uptake of the gold nanorods into vesicles within the cells. The same level of uptake was not observed with polyelectrolyte-coated nanorods. Their results demonstrated that there was potential application in cancer diagnosis with this technique.

Two-photon luminescence (TPL) is a non-linear process which has been observed in gold nanorods. In TPL, two photons of low energy (higher wavelength) excite the LSPR, and a single photon of high energy (lower wavelength) is released, and the system relaxes back to the ground state. Because simultaneous

absorption of two photons of comparable energy is a rare event, TPL has a much lower cross-section than single-photon scattering.[19] It is thought that TPL can be enhanced under plasmon-resonant conditions.[22] TPL has been used in a variety of applications for imaging/detection of many biological species including: skin cancer cells,[23] *Bacillus anthracis* spores,[24] and mouse ear blood vessels *in vivo*.[25] However, we note that the mechanism of TPL is still somewhat controversial. A recent report has demonstrated that emitted light, which is thought to be two-photon emission, may actually be due to anti-Stokes electronic Raman scattering from single-particle electron-hole pair excitations resonantly enhanced by the plasmon.[26] Therefore, TPL clearly merit further study before further investigation of these applications.

Gold nanorods have also been used as contrast agents for *in vivo* photoacoustic imaging. The basis of photoacoustic imaging is generation of acoustic waves after absorption of electromagnetic energy.[27] Jokerst *et al.*[28] exploited the strong optical absorbance of gold nanorods to enhance the photoacoustic signal from a tumor after nanorod accumulation in ovarian cancer tumors in mice. Additionally, the photoacoustic enhancement was aspect ratio and dose-dependent, which demonstrated that there was potential to further optimize the imaging process with the gold nanorod based imaging agent.

Quantification of disease biomarkers can be achieved using gold nanorod biosensors. The LSPR peak position in gold nanorods is highly sensitive aspect ratio, but also the dielectric constant of the immediate surroundings. Binding of molecules, which have a different refractive index than the surface, to a gold surface, can be detected in real-time by observing a shift in the LSPR peak position. Because of high refractive index sensitivity, small analyte volumes having extremely low concentrations can be detected by gold nanorod biosensors.[29,30] For instance, Mayer *et al.*[31] prepared gold nanorod substrates functionalized with a rabbit IgG antibody *via* carbodiimide chemistry. Exposure of the substrates to goat antirabbit IgG (100 pM to 30 nM) resulted in a red shift in the peak position in a concentration dependent manner. In contrast, when antimouse IgG was delivered, very little binding was observed. Using a similar antibody capture technique, Truong *et al.*[32] demonstrated detection of prostate specific antigen, which is a marker for prostate cancer, down to a concentration of 111 aM. Together, these examples demonstrate that there is specificity and low detection limits with gold nanorod biosensing techniques.

Delivery of drugs has been carried out using gold nanorods as drug carriers. Min *et al.*[33] conjugated the anti-tumor cisplatin prodrug Pt(IV) to gold nanorods functionalized with the biocompatible polymer polyethylene glycol. After uptake into the acidic endosome environment in cells, the prodrug was reduced to the active diplatinum form. The researchers found that the gold nanorods enhanced delivery of Pt(IV) to cancer cells and consequently, the IC_{50} was an order of magnitude lower than free cisplatin in three types of cancer cells. It is also possible to use gold nanorods as stimuli-responsive drug carriers. Wei *et al.*[34] coated gold nanorods with the thermo-sensitive polymer poly(*N*-isopropyl acrylamide) and loaded the polymer with the antibiotic drug Norvancomycin. Laser irradiation of the gold nanorods induced photothermal heating, shrinking of the polymer and controlled drug release. The benefits nanoparticle drug delivery systems such as these may include more rapid drug delivery to cells/tumors and reduced toxicity and side-effects to patients.[35]

Absorbed photons are converted to heat *via* a pathway of photophysical properties in gold nanorods, and laser-based photothermal therapy is a potential therapeutic application of this effect.[36] Huang *et al.*[37] were some of the first to demonstrate photothermal killing of cancer cells using gold nanorods. Gold nanorods were functionalized with anti-epidermal growth factor receptor monoclonal antibodies, which are often overexpressed in cancer cells. Incubation of the gold nanorods and subsequent laser irradiation resulted in more effective destruction of malignant oral epithelial cancer cells than nonmalignant cells. Norman *et al.*[38] used antibody-functionalized gold nanorods to target the surface of the pathogenic bacterium *Pseudomonas aeruginosa*. Laser irradiation of bacteria incubated with gold nanorods resulted in 75% bacterial cell death and irreparable damage to cell walls. These two examples demonstrate photothermal killing can be quite effective by using targeted gold nanorods.

While many applications of gold nanorods are biomedical in nature, there is also potential use of gold nanorods in a range of other industries. For example, detection of low concentrations of Raman active molecules is possible with surface-enhanced Raman spectroscopy (SERS). Raman scattering is an inelastic scattering process which occurs when a molecule absorbs a photon of light, and there is a shift in the scattered light to lower frequency. Because Raman scattering only occurs in 1 in 10^6 incident photons, Raman signals are notoriously low. However, the presence of plasmonic metals, with nanometer scale features, can provide 10^{10} - 10^{11} fold signal enhancement.[39,40] Saute *et al.*[41] employed SERS with gold nanorods to discriminate between three dithiocarbamate fungicides, which are used as pesticides in the United States. Their system demonstrated great sensitivity with limits of detection in the nanomolar range. Because of this sensitivity SERS is a highly useful technique with applications ranging from pigment identification and art preservation,[42] to detection of environmental toxins,[43] and other chemical and biological species which may threaten national security.[44]

Fluorescence is yet another photophysical process which may be altered near a gold nanorod surface.[11,45] Fluorophores can be used in bioimaging and sensing studies,[46] and also have use in organic electronics,[47] and light emitting diodes.[48,49] However, fluorophores can be unstable, are susceptible to photobleaching, and can have low quantum yields.[11] Enhancement of fluorescence emission v*ia* plasmonic coupling is one method to increase their effectiveness in these applications.[50.51] Distance dependent fluorescence emission near a plasmonic surface has been observed by several researchers,[52,53] and may be explained by Figure 1.6. When a fluorophore is too close to a metal surface, there is transfer of emitted energy from the fluorophore to the nanoparticle. However, when the fluorophore is sufficiently far away the electromagnetic field strength is sufficient to enhance emission *via* increased excitation and emission rates.

Researchers have investigated distance-dependent fluorescence emission near gold nanorods. Li *et al.*[54] prepared nanocomposite materials of quantum dots conjugated to silica-coated gold nanorods. Quantum dots are 1 – 100 nm light-emitting semiconductor nanocrystals, and are known to exhibit narrow, size-dependent absorption and fluorescence emission profiles.[55,56] Because of their optoelectronic properties, quantum dots are used in bioimaging and electronics applications including solar cells, memory elements, photodetectors, thermoelectrics and light emitting diodes.[57,58] Li *et al.* found that quantum dot

fluorescence emission near gold nanorods was distance dependent. There was quenching at fluorophore-nanorod separations less than 10 nm, but there was a 50% increase in fluorescence emission 15 nm from the surface. Fluorescence lifetime measurements revealed that the increase in emission at this distance was due to increased excitation rates in the presence of the strong electromagnetic field.[50] This result is a good demonstration of how the ability to tailor the design and structure of gold nanorods may increase their potential success in a particular application.

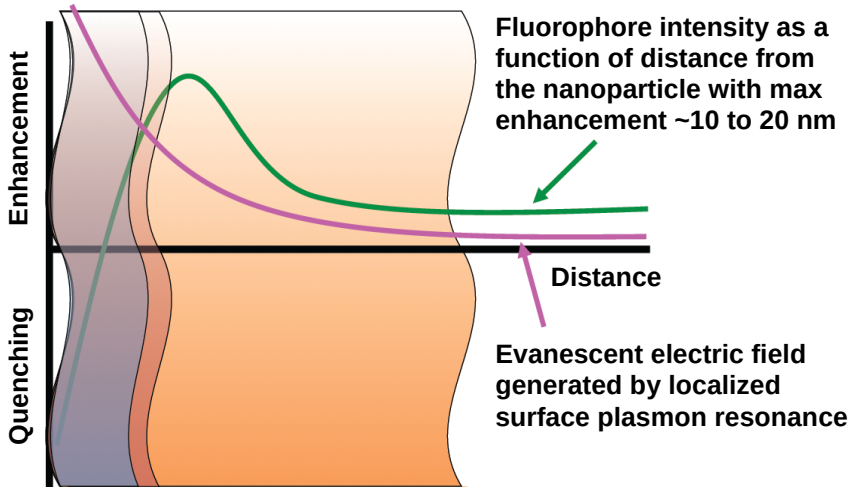

Figure 1.6 Fluorescence intensity as a function of distance from a plasmonic metal surface. A few nm from the surface, fluorescence is quenched due to energy transfer into the plasmon band. At a certain distance the energy transfer is reduced and the electromagnetic field strength can be great enough to enhance fluorescence emission. At a distance more than 20 nm away, the electric field decays and does not greatly increase fluorescence emission.

1.3 GOLD NANOROD SYNTHESIS

There has been a great deal of published work describing applications of gold nanorods.[59,60] These applications are possible because of the exquisite ability scientists have to control nanoparticle shape, size, and surface chemistry.[61] Gold nanorods can be synthesized by a variety of methods, such as by photochemical reactions,[62] electrochemistry,[63,64] or lithographical techniques.[65,66] These processes form gold nanorods with different absolute dimensions, crystallographic facets, surface coatings, and size dispersity, and may be useful depending on the desired application. However, the most popular approach for the preparation of gold nanorods is by seeded wet chemical synthesis. This method separates the nucleation and growth steps, and allows for good control of size and gold nanorod aspect ratio.[67]

The original seeded growth paper by Jana *et al.*[68] in 2001 was a three step process and used citrate-coated gold nanoparticle seeds which are ~3.5 nm in diameter and multiply twinned.[69] The gold nanorods formed following that procedure are higher aspect ratio (10 to 25), face-centered cubic, penta-twinned, and have (111) crystal faces at the ends and (100) or (110) faces at the sides.[70] In later work, Gole and Murphy[71]

demonstrated that the crystal structure and size dispersity of the gold nanoparticle seeds greatly impacted the crystal structure, dimensions, and size dispersity of gold nanorods prepared from the seed.

The preparation in this thesis (Figure 1.7) uses a seed preparation procedure developed by El-Sayed and coworkers. These smaller 1.5 to 2 nm single crystalline seeds are coated in the surfactant cetyltrimethylammonium bromide (CTAB). CTAB stabilizes the surfaces of both the seeds and nanorods, and prevents nanoparticle aggregation after synthesis. The nanorods formed from this procedure are formed in the presence of silver ions which is a shape-directing agent and the shape yield is around 95%. In addition, they have smaller aspect ratios (1 to 5), with LSPRs ranging from 500 - 850 nm. These gold nanorods are single crystalline, and have (100) crystal faces at the ends and (110) faces at the sides.[72]

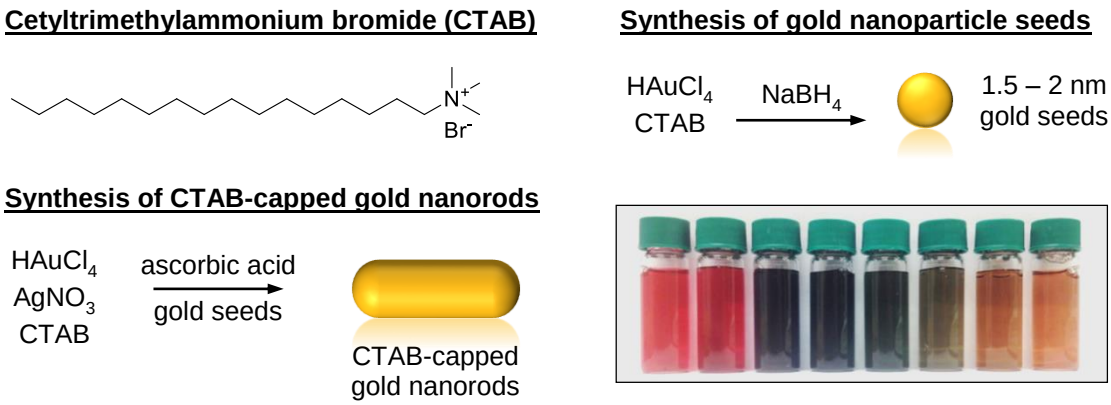

Figure 1.7 Wet chemical synthesis for aspect ratio 1 to 5 gold nanorods. The molecular structure of the surfactant CTAB is shown. Gold nanoparticle seeds capped in CTAB are prepared in a solution of CTAB and $HAuCl_4$, *via* reduction of Au^{3+} to Au^0 by $NaBH_4$. The gold seeds are added to a growth solution containing $HAuCl_4$, $AgNO_3$, and CTAB which has been reduced from Au^{3+} to Au^+ by ascorbic acid. CTAB-capped gold nanorods form and the aspect ratio is influenced by varying the amount of $AgNO_3$ in the growth solution. The photograph shows gold nanorods in water with increasing aspect ratio left to right.

The procedure described here is an aqueous, silver-assisted, seed-mediated synthesis which is carried out at room temperature and produces CTAB-coated gold nanorods.[73,74] First gold seeds (1.5 - 2 nm in diameter) are prepared in the presence of the surfactant CTAB and the gold salt precursor $HAuCl_4$. The solution is stirred vigorously, and ice-cold $NaBH_4$ is added to reduce Au^{3+} to Au^0 forming CTAB-capped gold nanoparticle seeds. The solution immediately changes from a pale yellow to a pale brown color upon addition of $NaBH_4$, which is an indication of successful reduction. CTAB-stabilized gold nanorods are prepared from a growth solution containing 0.1 M CTAB, 0.50 mM $HAuCl_4$ and varying concentrations of $AgNO_3$ (up to 150 µM). Ascorbic acid is added to the growth solution to reduce Au^{3+} to Au^+. After the addition of the reducing agent, the light yellow solution turns colorless, and the gold seeds are added to the growth solution. Because ascorbic acid is a weaker reducing agent, growth is slower, allowing for the formation of CTAB-capped gold nanorods with lengths ranging from 20 - 90 nm and widths from 10 - 25 nm. The presence of $AgNO_3$ promotes formation of higher aspect ratio nanoparticles. As the amount of the silver is

increased, different colors of gold nanorod solutions are produced with red-shifted LSPR maxima (Figure 1.3). Nanorod solutions are typically purified by centrifugation, then the pellets are resuspended in deionized water, and can be stored at room temperature for several months.

Gold nanorod synthesis must be carried out carefully, and each reagent plays an important role in the growth of gold nanorods. Some researchers have examined the function of the surfactant in gold nanorod synthesis. Nikoobakht *et al.*[75] investigated the role of CTAB and the co-surfactant tetraoctylammonium bromide on the surface of gold nanoparticles and nanorods using a combination of Fourier-transform infrared spectroscopy, thermogravimetric analysis, and TEM. Their studies revealed that the surfactant molecules formed a bilayer on the gold, with the ionic head groups bound to the gold surface. However, because the crystal facets can be different, packing density and binding of the surfactant molecules to the facets is also varied. Gao *et al.*[76] investigated the impact of the length of the surfactant chain on gold nanorod aspect ratio. They found that as alkyltrimethylammonium bromide chain length was increased from 10 to 16 carbons, they could increase aspect ratio from 1 to 23. Purity of the surfactant is also important. Smith *et al*.[77] tried to synthesize gold nanorods using CTAB from ten different suppliers and they observed significant differences in the size and monodispersity of as-synthesized gold nanorods. In some cases, it was not even possible to form nanorods with a specific brand of CTAB, and only spheres were formed. The researchers suspected this was due to variation in iodide concentration between the different suppliers so they deliberately added different concentrations of potassium iodide to the growth solution. Addition of KI completely prevented nanorod growth at 50 ppm, potentially due to iodide adsorption on the Au (111) face. In a separate study, Rayavarapu *et al.*[78] examined different lots of CTAB from some of these sources. They found that iodide impurities varied lot-to-lot, not just by supplier, and they suggested researchers should test reagents to better ensure successful synthesis.

Not all synthetic procedures for gold nanorods use silver to alter aspect ratio,[79] but there certainly is a correlation between silver concentration and nanoparticle shape.[80,81] A 2003 paper by El-Sayed and coworkers,[82] was the first to describe control of gold nanorod aspect ratio by using silver in the seed-mediated procedure. They suggested Ag-Br pairs decrease charge density and repulsion between CTAB headgroups. This could potentially alter the behavior of CTAB micelles, changing them from spherical to cylindrical, and increasing the aspect ratio. There are few other theories which may explain the role of silver in controlling gold nanorod aspect ratio. Hubert *et al.*[83] have suggested that a complex of AgBr and CTAB is formed *in situ* and deposits onto the gold surface, preventing further gold deposition, and allowing for anisotropic growth at the nanorod ends. Liu *et al.*[84] proposed that underpotential deposition of Ag^+ at the gold surface occurs at different rates on the (110), (100), and (111) crystal facets, therefore promoting nanorod formation. Orendorff *et al.*[85] analyzed the metal content in gold nanorods using inductively coupled plasma mass spectrometry. They found that the amount of silver is around 2.5 to 4.5% of the amount of gold present which is enough to form 3 to 4 monolayers of silver on the surface. Jackson *et al.*[86] mapped the location of silver on individual gold nanorods using Super-X energy dispersive X-ray spectroscopy and

found silver on all faces of the nanorod ends and sides. While the form silver takes is still not known, these studies demonstrate that there is silver present in gold nanorods, and it appears to have an important role.

In the last decade, there has been continuous work to modify the seeded growth procedure to increase the monodispersity and improve size control in gold nanorods. Vigderman *et al.*[87] used hydroquinone as a reducing agent instead of ascorbic acid. Because it is a weaker reducing agent, the growth time was slower, but they were able to tune nanorod LSPRs from 770 to 1230 nm, and they demonstrated near quantitative conversion of gold into nanorods. Murray and coworkers, have published reports which also demonstrate impressive size control. They used salicylate-based sodium salts and other aromatic additives at a reduced CTAB concentration (0.05 M) to produce gold nanorods with LSPR maxima from 624 to 1246 nm.[88] In another paper, the same group used binary surfactant mixture of CTAB (0.037 - 0.047 M) and sodium oleate to produce monodisperse gold nanorods of various widths.[89] Scarabelli *et al.*[90] investigated the combination of ascorbic acid and salicylic acid as a double-reducing-agent system to understand the role of these additives in improving monodispersity. They concluded the additive influences both the thermodynamics and kinetics of growth by participating in Au^{+} reduction to Au^{0} at the gold surface.

Synthesis of gold nanorods is typically carried out in batch, which limits the volume to ~1 L, and only ~15% of the gold is formed into nanorods. Boleininger *et al.*[91] developed a microfluidic reactor system for continuous flow synthesis of gold nanorods, but aspect ratio and LSPR were not well-controlled. In 2005, Jana described a seedless synthesis of gold nanorods, which could produce nanorods on the gram-scale.[92] In that method, nucleation and growth of nanorods was controlled kinetically using a mixture of strong and weak reducing agents ($NaBH_4$ and ascorbic acid). Seedless synthesis allowed for further development of scaled up procedures. Lohse *et al.*[93] recently developed a millifluidic reactor system which could form gold nanoparticles of varying shapes, sizes and surface coatings. The preparation of gold nanorods used two reagent streams: the standard growth solution and a reaction initiator solution comprised of gold seeds or a strong reducing agent ($NaBH_4$). In both cases, it was possible to form gold nanorods with the same control over aspect ratio and LSPR. Advancements in large-scale synthesis such as this are particularly useful as industrial demand for nanoparticles and commercialization of nano-enabled technologies increases.[94]

1.4 STRATEGIES FOR SURFACE MODIFICATION OF GOLD NANORODS

Analysis of as-synthesized gold nanorods has shown that they may be coated in a bilayer of the cationic surfactant CTAB. The gold nanorod surface is likely not static, and there likely is dynamic exchange of molecules between CTAB micelles in solution and on the surface.[95] While CTAB plays an important role as a structure-directing agent in gold nanorod formation and in preventing aggregation, it is not an ideal ligand for many applications. Heating can destabilize the CTAB bilayer, resulting in changes in nanorod morphology.[96] It is also known that CTAB gold nanorods are prone to aggregation because CTAB is desorbed from the surface at high salt concentrations, in physiological environments, and in organic solvents.[97,98] Additionally, free CTAB, can be cytotoxic at micromolar concentrations which limits biomedical applications of CTAB gold nanorods.[99] However, there are several methods to tailor the surface chemistry

of gold nanorods to avoid these issues which could prevent nanotechnology applications from being realized.[100] Here, we focus on a few fairly common techniques which are often utilized in this thesis including the methods of ligand exchange, inorganic silica coating, and layer-by-layer wrapping (Figure 1.8).

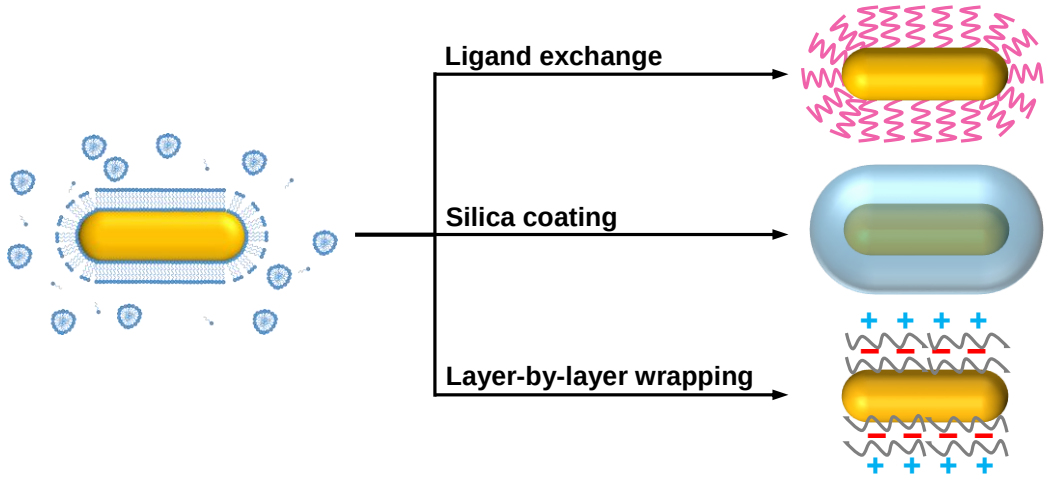

Figure 1.8 A few general routes to modification of gold nanorod surface chemistry. CTAB can be displaced on the gold surface by covalent attachment of thiol-functionalized ligands. The CTAB-covered surface can be coated in a silica shell *via* a modified Stöber method. Alternative layers of negatively and positively charged polyelectrolytes can coat the surface using layer-by-layer wrapping, which is based on electrostatic attraction.

It is known that sulfur organic groups (R-SH and R-SS-R) can covalently bind to gold surfaces by forming self-assembled monolayers.[101] In a 1983 report, Nuzzo *et al.*[102] described the preparation of oriented organic disulfide monolayers on flat gold surfaces. Later, Nuzzo and coworkers[103] reported spontaneous, but well-ordered assembly of long-chain alkane thiols onto gold surfaces. Mulvaney and coworkers[104] were the first to extend this and formed ordered monolayers on gold nanoparticles. Since then, a variety of thiol-containing ligands have been synthesized and can be used to functionalize and stabilize gold nanoparticles.[105]

The most common strategies for thiol functionalization include forming nanoparticles in the presence of thiolated molecules, exchanging the ligand on the surface for functionalized thiols, and modifying the terminal functional group on an existing thiolated ligand.[106] Of these techniques, ligand exchange on gold nanorods is the easiest method because thiols can easily displace weakly bound CTAB. Thiolated polyethylene glycol (PEG-SH) is probably the most common ligand used to modify gold nanorods. PEG renders the nanorod surface neutral, is more biocompatible than CTAB, and also prevents aggregation of gold nanorods because it is soluble in a variety of conditions. Additionally, PEGylation provides stealth characteristics to gold nanorods because adsorption of biomolecules to the nanorod surface is reduced, and blood circulation time is increased *in vivo* compared to CTAB nanorods.[107] CTAB can also be replaced by a monolayer of thiolated analogues of CTAB such as (16-mercaptohexadecyl) trimethylammonium bromide (MTAB). Zubarev and coworkers[108] demonstrated that MTAB-functionalized nanorods are

positively charged on the surface and are more efficiently taken up by cancer cells compared to PEGylated nanorods. In addition, they could be dried without losing water solubility, are stable against repeated rounds of centrifugation, and demonstrate decreased cytotoxicity compared to CTAB nanorods. Other thiols are more specific such as thiolated DNA oligonucleotides for drug delivery,[109] biotin disulfide which can bind streptavidin for nanorod self-assembly,[110] and lipoic acid which can be chemically modified to bind targeting proteins.[111] These examples demonstrate that the versatility of thiol chemistry may be used to extend the functionality of gold nanorods.

Silica coating is a useful technique for gold nanorod surface modification. Silica can increase the colloidal stability of gold nanorods in organic solvents while enhancing the thermal stability to preserve gold nanorod optical properties.[11,112] A silica surface is also quite versatile. The presence of reactive silanols means a silica surface can be modified with other silane-functionalized ligands such as PEG, or targeting ligands.[113] Additionally, mesoporous silica coatings can carry payloads of chemotherapeutic drugs, photosensitizers or other small molecules which can be released in a controlled fashion from the surface by photothermal heating of gold nanorods.[114,115]

The Stöber process is used to form silica *via* hydrolysis and condensation of tetraalkyl silicates at pH 11-12.[116] Mesoporous silica is simply formed by carrying out the reaction in the presence of a surfactant, which provides a template for silica formation. Gorelikov *et. al.*[117] directly coated mesoporous silica onto CTAB gold nanorods *via* a modified Stöber process. NaOH is added to gold nanorods to adjust the pH to 11 and is followed by injections of tetraethylorthosilicate (TEOS) which polymerizes to form silica in a base-catalyzed reaction. With this simple method, they produced 15 nm thick silica shells. Furthermore, 60 nm thick non-porous silica shells were prepared by injecting additional TEOS into the reaction solution after the initial coating (Equations 1.2 and 1.3).[118] Since their report, other researchers have modified reaction parameters such as temperature, TEOS, and CTAB to control mesoporous silica shell thickness on gold nanorods.[11,119,120] Wang and coworkers[121] recently reported site-selective, side and end mesoporous silica coating on gold nanorods. In their procedure CTAB and TEOS concentrations are carefully controlled to allow the preferential deposition of silica on the nanorod ends. The addition of a PEG-SH to selectively functionalize the nanorod ends allowed for the formation of side silica-coated nanorods.

$$Si(OC_2H_5)_4 + 4H_2O \rightarrow Si(OH)_4 + 4C_2H_5OH \quad (1.2)$$

$$Si(OH)_4 \rightarrow SiO_2 + 2H_2O \quad (1.3)$$

Other researchers have coated gold nanorods with uniform, nonporous silica shells. Pastoriza-Santos *et al.* [122] first coated CTAB gold nanorods with the polyelectrolytes polystyrene sulfonate and poly(allylamine hydrochloride) using layer-by-layer wrapping. The wrapped gold nanorods were transferred into a propanol-water mixture, and silica coating was carried out by a modified Stöber process forming silica shells 12 - 60 nm thick. Another group functionalized gold nanorod with PEG-SH before transferring the particles to isopropyl alcohol for silica coating, and this resulted in 6 - 20 nm thick silica shells.[123] Using a different

method, Sendroui *et al.*[124] first functionalized gold nanorods with 3-mercaptopyropyltrimethoxy silane to generate silanol groups on the gold surface. They grew thin silica shells (3 - 5 nm) by adding sodium silicate at pH 10. The silica-coated nanorods were then functionalized with 3-aminopropyltrimethoxy silane, and single strand DNA could be conjugated to the surface *via* a reductive amination reaction. The DNA-functionalized nanorods were still capable of hybridization with a complementary DNA strand and could be used to enhance SPR imaging measurements on a DNA microarray.

Nanoparticles can also be functionalized using layer-by-layer wrapping techniques.[125,126] Layer-by-layer coating is the sequential deposition of layers of polyanions and polycations and is based on electrostatic attraction between oppositely charged surfaces. This technique was initially developed by Kirland,[127] and Iler,[128] but was popularized by Decher and coworkers[129] as a method to functionalize flat surfaces and to create multilayer assemblies. Charged materials such as small organic molecules, proteins, inorganic clusters, and colloids can be assembled; however, polyelectrolytes are the most useful in this type of fabrication because better adhesion is observed with an increased number of atomic bonds.[130]

There have been several reports for functionalization of gold nanorods using layer-by-layer wrapping. Polyelectrolyte coating on nanorods is most successful when polymer chain length is comparable to nanoparticle size. Also, salt concentration is adjusted to screen the charged groups so a polymer does not remain extended by charge repulsion, but can wrap around a nanoparticle. Gole and Murphy first reported layer-by-layer polyelectrolyte deposition on CTAB gold nanorods using anionic poly (sodium-4-styrenesulfonate) and cationic poly(diallyldimethylammonium chloride) in the presence of NaCl. Wrapping up to four layers was confirmed by TEM, shifts in the LSPR as seen by UV-vis absorbance, and by ζ-potential measurements, which showed a flip in surface charge with each successive layer.[131] Later work by the same authors demonstrated wrapping CTAB of gold nanorods with poly(4-styrenesulfonic acid co-maleic acid) sodium salt, which generated maleic and sulfonic acid groups on the nanorod surface. Then, the enzyme trypsin was bound to the functionalized surface *via* click chemistry, EDC-mediated covalent attachment or electrostatic attachment. The biocatalytic activity of trypsin was quantified, and attachment *via* click chemistry was observed to reduce biological activity the least among the protein conjugation methods.[132] In another application, Huang *et al.*[133] loaded the dye Rhodamine 6G between layers of polyelectrolyte on gold nanorods and measured dye release after laser irradiation. Their results demonstrated photothermal molecular release was dependent upon the quantity and type of polyelectrolyte layers, which could be applicable to controlling release rates of drugs from a nanorod surface.

There are more methods to coat gold nanorods beyond what has been described here. Overgrowth of metals such as gold, silver, palladium and platinum can be carried out to produce bimetallic nanorods for catalysis[134] or SERS.[135,136] Polymers can be grafted to a gold surface *via* reversible addition-fragmentation chain transfer,[137] or grafted from the surface *via* atom-transfer radical polymerization.[34] A lipid bilayer can coat gold nanorods through self-assembly[138] or a thiol-gold linkage.[139] Anisotropic coatings of various kinds have been developed which might lead researchers to exploit field-dependent enhancements or self-

assembly of nanorods into interesting structures.[140] These reports represent how gold nanorods are a unique platform on which both organic and inorganic coatings of various morphologies can be supported.

In order for functionalized nanorods to be effective in a particular application there are many factors which may be taken into account. In biomedical applications stability against aggregation, cellular targeting, protein adsorption and nanoparticle toxicity are important considerations in ligand choice. Functionalized gold nanorods require nanorods to be stable in physiological environments, but aggregation is a common problem. However, investigating size stability of functionalized nanoparticles in cell culture media is a useful method to determine the likelihood of this issue.[141] Some researchers attach cell-targeting ligands to gold nanorods to achieve increased cell uptake. The chosen ligand and attachment method can also alter the effectiveness of a targeting method.[142] However, the effect of targeting may also be reduced by the presence of proteins, which are well-known to adsorb to nanoparticle surfaces in physiological environments.[143,144] Nanoparticle toxicity is another issue in biological environments, and cell death has been observed after nanoparticle exposure.[145] However, toxicity is not limited to whether cells live or die. Researchers have reported unanticipated surface chemistry-dependent changes in cell migratory behavior and gene expression after nanoparticle exposure.[146-148]

There are other factors which may be more important for energy, safety or measurement based applications of gold nanoparticles. CTAB gold nanorods are not stable in non-aqueous conditions, but there are coating methods which make it possible to transfer nanoparticles to organic solvents or to embed nanoparticles in polymeric films.[149,150] It is not always necessary to quantify surface coverage of a particular molecule, but ligand density can vary based on orientation, size, and crystal face. Methods such as X-ray photoelectron spectroscopy,[151] NMR spectroscopy,[152] and SERS[153] can be used to quantify and/or monitor ligand binding to a nanorod surface. While there are many surface chemistry-dependent factors which effect the success of gold nanorods in applications in the short-term, it is also important to consider long-term stability. Surface functionalization will play a large role in the environmental fate of gold nanorods, which is currently unknown, but a growing area of research interest.[154,155]

1.5 METHODS TO CHARACTERIZE GOLD NANORODS

There are many methods researchers can use to understand material characteristics of gold nanorods. Some nanomaterial properties which may be investigated include absolute dimensions, hydrodynamic size, nanoparticle concentration, aggregation state, ligand identity, ligand density, relative surface charge, optical absorbance, thermal transport, atomic composition, mechanical strength, and electromagnetic field strength.[156] Here, the discussion of techniques is focused on the methods frequently used to characterize gold nanorods and the material characteristics which can be examined by these techniques (Figure 1.9).

UV-vis absorbance spectroscopy is perhaps the most popular method used to characterize gold nanorods. UV-vis absorbance can be used to determine the locations of the transverse and longitudinal surface plasmon bands. This is useful because many applications require the longitudinal LSPR to be tuned to a particular wavelength, such as in laser photothermal heating.[36] The location of the longitudinal LSPR

is dependent on gold nanorod aspect ratio, but is also dependent on the medium dielectric constant and can indicate molecular binding on the gold surface.[7,30] Additionally, absorbance spectra are useful in understanding nanorod aggregation or assembly.[157,158] If the magnitude of a peak decreases, or if a peak shifts and become broader, this is a signal that the nanorods could be fusing together, are in close proximity, or are changing morphology.[159] The width of the peak is also an indication of the size dispersity of a gold nanorod solution. A narrower peak can indicate a narrow size distribution while a broader peak suggests a wider range of nanorod sizes are present.[87] A final application of UV-vis is in determining gold nanorod concentration. Absorbance is proportional to concentration and extinction. Extinction can be estimated using simulation,[7] but experimental calculation more accurately reflects nanorod size dispersity. Extinction coefficients for gold nanorods have been experimentally calculated by correlating absorbance with mass of gold (quantified by inductively-coupled plasma mass spectrometry) and atoms per nanorod (estimated by TEM). By this method, extinction coefficients for the longitudinal LSPR for gold nanorods with aspect ratio 2 to 4.5 can range from 2.5×10^9 to 5.5×10^9 $M^{-1}cm^{-1}$.[85] Therefore, it is possible to determine concentrations for gold nanorods in sub nanomolar concentration regimes.

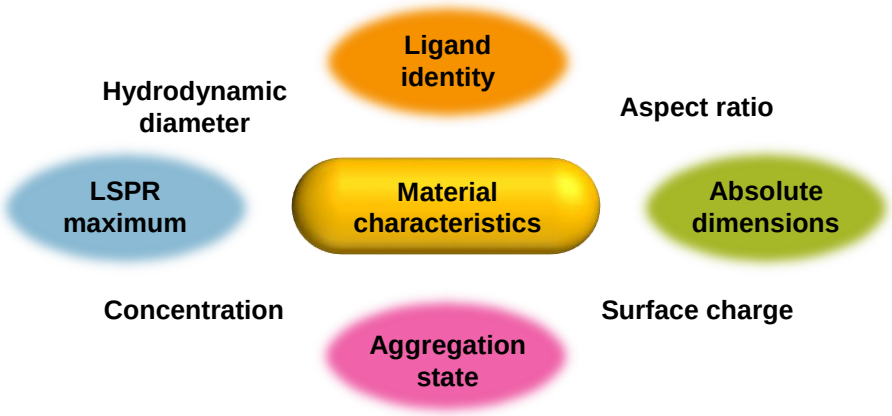

Figure 1.9 Some material characteristics of gold nanorods which can be determined using UV-vis absorbance spectroscopy, dynamic light scattering, ζ-potential measurements and electron microscopy.

Dynamic light scattering (DLS) is a technique used to determine hydrodynamic size and size distribution of nano and micro-sized particles in the 5 – 3000 nm size range. Nanoparticles exhibit Brownian motion so their individual positions in dispersion can fluctuate. A laser is passed through a colloidal dispersion and scattered light is collected by a detector. The angle and intensity of scattered light fluctuates in time depending on particle size. The Stokes-Einstein relationship (Equation 1.4) is the basis for the calculation of the radius (R) of spherical particles, where k_B is the Boltzmann constant, T is absolute temperature, η is solvent viscosity and D_H is the diffusion coefficient which is calculated from the scattering data.[160] Although the calculation assumes a spherical shape, DLS can still be useful for characterizing gold nanorods. A DLS histogram for gold nanorods exhibits two size distribution peaks, which may be correlated with the transverse and longitudinal axes. Additionally, because the diffusion coefficient is dependent on nanorod

shape and surface chemistry, changes in surface coating may be seen as differences in hydrodynamic size. These changes can also be monitored over time to investigate particle aggregation, nanorod-biomolecule, or nanorod-ligand interactions.[161,162]

$$D_H = \frac{k_B T}{3\pi\eta R} \tag{1.4}$$

Zeta potential measurements are usually performed by the same instrument as DLS because the technique also relies upon nanoparticle mobility. An electrode is inserted into the colloidal dispersion, and particles move in the field created by this electrode, in a direction which is dependent on their electrophoretic mobility. The direction of motion is determined by scattering from an incident laser, and is used to calculate the ζ-potential.[163] Nanoparticle ζ-potentials indicate the average surface charge and are useful for confirming if a surface functionalization of nanoparticles is successful. This has been demonstrated in thiol functionalization, layer-by-layer wrapping, and silica coating of gold nanorods.[11,30]

Characterization of individual gold nanorods is possible by electron microscopy. Scanning electron microscopy (SEM) and transmission electron microscopy (TEM) are optical characterization techniques used to obtain high resolution images of nanometer scale materials with a finely focused electron beam. Because electrons interact strongly with matter, and gold has a high Z value, gold nanoparticles scatter electrons. In SEM, scattered electrons are collected by a detector, so gold is seen as the bright areas in an image.[164] In TEM, the unscattered electrons pass through the sample, and form the bright regions of the image. The scattered electrons are not collected, so gold nanoparticles appear dark under TEM. Electron microscopy images can be analyzed to determine the absolute dimensions of nanoparticles, the thickness of a coating, interparticle interactions, and nanoparticle crystal structure in dried nanoparticle samples.[165,166]

A suite of techniques exist which can be used to characterize gold nanorods in both ensemble and individual measurements. These methods can be used jointly to confirm whether a synthesis or coating has been successful. Material characterization is critical to furthering applications of gold nanorods because materials design affects properties and therefore the success of a potential application.[167]

1.6 DISSERTATION OVERVIEW

The focus of this dissertation is in exploring how gold nanorod optical properties can be exploited for various applications. In each chapter, gold nanorods are prepared, the surface coating is modified and the materials are characterized by a variety of methods. We then demonstrate how these materials may be useful in order to gain a better understanding of material interactions, with a focus on three particular applications (Figure 1.10).

Chapter 2 explores how the fluorescence behavior of the infrared dye IRDye 800 is altered when near a gold nanorod surface. A method of mesoporous silica coating of gold nanorods is developed. The silica surface is functionalized with an azido silane, and the alkyne-modified dye is bound to the coated gold nanorods by copper-free click chemistry. Distance and wavelength dependent changes in fluorescence

behavior are examined by fluorescence emission and lifetime measurements. Additionally, fluorescence behavior of the dyes attached to mesoporous silica nanoparticles and dye-dye interactions are explored.

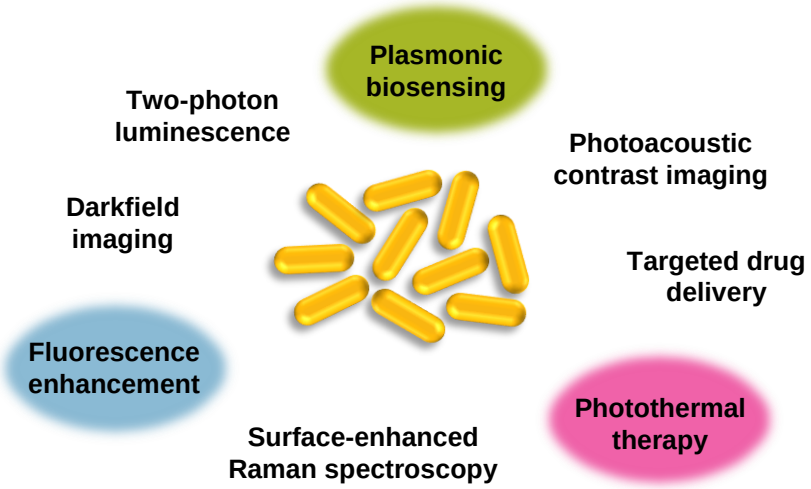

Figure 1.10 Examples of applications which make use of the optical properties of gold nanorods. In this dissertation the applications of interest are fluorescence enhancement, plasmonic biosensing and photothermal therapy.

In Chapter 3, we investigate how nanoparticles might interact with bacteria by monitoring the binding of bacterial lipopolysaccharides (LPS) to gold nanorods. Polymer-coated gold nanorod substrates are prepared and characterized. Attachment of LPS extracted from *Pseudomonas aeruginosa*, *Salmonella enterica*, and *Escherichia coli* to gold nanorods is monitored using LSPR-based plasmonic sensing and the number of LPS per nanorod is quantified. In addition, the association constants for LPS and each surface coating are determined by incubating LPS with colloidal gold nanorods.

Chapter 4 reviews the progress in thermal cancer treatments using gold nanoparticles. The optical properties of gold nanoparticles and mechanisms of heating are explained. The pioneering work of Halas, West, and El-Sayed in photothermal therapy is discussed. Additionally, radiofrequency-mediated thermal therapy with gold nanoparticles is reviewed. The majority of the chapter is focused on developments in nanoparticle design for photothermal therapy which have occurred since 2010. This includes nanoparticles with targeting ligands, imaging agents, photosensitizers, and chemotherapeutic drug loads. Both *in vitro* and *in vivo* studies are explored along with the progress of therapies toward clinical application. We conclude the discussion with a perspective on research directions those interested in this field may take.

Chapter 5 expands the range of photothermal therapy applications to inactivation of vegetative cells and endospores of the bacterium *Geobacillus stearothermophilus.* Gold nanorods having different surface chemistries are prepared and characterized. The nanorods are incubated with spores and vegetative cells and then irradiated with a continuous wave 785 nm laser diode. The effect of nanorod exposure and photothermal treatment on spores and cells is measured by colony counting. In addition, spores are imaged

by scanning electron microscopy to determine if there is any change in their morphology after gold nanorod exposure or photothermal treatment.

In Chapter 6 we consider how gold nanorod surface chemistry may be modified to maintain morphology and increase the stability of gold nanorod optical properties after exposure to high energy conditions. Gold nanorods are coated in mesoporous silica and then functionalized with various silanes. The stability of CTAB, silica-coated and silane functionalized nanorods against heating, up to 150°C, is explored using UV-vis and TEM measurements. Additionally, we examine how morphology of CTAB, silica-coated and silane-functionalized gold nanorods is altered when the nanorods are exposed to charging effects from a high-energy electron beam or high-energy femtosecond pulsed lasers.

Chapter 7 moves past nanotechnology applications to consider the environmental fate of gold nanomaterials. A library of gold nanoparticles having varied shape and surface chemistry is prepared and we examine the stability and mobility of engineered nanoparticles in environmental media. Nanoparticle stability against aggregation in simulated groundwater and two types of soil samples is explored by examining changes in absorbance characteristics and morphology. In addition, nanoparticle retention in columns containing soil and the polysaccharide alginate is quantified. The results of these studies may be useful to those considering how nanomaterial characteristics may influence the long-term fate of nanomaterial exposure in various environmental conditions.

1.7 REFERENCES

1. Freestone, I.; Meeks, N.; Sax, M.; Higgitt, C. The Lycurgus Cup – A Roman Nanotechnology. *Gold Bull.* **2007,** 40, 270-277.
2. Tanuma, S.; Powell, C. J.; Penn, D. R. Calculations of Electron Inelastic Mean Free Paths. IX. Data for 41 Elemental Solids Over the 50 eV to 30 keV Range. *Surf. Interface Anal.* **2011,** *43,* 689-713.
3. Huang, X.; Neretina, S.; El-Sayed, M. A. Gold Nanorods: From Synthesis and Properties to Biological and Biomedical Applications. *Adv. Mater.* **2009,** *21,* 4880-4910.
4. Mie, G. Beiträge zur Optik Trüber Medien, Speziell Kolloidaler Metallösungen *Ann. Phys.* **1908,** *330,* 377-445.
5. Horvath, H. Gustav Mie and the Scattering and Absorption of Light by Particles: Historic Developments and Basics. *J. Quant. Spectrosc. Radiat. Transfer* **2009,** *110,* 787-799.
6. Gans, R. Über die Form Ultramikroskopischer Goldteilchen. *Ann. Phys.* **1912,** *342,* 881-900.
7. Link, S.; Mohamed, M. B.; El-Sayed, M. A. Simulation of the Optical Absorption Spectra of Gold Nanorods as a Function of Their Aspect Ratio and the Effect of the Medium Dielectric Constant. *J. Phys. Chem. B* **1999,** *103,* 3073-3077.
8. Jain, P. K.; Lee, K. S.; El-Sayed, I. H.; El-Sayed, M. A. Calculated Absorption and Scattering Properties of Gold Nanoparticles of Different Size, Shape, and Composition: Applications in Biological Imaging and Biomedicine. *J. Phys. Chem. B* **2006,** *110,* 7238-7248.
9. Kelly, K. L.; Coronado, E.; Zhao, L. L; Schatz, G. C. The Optical Properties of Metal Nanoparticles: The Influence of Size, Shape, and Dielectric Environment. *J. Phys. Chem. B* **2003,** *107,* 668-677.
10. Huang, X.; Jain, P. K.; El-Sayed, I. H.; El-Sayed, M. A. Gold Nanoparticles: Interesting Optical Properties and Recent Applications in Cancer Diagnostics and Therapy. *Nanomedicine* **2007,** *2,* 681-693.
11. Abadeer, N. S.; Brennan, M. R.; Wilson, W. L.; Murphy, C. J. Distance and Plasmon Wavelength Dependent Fluorescence of Molecules Bound to Silica-Coated Gold Nanorods. *ACS Nano* **2014,** *8,* 8392-8406.
12. Sivapalan, S. T.; DeVetter, B. M.; Yang, T. K.; van Dijk, T.; Schulmerich, M. V.; Carney, P. S.; Bhargava, R.; Murphy, C. J. Off-Resonance Surface-Enhanced Raman Spectroscopy from Gold

Nanorod Suspensions as a Function of Aspect Ratio: Not What We Thought. *ACS Nano* **2013,** *7,* 2099-2105.
13. Sivapalan, S. T.; Vella, J. H.; Yang, T. K.; Dalton, M. J.; Swiger, R. N.; Haley, J. E.; Cooper, T. M.; Urbas, A. M.; Tan, L.-S.; Murphy, C. J. Plasmonic Enhancement of the Two Photon Absorption Cross Section of an Organic Chromophore Using Polyelectrolyte-Coated Gold Nanorods. *Langmuir* **2012,** *28,* 9147-9154.
14. Zijlstra, P.; Paulo, P. M. R.; Orrit, M. Optical Detection of Single Non-Absorbing Molecules Using the Surface Plasmon Resonance of a Gold Nanorod. *Nature Nanotech.* **2012,** *7,* 379-382.
15. Chon, J. W. M.; Bullen, C.; Zijlstra, P.; Gu, M. Spectral Encoding on Gold Nanorods Doped in a Silica Sol–Gel Matrix and Its Application to High-Density Optical Data Storage. *Adv. Funct. Mater.* **2007,** *17,* 875-880.
16. Zijlstra, P.; Chon, J. W. M. Five-Dimensional Optical Recording Mediated by Surface Plasmons in Gold Nanorods. *Nature* **2009,** *459,* 410-413.
17. Chang, S.; Li, Q.; Xiao, X.; Wong, K. Y.; Chen, T. Enhancement of Low Energy Sunlight Harvesting in Dye-Sensitized Solar Cells using Plasmonic Gold Nanorods. *Energy Environ. Sci.* **2012,** *5,* 9444-9448.
18. Chen, H.; Shao, L.; Li, Q.; Wang, J. Gold Nanorods and their Plasmonic Properties. *Chem. Soc. Rev.* **2013,** *42,* 2679-2724.
19. Murphy ,C. J.; Sau, T. K.; Gole, A. M.; Orendorff, C. J.; Gao, J.; Gou, L.; Hunyadi, S. E.; Li, T. Anisotropic Metal Nanoparticles: Synthesis, Assembly, and Optical Applications. *J. Phys. Chem. B* **2005,** *109,* 13857-13879.
20. Tong, L.; Wei, Q.; Wei, A.; Cheng, J.-X. Gold Nanorods as Contrast Agents for Biological Imaging: Optical Properties, Surface Conjugation and Photothermal Effects. *Photochem. Photobiol.* **2009,** *85,* 21-32.
21. Hu, R.; Yong, K.-T.; Roy, I.; Ding, H.; He, S.; Prasad, P. N. Metallic Nanostructures as Localized Plasmon Resonance Enhanced Scattering Probes for Multiplex Dark-Field Targeted Imaging of Cancer Cells. *J. Phys. Chem. C* **2009,** *113,* 2676-2684.
22. Wang, D.-S.; Hsu, F.-Y.; Lin, C. W. Surface Plasmon Effects on Two Photon Luminescence of Gold Nanorods. *Opt. Express* **2009,** *17,* 11350-11359.
23. Durr, N. J.; Larson, T.; Smith, D. K.; Korgel, B. A.; Sokolov, K.; Ben-Yakar, A. Two-Photon Luminescence Imaging of Cancer Cells Using Molecularly Targeted Gold Nanorods. *Nano Lett.* **2007,** *7,* 941-945.
24. He, W.; Henne, W. A.; Wei, Q.; Zhao, Y.; Doorneweerd, D. D.; Cheng, J.-X.; Low, P. S.; Wei, A. Two-Photon Luminescence Imaging of *Bacillus* Spores Using Peptide-Functionalized Gold Nanorods. *Nano Res.* **2008,** *1,* 450-456.
25. Wang, H.; Huff, T. B.; Zweifel, D. A.; He, W.; Low, P. S.; Wei, A.; Cheng, J.-X. *In vitro* and *In vivo* Two-Photon Luminescence Imaging of Single Gold Nanorods. *Proc. National Acad. Sci., U. S. A.* **2005,** *102,* 15752-15756.
26. Huang, J.; Wang, W.; Murphy, C. J.; Cahill, D. G. Resonant Secondary Light Emission from Plasmonic Au Nanostructures at High Electron Temperatures Created by Pulsed Laser Excitation. *Proc. Natl. Acad. Sci. U. S. A.* **2014,** *111,* 906-911.
27. Xu, M.; Wang, L. V. Photoacoustic Imaging in Biomedicine. *Rev. Sci. Instrum.* **2006,** *77,* 041101.
28. Jokerst, J. V.; Cole, A. J.; Van de Sompel, D.; Gambhir, S. S. Gold Nanorods for Ovarian Cancer Detection with Photoacoustic Imaging and Resection Guidance *via* Raman Imaging in Living Mice. *ACS Nano* **2012,** *6,* 10366-10377.
29. Becker, J.; Trügler, A.; Jakab, A.; Hohenester, U.; Sönnichsen, C. The Optimal Aspect Ratio of Gold Nanorods for Plasmonic Bio-sensing. *Plasmonics* **2010,** *5,* 161-167.
30. Abadeer, N. S.; Fülöp, G.; Chen, S.; Käll, M.; Murphy, C. J. Interactions of Bacterial Lipopolysaccharides with Gold Nanorod Surfaces Investigated by Refractometric Sensing. *ACS Appl. Mater. Interfaces* **2015,** *7,* 24915-24925.
31. Mayer, K. M.; Lee, S.; Liao, H.; Rostro, B. C.; Fuentes, A.; Scully, P. T.; Nehl, C. L.; Hafner, J. H. A Label-Free Immunoassay Based Upon Localized Surface Plasmon Resonance of Gold Nanorods. *ACS Nano* **2008,** *2,* 687-692.
32. Truong, P. L.; Cao, C.; Park, S.; Kim, M.; Sim, S. J. A New Method for Non-Labeling Attomolar Detection of Diseases Based on an Individual Gold Nanorod Immunosensor. *Lab Chip* **2011,** *11,* 2591-2597.

33. Min, Y.; Mao, C.; Xu, D.; Wang, J.; Liu, Y. Gold Nanorods for Platinum Prodrug Delivery. *Chem. Commun.* **2010,** *46,* 8424-8426.
34. Wei, Q.; Ji, J.; Shen, J. Synthesis of Near-Infrared Responsive Gold Nanorod/PNIPAAm Core/Shell Nanohybrids via Surface Initiated ATRP for Smart Drug Delivery. *Macromol. Rapid Commun.* **2008,** *29,* 645-650.
35. Jong, W. H. D.; Zuyd, H. Drug Delivery and Nanoparticles: Applications and Hazards. *Int. J. Nanomedicine* **2008,** *3,* 133-149.
36. Abadeer, N. S.; Murphy, C. J. Recent Progress in Cancer Thermal Therapy using Gold Nanoparticles. *J. Phys. Chem. C* **2016,** *120,* 4691-4716.
37. Huang, X.; El-Sayed, I. H.; Qian, W.; El-Sayed, M. A. Cancer Cell Imaging and Photothermal Therapy in the Near-Infrared Region by Using Gold Nanorods. *J. Am. Chem. Soc.* **2006,** *128,* 2115-2120.
38. Norman, R. S.; Stone, J. W.; Gole, A.; Murphy, C. J.; Sabo-Atwood, T. L. Targeted Photothermal Lysis of the Pathogenic Bacteria, *Pseudomonas aeruginosa*, with Gold Nanorods. *Nano Lett.* **2008,** *8,* 302-306.
39. Haynes, C. L.; McFarland, A. D.; Van Duyne, R. P. Surface-Enhanced Raman Spectroscopy. *Anal. Chem.* **2005,** *77,* 338-346.
40. Sharma, B.; Frontiera, R. R.; Henry, A.-H.; Ringe, E.; Van Duyne, R. P. SERS: Materials, Applications, and the Future. *Mater. Today* **2012**, *14*, 16-25.
41. Saute, B.; Premasiri, R.; Ziegler, L.; Narayanan, R. Gold Nanorods as Surface Enhanced Raman Spectroscopy Substrates for Sensitive and Selective Detection of Ultra-Low Levels of Dithiocarbamate Pesticides. *Analyst* **2012,** *137,* 5082-5087.
42. Brosseau, C. L.; Casadio, F.; Van Duyne, R. P. Revealing the Invisible: Using Surface-Enhanced Raman Spectroscopy to Identify Minute Remnants of Color in Winslow Homer's Colorless Skies. *J. Raman Spectrosc.* **2011,** *42,* 1305-1310.
43. Zhu, Y.; Kuang, H.; Xu, L.; Ma, W.; Peng, C.; Hua, Y.; Wang, L.; Xu, C. Gold Nanorod Assembly Based Approach to Toxin Detection by SERS. *J. Mater. Chem.* **2012,** *22,* 2387-2391.
44. Golighty, R. S.; Doering, W. E.; Natan, M. J. Surface-Enhanced Raman Spectroscopy and Homeland Security: A Perfect Match? *ACS Nano* **2009,** *3,* 2859-2869.
45. Bardhan, R.; Grady, N. K.; Cole, J. R.; Joshi, A.: Halas, N. J. Fluorescence Enhancement by Au Nanostructures: Nanoshells and Nanorods. *ACS Nano* **2009,** *3,* 744-752.
46. Stranik, O.; McEvoy, H. M.; McDonagh, C.; MacCraith, B. D. Plasmonic Enhancement of Fluorescence for Sensor Applications. *Sensors Actuators, B* **2005,** *107,* 148-153.
47. Lim ,S.-J.; An, B.-K.; Jung, S. D.; Chung, M.-A.; Park, S. Y. Photoswitchable Organic Nanoparticles and a Polymer Film Employing Multifunctional Molecules with Enhanced Fluorescence Emission and Bistable Photochromism. *Angew. Chem., Int. Ed.* **2004,** *43,* 6346-6350.
48. Vučković, J.; Lončar, M.; Scherer, A. Surface Plasmon Enhanced Light-Emitting Diode. *IEEE J. Quantum Electron.* **2000,** *36,* 1131-1144.
49. Shimizu, M.; Hiyama, T. Organic Fluorophores Exhibiting Highly Efficient Photoluminescence in the Solid State. *Chem. -Asian J.* **2010,** *5,* 1516-1531.
50. Aslan, K.; Gryczynski, I.; Malicka, J.; Matveeva, E.; Lakowicz, J. R.; Geddes, C. D. Metal-Enhanced Fluorescence: an Emerging Tool in Biotechnology. *Curr. Opin. Biotechnol.* **2005,** *16,* 55-62.
51. Mackowski, S.; Wörmke, S.; Maier, A. J.; Brotosudarmo, T. H. P.; Harutyunyan, H.; Hartschuh, A.; Govorov, A. O.; Scheer, H.; Bräuchle, C. Metal-Enhanced Fluorescence of Chlorophylls in Single Light-Harvesting Complexes. *Nano Lett.* **2008,** *8,* 558-564.
52. Chi, Y. S.; Byon, H. R.; Lee, B. S.; Kong, B.; Choi, H. C.; Choi, I. S. Polymeric Rulers: Distance-Dependent Emission Behaviors of Fluorophores on Flat Gold Surfaces and Bioassay Platforms Using Plasmonic Fluorescence Enhancement. *Adv. Funct. Mater.* **2008,** *18,* 3395-3402.
53. Ray, K.; Badugu, R.; Lakowicz, J. R. Distance-Dependent Metal-Enhanced Fluorescence from Langmuir-Blodgett Monolayers of Alkyl-NBD Derivatives on Silver Island Films. *Langmuir* **2006,** *22,* 8374-8378.
54. Li, X.; Kao, F.-J.; Chuang, C.-C.; He, S. Enhancing Fluorescence of Quantum Dots by Silica-Coated Gold Nanorods Under One- and Two-Photon Excitation. *Opt. Express* **2010,** *8,* 11335-11346.
55. Smith, A. M.; Nie, S. Semiconductor Nanocrystals: Structure, Properties, and Band Gap Engineering. *Acc. Chem. Res.* **2010,** *43,* 190-200.

56. Alivisatos, A. P. Semiconductor Clusters, Nanocrystals, and Quantum Dots. *Science,* **1996,** *272,* 933-937.
57. Bera, D.; Qian, L.; Tseng, T.-K.; Holloway, P. H. Quantum Dots and Their Multimodal Applications: A Review. *Materials* **2010,** *3,* 2260-2345.
58. Talapin, D. V.; Lee, J.-S.; Kovalenko, M. V.; Shevchenko, E. V. Prospects of Colloidal Nanocrystals for Electronic and Optoelectronic Applications. *Chem. Rev.* **2010,** *110,* 389-458.
59. Uechi, I.; Yamada, S. Photochemical and Analytical Applications of Gold Nanoparticles and Nanorods Utilizing Surface Plasmon Resonance. *Anal. Bioanal. Chem.* **2008,** *391,* 2411-2421.
60. Dreaden, E. C.; Alkilany, A. M.; Huang, X.; Murphy, C. J.: El-Sayed, M. A. The Golden Age: Gold Nanoparticles for Biomedicine. *Chem. Soc. Rev.* **2012,** *41,* 2740-2779.
61. Sau, T. K.; Murphy, C. J. Room Temperature, High-Yield Synthesis of Multiple Shapes of Gold Nanoparticles in Aqueous Solution. *J. Am. Chem. Soc.* **2004,** *126,* 8648-8649.
62. Kim, F.; Song, J. H.; Yang, P. Photochemical Synthesis of Gold Nanorods. *J. Am. Chem. Soc.* **2002,** *124,* 14316-14317.
63. Yu, Y.-Y.; Chang, S.-S.; Lee, C.-L.; Wang, C. R. C. Gold Nanorods: Electrochemical Synthesis and Optical Properties. *J. Phys. Chem. B* **1997,** *101,* 6661-6664.
64. Mohamed, M. B.; Ismail, K. Z.; Link, S.; El-Sayed, M. A. Thermal Reshaping of Gold Nanorods in Micelles. *J. Phys. Chem. B* **1998,** *102,* 9370-9374.
65. Lohse, S. E.; Murphy, C. J. The Quest for Shape Control: A History of Gold Nanorod Synthesis. *Chem. Mater.* **2013,** *25,* 1250−1261.
66. Xu, Q.; Bao, J.; Capasso, F.; Whitesides, G. M. Surface Plasmon Resonances of Free-Standing Gold Nanowires Fabricated by Nanoskiving. *Angew. Chem., Int. Ed.* **2006,** *45,* 3631-3635.
67. Murphy, C. J.; Thompson, L. B.; Chernak, D. J.; Yang, J. A.; Sivapalan, S. T.; Boulos, S. P.; Huang, J.; Alkilany, A. M.; Sisco, P. N. Gold Nanorod Crystal Growth: From Seed-Mediated Synthesis to Nanoscale Sculpting. *Curr. Opin. Colloid Interface Sci.* **2011,** *16,* 128-134.
68. Jana, N. R.; Gearheart, L.; Murphy, C. J. Wet Chemical Synthesis of High Aspect Ratio Cylindrical Gold Nanorods. *J. Phys. Chem. B* **2001,** *105,* 4065-4067.
69. Busbee, B. D.; Obare, S. O.; Murphy, C. J. An Improved Synthesis of High-Aspect-Ratio Gold Nanorods. *Adv. Mater.* **2003,** *15,* 414-416.
70. Johnson, C. J.; Dujardin, E.; Davis, S. A.; Murphy, C. J.: Mann, S. Growth and Form of Gold Nanorods Prepared by Seed-Mediated, Surfactant-Directed Synthesis. *J. Mater. Chem.* **2002,** *12,* 1765–1770.
71. Gole, A.; Murphy, C. J. Seed-Mediated Synthesis of Gold Nanorods: Role of the Size and Nature of the Seed. *Chem. Mater.* **2004,** *16,* 3633-3640.
72. Carbó-Argibay, E.; Rodríguez-González, B.; Gómez-Graña, S.; Guerrero-Martínez, A.; Pastoriza-Santos, I.; Pérez-Juste, J.; Liz-Marzán, L. M. The Crystalline Structure of Gold Nanorods Revisited: Evidence for Higher-Index Lateral Facets. *Angew. Chem., Int. Ed.* **2010,** 122, 9587-9590.
73. Edgar, J. A.; McDonagh, A. M.; Cortie, M. B. Formation of Gold Nanorods by a Stochastic “Popcorn” Mechanism. *ACS Nano* **2012,** *6,* 1116-1125.
74. Xial, J.; Qi, L. Surfactant-Assisted, Shape-Controlled Synthesis of Gold Nanocrystals. *Nanoscale,* **2011,** *3,* 1383-1396.
75. Nikoobakht, B.; El-Sayed, M. A. Evidence for Bilayer Assembly of Cationic Surfactants on the Surface of Gold Nanorods. *Langmuir* **2001,** *17,* 6368-6374.
76. Gao, J.; Bender, C. M.; Murphy, C. J. Dependence of the Gold Nanorod Aspect Ratio on the Nature of the Directing Surfactant in Aqueous Solution. *Langmuir* **2003,** *19,* 9065-9070.
77. Smith, D. K.; Miller, N. R.; Korgel, B. A. Iodide in CTAB Prevents Gold Nanorod Formation. *Langmuir* **2009,** *25,* 9518–9524.
78. Rayavarapu, R. G.; Ungureanu, C.; Krystek, P.; van Leeuwen, T. G.; Manohar, S. Iodide Impurities in Hexadecyltrimethylammonium Bromide (CTAB) Products: Lot-Lot Variations and Influence on Gold Nanorod Synthesis. *Langmuir* **2010,** *26,* 5050-5055.
79. Sau, T. K.; Murphy, C. J. Seeded High Yield Synthesis of Short Au Nanorods in Aqueous Solution. *Langmuir* **2004,** *20,* 6414-6420.
80. Sun, Y.; Xia, Y. Shape-Controlled Synthesis of Gold and Silver Nanoparticles. *Science,* **2002,** *298,* 2176-2179.

81. Niidome, Y.; Nishioka, K.; Kawasaki, H.; Yamada, S. Rapid Synthesis of Gold Nanorods by the Combination of Chemical Reduction and Photoirradiation Processes; Morphological Changes Depending on the Growing Processes. *Chem. Commun.* **2003,** *39,* 2376-2377.
82. Nikoobakht, B.; El-Sayed, M. A. Preparation and Growth Mechanism of Gold Nanorods (NRs) Using Seed-Mediated Growth Method. *Chem. Mater.* **2003,** *15,* 1957-1962.
83. Hubert, F.; Testard, F.; Spalla, O. Cetyltrimethylammonium Bromide Silver Bromide Complex as the Capping Agent of Gold Nanorods. *Langmuir* **2008,** *24,* 9219-9222.
84. Liu, M.; Guyot-Sionnest, P. Mechanism of Silver(I)-Assisted Growth of Gold Nanorods and Bipyramids. *J. Phys. Chem. B* **2005,** *109,* 22192-22200.
85. Orendorff, C. J.; Murphy, C. J. Quantitation of Metal Content in the Silver-Assisted Growth of Gold Nanorods. *J. Phys. Chem. B* **2006,** *110,* 3990-3994.
86. Jackson, S. R.; McBride, J. R.; Rosenthal, S. J.; Wright, D. W. Where's the Silver? Imaging Trace Silver Coverage on the Surface of Gold Nanorods. *J. Am. Chem. Soc.* **2014,** *136,* 5261−5263.
87. Vigderman, L.; Zubarev, E. R. High-Yield Synthesis of Gold Nanorods with Longitudinal SPR Peak Greater than 1200 nm Using Hydroquinone as a Reducing Agent. *Chem. Mater.* **2013,** *25,* 1450−1457.
88. Ye, X.; Jin, L.; Caglayan, H.; Chen, J.; Xing, G.; Zheng, C.; Doan-Nguyen, V.; Kang, Y.; Engheta, N.; Kagan, C. R.; Murray, C. B. Improved Size-Tunable Synthesis of Monodisperse Gold Nanorods through the Use of Aromatic Additives. *ACS Nano* **2012,** *6,* 2804-2817.
89. Ye, X.; Zheng, C.; Chen, J.; Gao, Y.; Murray, C. B. Using Binary Surfactant Mixtures To Simultaneously Improve the Dimensional Tunability and Monodispersity in the Seeded Growth of Gold Nanorods. *Nano Lett.* **2013,** *13,* 765−771
90. Scarabelli, L.; Grzelczak, M.; Liz-Marzán, L. M. Tuning Gold Nanorod Synthesis through Prereduction with Salicylic Acid. *Chem. Mater.* **2013,** *25,* 4232-4238.
91. Boleininger, J.; Kurz, A.; Reuss, V.; Sönnichsen, C. Microfluidic Continuous Flow Synthesis of Rod-Shaped Gold and Silver Nanocrystals. *Phys. Chem. Chem. Phys.* **2006,** *8,* 3824–3827.
92. Jana, N. R. Gram-Scale Synthesis of Soluble, Near-Monodisperse Gold Nanorods and Other Anisotropic Nanoparticles. *Small* **2005,** *1,* 875-882.
93. Lohse, S. E.; Eller, J. R.; Sivapalan, S. T.; Plews, M. R.; Murphy, C. J. A Simple Millifluidic Benchtop Reactor System for the High-Throughput Synthesis and Functionalization of Gold Nanoparticles with Different Sizes and Shapes. *ACS Nano* **2013,** *7,* 4135-4150.
94. Skrabalak, S. E.; Brutchey, R. L. Going with the Flow: Continuous Flow Routes to Colloidal Nanoparticles. *Chem. Mater.* **2016,** *28,* 1003-1005.
95. Gómez-Graña, S.; Hubert, F.; Testard, F.; Guerrero-Martínez, A.; Grillo, I.; Liz-Marzán, L. M.; Spalla, O. Surfactant (Bi)Layers on Gold Nanorods. *Langmuir* **2012,** *28,* 1453-1459.
96. Murphy, C. J.; Thompson, L. B.; Alkilany, A. M.; Sisco, P. N.; Boulos, S. N.; Sivapalan, S.; Yang, J. A.; Chernak, D. J.; Huang, J. The Many Faces of Gold Nanorods. *J. Phys. Chem. Lett.* **2010**, *1*, 2867-2875.
97. Hauck, T. S.; Ghazani, A. A.; Chan, W. C. W. Assessing the Effect of Surface Chemistry on Gold Nanorod Uptake, Toxicity, and Gene Expression in Mammalian Cells. *Small* **2008,** *4,* 153-159.
98. El Khoury, J. M. E.; Zhou, X.; Qu, L.; Dai, L.; Urbas, A.; Li, Q. Organo-Soluble Photoresponsive Azo Thiol Monolayer-Protected Gold Nanorods. *Chem. Commun.* **2009,** *45,* 2109-2111.
99. Alkilany, A. M.; Nagaria, P.; Hexel, C. R.; Shaw, T. J.; Murphy, C. J.; Wyatt, M. D. Cellular Uptake and Cytotoxicity of Gold Nanorods: Molecular Origin of Cytotoxicity and Surface Effects. *Small* **2009**, *5*, 701-708.
100. Sperling, R. A.; Parak, W. J. Surface Modification, Functionalization and Bioconjugation of Colloidal Inorganic Nanoparticles. *Phil. Trans. R. Soc. A* **2010,** *368,* 1333-1383.
101. Grönbeck, H.; Curioni, A.; Andreoni, W. Thiols and Disulfides on the Au(111) Surface: The Headgroup-Gold Interaction. *J. Am. Chem. Soc.* **2000,** *122,* 3839-3842.
102. Nuzzo, R. G.; Allara, D. L. Adsorption of Bifunctional Organic Disulfides on Gold Surfaces. *J. Am. Chem. Soc.* **1983,** *105,* 4481-4483.
103. Bain, C. D.; Troughton, E. B.; Tao, Y.-T.; Evall, J.; Whitesides, G. M.; Nuzzo, R. G. Formation of Monolayer Films by the Spontaneous Assembly of Organic Thiols from Solution onto Gold. *J. Am. Chem. Soc.* **1989,** *111,* 321-335.
104. Giersig, M.; Mulvaney, P. Preparation of Ordered Colloid Monolayers by Electrophoretic Deposition. *Langmuir* **1993,** *9,* 3408-3413.

105. Woehrle, G. H.; Brown, L. O.; Hutchison, J. E. Thiol-Functionalized, 1.5-nm Gold Nanoparticles through Ligand Exchange Reactions: Scope and Mechanism of Ligand Exchange. *J. Am. Chem. Soc.* **2005,** *127,* 2172-2183.
106. Love, J. L.; Estroff, L. A.; Kriebel, J. K.; Nuzzo, R. G.; Whitesides, G. M. Self-Assembled Monolayers of Thiolates on Metals as a Form of Nanotechnology. *Chem. Rev.* **2005,** *105,* 1103-1169.
107. Niidome, T.; Yamagata, M.; Okamoto, Y.; Akiyama, Y.; Takahashi, H.; Kawano, T.; Katayama, Y.; Niidome, Y. PEG-Modified Gold Nanorods with a Stealth Character for *In vivo* Applications. *J. Controlled Release* **2006,** *114,* 343-347.
108. Vigderman, L.; Manna, P.; Zubarev, E. R. Quantitative Replacement of Cetyl Trimethylammonium Bromide by Cationic Thiol Ligands on the Surface of Gold Nanorods and Their Extremely Large Uptake by Cancer Cells. *Angew. Chem., Int. Ed.* **2012,** *51,* 636 –641
109. Wijaya, A.; Schaffer, S. B.; Pallares, I. G.; Hamad-Schifferli, K. Selective Release of Multiple DNA Oligonucleotides from Gold Nanorods. *ACS Nano* **2009,** *3,* 80-86.
110. Caswell, K. K.; Wilson, J. N.; Bunz, U. H. F.; Murphy, C. J. Preferential End-to-End Assembly of Gold Nanorods by Biotin-Streptavidin Connectors. *J. Am. Chem. Soc.* **2003,** *125,* 13914-13915.
111. Chang, J.-Y.; Wu, H.; Chen, H.; Ling, Y.-C.; Tan, W. Oriented Assembly of Au Nanorods using Biorecognition System. *Chem. Commun.* **2005,** *41,* 1092-1094.
112. Wu, W.-C.; Tracy, J. B. Large-Scale Silica Overcoating of Gold Nanorods with Tunable Shell Thicknesses. *Chem. Mater.* **2015**, *27,* 2888-2894.
113. Lin, Y.-S.; Abadeer, N.; Hurley, K. R.; Haynes, C. L. Ultrastable, Redispersible, Small, and Highly Organomodified Mesoporous Silica Nanotherapeutics. *J. Am. Chem. Soc.* **2011**, *133,* 20444-20457.
114. Slowing, I. I.; Trewyn, B. G.; Giri, S.; Lin, V. S.-Y. Mesoporous Silica Nanoparticles for Drug Delivery and Biosensing Applications. *Adv. Funct. Mater.* **2007,** *17,* 1225-1236.
115. Liu, J.; Detrembleur, C.; De Pauw-Gillet, M.-C.; Mornet, S.; Jérôme, C.; Duguet, E. Gold Nanorods Coated with Mesoporous Silica Shell as Drug Delivery System for Remote Near Infrared Light-Activated Release and Potential Phototherapy. *Small* **2015**, *11,* 2323-2332.
116. Stöber, W.; Fink, A.; Bohn, E. Controlled Growth of Monodisperse Silica Spheres in the Micron Size Range. *J. Colloid Interface Sci.* **1968**, *26,* 62-69.
117. Gorelikov, I.; Matsuura, N. Single-Step Coating of Mesoporous Silica on Cetyltrimethyl Ammonium Bromide-Capped Nanoparticles. *Nano Lett.* **2008**, *8* (1), 369-373.
118. Brinker, C. J.; Scherer, G. W. *Sol-Gel Science*; Academic Press, 1990.
119. Zhan, Q.; Qian, J.; Li, X.; He, S. A Study of Mesoporous Silica-Encapsulated Gold Nanorods as Enhanced Light Scattering Probes for Cancer Cell Imaging. *Nanotechnology* **2010,** *21,* 055704.
120. Cong, H.: Toftegaard, R.; Arnbjerg, J.; Ogilby, P. R. Silica-Coated Gold Nanorods with a Gold Overcoat: Controlling Optical Properties by Controlling the Dimensions of a Gold-Silica-Gold Layered Nanoparticle. *Langmuir* **2010,** *26,* 4188-4195.
121. Wang, F.; Cheng, S.; Bao, Z.; Wang, J. Anisotropic Overgrowth of Metal Heterostructures Induced by a Site-Selective Silica Coating. *Angew. Chem., Int. Ed.* **2013**, *52,* 10344-10348.
122. Pastoriza-Santos, I.; Pérez-Juste, J.; Liz-Marzán, L. M. Silica-Coating and Hydrophobation of CTAB-Stabilized Gold Nanorods. *Chem. Mater.* **2006,** *18,* 2465-2467.
123. Chen, Y.-S.; Frey, W.; Kim, S.; Homan, K.; Kruizinga, P.; Sokolov, K.; Emelianov, S. Enhanced Thermal Stability of Silica-Coated Gold Nanorods for Photoacoustic Imaging and Image-Guided Therapy. *Opt. Express* **2010,** *18,* 8867-8878.
124. Sendroiu, I. E.; Warner, M. E.; Corn, R. M. Fabrication of Silica-Coated Gold Nanorods Functionalized with DNA for Enhanced Surface Plasmon Resonance Imaging Biosensing Applications. *Langmuir* **2009,** *25,* 11282-11284.
125. Caruso, F.; Caruso, R. A.; Möhwald, H. Nanoengineering of Inorganic and Hybrid Hollow Spheres by Colloidal Templating. *Science* **1998,** *282,* 1111-1116.
126. Caruso, F. Nanoengineering of Particle Surfaces. *Adv. Mater.* **2001,** *13,* 11-22.
127. Kirkland, J. J. Porous Thin-Layer Modified Glass Bead Supports for Gas Liquid Chromatography. *Anal. Chem.* **1965,** *37,* 1458-1461.
128. Iler, R. K. Multilayers of Colloidal Particles. *J. Colloid Interface Sci.* **1966,** *21,* 569-594.
129. Lvov, Y.; Decher, G.; Sukhorukov, G. Assembly of Thin Films by Means of Successive Deposition of Alternate Layers of DNA and Poly(allylamine). *Macromolecules* **1993,** *26,* 5396-5399.
130. Decher, G. Fuzzy Nanoassemblies: Toward Layered Polymeric Multicomposites. *Science* **1997,** *277,* 1232-1237

131. Gole, A.; Murphy, C. J. Polyelectrolyte-Coated Gold Nanorods: Synthesis, Characterization and Immobilization. *Chem. Mater.* **2005,** *17,* 1325-1330.
132. Gole, A.; Murphy, C. J. Azide-Derivatized Gold Nanorods: Functional Materials for "Click" Chemistry. *Langmuir* **2008,** *24,* 266-272.
133. Huang, J.; Jackson, K. S.; Murphy, C. J. Polyelectrolyte Wrapping Layers Control Rates of Photothermal Molecular Release from Gold Nanorods. *Nano Lett.* **2012,** *12,* 2982-2987.
134. Khanal, B. P.; Zubarev, E. R. Polymer-Functionalized Platinum-On-Gold Bimetallic Nanorods. *Angew. Chem., Int. Ed.* **2009,** *48,* 6888 –6891.
135. Song, J. H.; Kim, F.; Kim, D.; Yang, P. Crystal Overgrowth on Gold Nanorods: Tuning the Shape, Facet, Aspect Ratio, and Composition of the Nanorods. *Chem. Eur. J.* **2005,** *11,* 910-916.
136. Cho, E. C.; Camargo, P. H. C.; Xia, Y. Synthesis and Characterization of Noble-Metal Nanostructures Containing Gold Nanorods in the Center. *Adv. Mater.* **2010,** *22,* 744-748.
137. Hotchkiss, J. W.; Lowe, A. B.; Boyes, S. G. Surface Modification of Gold Nanorods with Polymers Synthesized by Reversible Addition-Fragmentation Chain Transfer Polymerization. *Chem. Mater.* **2007,** *19,* 6-13.
138. Orendorff, C. J.; Alam, T. M.; Sasaki, D. Y.; Bunker, B. C.; Voigt, J. A. Phospholipid-Gold Nanorod Composites. *ACS Nano* **2009,** *3,* 971-983.
139. Castellana, E. T.; Gamez, R. C.; Russel, D. H. Label-Free Biosensing with Lipid-Functionalized Gold Nanorods. J*. Am. Chem. Soc.* **2011,** *133,* 4182-4185.
140. Burrows, N. D.; Vartanian, A. M.; Abadeer, N. S.; Grzincic, E. M.; Jacob, L. M.; Lin, W.; Li, J.; Dennison, J. M.; Hinman, J. G.; Murphy, C. J. Anisotropic Nanoparticles and Anisotropic Surface Chemistry. *J. Phys. Chem. Lett.* **2016,** *7,* 632-641.
141. Yang, J. A.; Lohse, S. E.; Murphy, C. J. Tuning Cellular Response to Nanoparticles *via* Surface Chemistry and Aggregation," *Small* **2014,** *10,* 1642-1651.
142. Alkilany, A. M.; Boulos, S. P.; Lohse, S. E.; Thompson, L. B.; Murphy, C. J. Homing Peptide-Conjugated Gold Nanorods: The Effect of Amino Acid Sequence Display on Nanorod Uptake and Cellular Proliferation. *Bioconjugate Chem.* **2014,** *25,* 1162-1171.
143. Lundqvist, M.; Stigler, J.; Elia, G.; Lynch, I.; Cedervall, T.; Dawson, K. A. Nanoparticle Size and Surface Properties Determine the Protein Corona with Possible Implications for Biological Impacts. *Proc. Natl. Acad. Sci. U. S. A.* **2008,** *105,* 14265-14270.
144. Lin, W.; Insley T.; Tuttle, M. D.; Zhu, L.; Berthold, D. A.; Král, P.; Rienstra, C. M.; Murphy, C. J. Control of Protein Orientation on Gold Nanoparticles. *J. Phys. Chem C* **2015,** *119,* 21035-21043.
145. Feng, Z. V.; Gunsolus, I. L.; Qiu, T. A.; Hurley, K. R.; Nyberg, L. H.; Frew, H.; Johnson, K. P.; Vartanian, A. M.; Jacob, L. M.; Lohse, S. E.; Torelli, M. D.; Hamers, R. J.; Murphy, C. J.; Haynes, C. L. Impacts of Gold Nanoparticle Charge and Ligand Type on Surface Binding and Toxicity to Gram-Negative and Gram-Positive Bacteria. *Chem. Sci.* **2015,** *6,* 5186-5196.
146. Grzincic, E. M.; Murphy, C. J. Gold Nanorods Indirectly Promote Migration of Metastatic Human Breast Cancer Cells in Three-Dimensional Cultures. *ACS Nano* **2015,** *9,* 801-6816.
147. Grzincic, E. M.; Yang, J. A.; Drnevich, J.; Falagan-Lotsch, P.; Murphy, C. J. Global Transcriptomic Analysis of Model Human Cell Lines Exposed to Surface-Modified Gold Nanoparticles: The Effect of Surface Chemistry. *Nanoscale* **2015,** *7,* 1349-1362.
148. Dominguez, G. A.; Lohse, S. E.; Torelli, M. D.; Murphy, C. J.; Hamers, R. J.; Orr, G.; Klaper, R. D. Effects of Charge and Surface Ligand Properties of Nanoparticles on Oxidative Stress and Gene Expression within the Gut of *Daphnia magna*. *Aquat. Toxicol.* **2015,** *162,* 1-9.
149. Alkilany, A. M.; Yaseen, A. I. B.; Park, J.; Eller, J. R.; Murphy, C. J. Facile Phase Transfer of Gold Nanoparticles from Aqueous Solution to Organic Solvents with Thiolated Poly(ethylene glycol). *RSC Adv.* **2014,** *4,* 52676-52679.
150. Alkilany, A. M.; Thompson, L. B.; Murphy, C. J. Polyelectrolyte Coating Provides a Facile Route to Suspend Gold Nanorods in Polar Organic Solvents and Hydrophobic Polymers. *ACS Appl. Mater. Interfaces* **2010,** *2,* 3417-3421.
151. Torelli, M. D.; Putans, R. A.; Tan, Y.; Lohse, S. E.; Murphy, C. J.; Hamers, R. J. Quantitative Determination of Ligand Densities on Nanomaterials by X-ray Photoelectron Spectroscopy. *ACS Appl. Mater. Interfaces* **2015,** *7,* 1720-1725.
152. Smith, A. M.; Marbella, L. E.; Johnston, K. A.; Hartmann, M. J.; Crawford, S. E.; Kozycz, L. M.; Seferos, D. S.; Millstone, J. E. Quantitative Analysis of Thiolated Ligand Exchange on Gold Nanoparticles Monitored by 1H NMR Spectroscopy. *Anal. Chem.* **2015,** *87,* 2771-2778.

153. DeVetter, B. M.; Mukherjee, P.; Murphy, C. J.; Bhargava, R. Measuring Binding Kinetics of Aromatic Thiolated Molecules with Nanoparticles *via* Surface-Enhanced Raman Spectroscopy. *Nanoscale* **2015,** *7,* 8766-8775.
154. Burns, J. M.; Pennington, P. L.; Sisco, P. N.; Frey, R.; Kashiwada, S.; Fulton, M. H.; Scott, G. I.; Decho, A. W.; Murphy, C. J.; Shaw, T.; Ferry, J. L. Surface Charge Controls the Fate of Au Nanorods in Saline Estuaries. *Environ. Sci. Technol.* **2013,** *47,* 12844-12851.
155. Sabo-Attwood, T.; Unrine, J. M.; Stone, J. W.; Murphy, C. J.; Ghoshroy, S.; Blom, D.; Bertsch, P. M.; Newman, L. A. Uptake, Distribution and Toxicity of Gold Nanoparticles in Tobacco (*Nicotiana xanthi*) Seedlings. *Nanotoxicology,* **2012, 6,** 353-360.
156. López-Serrano, A.; Olivas, R. M.; Landaluze, J. S.; Cámara, C. Nanoparticles: A Global Vision. Characterization, Separation, and Quantification Methods. Potential Environmental and Health Impact. *Anal. Methods* **2014,** *6,* 38-56.
157. Ma, Z.; Tian, L.; Wang, T.; Wang, C. Optical DNA Detection Based on Gold Nanorods Aggregation. *Anal. Chim, Acta* **2010,** *673,* 179-184.
158. Gole, A.; Murphy, C. J. Biotin-Streptavidin-Induced Aggregation of Gold Nanorods: Tuning Rod-Rod Orientation. *Langmuir* **2005,** *21,* 10756-10762.
159. Dujardin, E.; Hsin, L.-B.; Wang, C. R.; Mann, S. DNA-Driven Self-Assembly of Gold Nanorods. *Chem. Commun.* **2001,** *37,* 1264-1265.
160. Pecora, R. Dynamic Light Scattering Measurement of Nanometer Particles in Liquids. *J. Nanoparticle Res.* **2000,** *2,* 123-131.
161. Liu, H.; Pierre-Pierre, N.; Huo, Q. Dynamic Light Scattering for Gold Nanorod Size Characterization and Study of Nanorod-Protein Interactions. *Gold Bull.* **2012,** *45,* 187-195.
162. Jans, H.; Liu, X.; Austin, L.; Maes, G.; Huo, Q. Dynamic Light Scattering as a Powerful Tool for Gold Nanoparticle Bioconjugation and Biomolecular Binding Studies. *Anal. Chem.* **2009,** *81,* 9425-432.
163. Xu, R. Progress in Nanoparticles Characterization: Sizing and Zeta Potential Measurement. *Particuology* **2008,** *6,* 112-115.
164. Van Dyck, D.; de Jong, A. F. Ultimate Resolution and Information in Electron Microscopy: General Principles. *Ultramicroscopy* **1992,** *47,* 266-281.
165. Wang, Z. L. Transmission Electron Microscopy of Shape-Controlled Nanocrystals and Their Assemblies. *J. Phys. Chem. B* **2000,** *104,* 1153-1175.
166. Flannigan, D. J.; Zewail, A. H. 4D Electron Microscopy: Principles and Applications. *Acc. Chem. Res.* **2012,** *45,* 1828-1839.
167. Pérez-Juste, J.; Pastoriza-Santos, I.; Liz-Marzán, L. M.; Mulvaney, P. Gold Nanorods: Synthesis, Characterization and Applications. *Coord. Chem. Rev.* **2005,** *249,* 1870-1901.

CHAPTER 2:
DISTANCE AND PLASMON WAVELENGTH DEPENDENT FLUORESCENCE OF MOLECULES BOUND TO SILICA-COATED GOLD NANORODS

2.1 INTRODUCTION

Gold nanorods are rod-shaped plasmonic nanoparticles with tunable, size-dependent optical responses.[1-3] The collective oscillation of conduction band electrons gives rise to two plasmon resonance bands, which can be tuned from the visible to the near infrared.[4-6] Gold nanorods strongly absorb and scatter light, especially at wavelengths resonant with their surface plasmons. Due to photon confinement, strong electromagnetic fields are generated at the metal surface.[4,7] Electromagnetic field effects give rise to a variety of optical processes such as laser photothermal heating,[8] Raman resonances,[9] two-photon absorption[10] and emission[11-15] which are often enhanced near a gold nanorod surface.

It is known that fluorescence excitation and emission can be altered near a plasmonic nanoparticle.[16,17] The electromagnetic field strength is most concentrated at the surface of plasmonic nanoparticles and decays exponentially as a function of distance. The nanoparticle and fluorophore form an electromagnetically coupled system, which when excited, leads to additional de-excitation pathways. This results in higher excitation rates and/or enhanced radiative decay rates of the fluorophore and fluorescence emission enhancement.[11-13] However, in some systems, fluorescence may instead be quenched if the excited fluorophores relax rapidly by nonradiative energy transfer into the surface plasmon resonance.[18,19]

Because of these two competing processes, literature values of enhancement are strongly varied. Researchers have observed nearly 100% emission quenching to over 1000 fold enhancement in emission intensity.[11-25] Of course, both enhancement and quenching of fluorescence are distance dependent. At a certain distance from the plasmonic surface, energy transfer into the plasmon band is reduced but the electromagnetic field strength can still be great enough to enhance fluorescence emission.[15,16] Strongest enhancement is usually observed in the 10 – 20 nm range from the plasmonic surface.[20-23] In addition, fluorescence near plasmonic nanoparticles is dependent on plasmon wavelength. Some researchers have suggested that fluorescence coupling to the nanoparticle may be stronger when the plasmon band overlaps with a fluorophore's absorbance or emission profile. Since gold nanorod plasmon bands are easily tuned between 500 and 900+ nm, gold nanorods are useful for studies of plasmon-enhanced fluorescence.[15,24,25]

If applications of plasmon-enhanced fluorescence techniques are to be realized, it is essential to gain more insight into the phenomenon of plasmon-enhanced fluorescence. Fluorescent molecules are used in imaging and sensing with biological and electronic applications ranging from detection of disease biomarkers to single molecule imaging and organic electronics. However, fluorophores are often unstable, with low quantum yields and can be sensitive to photobleaching. This is especially true for near infrared

---

[*] This chapter is reprinted with permission from: Nardine S. Abadeer, Marshall R. Brennan, William L. Wilson and Catherine J. Murphy. *ACS Nano* **2014,** *8,* 8392-8406. Copyright (2014) American Chemical Society.

fluorophores, limiting their applications.[11,15,16,26] Enhancement of fluorescence emission *via* coupling to plasmonic particles is one potential method to increase the effectiveness of weak fluorophores.[14,15]

To date, fluorescence enhancement studies have focused on gold or silver nanostructured surfaces or nanoparticles immobilized on a surface.[16,25] This allows for good control of nanoparticle-fluorophore distance and nanoparticle aggregation is reduced; however, applications of fluorescence enhancement in this geometry are rather limited.[27] There are some examples of fluorescence enhancement with colloidal nanomaterials, but control of fluorophore-particle distance is more difficult to achieve. Oftentimes, the fluorophore is incorporated into a shell or between polymer layers *versus* on the surface.[11-24] In addition, dye-surface and dye-dye interactions are rarely accounted for when trying to understand changes in fluorescence.[21] To our knowledge, there are no solution-based studies, with gold nanorods, that include both distance and plasmon wavelength dependent fluorescence. Moreover, none explore and exclude possible dye-dye interactions or dye-surface interactions that may impact fluorescence behavior.

In order to gain a deeper understanding of plasmon-enhanced fluorescence, we carried out a study of distance and plasmon wavelength dependent fluorescence of an infrared dye ("IRDye") bound to silica-coated gold nanorods. IRDye 800CW DBCO has a dibenzylcyclooctyne (DBCO) functionality allowing for attachment *via* click chemistry. The IRDye imaging agents, developed by LI-COR, are specially designed to potentially aid in disease detection and to monitor drug treatments.[28] IRDye absorbance/emission profiles are in the "water window" (700-1100 nm), so they are potentially useful in biological applications. However, IRDye 800CW DBCO has a quantum yield of only 0.07, limiting its application. Therefore, it could serve as a good candidate for plasmon-enhanced fluorescence.[11] Gold nanorods are ideal for studies of plasmon-enhanced fluorescence. Gold does not experience oxidation that often occurs with silver, and gold nanorods absorb/scatter more strongly than smaller gold spheres resulting in stronger field effects. In addition, gold nanorod plasmon bands are readily tuned by changing the aspect ratio; this enables the wavelength dependence of fluorescence to be easily studied.[4,15,21]

To this end, gold nanorods having plasmon maxima ranging from 530 – 850 nm are prepared. At 530 nm there is no spectral overlap with IRDye 800CW DBCO which absorbs/emits at 779/794 nm, but there is stronger overlap with higher aspect ratios. A dielectric spacer is used to achieve distance dependence. The gold nanorods are coated in mesoporous silica 11 – 26 nm thick *via* modification of the Stöber process.[29,30] The silica surface is functionalized with 3-azidopropyltrimethoxysilane. IRDye is then conjugated to the azide-functionalized surface *via* a copper-free click reaction and the amount of IRDye attached to the surface of the nanorods is quantified.[31,32] Fluorescence of IRDye-nanorod conjugates is monitored using steady-state and time-resolved measurements to determine changes in fluorescence intensity and lifetime. Control experiments of IRDye bound to silica nanoparticles are carried out to confirm that changes in fluorescence are due to plasmonic interactions, not attachment of the fluorophore to a silica surface. In addition, an experiment varying the number of dye molecules per particle is carried out to assess how separation between dye molecules on the surface of the nanoparticles affects IRDye fluorescence. Based on this result, IRDye loading is limited to prevent dye-dye quenching.

2.2 MATERIALS AND METHODS

2.2.1 MATERIALS

Cetyltrimethylammonium bromide (CTAB), gold tetrachloroaurate ($HAuCl_4 \bullet 3H_2O$), sodium borohydride ($NaBH_4$), silver nitrate ($AgNO_3$), ascorbic acid, sodium hydroxide (NaOH), tetraethylorthosilicate (TEOS), ethanol (EtOH), indocyanine green dye, 3-chloropropyltrimethoxysilane, sodium azide, sodium iodide, dimethylformamide (DMF) and methanol (MeOH) were purchased from Sigma-Aldrich (USA). IRDye 800CW DBCO was purchased from LI-COR Biosciences. All chemicals were used as received.

2.2.2 SYNTHESIS OF GOLD NANORODS

Gold nanorods were prepared using our well-known seed-mediated growth procedure.[33] First, 9.75mL of 0.1 M CTAB was added to 0.25 mL of 0.01 M $HAuCl_4 \bullet 3H_2O$ and the solution was kept stirring for 10 min. Next, 0.043 g of $NaBH_4$ was added to 10 mL of ice cold deionized water. Immediately, the 0.1 M $NaBH_4$ solution was mixed and 1 mL of it was transferred into a second tube containing 9 mL of ice cold deionized water. Then, 0.60 mL of the 0.01 M $NaBH_4$ was quickly added to the solution of CTAB and $HAuCl_4$ forming gold seeds. The gold seed solution was stirred for 10 min and then aged for 1 h before gold nanorod synthesis.

Five, 500 mL batches of CTAB-coated gold nanorods were prepared. A growth solution containing 475 mL of 0.1 M CTAB, 25 mL of 0.01 M $HAuCl_4 \bullet 3H_2O$ and varied amounts of 0.01 M $AgNO_3$ (0.10, 1.25, 2.50, 3.75, or 5.50 mL) was prepared. Increasing amounts of $AgNO_3$ resulted in higher aspect ratio nanorods formed. Next, 2.75 mL of 0.1 M ascorbic acid was added to the growth solutions, which turned colorless upon addition of ascorbic acid. Then, 0.6 mL of gold seed solution was added under vigorous stirring. The solutions began changing color after 15 min, then stirring was slowed, and the solution was allowed to age overnight (16 h at 27°C). The next day the gold nanorod solutions were purified *via* centrifugation at 13,500 rcf for 20 min, and the solutions were diluted with deionized water for further characterization and functionalization.

Absorbance spectra were obtained using a Cary 500 UV-vis spectrometer (Agilent, USA) to determine plasmon band maxima and nanorod concentration. Concentration of gold nanorod solutions was determined from calculated extinction coefficients at each plasmon maximum, which has been calibrated using inductively-coupled plasma atomic emission spectroscopy. Transmission electron microscopy images were obtained on a JEOL 2100 cryo TEM (JEOL, Japan). ImageJ analysis of TEM images (300 particles per sample) was carried out to determine average length/width and aspect ratio.

2.2.3 SILICA-COATED GOLD NANORODS

Silica coating was carried out using a modified Stöber method.[29] CTAB concentration was tightly controlled during silica coating. After initial synthesis and purification, the gold nanorod solutions were centrifuged a second time at 11,200 rcf for 20 min. The supernatant was removed, and the pellets were separated to five tubes, each diluted to 10 mL for a final nanorod concentration of 1 nM. After two

centrifugations, the concentration of CTAB was <0.01 mM. Then, 0.1 M CTAB was added to each of the five tubes to adjust the CTAB concentration to 0.4, 0.7, 0.9, 1.0, or 1.2 mM. The solutions were mixed overnight to allow the CTAB to equilibrate on the surface of the gold nanorods. Then, 40 µL of 0.1 M NaOH was added to adjust pH to 10.6, and the solutions were mixed for 30 min. Next, 90 µL of 20% TEOS in methanol was added, and the solutions were mixed for 20 h at room temperature. The nanorods were transferred to new centrifuge tubes and then purified *via* centrifugation at 8,000 rcf for 20 min. The supernatant was removed, and the pellets were dispersed in 5 mL of EtOH.

2.2.4 SYNTHESIS OF THE AZIDE, 3-AZIDOPROPYLTRIMETHOXY SILANE

Sodium azide (493 mg, 7.5 mmol) and sodium iodide (28 mg, 0.1875 mmol) were added to a 100 mL round-bottom flask followed by 20 mL of DMF. The suspension was stirred 5-10 min, allowing the solids to dissolve. 3-Chloropropyltrimethoxysilane (1.25 g, 6.3 mmol) was added, and the reaction was capped and stirred for 12 h at 100˚C.The compound was used as a solution in DMF isolated directly from the reaction mixture as follows. The crude mixture was filtered through Celite and the resulting solution layered with 80 mL hexanes. The biphasic mixture was stirred vigorously for 4 h, at which time the phases were separated and the hexanes fraction was concentrated to clear oil. The concentration of the azide was determined by ^{1}H NMR (400 MHz Varian Inova UI400 spectrometer). The DMF layer was resubmitted to the above procedure until the hexanes layer no longer contained product. The resulting product was stable when diluted to 25% in DMF and was used without further purification.

***Warning*:** While the alkyl azide did not exhibit shock or impact sensitivity, it should be noted that the reagent is unstable as a neat liquid, completely decomposing within 48 h at room temperature. While this has been a relatively safe reagent in our laboratory, this should not excuse anyone from exercising proper caution in its use.

2.2.5 AZIDE FUNCTIONALIZATION OF SILICA-COATED GOLD NANORODS

One hundred microliters of the azide (25% in DMF) was added to the silica-coated gold nanorods in EtOH. The solutions were heated overnight (10 h at 80°C) to ensure complete functionalization of the surface. Purification was carried out *via* centrifugation at 10,000 rcf for 20 min. The solutions were centrifuged, the supernatant was removed, and the pellet was redispersed three times in MeOH to remove excess azide. The azide-functionalized, silica-coated gold nanorods were characterized by UV-vis absorbance spectroscopy to determine concentration and plasmon band maximum. The samples were all diluted to 0.8 nM for further characterization and IRDye attachment.

TEM image analysis was carried out with ImageJ with 300 particles measured for each sample to determine average silica shell thickness. Zeta potentials of CTAB, silica-coated and azide-functionalized gold nanorods were measured using a ZetaPals ζ-potential analyzer (Brookhaven, USA). In addition, a few samples of azide-functionalized silica-coated gold nanorods were purified by dialysis and three additional centrifugation steps to ensure removal of all free azide. Fourier transform infrared spectroscopy of these

highly purified samples was carried out using a PerkinElmer Spectrum 100 (PerkinElmer, USA) to confirm the presence of the azide on the nanorod surface.

2.2.6 IRDYE ATTACHMENT TO AZIDE-FUNCTIONALIZED SILICA-COATED GOLD NANORODS

The concentration of an IRDye stock solution in MeOH was determined by measuring absorbance of IRDye (ε = 300,000 M/cm in MeOH).[28] Then, 50 µL of 10 µM IRDye was added to 3 mL of 0.8 nM azide-functionalized silica-coated gold nanorods in MeOH. The IRDye/nanorod solutions were mixed overnight (>12 h) at room temperature for IRDye coupling. The solutions were centrifuged at 15,000 rcf for 20 min, the supernatant was removed, and the pellets containing IRDye-loaded nanorods were suspended in 3 mL of MeOH. The supernatants were centrifuged a second time at 15,000 rcf for 20 min to ensure removal of any residual nanorods. Fluorescence emission peak area of each supernatant was measured to determine IRDye loading (see procedure below). Loading was calculated assuming dye molecules bound = original – free. Typically, dye loading was ~80% with 160 IRDye molecules/nanorod. All fluorescence analysis was carried out in MeOH with three samples of IRDye-loaded gold nanorods prepared and analyzed for each of the five aspect ratios and five silica shell thicknesses used. In addition, all samples with IRDye were covered with aluminum foil to reduce photobleaching.

2.2.7 STEADY-STATE FLUORESCENCE MEASUREMENTS

Steady-state fluorescence was carried out on a Fluoromax-3 (Horiba Scientific, Japan) to determine fluorescence enhancement and quenching. Fluorescence emission spectra of IRDye and IRDye/nanorod solutions were collected with excitation set at 779 nm and emission measured in the region from 785 to 900 nm. By beginning emission collection at 785 nm, gold nanorod scattering was minimized and the only fluorescence emission observed was due to IRDye fluorescence. Since each sample had varied dye loading it was necessary to calculate expected fluorescence emission for each sample. A calibration curve of fluorescence peak area *versus* free IRDye concentration was constructed. The fluorescence intensity of IRDye-loaded nanorods was calculated by dividing the measured peak area by the expected peak area calculated from the calibration curve.

An inner filter correction was applied to obtain an accurate value for fluorescence intensity since the gold nanorods strongly absorb at wavelengths of IRDye absorption/emission. Absorbance of the solutions of IRDye-loaded nanorods was measured at the excitation and emission wavelengths. The corrected emission intensity was calculated from Equation 2.8.

2.2.8 TIME-RESOLVED PHOTOLUMINESCENCE MEASUREMENTS

Time-resolved photoluminescence (TRPL) measurements were carried out using a home-built correlated single-photon counting system at the Materials Research Laboratory, University of Illinois. The system uses a Becker and Hickel SPC-150 photon counting board to process signals with a silicon avalanche photodiode. The excitation source is a NKT Photonics pulsed supercontinuum source. In the

TRPL measurements, the dye/nanorod solutions were excited with a 740 nm (10 nm bandpass), 6 ps pulse. The system impulse response is ~50 ps. Fluorescence emission was collected in the region from 795 to 805 nm. Because the emission filter used limited the emission wavelengths to 10 nm, gold nanorod scattering was minimal and the only emission observed was due to IRDye fluorescence. The data from TRPL measurements were used to construct a curve of time *versus* emission which exhibited multi-exponential decay. The fit was calculated using Origin and Equation 2.10 was used to calculate the lifetimes present.

2.2.9 IRDYE ATTACHMENT TO MESOPOROUS SILICA NANOPARTICLES

Mesoporous silica nanoparticles were prepared following similar procedures used for silica coating, but without the gold nanorod cores. First, 400 µL of 0.1 M CTAB was diluted to 50 mL to give a final CTAB concentration of 0.8 mM. Then, 200 µL of 0.1 M NaOH was added. The solution was mixed for 30 min, then 450 µL of 20% TEOS in MeOH was added. The solution was aged for 20 h and was purified *via* centrifugation at 8,000 rcf for 20 min. The mesoporous silica nanoparticles were suspended in EtOH (4 mL) and then 500 µL of the azide (25% in DMF) was added. The solution was heated overnight at 80°C (>10 h) and purified *via* centrifugation. IRDye attachment, steady-state fluorescence and TRPL measurements were carried out as previously described with three separate samples of mesoporous silica nanoparticles.

2.2.10 IRDYE FLUORESCENCE AS A FUNCTION OF SEPARATION BETWEEN FLUOROPHORES

Gold nanospheres (AR 1.1) were synthesized and coated with silica as previously described. The CTAB concentration was 0.3 mM during silica coating, resulting in 33 nm thick silica shell. First, 3 mL of 0.5 nM gold nanoparticles was incubated overnight (>12 h) with IRDye ranging in concentration from 50 to 2000 dyes/particle. Surface area was calculated assuming the dimensions can be approximated by a sphere. These concentrations gave dye-dye separations ranging from 6 to 22 nm. Quantification of IRDye attachment and steady-state fluorescence intensity was carried out as previously described with three replicates analyzed for each sample type.

2.2.11 CALCULATION OF IRDYE QUANTUM YIELD

Quantum yield of IRDye 800CW DBCO in MeOH was determined using indocyanine green as a standard reference (absorbance/emission at 785/806 nm). Three solutions each of IRDye and indocyanine green were prepared with identical dye concentrations (0.2 µM). Fluorescence emission was measured as previously described. Quantum yield of IRDye was calculated from Equation 2.1, where Q_R is the quantum yield of the reference standard in MeOH, OD and OD_R are the absorbance and I and I_R are fluorescence emission peak areas of IRDye and the reference standard, respectively.[46]

$$Q = Q_R \frac{I}{I_R} \frac{OD}{OD_R} \tag{2.1}$$

2.3 RESULTS AND DISCUSSION

2.3.1 NANOPARTICLE DESIGN

IRDye 800CW DBCO was chosen for this study because of its potential biological application, low quantum yield and absorbance/emission profile. The molecular structure of IRDye 800CW DBCO (Figure 2.1a) contains a DBCO tether.[28] The DBCO group allows for conjugation to azides *via* 1,3 dipolar cycloaddition generating a 1,2,3-triazole. Traditionally, click chemistry with azides and terminal alkynes is carried out using a copper catalyst; however, azides can also react with internal alkynes in a strain-promoted reaction.[31] This eliminates the need for copper, which is cytotoxic and the click reaction can proceed quickly at room temperature, in a range of solvents.[32] The absorbance and emission spectra of IRDye in methanol (Figure 2.1b) indicate maximum absorbance/emission at 779/794 nm. The quantum yield of IRDye 800CW DBCO in methanol (MeOH) is 0.075 ± 0.005 (Table 2.1). The obtained value is close to a previous calculation of IRDye in water.[11] Because IRDye 800CW DBCO has such a low quantum yield; it is an ideal candidate for studies of plasmon-enhanced fluorescence.

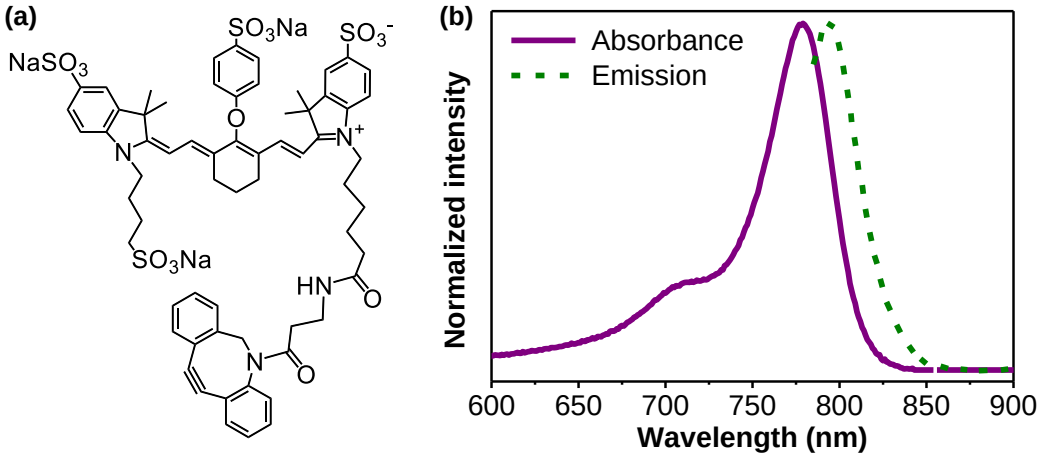

Figure 2.1 (a) Structure of IRDye 800CW DBCO. (b) IRDye absorbance and emission in MeOH with maximum absorbance/emission at 779/794 nm.

Table 2.1 Quantum yield of dyes in MeOH.

Dye	Quantum yield
Indocyanine green	0.04
IRDye 800CW	0.075 ± 0.005

A library of cetyltrimethylammonium bromide (CTAB) coated gold nanorods of varying aspect ratio was prepared using our well-known seed-mediated growth procedure.[33] Gold seeds were added to a growth solution containing CTAB, $HAuCl_4 \cdot 3H_2O$, $AgNO_3$, and ascorbic acid. A CTAB bilayer on the surface of gold nanorods helps to prevent nanorod aggregation and the addition of $AgNO_3$ to the growth solution facilitates anisotropic growth, allowing for control of aspect ratio (AR).[2] With this procedure, it is possible to control

aspect ratio, allowing for variation in longitudinal plasmon maxima and therefore variation in spectral overlap between gold nanorods and IRDye. Five aspect ratios of CTAB gold nanorods were prepared and purified (Figure 2.2a). UV-vis absorbance measurement of the CTAB-coated gold nanorods in water show plasmon band maxima located at 533, 653, 724, 790 and 851 nm (Figure 2.2b). These wavelengths correspond to AR 1.1, AR 2.0, AR 2.7, AR 3.7 and AR 4.4 nanorods, respectively. These aspect ratios of nanorods were selected because the plasmon bands ranged from almost no overlap to strong spectral overlap with IRDye absorbance/emission. Transmission electron microscopy (TEM) micrographs are shown in Figure 2.2c-g and were used to calculate aspect ratio. The absolute dimensions, plasmon maxima, and calculated aspect ratios of the CTAB gold nanorods are listed in Table 2.2.

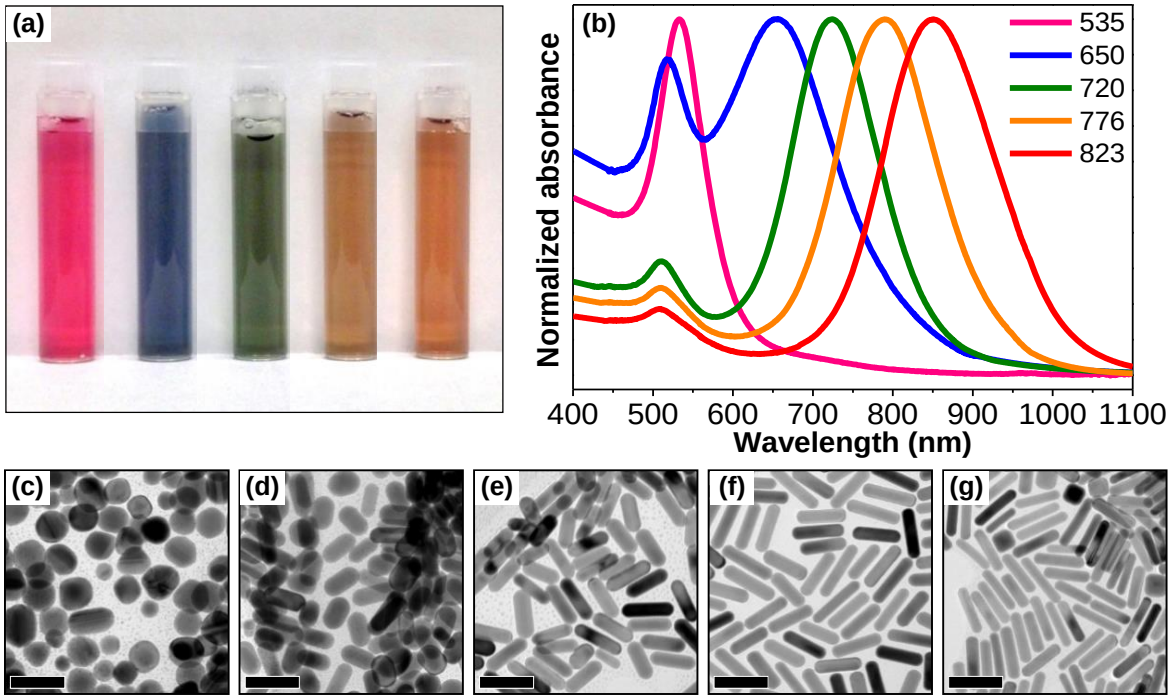

Figure 2.2 (a) Photograph of gold nanorod solutions with increasing aspect ratio left to right. (b) UV-vis absorbance spectra of gold nanorods with different LSPRs (nm). (c-e) TEM images of gold nanorods (c) AR 1.1, (d) AR 2.0, (e) AR 2.7, (f) AR 3.7, and (g) AR 4.4. Scale bars = 50 nm.

Table 2.2 Plasmon band maxima, length, width and aspect ratios of CTAB gold nanorods.

Aspect ratio	Transverse plasmon	Longitudinal plasmon	Length	Width	Aspect ratio (length/width)
AR 1.1	533 nm	-	28.9 ± 6.7 nm	25.3 ± 5.1 nm	1.14 ± 0.04
AR 2.0	517 nm	653 nm	35.8 ± 6.6 nm	17.8 ± 3.4 nm	2.01 ± 0.01
AR 2.7	511 nm	724 nm	37.4 ± 7.0 nm	13.6 ± 2.0 nm	2.74 ± 0.12
AR 3.7	509 nm	790 nm	45.6 ± 5.6 nm	12.4 ± 1.3 nm	3.67 ± 0.07
AR 4.4	507 nm	851 nm	44.5 ± 5.3 nm	10.1 ± 1.2 nm	4.40 ± 0.01

Attachment of IRDye and variation of dye-metal distance was achieved through silica coating and silane functionalization of the CTAB-coated gold nanorods (Scheme 2.1). A dielectric spacer allows for good control of dye-metal distance and it is easy to measure thickness by TEM. In addition, a silica coating reduces nanorod aggregation, increases solubility of gold nanorods in organic solvents, and is easy to functionalize with functional silanes.[29] Silica is known to modify the electromagnetic field around plasmonic nanoparticles, but the effect on electromagnetic field strength is minimal past 10 nm when there is a complete silica shell.[34,35] Silica-coated gold nanorods were functionalized with an azido silane to facilitate IRDye 800CW DBCO attachment to surface. Since azide-alkyne click reactions are highly specific, unwanted side reactions within the IRDye molecule were prevented with this attachment method.[32] Potential dye-dye interactions on the silica surfaces were also avoided by limiting IRDye loading. This allowed us to accurately determine distance and plasmon wavelength dependent fluorescence behavior.

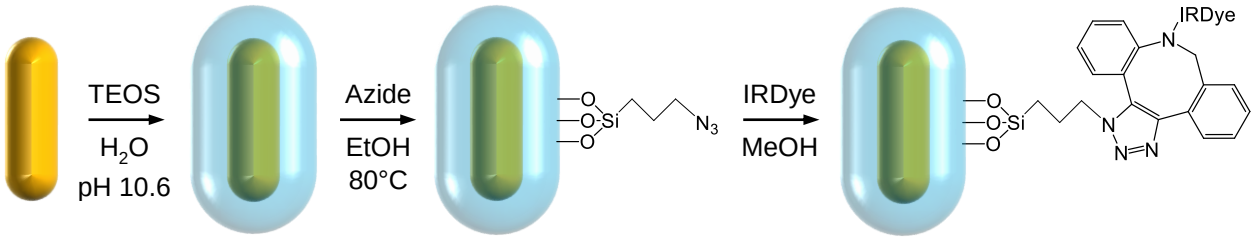

Scheme 2.1 Attachment of IRDye to gold nanorods. Gold nanorods were coated in mesoporous silica, and then functionalized with 3-azidopropyltrimethoxysilane. IRDye molecules were linked to the azide-functionalized surface *via* copper-free azide-alkyne cycloaddition.

Silica-coating was carried out through modification of the well-known Stöber process.[30] The hydrolysis and condensation of tetralkylsilicates to form silica can be catalyzed by a change in pH. Previous researchers have demonstrated 15 nm thick coatings of mesoporous silica on CTAB-coated metal nanoparticles, including gold nanorods.[29] CTAB micelles are a template for silica deposition through the hydrolysis and condensation of the silica precursor tetraethylorthosilicate (TEOS). Growth of mesoporous silica on the nanoparticle surface is attributed to a three-stage mechanism: silica oligomerization, formation of silica/CTAB particles, and aggregation of these silica/CTAB particles.[36] Since CTAB is mostly surrounding the nanorods, the silica/CTAB particles form and aggregate on the nanorod surface, limiting formation of free silica nanoparticles.[29,36]

Through careful control of reaction parameters, we were able to achieve highly reproducible and robust silica coatings. Five silica shell thicknesses ranging from 11 to 26 nm were coated on each of the five aspect ratios of gold nanorods used. Previous researchers have demonstrated that reaction time or TEOS concentration can be used to control silica thickness on gold nanorods. However, we find that these procedures were difficult to reproduce batch-to-batch and 2 – 5 nm increments in shell thickness were difficult to achieve.[29,37] Instead, we demonstrate here that a critical component to control silica coating of gold nanorods is CTAB concentration. As-synthesized gold nanorods are prepared in 0.1 M CTAB which is

far above the critical micelle concentration of 1 mM in pure water.[38] In order to control CTAB concentration, gold nanorods were centrifuged twice after synthesis, so the concentration of CTAB was less than 0.01 mM. Additional centrifugation steps were not carried out because complete CTAB removal from the surface causes gold nanorod aggregation. Then, different amounts CTAB were added to the gold nanorod solutions and the solutions were mixed to allow the CTAB to equilibrate on the surface. Silica coating was carried out by first adjusting the pH using NaOH, then adding TEOS and mixing the solutions for several hours. In the silica coating reactions, concentration of CTAB was varied between 1.2 and 0.4 mM to obtain porous shells about 11, 14, 17, 22, and 26 nm thick (Figure 2.3).

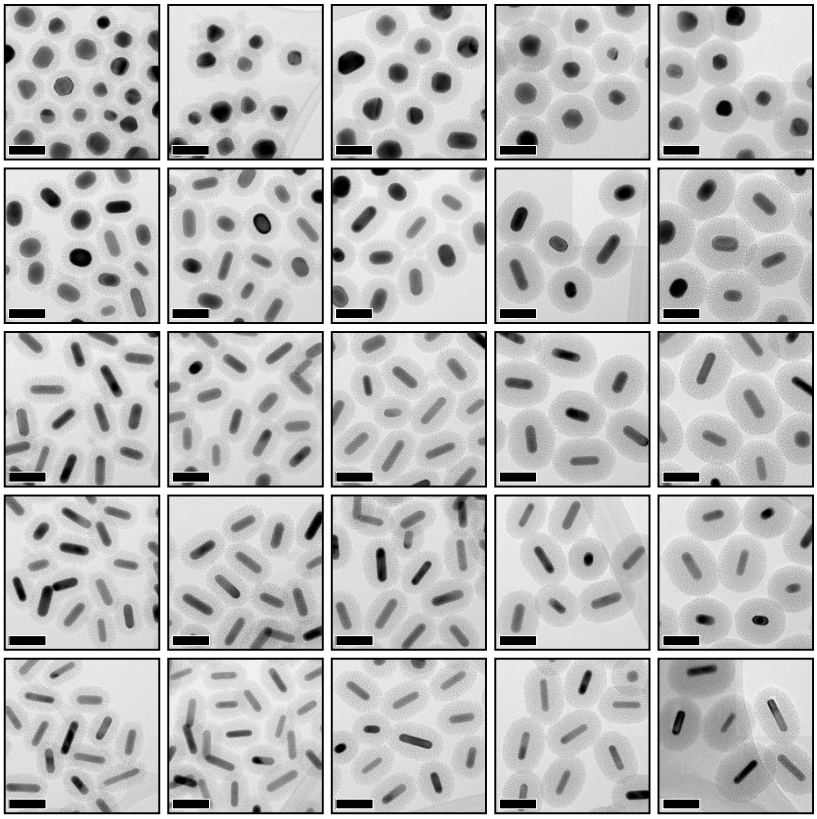

Figure 2.3 TEM images of azide-functionalized, silica-coated gold nanorods with increasing silica shell thickness left to right (11, 14, 17, 22, and 26 nm) and with increasing aspect ratio top to bottom (AR 1.1, 2.0, 2.7, 3.7, and 4.4). Scale bars = 50 nm.

The amount of CTAB free in solution is critical to silica shell thickness. As the CTAB concentration is increased, more CTAB is in solution *versus* on the nanorods, and silica shell thickness decreases (Figure 2.4a). When the concentration is well past the critical micelle concentration of CTAB, around 2 mM, we find that no silica is formed on the nanorod surface. Fortunately, most silica formed apart from the nanorods is removed by centrifugation after the coating reaction. In addition to CTAB concentration, gold nanorod concentration, pH, TEOS concentration, reaction temperature and reaction time were all tightly controlled. The concentration of each batch of gold nanorods used during silica coating was kept high, further limiting

excess silica particles formed. We also found that adjusting the pH to 10 was optimal. At higher pH values, the silica shells were of poor quality and no silica shell formed below pH 9. Silica-coated gold nanorods were purified and then characterized by TEM imaging and UV-vis absorbance spectroscopy. The calculated silica shell thickness for each of the five aspect ratios and five silica shell thickness is listed in Table 2.3. UV-vis absorbance spectra of silica-coated gold nanorods in ethanol (EtOH) (not shown) show no nanorod aggregation. Only small shifts in plasmon maxima, less than 10 nm between different shell thicknesses, are observed (Table 2.4).

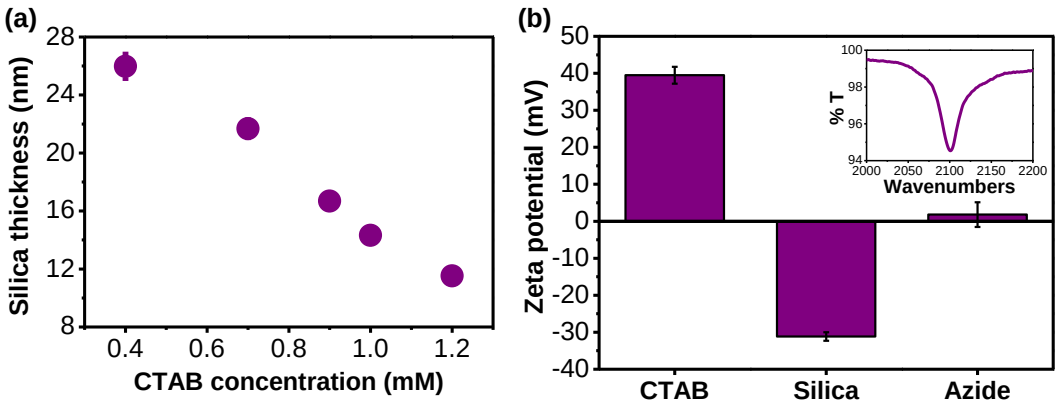

Figure 2.4 (a) CTAB concentration *versus* average silica shell thickness for the five shell thicknesses used. (b) ζ-potential of AR 2.7 gold nanorods coated in CTAB, a 22 nm thick silica shell, and functionalized with 3-azidopropyltrimethoxy silane. Inset is the N_3 peak in an FT-IR spectrum of azide-functionalized nanorods.

Table 2.3 Silica shell thickness of azide-functionalized, silica-coated gold nanorods.

Aspect ratio	Shell #1	Shell #2	Shell #3	Shell #4	Shell #5
AR 1.1	11.2 ± 1.2 nm	14.1 ± 1.2 nm	16.5 ± 1.0 nm	20.9 ± 1.4 nm	24.6 ± 1.5 nm
AR 2.0	11.3 ± 1.1 nm	14.2 ± 1.1 nm	16.3 ± 1.1 nm	21.8 ± 1.4 nm	25.7 ± 1.7 nm
AR 2.7	11.2 ± 1.3 nm	14.1 ± 1.1 nm	16.9 ± 1.1 nm	22.7 ± 1.3 nm	26.2 ± 1.4 nm
AR 3.7	12.0 ± 1.0 nm	14.7 ± 1.0 nm	16.9 ± 1.1 nm	21.6 ± 1.1 nm	26.6 ± 1.9 nm
AR 4.4	12.1 ± 0.9 nm	14.5 ± 0.9 nm	16.8 ± 1.0 nm	21.4 ± 1.2 nm	26.8 ± 3.4 nm

Table 2.4 Plasmon band maxima for silica-coated gold nanorods in EtOH.

Aspect ratio	11 nm shell	14 nm shell	17 nm shell	22 nm shell	26 nm shell
AR 1.1	533 nm	532 nm	533 nm	532 nm	531 nm
AR 2.0	651 nm	657 nm	658 nm	655 nm	652 nm
AR 2.7	727 nm	727 nm	730 nm	727 nm	734 nm
AR 3.7	791 nm	792 nm	791 nm	797 nm	790 nm
AR 4.4	852 nm	851 nm	852 nm	849 nm	850 nm

Silica-coated gold nanorods were then functionalized with an organic azide, which could participate in the cycloaddition reaction to bind IRDye 800CW DBCO to the surface.[39] The azide, 3-azidopropyltrimethoxysilane, was prepared from 3-chloropropyltrimethoxysilane *via* a modification of the published Finkelstein reaction (Figure 2.5).[40] Heating 3-chloropropyltrimethoxysilane and sodium azide in *N*, *N*-dimethylformamide (DMF) yielded the azide product in greater than 90% yield, as assessed by gas chromatography mass spectrometry (not shown). The reaction mixture was then extracted into hexanes, which yielded a solution of pure azide in DMF and was stable at room temperature. Azide functionalization was carried out by simply adding the azide, in DMF, to a solution of the silica-coated gold nanorods in EtOH. Complete silane condensation on the silica surface was further driven by heating the solution. After functionalization, the gold nanorod solutions were purified by centrifugation multiple times to ensure complete removal of excess azide and were then dispersed in MeOH in preparation for IRDye conjugation.

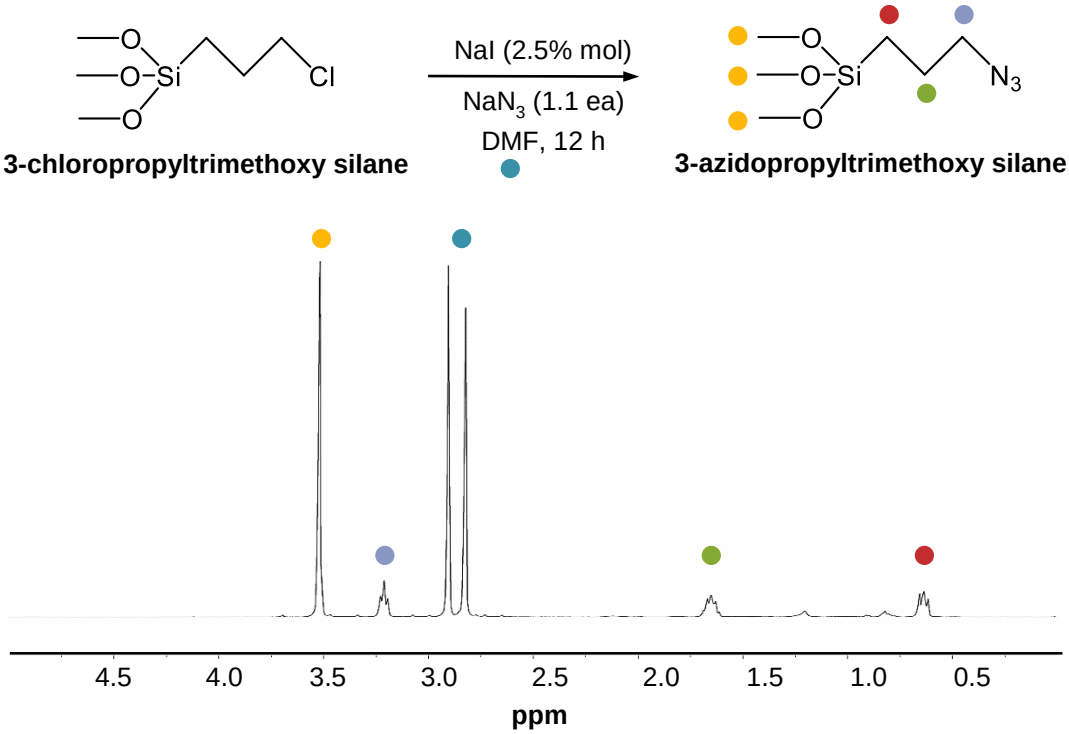

Figure 2.5 Synthesis procedure for 3-azidopropyltrimethoxysilane from 3-chloropropyltrimethoxysilane and corresponding ^{1}H NMR spectrum. ^{1}H NMR (400 MHz, $CDCl_3$) δ 3.52 (s, 9H), 3.21 (t, *J* = 6.9 Hz, 2H), 1.66 (tt, *J* = 11.8, 6.9 Hz, 2H), 0.63 (t, *J* = 11.8 Hz, 2H).

Azide-functionalized gold nanorods were characterized by UV-vis absorbance, ζ-potential measurements and Fourier transform infrared spectroscopy (FT-IR). UV-vis absorbance spectra of azide-functionalized, silica-coated gold nanorods in MeOH (not shown) show no nanorod aggregation. However, due to heating, multiple centrifugation steps, and dispersion in various solvents, the average nanorod plasmon maxima shifts to 535, 650, 720, 776, and 823 nm for AR 1.1, AR 2.0, AR 2.7, AR 3.4 and AR 4.4, respectively. Only small shifts in absorbance maxima, less than 18 nm between different shell thicknesses,

are observed (Table 2.5). ζ-potential measurements confirm functionalization of the gold nanorods (Figure 2.4b). CTAB gold nanorods are positively charged, and after silica coating and purification, the surface charge is negative. Upon azide functionalization, the surface charge of the nanorods goes to zero due to the presence of the neutral azide. Further confirmation of azide functionalization is demonstrated by FTIR. These nanorods were purified by dialysis and extra centrifugation steps to ensure that all free azide was removed before FTIR analysis. An azide stretch is visible at 2100 cm^{-1} in a spectrum of azide-functionalized nanorods, further confirming azide functionalization (Figure 2.4b).

Table 2.5 Plasmon band maxima for azide-functionalized, silica-coated gold nanorods in MeOH.

Aspect ratio	11 nm shell	14 nm shell	17 nm shell	22 nm shell	26 nm shell
AR 1.1	535 nm	534 nm	535 nm	535 nm	534 nm
AR 2.0	648 nm	653 nm	648 nm	648 nm	653 nm
AR 2.7	718 nm	718 nm	725 nm	710 nm	728 nm
AR 3.7	776 nm	774 nm	772 nm	778 nm	782 nm
AR 4.4	830 nm	819 nm	816 nm	816 nm	833 nm

IRDye was attached to azide-functionalized silica-coated gold nanorods *via* a copper-free click reaction. The concentration of an IRDye stock solution was determined by absorbance at 779 nm (ε = 300,000 M/cm in MeOH).[28] Then, IRDye was added to azide-functionalized silica-coated gold nanorods in MeOH. The click reaction can occur in 45 min but the IRDye/nanorod solutions were mixed overnight to ensure maximum coupling.[39] The solutions were centrifuged, the supernatant was removed, and the pellets containing IRDye-loaded nanorods were suspended in MeOH. The supernatants were centrifuged a second time to completely remove any residual nanorods. Fluorescence emission peak area of each supernatant was measured to determine IRDye loading, and loading was calculated from a calibration curve or IRDye peak area *versus* concentration. We assumed dye molecules bound = original – free. Initially, 200 dye molecules were added per particle and dye loading was ~80% with 160 IRDye molecules/nanorod. This allowed for an average dye-dye distance of greater than 9 nm on the silica surface, reducing potential dye-dye interactions during fluorescence studies.

2.3.2 PLASMON-ENHANCED FLUORESCENCE

The complex physics of a quantum emitter coupled to a metal nanoparticle has been explored in the literature.[41-45] Unfortunately, these treatments do not completely address the situation here. Molecular fluorescence is well understood and simply described by Equation 2.2 where quantum yield or quantum efficiency (Q) is the ratio of the radiative decay rate (k_{rad}) to the total of all contributions to excited state decay, both radiative and nonradiative (k_{nr}).

$$Q = \frac{k_{rad}}{k_{rad} + k_{nr}} = k_{rad} \cdot \tau \tag{2.2}$$

Alternatively, Q can be calculated from knowledge of the k_{rad} and fluorescence lifetime (τ). The fluorescence lifetime (Equation 2.3) is the average time a fluorophore spends in the excited state before it relaxes to the ground state and is the inverse of the sum of the decay rates of all the relaxation pathways (k).[46]

$$\tau = \frac{1}{k_{rad} + k_{nr}} = \frac{1}{k} \tag{2.3}$$

For a free fluorophore in solution, nonradiative decay is caused by processes such as internal conversion, intersystem crossing, or collisional quenching.[46] However, when a fluorophore is attached to the surface of a nanorod, the relaxation dynamics will become quite complex. Both radiative and nonradiative decay can be changed when there is coupling near a plasmonic surface. The presence of the metal particle provides a continuum of states to which the molecule can couple. The potential decay pathways become more numerous, complicating the emission dynamics which define the new fluorescence lifetime (τ_0) and new total decay rate (k_0) shown in Equation 2.4. We can incorporate changes in free dye k_{rad} and k_{nr} by adding the new terms K_{rad} and K_{nr}, where the former refers to plasmon-induced radiative rate enhancement and the latter the non-radiative dye-rod interactions driven by energy dissipation to the nanorod continuum states. Finally, there can potentially be associated dye-surface interactions (k_s) or dye-dye fluorescence coupling (k_{dd}) on the nanoparticle surface that may also modify the fluorophore dynamics.

$$\tau_0 = \frac{1}{k_{rad} + k_{nr} + K_{rad} + K_{nr} + k_s + k_{dd}} = \frac{1}{k_0} \tag{2.4}$$

Depending on the nanoparticle-fluorophore system used, these processes may result in a change in the fluorescence lifetime.[21] All these interactions must be taken into account before making conclusions about changes in fluorescence behavior. By combining steady-state intensity measurement data with lifetime measurement data, it is possible to obtain a comprehensive picture of observed changes in fluorescence decay pathways relative to free dye.

If we consider the basic physics involved we can bound our observational expectations. The general approximate expression for the one photon absorption cross-section, $\sigma^{(1)}(\omega)$ for a dipolar quasi two-level fluorophore excited at frequency (ω) is shown in Equation 2.5, where μ is the transition dipole of the emitter, ρ(ω) is the molecular density of states (effectively the absorption spectral shape), and n and c are the index of refraction and speed of light, respectively.

$$\sigma^{(1)}_{IRDye}(\omega) = \frac{4\pi^2\omega}{nc} \left|\mu_{IRDye}\right|^2 \rho(\omega_{IRDye}) \tag{2.5}$$

The full transition rate R is defined by Equation 2.6 where I_{exc} is the excitation field intensity:

$$R_{IRDye}=\sigma^{(1)}_{IRDye}(\omega)I_{exc} \tag{2.6}$$

Our question here is simply, is one or both of these molecular quantities in Equation 2.6 modified by dye molecule-nanorod coupling?[47,48] The plasmon-induced E-field enhancement makes I_{exc} much larger, which of course would drive a larger excited-state population of the dye *via* R. If that was the dominant effect, the plasmon-induced/enhanced population of the excited state would result in detection of enhanced fluorescence emission, but there need be no change of the observed dye kinetics (*i.e.*, the radiative rate would not be modified). If the cross-section, $\sigma^{(1)}$, is affected, on the other hand, the actual radiative rate will be changed with that change manifest in the observed decay dynamics of the emitter.

A formalism describing the field interactions involved has been developed in the literature.[49-52] It has been shown that the decay rate, K_{rad}, of a dipolar emitter near a plasmonic structure can be written as Equation 2.7 where k_{rad} is the radiative rate of the free dye. The second term on the right contains the imaginary part of dipolar coupling scaled by the amplitude of μ and the field free space wavevector $\vec{k}$.[49]

$$\frac{K_{rad}}{k_{rad}}\approx 1+\frac{3}{2}\,\mathrm{Im}\frac{\vec{\mu}\cdot\mathbf{E}(\vec{r},\omega_0)}{|\mu|^2\vec{k}^3} \tag{2.7}$$

The complete analytical solution to this problem requires full multipole expansion of the electric field, $\mathbf{E}(\vec{r},\omega_0)$ and is very complex, but the result gives rise to the two key dynamic observables of the system: the well-known Förster transfer process for the plasmon induced non-radiative contribution, and a complex radiative contribution driven by the "Drude metal" polar nature of the plasmon resonance. In general, the non-radiative rate modification results from energy dissipation of the emitter to the nanorod *via* dipole-dipole coupling, while the radiative contribution is driven by the polarizability of the total system, dye coupled to rod, and its impact on the transition dipole. While the components of radiative enhancement are hard to discern independently, we will show that its signature is observed in our lifetime data.

2.3.3 FLUORESCENCE STUDIES

Fluorescence intensity analysis of IRDye-loaded silica-coated, gold nanorods was first carried out by steady-state measurements. The solutions were excited at the dye absorbance maximum (779 nm) and fluorescence emission was measured from 785 to 875 nm. Comparison of the fluorescence emission curves to curves of IRDye alone shows no change in shape or emission maxima (fluorescence spectra are not shown). No emission was detected from silica-coated gold nanorods alone, without dye, suggesting that scattering from the nanorods alone is minimal. Since each sample has slightly varied dye loading it was necessary to calculate separate expected emission. A calibration curve of fluorescence peak area *versus* IRDye concentration was constructed. The relative fluorescence intensity of IRDye-loaded nanorods was

calculated by dividing the measured peak area by the expected peak area. Since gold nanorods strongly absorb in regions of IRDye absorption/emission and their extinction can be orders of magnitude stronger than IRDye, measured fluorescence emission can be reduced. This is called the inner-filter effect and it is necessary to correct for this effect in solution-based measurements. The corrected emission intensity was calculated from Equation 2.8 where I_{corr} is the corrected emission intensity, I_0 is the relative fluorescence intensity calculated from steady-state measurements, and OD_{ex} and OD_{em} are the optical density values for each dye/nanoparticle solution at 779 and 794 nm, respectively.[46]

$$I_{corr} = I_0 \cdot 10^{(OD_{ex} + OD_{em})/2} \tag{2.8}$$

Equation 2.8 does not account for light scattering, which also occurs when the surface plasmon resonance is excited. The scattering contribution from gold nanorods in this size range has been measured for 800 nm incident light and the maximum contribution of scattering to the total extinction as a function of aspect ratio was 9%, 15%, 10%, 6%, 5%, for aspect ratios 2.5, 3.0, 4.0, 4.5, 5.1, respectively.[53] Therefore, 85-95% of the light is absorbed by the nanorods rather than scattered. Consequently, the likelihood of scattered light being reabsorbed by nearby dye molecules is quite low and should not be a significant contribution to detected fluorescence emission.

The results of the steady-state fluorescence measurements are shown in Figure 2.6. The line cuts show where intensities are plotted relative to free IRDye as a function of silica shell thickness and plasmon band maximum (Figure 2.6a-e). Both distance and plasmon wavelength dependent changes in fluorescence are observed. At the plasmon band furthest away from the emission wavelength at 535 nm, where there is minimal spectral overlap with the emission of IRDye, no significant intensity enhancement is observed. Only a decrease in fluorescence is observed with decreasing silica shell thickness (Figure 2.6a). This is consistent with increasing nonradiative relaxation (K_{nr}) as the fluorophore gets closer to the continuum states of the nanorod. When there is stronger overlap between the plasmon band and IRDye absorbance/emission, fluorescence intensity enhancement becomes apparent (Figure 2.6b-e). Interestingly, at these plasmon frequencies, the maximum fluorescence intensity is observed at approximately 17 nm. The strongest enhancement is observed when the plasmon maximum of the nanorods is 776 nm, near resonant with IRDye absorption, resulting in an approximately 10-fold increase in fluorescence intensity. The trends and scale of the fluorescence intensity are more clearly observed in Figure 2.6f which is a three-dimensional contour plot of emission intensity as a function of distance and plasmon maximum. The “hotspot” of fluorescence intensity (the dark red area) occurs in the region from 14 to 22 nm silica shell thickness between plasmon maxima at 750 and 800 nm.

A possible concern is the contribution of scattering by the nanorods to an “apparent” fluorescence enhancement, either directly or by reabsorption of scattered photons by dyes in the sample. At aspect ratio 3.0, where there would be ~15% scattering[53] (Figure 2.6c) we observe decreased fluorescence intensity compared to aspect ratio 4.5, where there would be ~6% scattering (Figure 2.6e).[53] This supports the notion

that increased dye excitation due to light scattering from the nanorods is not the major contributor to IRDye fluorescence emission.

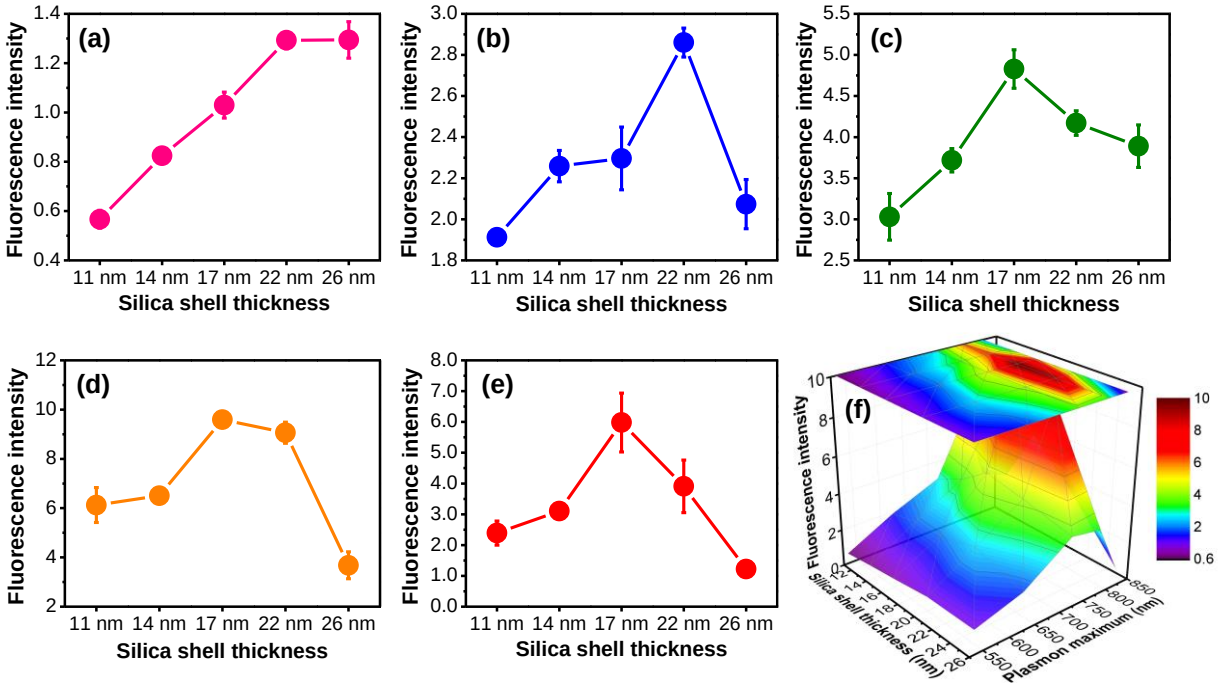

Figure 2.6 Steady-state fluorescence intensity of IRDye bound to gold nanorods relative to free IRDye emission corrected for the inner-filter effect. Intensity as a function of silica shell thickness with plasmon band maxima located at (a) 535 nm, (b) 650 nm, (c) 720 nm, (d) 776 nm, and (e) 823 nm. (f) Two-tier contour plot of fluorescence intensity as a function of silica shell thickness and plasmon maximum.

The observed increases in fluorescence intensity can be attributed to strong coupling between the fluorophores and the plasmonic structure, but how the changes are manifest are not obvious. As noted there can be several possible reasons for an increased detection of emission. There can be a change of the emission cross-section (radiative decay rate) relative to the non-radiative decay or there simply could be an effective increase in excited state population which experiences radiative decay with no change in radiative emission dynamics. We can explore these questions more effectively by examining the system's time-resolved fluorescence characteristics. Time-resolved photoluminescence (TRPL) measurements were carried out to determine fluorescence lifetime as a function of fluorophore-nanorod distance and plasmon maximum. In the TRPL measurements, the dye/nanorod solutions were excited with a 740 nm pulsed laser and emitted photons were collected in the region from 795 to 805 nm. An emission filter was used to limit the detected emission bandwidth to 10 nm. We note that only emission from IRDye is observed.

The data from TRPL measurements, which are decay curves of time *versus* emission are shown in Figure 2.7. The decay of free IRDye (Figure 2.7a) exhibits a single exponential decay while nearly all curves of IRDye bound to silica-coated gold nanorods, especially in the strongly coupled regions, exhibit multi-exponential decays (Figure 2.7b-f). This is an indication that there are new multiple pathways of decay

present in the dye-nanorod system which are not present when IRDye is free in solution as implied by Equation 2.4. In all cases, decay appears faster as silica shell thickness decreases. This is consistent with increased K_{nr}. As stated, an increase in the decay rate is expected due to the higher electromagnetic field strength induced at the nanorod surface, resulting in potentially a larger *emission cross-section.* However, there will be more efficient nonradiative Förster coupling (which would also lead to much faster decay) when there is stronger spectral overlap between the plasmon band of the nanorods and IRDye absorbance/emission. Comparison of the fluorescence intensity results with the decay dynamics, suggests that when the plasmon is far off the emission resonance (Figure 2.7b); the increase in "nonradiative" rate, K_{nr}, drives evolution of the decay dynamics. As the fluorophore is further away from the rod core (>20nm) dynamics are consistent with the free dye. It is interesting to note that the detected intensity at the largest distance is still larger than the free dye. This could signify a pure R_{IRDye} contribution at long distance (*i.e.*, a pure population enhancement). Near resonant (Figure 2.7e), the plasmon-fluorophore interaction comes strongly into play. Interestingly, if one focuses on the 22-26 nm spacing, the lack of large change in decay rates between (e) and (f) suggests that our enhancement is primarily radiative. Here, there is a large difference in absorptive behavior (Figure 2.2b), but no substantial change in kinetics.

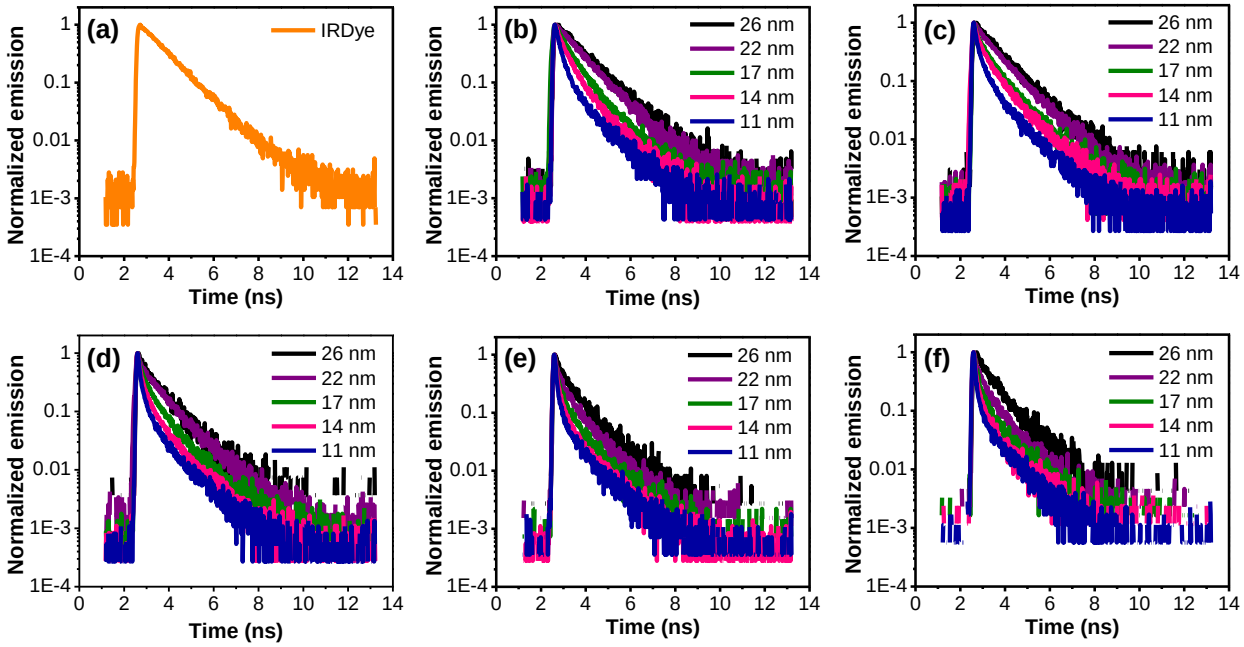

Figure 2.7 Fluorescence decay curves of (a) free IRDye and IRDye bound to gold nanorod as a function of silica shell thickness with plasmon band maxima located at (b) 535 nm, (c) 650 nm, (d) 720 nm, (e) 776 nm, and (f) 823 nm.

The decay of the excited state of an isolated molecule to the ground state can be generally described by a single exponential fit (Equation 2.9) where intensity (I) is plotted as a function of the initial intensity (A), time (t), and the fluorescence lifetime.

$$I(t) = Ae^{-t/\tau} \quad (2.9)$$

The free dye exhibits this behavior and using this equation, the lifetime of free IRDye was calculated to be 1.12 ns. This is nearly the same value as our limiting lifetimes when beyond 25 nm shell thickness and far off resonance. However, a single exponential did not fit the majority of the decay curves. For simplicity, we fit the data to a bi-exponential decay (Equation 2.10), where A_1 and A_2 are the initial intensities from the "fast" and "slow" components of fluorescence decay, respectively and τ_1 and τ_2 are their respective fluorescence lifetimes. We note that this functional form generated the best fits in nearly every case.

$$I(t) = A_1e^{-t/\tau_1} + A_2e^{-t/\tau_2} \quad (2.10)$$

The "fast" and "slow" fluorescence lifetimes as a function of silica shell thickness and plasmon maximum are shown as contour plots in Figure 2.8. In the fast component, both decreasing silica shell thickness and increasing plasmon/IRDye spectral overlap result in a very strong and abrupt reduction in the fluorescence lifetime (Figure 2.8a). As discussed above, the degree of spectral overlap can impact both radiative and nonradiative processes. The rather weak spectral resonance dependence suggests that the driver is primarily radiative. As mentioned above, there are rather large change in absorption from 720 nm to 820 nm, but the kinetics changes are modest. The only region where the calculated lifetime is the same as free IRDye with nanorods absorbing at 535 nm and when silica shell thickness is greater than 20 nm. If we directly compare the two regimes (*i.e.*, fast and slow), the trend of shell thickness and spectral overlap is similar but the changes in lifetime are much more gradual in the slow component.

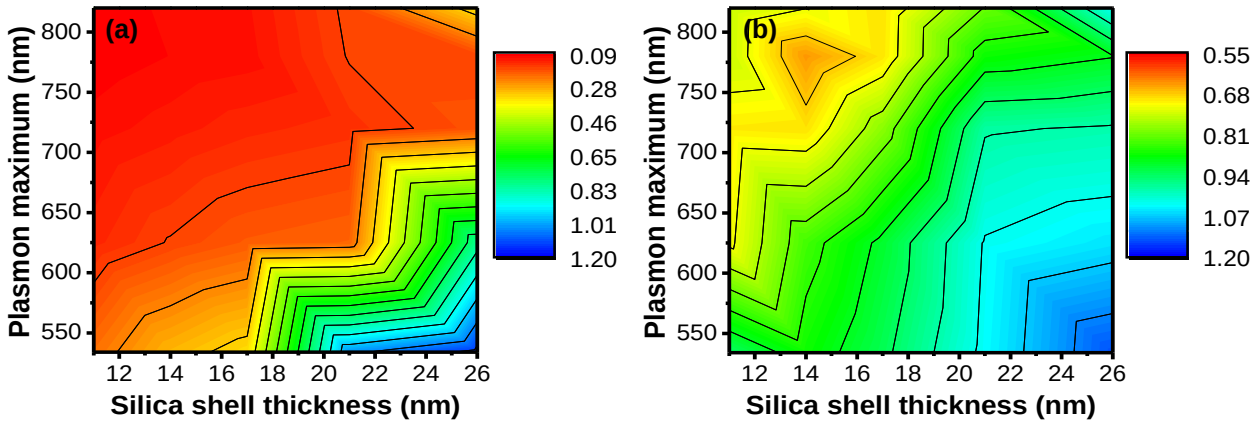

Figure 2.8 Contour maps showing fluorescence lifetimes (ns) of IRDye bound to silica-coated gold nanorods. Lifetimes were calculated from Equation 2.10 giving two lifetime values, one "fast" and one "slow". The (a) faster and (b) slower lifetime components are plotted as a function of silica shell thickness and plasmon band maximum. The lifetime of free IRDye is 1.12 ns.

Interestingly, the region of strongest reduction in fluorescence lifetime is not where maximum fluorescence intensity is observed. This indicates that the observed intensity enhancements cannot be completely attributed to an increase in the radiative decay rate K_{rad} (Equation 2.3), but is a complex interplay of all the processes involved. Such lifetime changes are inconsistent with scattering as the main mechanism for increased light emission. We would expect that, at distances less than 20 nm, there is a simultaneous increase in the nonradiative decay rate that leads to the smaller increase in fluorescence intensity at these distances. This demonstrates the complexity of plasmon-enhanced fluorescence – it cannot simply be described as increased radiative decay rates near a plasmonic structure. Both distance and plasmon maximum are important factors in the changing decay rates and measured fluorescence lifetimes.

The percent of the slow component of the full fluorescence lifetime decay is shown in Figure 2.9. The data show some interesting trends. For example, at the thick shell limit (> 25 nm) we see what is likely the pure plasmonic contribution mediated by its dependence on the orientation of each dye's molecular transition dipole relative to the longitudinal plasmonic axis. At the other limit (<15 nm), nonradiative contributions become more important, but they clearly compete with the other plasmon-enhanced processes (*vide supra*). We note that the slow component is generally a significant fraction of the total emission dynamics, and has both plasmonic and shell thickness dependence to its dynamics so it is not attributed to unbound IRDye in solution.

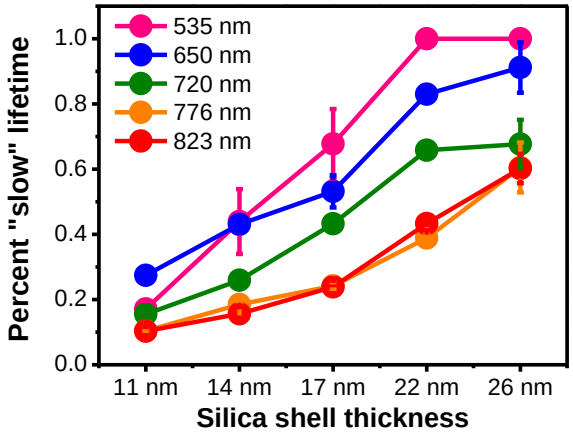

Figure 2.9 Percent of the slow component of the fluorescence lifetime as a function of silica shell thickness and plasmon band maximum.

These results suggest that there are possibly two or more distinct environments that the fluorophores experience on the nanoparticle surface. One possibility is the faster lifetime results from more strongly coupled species, whereas the slower lifetimes come from more weakly coupled dye molecules. Another reason for multiple apparent environments is nonrandom dye orientation and positions. We assume that orientation of IRDye molecules on the surface is random, but this may not be the case. It is also possible that we are observing the effect of IRDye location (*i.e.*, fluorophores attached at the nanorod ends *versus* the rod sides). Dyes tethered near the ends of the rods would experience very different field strengths and

could behave very differently than dyes attached near the rod shaft center.[49,54] However, definitive experiments on the effect of end *versus* side dye loading on fluorescence behavior is beyond the scope of this work. A potential complicating factor is the possibility that IRDye could be loaded in the shell pores and therefore not at unique distance away from the metal. However the pore size with this coating method is 2 – 2.5 nm,[55,56] and the IRDye diameter is approximately 2 nm.[11] With the additional reduction in pore size due to azide functionalization expected, it is unlikely that any significant fraction of IRDye would diffuse deep into the pores.

2.3.4 DYE-NANOPARTICLE INTERACTIONS

Molecular fluorescence can be altered by simply changing the local environment that a fluorescent dye experiences, aside from any plasmonic effects.[11,21] It was therefore necessary to account for any possible dye-nanoparticle interactions such as dye-surface or dye-dye interactions that may have occurred, apart from an "antenna-like" or other plasmonic coupling. IRDye was attached to mesoporous silica nanoparticles (MSNs) to determine whether IRDye attachment to a silica surface resulted in any change in fluorescence. Azide-functionalized MSNs were prepared following the same Stöber preparation and azide functionalization methods used for silica coating and functionalization of gold nanorods (Figure 2.10a). The as-synthesized MSNs are about 36 nm in diameter and show mesoporosity which is similar to the silica-coated gold nanorods.

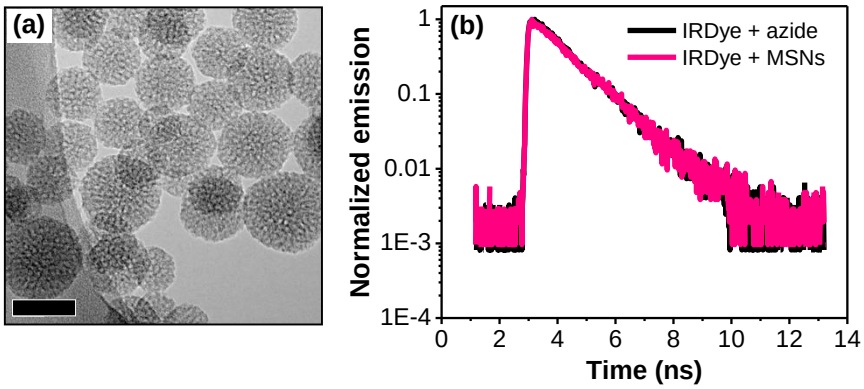

Figure 2.10 (a) TEM image of MSNs 36 ± 9 nm. Scale bar = 50 nm. (b) Fluorescence decay curves of IRDye bound to 3-azidopropyltrimethoxysilane and MSNs.

Fluorescence of IRDye bound to MSNs was monitored *via* TRPL and steady-state measurements. TRPL measurements of IRDye-loaded MSNs and IRDye with the azide demonstrate single exponential decay behavior similar to free IRDye (Figure 2.10b). Calculated fluorescence lifetimes are shown in Table 2.1. The fluorescence lifetime of IRDye bound to the azide and the silica surface show only slight increases compared to free IRDye. This small increase may be attributed to solvent properties or the change in refractive index a fluorophore experiences near a silica surface. In addition, there is no change in steady-state fluorescence intensity compared to free IRDye (Table 2.6) which confirms that the slight increase in

lifetime with the MSNs is not significant. These results demonstrate that simply binding IRDye to the silica surface does not significantly change fluorescence behavior.

Table 2.6 Fluorescence lifetime and steady-state intensity of IRDye bound to azide and MSNs.

Sample	Lifetime	Steady-state intensity
IRDye	1.12 ± 0.02 ns	-
IRDye + azide	1.19 0.03 ns	1.00
IRDye + MSNs	1.24 ± 0.04 ns	1.04 ± 0.02

Interactions between dye molecules on a surface can also modify fluorescence behavior, resulting in fluorescence quenching. At short dye separations, Förster resonance energy transfer can occur between neighboring fluorophores where a donor fluorophore transfers energy to an acceptor *via* nonradiative coupling, resulting in fluorescence quenching. This effect is dependent on the separation and degree of spectral overlap between neighboring fluorophores, and it is generally more pronounced when there is strong local dye concentration (*i.e.,* on a nanoparticle surface).[57] It is therefore necessary to limit dye loading on a nanoparticle to avoid issues of quenching which can result in decreased fluorescence lifetime and steady-state intensity relative to free dye.

The effect of dye-dye separation on fluorescence behavior was investigated by changing the number of IRDye molecules loaded on the surface of silica-coated gold nanorods. AR 1.1 gold nanorods with a plasmon maximum at 535 nm were synthesized and coated with 33 nm thick silica (Figure 2.11 inset). The nanoparticles were loaded with varying amounts of IRDye to give approximate dye-dye separations ranging from 6 to 22 nm.

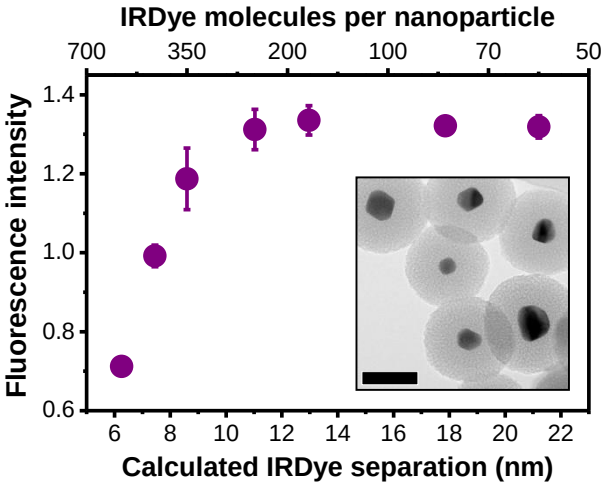

Figure 2.11 Steady-state fluorescence intensity relative to free IRDye as a function of dye molecules per molecule or calculated separation between IRDye molecules. Inset is an image of AR 1.1 nanorods with 33 nm thick silica shells. Scale bars = 50 nm.

Steady-state fluorescence analysis of these samples reveals that below 9 nm dye-dye separation (~275 dyes/nanoparticle), a significant decrease in fluorescence intensity occurs (Figure 2.11). However, at separations above 9 nm, the fluorescence intensity levels off due to the reduced interactions between neighboring fluorophores. Based on this result, IRDye loading was limited in all experiments to give separations at or greater than 9 nm (~160 dyes/particle). This prevented any dye-dye interactions. Therefore, the observed changes in fluorescence of IRDye bound to silica-coated gold nanorods can only be due to plasmonic interactions not dye-dye or dye-surface interactions. We note that Wang *et al.* has modeled donor-acceptor energy transfer mediated by plasmonic coupling. Their work suggests that the plasmonic interaction is competitive with conventional Förster processes.[58]

2.4 COMPARISON TO RELEVANT WORK

Halas *et al.* have published several key papers on near-infrared-absorbing dyes' photophysical properties in the presence of plasmonic nanoparticles.[11,24,59] In reference 24, her group demonstrated that near-infrared absorbing dyes near a plasmonic nanoparticle exhibited increased fluorescence quantum yield (up to 50X) for the case of a nanoparticle with a large scattering cross-section and a plasmon maximum near the emission energy of the dye.[24] In reference 11, Halas *et al.* found that the steady-state fluorescence emission of IRDye (called IR800) was enhanced by a factor of 9 on gold nanorods bearing an 8 nm protein layer, and that the fluorescence decay of the dye on the nanoparticle exhibited shorter lifetimes compared to free dye.[11] In reference 59, Halas *et al*. placed IRDye (called IR800 again) in a thin silica layer between a gold core and a gold shell, with the dye emission maximum resonant with a plasmon band maximum. The Halas group found a steady-state fluorescence enhancement by 16-fold for IRDye, comparing the gold-silica precursor seed to the final gold-silica-gold nanostructure, with the dyes approximately 4-10 nm away from the inner gold core.[59]

As Wang has pointed out,[54] the plasmonic field can alter both radiative and nonradiative decay rates in nearby molecules, even though it is frequently assumed that the nonradiative rate is not changing upon molecular adsorption onto a spacer layer on top of a plasmonic nanoparticle. In general, distances ~10 nm from the metal surface, and plasmon peak positions between the absorption and emission maximum of the dye are considered optimal to observe plasmon-enhanced fluorescence.[54] Halas *et al*. have also suggested that, when the plasmon band is between absorbance and emission, enhancement is maximized.[59] In our case, IRDye's absorption and emission maxima are so close together that no plasmon band is "between" them; nonetheless, the nanorods that give the largest fluorescence enhancement are indeed the ones with a plasmon maximum that overlaps the molecular bands.

In addition, our fine gradation of silica shell thicknesses allows us to pinpoint the "best" spacer thickness at 17 nm. We find multi-exponential fluorescence decays that show fast components for dyes on plasmonic nanoparticles, but these components vary as a function of silica shell thickness and plasmon band maximum in a complex manner. Quantum mechanical calculations of relative radiative and nonradiative decays for a dye molecule near a gold "nanorod" (which is taken as two spheres next to each other) show

that for a constant size of nanorod, moving the dye from 5 to 20 nm away increases both radiative and nonradiative rates from 5 – 15 nm, but at ~15 nm away, the nonradiative decay rate change turns off, and the radiative rate continues to increase, giving a higher relative brightness of emitted light from the dye.[60] The distance at which the behavior changes, 15 nm, is identical to what we find in our data (*vide supra*). A very recent report finds 1000-fold fluorescence enhancement of dyes near single gold nanorods in single-molecule experiments, especially when the plasmon is resonant with the laser and dye emission maximum, as observed here; the larger enhancements could be due to individual dye binding events near the ends of gold nanorods, a process that is not directly resolved in our data.[61]

2.5 CONCLUSIONS

We have observed distance and plasmon wavelength dependent fluorescence of IRDye 800CW DBCO bound to silica-coated gold nanorods. Steady-state measurements demonstrate wavelength and distance dependent emission with approximately 10-fold maximum fluorescence intensity enhancement was observed in the fluorescence hotspot. The presence of multi-exponential decay in the time-resolved measurements indicates that there were multiple decay pathways present in our system and are consistent with enhanced radiative and nonradiative contributions. A strong reduction in fluorescence lifetime was observed with decreasing silica shell thickness and when there was strong spectral overlap between nanorod plasmon band and IRDye absorption/emission. Control experiments confirmed that the observed changes in fluorescence were due to plasmonic interactions, not simply attachment to a silica surface. In addition, limiting IRDye loading assured minimal dye-dye interactions on the nanoparticle surfaces. Together, these results revealed that plasmon-fluorophore coupling, resulting in fluorescence intensity enhancement, is a complex process. Nevertheless, enhancement of low quantum yield fluorophores *via* coupling to plasmonic nanoparticles remains a viable option to increase their potential biological application.

2.6 REFERENCES

1. Lohse, S. E.; Murphy, C. J. The Quest for Shape Control: A History of Gold Nanorod Synthesis. *Chem. Mater*. **2013,** *25*, 1250-1261.
2. Nikoobakht, B.; El-Sayed, M. A. Preparation and Growth Mechanism of Gold Nanorods (NRs) Using Seed-Mediated Growth Method. *Chem. Mater*. **2003,** *15*, 1957-1962.
3. Murphy, C. J.; Thompson, L. B.; Chernak, D. J.; Yang, J. A.; Sivapalan, S. T.; Boulos, S. P.; Huang, J.; Alkilany, A. M.; Sisco, P. N. Gold Nanorod Crystal Growth: From Seed-Mediated Synthesis to Nanoscale Sculpting. *Curr. Opin. Colloid Interface Sci*. **2011,** *16,* 128-134.
4. El-Sayed, M. A. Some Interesting Properties of Metals Confined in Time and Nanometer Space of Different Shapes. *Acc. Chem. Res*. **2001,** *34,* 257-264.
5. Eustis, S.; El-Sayed, M. A. Why Gold Nanoparticles Are More Precious than Pretty Gold: Noble Metal Surface Plasmon Resonance and Its Enhancement of the Radiative and Nonradiative Properties of Nanocrystals of Different Shapes. *Chem. Soc. Rev*. **2006,** *35,* 209-217.
6. Link, S.; Mohamed, M. B.; El-Sayed, M. A. Simulation of the Optical Absorption Spectra of Gold Nanorods as a Function of Their Aspect Ratio and the Effect of the Medium Dielectric Constant. *J. Phys. Chem. B* **1999,** *103,* 3073-3077.
7. N'Gom, M.; Li, S.; Schatz, G.; Erni, R.; Agarwal, A.; Kotov, N. Norris, T. B. Electron-Beam Mapping of Plasmon Resonances in Electromagnetically Interacting Gold Nanorods. *Phys. Rev. B* **2008,** *80,* 113411.

8. Norman, R. S.; Stone, J. W.; Gole, A.; Murphy, C. J.; Sabo-Atwood, T. Targeted Photothermal Lysis of the Pathogenic Bacteria, *Pseudomonas aeruginosa*, by Gold Nanorods. *Nano Lett*. **2008,** *8,* 302-306.
9. Nikoobakht, B.; Wang, J.; El-Sayed, M. A. Surface-Enhanced Raman Scattering of Molecules Adsorbed on Gold Nanorods: Off-Surface Plasmon Resonance Condition. *Chem. Phys. Lett*. **2002,** *366,* 17-23.
10. Sivapalan, S. T.; Vella, J. H.; Yang, T. K.; Dalton, M. J.; Swiger, R. N.; Haley, J. E.; Cooper, T. M.; Urbas, A. M.; Tan, L.-S.; Murphy, C. J. Plasmonic Enhancement of the Two Photon Absorption Cross Section of an Organic Chromophore Using Polyelectrolyte-Coated Gold Nanorods. *Langmuir* **2012,** *28,* 9147-9154.
11. Bardhan, R.; Grady, N. K.; Cole, J. R.; Joshi, A.; Halas, N. J. Fluorescence Enhancement by Au Nanostructures: Nanoshells and Nanorods. *ACS Nano* **2009,** *3,* 744-752.
12. Fu, Y.; Zhang, J.; Lakowicz, J. R. Plasmon-Enhanced Fluorescence from Single Fluorophores End-Linked to Gold Nanorods. *J. Am. Chem. Soc*. **2010,** *132,* 5540-5541.
13. Nepal, D.; Drummy, L. F.; Biswas, S.; Park, K.; Vaia, R. A. Large Scale Solution Assembly of Quantum Dot-Gold Nanorod Architectures with Plasmon Enhanced Fluorescence. *ACS Nano* **2013,** *7,* 9064-9074.
14. Darvill, D.; Centeno, A.; Xie, F. Plasmonic Fluorescence Enhancement by Metal Nanostructures: Shaping the Future of Bionanotechnology. *Phys. Chem. Chem. Phys*. **2013,** *15,* 15709-15726.
15. Gandra, N.; Portz, C.; Tian, L.; Tang, R.; Xu, B.; Achilefu, S.; Singamaneni, S. Probing Distance-Dependent Plasmon-Enhanced Near-Infrared Fluorescence Using Polyelectrolyte Multilayers as Dielectric Spacers. *Angew. Chem., Int. Ed*. **2014,** *53,* 866-870.
16. Geddes, C. D.; Lakowicz, J. R. Metal-Enhanced Fluorescence. *J. Fluoresc*. **2002,** *12,* 121-129.
17. Lakowicz, J. R. Radiative Decay Engineering 5: Metal-Enhanced Fluorescence and Plasmon Emission. *Anal. Biochem*. **2005,** *337,* 171-194.
18. Li, X.; Qian, J.; Jiang, L.; He, S. Fluorescence Quenching of Quantum Dots by Gold Nanorods and Its Application to DNA Detection. *Appl. Phys. Lett*. **2009,** *94,* 063111.
19. Horimoto, N. N.; Imura, K.; Okamoto, H. Dye Fluorescence Enhancement and Quenching by Gold Nanoparticles: Direct Near-Field Microscopic Observation of Shape Dependence. *Chem. Phys. Lett*. **2008,** *467,* 105-109.
20. Schneider, G.; Decher, G. Distance-Dependent Fluorescence Quenching on Gold Nanoparticles Ensheathed with Layer-by-Layer Assembled Polyelectrolytes*. Nano Lett*. **2006,** *6,* 530-536.
21. Reineck, P.; Gómez, D.; Ng, S. H.; Karg, M.; Bell, T.; Mulvaney, P.; Bach, U. Distance and Wavelength Dependent Quenching of Molecular Fluorescence by Au@SiO_2 Core-Shell Nanoparticles. *ACS Nano* **2013,** *8,* 6636-6648.
22. Cheng, D.; Xu, Q.-H. Separation Distance Dependent Fluorescence Enhancement of Fluorescein Isothiocyanate by Silver Nanoparticles. *Chem. Commun*. **2007,** *43,* 248-250.
23. Kümmerlen, J.; Leitner, A.; Brunner, H.; Aussenegg, F. R.; Wokaun, A. Enhanced Dye Fluorescence over Silver Island Films: Analysis of the Distance Dependence. *Mol. Phys.* **1993,** *8,* 1031-1046.
24. Tam, F.; Goodrich, G. P.; Johnson, B. R.; Halas, N. J. Plasmonic Enhancement of Molecular Fluorescence. *Nano Lett*. **2007,** *7,* 496-501.
25. Geddes, C. D. *Metal-Enhanced Fluorescence*, 1st ed.; John Wiley & Sons, Inc.: Hoboken, NJ, 2010.
26. Arunkumar, E.; Fu, N.; Smith, B. D. Squaraine-Derived Rotaxanes: Highly Stable, Fluorescent Near-IR Dyes. *Chem. Eur. J.* **2006,** *12,* 4684-4690.
27. Lakowicz, J. R. Plasmonics in Biology and Plasmon-Controlled Fluorescence. *Plasmonics* **2006,** *1,* 5-33.
28. IRDye Infrared Dyes. http://www.licor.com/bio/products/reagents/irdye (accessed February 5, 2016).
29. Gorelikov, I.; Matsuura, N. Single-Step Coating of Mesoporous Silica on Cethyltrimethyl Ammonium Bromide-Capped Nanoparticles. *Nano Lett*. **2008,** *8,* 369-373.
30. Stöber, W.; Fink, A.; Bohn, E. Controlled Growth of Monodisperse Silica Spheres in the Micron Size Range. *J. Colloid Interface Sci*. **1968,** *26,* 62-69.
31. Holb, H. C.; Finn, M. G.; Sharpless, K. B. Click Chemistry: Diverse Chemical Function from a Few Good Reactions. *Angew. Chem., Int. Ed*. **2001,** *40,* 2004-2021.
32. Agard, N. J.; Prescher, J. A.; Bertozzi, C. R. A Strain-Promoted [3 + 2] Azide-Alkyne Cycloaddition for Covalent Modification of Biomolecules in Living Systems. *J. Am. Chem. Soc*. **2004,** *126,* 15046-15047.

33. Sau, T. K.; Murphy, C. J. Room Temperature, High-Yield Synthesis of Multiple Shapes of Gold Nanoparticles in Aqueous Solution. *J. Am. Chem. Soc*. **2004,** *126,* 8648-8649.
34. DeVetter, B. M.; Bhargava, R.; Murphy, C. J. Computational Study of the Surface-Enhanced Raman Scattering from Silica-Coated Silver Nanowires. *Photochem. Photobiol*. **2014,** *90,* 415-418.
35. Rodríguez-Fernández, J.; Pastoriza-Santos, I.; Pérez-Juste, J.; García de Abajo, F. J.; Liz-Marzán, L. M. The Effect of Silica Coating on the Optical Response of Sub-micrometer Gold Spheres. *J. Phys. Chem. C* **2007,** *111,* 13361-13366.
36. Nooney, R. I.; Dhanasekaran, T.; Chen, Y.; Josephs, R.; Ostafin, A. E. Self-Assembly of Mesoporous Nanoscale Silica/Gold Composites. *Langmuir* **2003,** *19,* 7628-7637.
37. Zhan, Q.; Qian, J.; Li, X.; He, S. A Study of Mesoporous Silica-Encapsulated Gold Nanorods as Enhanced Light Scattering Probes for Cancer Cell Imaging. *Nanotechnology* **2010,** *21,* 055704.
38. Cifuentes, A.; Bernal, J. L.; Diez-Masa, J. C. Determination of the Critical Micelle Concentration Values Using Capillary Electrophoresis Instrumentation. *Anal. Chem*. **1997,** *69,* 4271-4274.
39. Sun, S.; Wu, P. Mechanistic Insights into Cu(I)-Catalyzed Azide-Alkyne "Click" Cycloaddition Monitored by Real Time Infrared Spectroscopy. *J. Phys. Chem. A* **2010,** *114,* 8331-8336.
40. Kar, M.; Bharmana, M.; Das, A.; Panneri, S.; Gupta, S. S. Synthesis and Characterization of Poly-L-lysine Grafted SBA-15 Using NCA Polymerization and Click Chemistry. *J. Mater. Chem*. **2011,** *21,* 6690-6697.
41. Kühn, S.; Håkanson, U.; Rogobete, L.; Sandoghdar, V. Enhancement of Single-Molecule Fluorescence Using a Gold Nanoparticle as an Optical Nanoantenna. *Phys. Rev. Lett*. **2006,** *97,* 017402.
42. Dvoynenko, M. M.; Wang, J.-K. Revisiting Coupling between a Single Molecule and Surface Plasmons. *Opt. Lett.* **2013,** *5,* 760-762.
43. Nerkararyan, K. V.; Bozhevolnyi, S. I. Relaxation Dynamics of a Quantum Emitter Resonantly Coupled to a Metal Nanoparticle. *Opt. Lett*. **2014,** *6,* 1617-1620.
44. Barthes, J.; Bouhelier, A.; Dereux, A.; des Francs, G. C. Coupling of a Dipolar Emitter into One-Dimensional Surface Plasmon. *Sci. Rep.* **2013,** *3,* 2734.
45. Akimov, A. V.; Mukherjee, A.; Yu, C. L.; Chang, D. E.; Zibrov, A. S.; Hemmer, P. R.; Park, H.; Lukin, M. D. Generation of Single Optical Plasmons in Metallic Nanowires Coupled to Quantum Dots. *Nature* **2007,** *450,* 402-406.
46. Lakowicz, J. R. *Principles of Fluorescence Spectroscopy*, 2nd ed.; Kluwer Academic/Plenum Publishers: New York, 1999; pp 51-55, 95-101.
47. Anger, P.; Bharadwaj, P.; Novotny, L. Enhancement and Quenching of Single-Molecule Fluorescence. *Phys. Rev. Lett*. **2006,** *96,* 113002.
48. Lakowicz, J. R. Radiative Decay Engineering: Biophysical and Biomedical Applications. *Anal. Biochem.* **2001,** *298,* 1-24.
49. Guzatov, D. V.; Klimov, V. V. Radiative Decay Engineering by Triaxial Nanoellipsoids. *Chem. Phys. Lett.* **2005,** *412,* 341-346.
50. Moroz, A. Non-radiative Decay of a Dipole Emitter Close to a Metallic Nanoparticle: Importance of Higher-Order Multipole Contributions. *Opt. Commun.* **2010,** *283,* 2277-2287.
51. Carminati, R.; Greffet, J. J.; Henkel, C.; Vigoureux, J. M. Radiative and Non-radiative Decay of a Single Molecule Close to a Metallic Nanoparticle. *Opt. Commun.* **2006,** *261,* 368-375.
52. Novotny, L.; Hecht, B. *Principles of Nano-Optics,* 2nd ed.; Cambridge University Press: Cambridge, UK, 2012.
53. He, G. S.; Zhu, J.; Yong, K.-T.; Baev, A.; Cai, H.-Z.; Hu, R.; Cui, Y.; Zhang, X.-H.; Prasad, P. N. Scattering and Absorption Cross-Section Spectral Measurements of Gold Nanorods in Water. *J. Phys. Chem. C* **2010**, *114*, 2853-2860.
54. Ming, T.; Chen, H. J.; Jiang, R. B.; Li, Q.; Wang, J. F. Plasmon-Controlled Fluorescence: Beyond the Intensity Enhancement. *J. Phys. Chem. Lett.* **2012,** *3,* 191-202.
55. Yang, J.; Shen, D.; Zhou, L.; Li, W.; Fan, J.; El-Toni, A. M.; Zhang, W.; Zhang, F.; Zhao, D. Mesoporous Silica-Coated Plasmonic Nanostructures for Surface-Enhanced Raman Scattering Detection and Photothermal Therapy. *Adv. Healthcare Mater.* **2014,** *3,* 1620-1628.
56. Zhou, S.; Sha, H.; Liu, B.; Du, X. Integration of Simultaneous and Cascade Release of Two Drugs into Smart Single Nanovehicles Based on DNA-Gated Mesoporous Silica Nanoparticles. *Chem. Sci.* **2014,** *5,* 4424-4433.

57. Wu, P.; Brand, L. Resonance Energy Transfer: Methods and Applications. *Anal. Biochem*. **1994,** *218,* 1-13.
58. Zhao, L.; Ming, T.; Shao, L.; Chen, H. J.; Wang, J. F. Plasmon-Controlled Förster Resonance Energy Transfer. *J. Phys. Chem. C* **2012,** *116,* 8287-8296.
59. Ayala-Orozco, C.; Liu, J. G.; Knight, M. W.; Wang, Y.; Day, J. K.; Nordlander, P.; Halas, N. J. Fluorescence Enhancement of Molecules Inside a Gold Nanomatryoshka. *Nano Lett.* **2014,** *14,* 2926-2933.
60. Vukovic, S.; Corni, S.; Mennucci, B. Fluorescence Enhancement of Chromophores Close to Metal Nanoparticles. Optimal Setup Revealed by the Polarizable Continuum Model. *J. Phys. Chem. B* **2009,** *113,* 121-133.
61. Khatua, S.; Paulo, P. M. R.; Yuan, H.; Gupta, A.; Zijlstra, P.; Orrit, M. Resonant Plasmonic Enhancement of Single-Molecule Fluorescence by Individual Gold Nanorods. *ACS Nano* **2014**, *8*, 4440-4449.

CHAPTER 3:
INTERACTIONS OF BACTERIAL LIPOPOLYSACCHARIDES WITH GOLD NANOROD SURFACES INVESTIGATED BY REFRACTOMETRIC SENSING

3.1 INTRODUCTION

The promise of nanotechnology includes potential biological applications such as biomolecular sensing, photothermal therapy, bioimaging, and drug delivery. Gold nanoparticles are of particular interest for many of these applications due to their unique stability and size/shape-dependent optical properties. However, the nano-bio interface is quite complicated.[1,2] In order for potential *in vivo* biological applications to be realized, a good understanding of the nanoparticle-cell interface is essential.[3,4] To date, studies of gold nanoparticles and cells have mainly focused on mammalian cells, but there has been growing interest in interactions between bacteria and gold nanoparticles.[5-12] Nanoparticles have been shown to attach to bacterial cell walls but do not appear to be taken up by the cells, unlike with mammalian cells.[5,6,10,12,13] However, a majority of the work is dedicated to nanoparticle-induced antibacterial activity from small molecules bound to the particle surface, not modulation of nanoparticle-bacteria surface interactions.[6-11]

Because of the increasing prevalence of antibiotic resistance in pathogenic bacteria, newer and more effective strategies for combatting infections are necessary.[14] Researchers have recently demonstrated targeted attachment and photothermal killing of pathogenic bacteria using gold nanoparticles.[15-23] Gold nanoparticles (including gold nanorods) strongly absorb laser light at the wavelengths resonant with their surface plasmons. The light is then converted to heat *via* pathways of photophysical processes, causing photothermal-induced hyperthermia and irreversible damage to cell walls.[24] Examples of this include the application of gold nanorods for photothermal killing of Gram-negative, pathogenic bacteria such as *Pseudomonas aeruginosa*,[17] *Salmonella*,[18,19] *Escherichia coli*,[19-21] and *Staphylococcus aureus*.[22,23] These reports demonstrate how gold nanorods may be a potential tool where antibiotics are limited to destroy pathogenic bacteria. A better understanding of gold nanorod binding to bacterial surfaces and nanoparticle-bacteria interactions would increase the prospective use of gold nanorods in this application.[15,16]

It is likely that gold nanorod attachment to bacterial surfaces is influenced by interactions with lipopolysaccharides (LPS) which make up ~75% of the outer membrane surface of Gram-negative bacteria.[24] They are known to contribute to bacterial structure, toxicity, immunity, and also influence bacterial interactions with the outside environment. LPS molecules consist of three parts. The Lipid A portion contributes to bacterial pathogenesis, and anchors the molecule to the cell membrane while the oligosaccharide core is generally conserved across bacterial species. The O-antigen is a glycan polymer, the outermost portion and varies most from strain-to-strain.[25,26] To date, there are only a few studies of nanoparticle interactions with LPS in the literature.[27-31] To the best of our knowledge, no studies explore

[*] This chapter is reprinted with permission from: Nardine S. Abadeer, Gergő Fülöp, Si Chen, Mikael Käll and Catherine J. Murphy. *ACS Appl. Mater. Interfaces* **2015,** *7,* 24915–24925*.* Copyright (2015) American Chemical Society.

how variation in nanoparticle surface coating affects attachment of LPS to nanoparticle surfaces. Furthermore, no studies investigate interactions of various types of LPS with gold nanoparticles.

Researchers have successfully demonstrated localized surface plasmon resonance (LSPR) refractometric sensing using gold nanorods immobilized on substrates or in colloidal solutions. Detection of biomolecules attaching to/near these metal nanoparticles is accomplished by measuring the change in refractive index caused by the target binding.[32-34] We modified existing methods to assess LPS binding to gold nanorods. Gold nanorods were immobilized onto glass substrates, and then coated with various polymers. LSPR refractometric sensing was carried out to assess attachment of LPS from *P. aeruginosa*, *S. enterica* and *E. coli* to gold nanorod substrates or colloidal gold nanorods. By varying gold nanorod surface coating and LPS type, we are able to gain some insights into the potentially complex bacteria-nanoparticle interface.

3.2 MATERIALS AND METHODS

3.2.1 MATERIALS

Cetyltrimethylammonium bromide (CTAB, ≥99.0%), hydrogen tetrachloroaurate trihydrate ($HAuCl_4 \cdot 3H_2O$, ≥99.9%), sodium borohydride ($NaBH_4$, ≥99%), silver nitrate ($AgNO_3$, ≥99.0%), poly(acrylic acid sodium salt) (PAA, MW ~15,000, 35 wt.% in H_2O), polyallylamine hydrochloride (PAH, MW ~15,000) and LPS from *Pseudomonas aeruginosa* 10 (purified by phenol extraction) were purchased from Sigma-Aldrich (USA). Hydrogen peroxide (H_2O_2, ≥30%), ammonium hydroxide (NH_4OH, 28-30%), hydrochloric acid (HCl, ≥31.5%), 3-mercaptopropyltrimethoxy silane (MPTMS, 95%), poly(diallyldimethylammonium) chloride (PDDA, MW ~200,000-350,000), LPS from *Salmonella enterica* serotype typhimirium (purified by phenol extraction), LPS from *Escherichia coli* 0127:B8 (purified by phenol extraction), sodium chloride (NaCl, ≥99.5%), and heparin sodium salt from porcine intestinal mucosa (HEP, ≥150 IU/mg) were purchased from Sigma-Aldrich (Sweden). Methoxyl polyethylene glycol thiol (mPEG-SH, 5000 g/mol) was purchased from Nanocs (USA). L (+)-ascorbic acid (99%) was purchased from Acros Organics (USA). Ethanol (EtOH, 99.7%) was purchased from Solveco (Sweden). Nitric acid (HNO_3, 65%) was purchased from Merck (Sweden). Twenty-five mm circular glass coverslips were purchased from Menzel-Gläser (Germany, #1.5). Unless otherwise noted, all solutions and experiments used deionized water (18.2 MΩ) from a Milli-Q Millipore water purification system. All chemicals were used as received.

3.2.2 GOLD NANOROD SYNTHESIS

Five 500 mL batches of aspect ratio 3.6 CTAB gold nanorods were prepared, and a previous report outlines the synthesis procedure.[35] The only modification was the addition of 4 mL of 0.01 M $AgNO_3$ to the growth solution. As-synthesized gold nanorods were aged overnight (18 h at 27°C). Then, the gold nanorod solutions were purified *via* centrifugation at 13,500 rcf for 20 min and the pellets from the five batches were combined and diluted with water to 100 mL (~4 nM) for later use. UV-vis absorbance spectra were obtained using a Cary 5000 UV-vis spectrometer (Agilent, USA) to determine plasmon maximum and gold nanorod

concentration. Concentration of gold nanorod solutions was determined from extinction coefficients at each plasmon maximum, which had been previously calculated using inductively-coupled plasma atomic emission spectroscopy.[36] Transmission electron microscopy (TEM) images were obtained on a JEOL 2100 cryo TEM (JEOL, Japan). ImageJ analysis of TEM images (300 particles measured) was carried out to determine the average dimensions and aspect ratio of the gold nanorods. Dynamic light scattering and ζ-potential measurements were carried out on a ZetaPals zeta-potential analyzer (Brookhaven, USA).

3.2.3 IMMOBILIZATION OF GOLD NANORODS ON GLASS SUBSTRATES

Glass substrates (25 mm coverslips) were cleaned before nanorod immobilization to remove organic contaminants and hydroxylate the glass surface. The substrates were immersed in a solution of 6:2:1 H_2O:H_2O_2:NH_4OH at 70ºC for 20 min and then rinsed with water. Next, the substrates were immersed in a solution of 6:2:1 H_2O:H_2O_2:HCl at 70ºC for 20 min, rinsed with water and baked in an oven 130ºC for 1 h.

After drying, glass substrates were functionalized with MPTMS.[32,37] Substrates were individually immersed in 10 mL of EtOH containing 1 µL of MPTMS for 30 min and were rinsed twice with EtOH and dried under N_2 gas. Next, 1.75 mL of a concentrated gold nanorod solution (~4 nM) was diluted to 10 mL and centrifuged at 10,000 g for 25 min. We find that removal of excess CTAB *via* centrifugation is critical to successful nanorod immobilization. The supernatant was removed, then 1 mL of HNO_3 at pH 2 was added to the pellet, and the solution was diluted to 10 mL with water. An MPTMS-functionalized glass substrate was immersed in this solution of ~0.6 nM CTAB gold nanorods at pH 3 for 15-20 min. We note that it was possible to reuse the gold nanorod solutions one or two additional times, allowing for a more economical substrate preparation procedure. After immobilization, the substrates were carefully rinsed with water and dried under N_2. There was a noticeable color change and the substrates visibly changed from colorless to pale blue after immersion indicating successful nanorod immobilization.

UV-vis absorbance spectroscopy of gold nanorod substrates was used to confirm nanorod immobilization and to detect shifts in the longitudinal plasmon maximum. Scanning electron microscopy (SEM) images of the substrates were obtained on a Zeiss Supra60 VP microscope (Zeiss, Germany). E-spacer was spin-coated onto the substrates prior to imaging to reduce charging effects. ImageJ analysis of SEM images (3000 particles were counted in 3 samples) was carried out to determine the average nanorod density on the substrates.

3.2.4 POLYMER FUNCTIONALIZATION OF GOLD NANORODS

Gold nanorod substrates were functionalized with PAA, PAH, HEP, PDDA, or PEG. The layering order is listed in Table 3.1. For each polymer coating step with PAA, PAH, or PDDA, 1 mL of polymer stock (10 mg/mL of polymer + 1 mM NaCl) and 0.5 mL of 10 mM NaCl was added to 5 mL of water for layer-by-layer polyelectrolyte coating.[37,38] The solutions were mixed on a vortex mixer and the gold nanorod substrates were immersed in the solution for at least 6 h. In the case of HEP coating, the polymer stock was 2 mg/mL of HEP + 1 mM NaCl. For PEG coating, a substrate was immersed in 5 mL of 0.5 mg/mL mPEG-SH for at

least 6 h. The PEG solution had been sonicated for 15 min prior to use. After each polymer coating step, the gold nanorod substrates were rinsed with water and dried under N_2. UV-vis absorbance measurement of the substrates was used to detect shifts in longitudinal plasmon maximum. Colloidal nanorods were coated with polymers in the same way. The solutions were incubated at least 6 h, and then centrifuged at 10,000 rcf for 20 min. The coated gold nanorods were suspended in water and diluted to 0.25 nM.

Table 3.1 Selected polymers used to coat gold nanorod substrates and colloidal gold nanorods. Polymer name, abbreviation, molecular weight, polyelectrolyte layering order in the presence of NaCl and typical longitudinal plasmon shift observed of the substrates in air after polymer coating.

Name	Abbreviation	Molecular weight	Layering order	Longitudinal UV-Vis shift
Polyacrylic acid sodium salt	PAA	15,000 g/mol	CTAB/PAA	-8 ± 4 nm
Polyallylamine hydrochloride	PAH	15,000 g/mol	CTAB/PAA/ PAH	8 ± 4 nm
Heparin sodium salt	HEP	10,000 g/mol	CTAB/HEP	-5 ± 3 nm
Polydiallyldimethyl ammonium chloride	PDDA	200,000- 350,000 g/mol	CTAB/PAA/ PDDA	8 ± 5 nm
Methoxyl polyethylene glycol thiol	PEG	5000 g/mol	-	29 ± 2 nm

3.2.5 REFRACTIVE INDEX SENSITIVITY

Polymer-coated gold nanorod substrates were immersed in various refractive index solvents to determine refractive index sensitivity.[32] The substrates were inserted into a flow cell and then the nanorods on the outward-facing side were removed by tape-stripping. The nanorods were successfully removed from a substrate by the application and pulling off of tape on the surface. We note that the magnitude of the substrate absorbance was halved after tape stripping, which demonstrated that this was an effective method for nanorod removal. The refractive index of pure water and ethylene glycol are 1.333 and 1.431, respectively. Mixtures of water and ethylene glycol (0, 5, 10, 15, 20, 30, 40, 50 and 75%) by volume were then injected into the flow cell allowing for change in refractive index from 1.33 – 1.41.[39] UV-vis absorbance spectra demonstrated shifts in the plasmon maximum with increasing ethylene glycol. The longitudinal peak maxima were estimated by fitting the peak to quadratic polynomials with OriginPro. Refractive index sensitivity can be approximated by fitting a line to the plot of peak shift *versus* refractive index and the slope of the line is the refractive index sensitivity.

3.2.6 LSPR REFRACTOMETRIC SENSING WITH GOLD NANOROD SUBSTRATES

Gold nanorod substrates were inserted into a flow cell and then the nanorods on the outward-facing side were removed by tape-stripping. The optical setup used in these refractometric sensing experiments has been previously described.[40] The setup consisted of a white light source, illumination fiber, flow cell,

collection fiber, and miniature spectral analyzer (B&WTek, <0.2 nm spectral resolution), coupled to a personal computer. The flow cell was immobilized between the light source and the spectrometer during the experiments. The absorbance was monitored in the region from 700-900 nm. A MatLab program was used to estimate LSPR peak position from the collected spectral data. Typically, the initial LSPR peak maximum of the gold nanorod substrates was located between 780-810 nm.

Water was injected into the flow cell and peak position was monitored for at least 30 min to obtain an accurate baseline. Then, 1 mL of 33 μM (0.5 mg/mL) LPS in water was injected into the flow cell and the peak was monitored for 30 min to allow for adequate binding. LPS solutions were stored at 4ºC and vortex mixed prior to use as per manufacturer's guidelines.[41] Next, the flow cell was rinsed with 3 mL of water to remove unbound LPS, and the peak was monitored for 10 min or more to obtain the final peak maximum. Three repeat experiments were carried out for each of the six surface coatings and the three LPS bacterial strains.

The data from the optical setup were plotted as binding curves of peak shift *versus* time. The difference between the average peak position before and after the experiment was the peak shift used to calculate LPS per nanorod. In some cases, due to instrument drift, there was a slight positive or negative slope to the initial baseline. This slope was subtracted from the entire binding curve to get obtain an accurate value for the peak shift. The number of LPS bound per nanorod were calculated using Equations 3.1, 3.2, below.

3.2.7 LSPR REFRACTOMETRIC SENSING WITH COLLOIDAL GOLD NANORODS

Colloidal gold nanorods were incubated with LPS to determine plasmon shift as a function of LPS concentration and the association constants (K_a). 1.1 mL of 0.25 nM gold nanorods were incubated with increasing volumes from 1 – 80 μL of 6.7 μM (0.1 mg/mL) LPS for at least 1 h. The absorbance was measured from 400-900 nm and the longitudinal plasmon peak location was estimated by fitting the peak to quadratic polynomial following the same method of polynomial fit as described in the supplementary information for the calculation of peak location. The peak shifts relative to the original peak location were plotted as a function of LPS/nanorod and were normalized to [0,1] in OriginPro and the data were fit to a Langmuir adsorption isotherm to determine the association constants. Three repeat experiments were carried out for each of the six surface coatings and the three types of LPS studied. The association constants were calculated from the Langmuir fit using Equation 3.3, below.

3.2.8 CHARACTERIZATION OF LPS

The lyophilized, phenol-extracted LPS was used as received from Sigma-Aldrich. The product specification sheets provided by Sigma-Aldrich states that there is ≤3% protein present after phenol extraction as measured by a Lowry protein assay, but they do not provide the nucleic acid (RNA) content. Measurement of nucleic acid absorbance of nucleic acids at 260 nm is an established method to quantify nucleic acid content. However, in a mixture of nucleic acid and protein, the ratio of the absorbance at 260 and 280 nm is used to determine the relative amount of nucleic acid. We measured the absorbance of 1

mg/mL LPS at 260 and 280 nm. The 260/280 ratios were 1.3 – 1.5, so only 10-20% of the absorbance at 260 nm was due to the presence of nucleic acid and 80-90% was due to the presence of protein. At a 1 cm path length, the extinction coefficient for RNA is 0.025 $(\mu g/mL)^{-1}cm^{-1}$. The extinction coefficient was used to calculate the nucleic acid impurity.

3.3 RESULTS AND DISCUSSION

3.3.1 REFRACTOMETRIC SENSING

Here, we investigate attachment of LPS to gold nanorods using localized surface plasmon resonance (LSPR) refractometric sensing. Metal nanoparticles, such as gold nanorods, exhibit characteristic LSPRs which are tunable from the visible to the near-infrared. The surface plasmons generate regions of enhanced electromagnetic fields near the metal surface which are extremely sensitive to small changes in the local refractive index. Detection of biomolecules attached to/near these metal nanoparticles is accomplished by measuring the change in refractive index caused by the target binding. The LSPR wavelength (plasmon maximum) can be tracked over time with high accuracy, enabling picomolar detection limits.[40,42] The best plasmonic sensors exhibit large spectral shifts, even when there are relatively small changes in refractive index in the surrounding environment.[43] Gold nanorods are ideal for refractometric sensing because the longitudinal plasmon maximum can be tuned from 500 – 900 nm by changing the aspect ratio (length/width) of the nanorods and the longitudinal LSPR is highly sensitive to changes in refractive index.[34,43]

The observed wavelength shift in the LSPR maximum ($\Delta\lambda$) can be described by Equation 3.1, where m is the refractive index sensitivity of the substrate in nm per refractive index unit (RIU), Δn is the refractive index difference between the bound analyte and the medium, and a is the thickness of the adsorbed coating layer. l is the decay length of the evanescent electromagnetic field around the gold nanorods and is dependent upon nanorod diameter.[44]

$$\Delta\lambda = m\Delta n\left(1 - e^{-2a/l}\right) \tag{3.1}$$

The refractive index sensitivity can be determined experimentally, allowing for the calculation of Δn. The mass of analyte adsorbed on the sensor surface (Γ) is calculated using Equation 3.2, where d and $\delta n/\delta c$ are the diameter and refractive index increment of the analyte, respectively.[42] The diameter of each LPS type was measured experimentally *via* dynamic light scattering. A literature standard value for refractive index increment of lipids and polysaccharides is 0.15 mL/g.[45]

$$\Gamma = \frac{d\Delta n}{\delta n/\delta c} \tag{3.2}$$

3.3.2 PREPARATION AND CHARACTERIZATION OF GOLD NANORODS AND SUBSTRATES

We assessed LPS interaction with gold nanorods on substrates as outlined in Scheme 3.1. In water, the optimal aspect ratio for maximum LSPR sensitivity is in the range of 3 – 4, so aspect ratio 3.6 gold

nanorods were prepared.[43] Gold nanorods were chemically immobilized onto glass substrates *via* a thiol-silane coupling agent called 3-mercaptopropyltrimethoxy silane (MPTMS). Next, the substrates were coated with one of five different polymers (poly(acrylic acid) sodium salt, poly(allylamine hydrochloride), heparin sodium salt, polydiallyldimethyl ammonium chloride, and methoxyl polyethylene glycol thiol) using layer-by-layer polymer coating or ligand exchange. These are common nanoparticle surface coatings and have been employed in biological studies using gold nanorods.[46-49] In addition, the surface charges of nanorods associated with these coatings are cationic, anionic or neutral, allowing for an interesting variation in surface chemistry. Colloidal gold nanorods were characterized by UV-vis, TEM, and ζ-potential measurements. Gold nanorod substrates were characterized by UV-vis and SEM. The refractive index sensitivity of the polymer-coated substrates was determined experimentally. Then, LSPR sensing experiments were carried out to investigate LPS attachment to gold nanorods. LPS from *Pseudomonas aeruginosa*, *Salmonella enterica* and *Escherichia coli* were chosen for LSPR sensing studies because gold nanorods have been employed in photothermal destruction of these bacteria.[17-21]

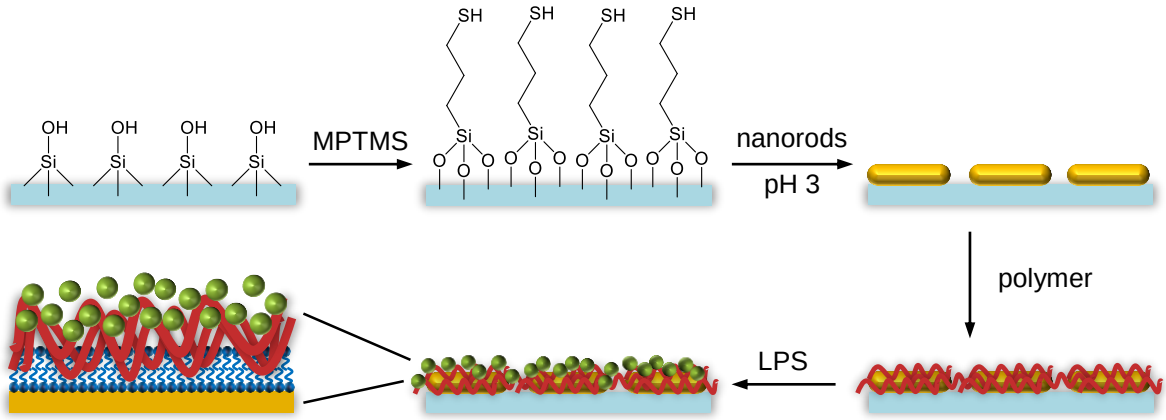

Scheme 3.1 Experiment scheme. Glass substrates (light blue) were functionalized with 3-mercaptopropyltrimethoxy silane (MPTMS) in EtOH. CTAB gold nanorods (yellow) were immobilized on the glass substrate *via* immersion into a gold nanorod solution at pH 3. Substrates were then coated with various polymers (red) *via* immersion into polymer solutions, and exposed to LPS (green) for sensing experiments. The potential interaction between the CTAB bilayer (dark blue), the polymer coating, and LPS is highlighted.

CTAB-coated gold nanorods (Figure 3.1a) were synthesized following a silver-assisted, seed mediated growth procedure.[35] TEM imaging revealed the absolute dimensions of the gold nanorods (Figure 3.1b) which are 42.3 ± 5.6 nm in length and 11.6 ± 1.6 nm in width. The nanorod aspect ratio is ~3.6 and the longitudinal peak maximum (λ_{max}) of colloidal nanorods is 783 nm. Gold nanorods were chemically immobilized onto glass substrates which were functionalized with MPTMS. MPTMS functionalization allows for chemical immobilization of gold nanorods to glass *via* Au-S chemistry. The glass substrates were functionalized with MPTMS by immersion into a solution of 0.5 mM MPTMS in EtOH. This low concentration of MPTMS was sufficient for immobilization because there was no change in substrate absorbance (a measurement of nanorod surface density) at higher MPTMS concentrations (Figure 3.2a). In fact, too much

MPTMS results in significant MPTMS polymerization on a glass substrate. The polymers of MPTMS appear as mushroom-shaped islands (SEM images not shown). Often, these islands are terminated in methyl groups instead of thiols, and are undesirable for good quality substrates.[50]

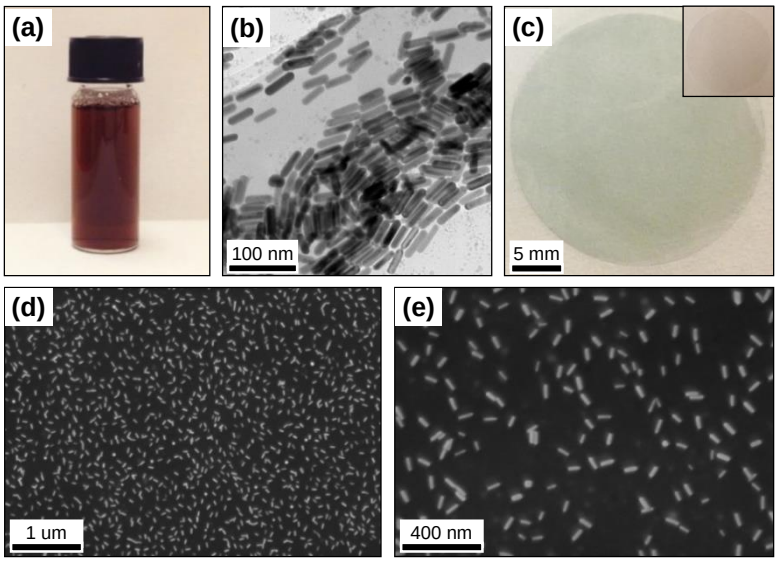

Figure 3.1 (a) Photograph and (b) TEM image of gold nanorods, λ_{max}= 783 nm. (c) Photograph of a gold nanorod substrate, inset is a glass substrate without nanorods and (d,e) SEM images of gold nanorods immobilized on a glass substrate.

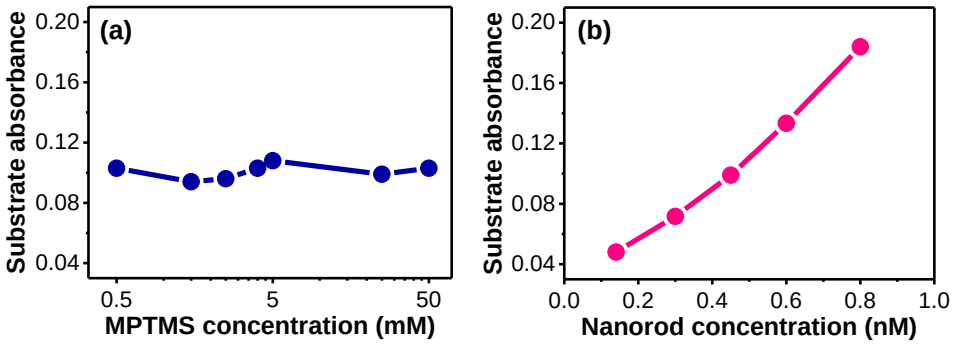

Figure 3.2 (a) UV-vis absorbance of gold nanorod substrates at ~720 nm *versus* concentration of MPTMS during silane functionalization of glass substrates. (b) UV-vis absorbance of gold nanorod substrates at ~720 nm *versus* concentration of gold nanorods during immobilization.

Thiol-functionalized substrates were immersed into a solution of CTAB nanorods at pH 3 for nanorod immobilization. Removal of excess CTAB from the nanorods is critical to successful nanorod immobilization. Some CTAB was initially removed *via* centrifugation of the nanorods before immobilization. Also, the pH was lowered during the nanorod immobilization step. Addition of acid to CTAB has been demonstrated to alter micelle behavior and potentially facilitated disruption of the CTAB bilayer on gold nanorods, allowing MPTMS access to the gold nanorod surface.[51] There was a noticeable color change in the substrates

indicating successful nanorod immobilization. An example substrate is shown in Figure 3.1c with obvious blue-green coloring on the glass which is not present in the colorless nanorod-free substrate. Generally, increasing nanorod concentration during immersion resulted in increasing nanorod immobilization on the glass substrate as measured by increasing substrate absorbance (Figure 3.2b). The concentration of 0.6 nM nanorods was chosen for gold nanorod immobilization because the average substrate absorbance was 0.13 ± 0.02, sufficient for sensing measurements. If the concentration of nanorods was higher than 0.6 nM, the nanorods were too densely packed on the substrate. This resulted in increased particle overlap and greater broadening of the plasmon resonance band which is undesirable in sensing experiments.

Gold nanorod substrates were characterized by SEM and UV-vis absorbance spectroscopy. Characteristic SEM images of the substrates are shown in Figure 3.1d,e. The particles on the glass substrates are clearly rod-shaped and appear to be immobilized on the sides. In addition, they appear to be randomly distributed on the glass substrate with only a little clumping or end-to-end or side-to-side overlap of particles. Analysis of SEM images reveals 124 ± 15 nanorods/μm^2, approximately 6% coverage of the glass substrate.

UV-vis spectra of the colloidal CTAB-coated gold nanorods and a gold nanorod substrate are shown in Figure 3.3a. There is slight tailing and broadening of the longitudinal peak for the gold nanorod substrate which does not appear in the UV-vis spectrum of the colloidal gold nanorods. This is an indication that there may be slight aggregation of the nanorods or plasmonic coupling resulting from nanoparticle overlap on a substrate. The longitudinal plasmon is located at 783 nm for the colloidal particles and shifts to 714 ± 5 nm when the nanorods are immobilized on a glass substrate. This is also visible in the change from brown to blue-green from Figure 3.1a to Figure 3.1c. A shift in the longitudinal peak is expected because gold nanorods are highly sensitive to changes in the dielectric environment. Because the refractive index of air is 1.00 and water is 1.33, a significant blue shift is associated with a decreasing refractive index around gold nanorods.[32,39] When the gold nanorod substrates are immersed in water, the average longitudinal peak shifts to 794 ± 15 nm (spectra not shown). Since the gold nanorods were immobilized onto glass, and the refractive index of glass is higher than that of water, there is a slight red-shift in the plasmon maximum relative to colloidal nanorods.

Gold nanorod substrates were coated with various polymers and their abbreviations and molecular weights are listed in Table 3.1. These polymers were chosen because they have all been employed in biological studies using gold nanorods.[46-49] PAA, PAH, HEP and PDDA were coated onto the cationic CTAB gold nanorods using a layer-by-layer coating technique of immersion into solutions of anionic, and then cationic polyelectrolyte solutions. The layering order of polyelectrolytes is listed in Table 3.1. The addition of NaCl to the polyelectrolyte solutions screens the charged groups, allowing for the polymer to wrap around the gold nanorods.[52] mPEG-SH was coated onto the nanorods using a ligand exchange technique where the thiolated polymer displaces some of the CTAB on the surface of the nanorods.[49] Colloidal nanorods were used for measurements of nanoparticle surface charge. The ζ- potentials are shown in Figure 3.3b. CTAB gold nanorods are cationic, and upon functionalization with anionic PAA or HEP the charges flip

negative. After functionalization of PAA-coated nanorods with cationic PAH or PDDA, the surfaces become positively charged. PEG is uncharged so the ζ-potential is near zero.

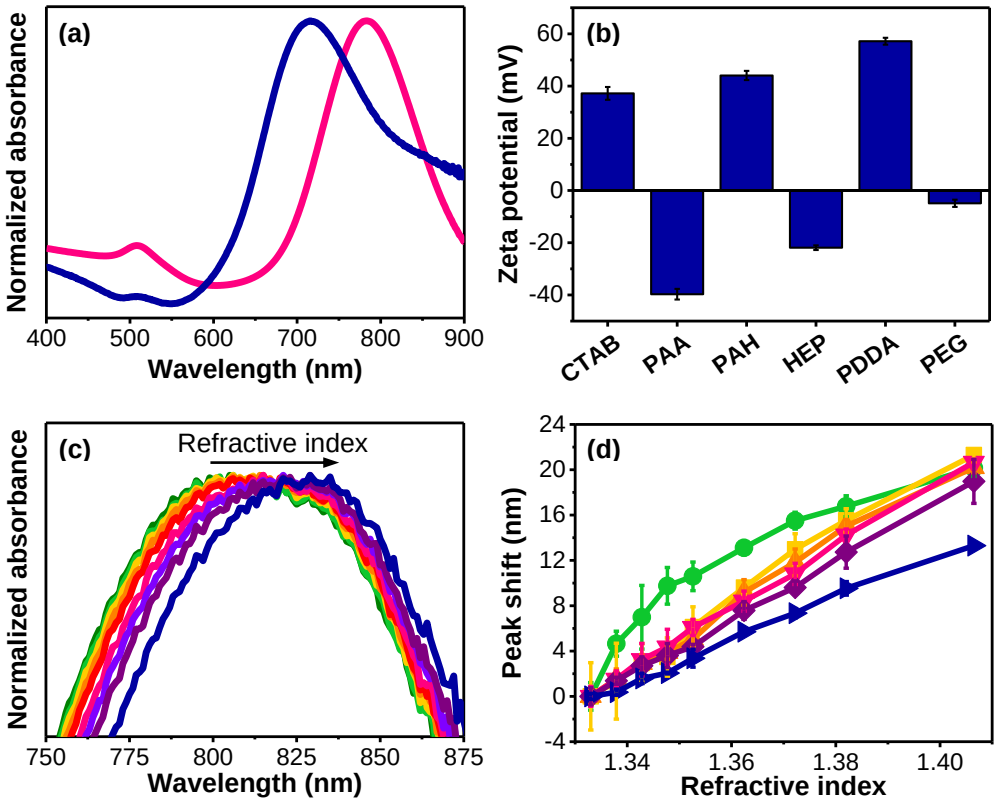

Figure 3.3 (a) UV-vis absorbance spectra of colloidal gold nanorods in water (pink) and a gold nanorod substrate in air (blue). (b) ζ-potentials of colloidal gold nanorods in water after coating with various polymers. (c) UV-vis absorbance spectra of the longitudinal peak of a PEG-coated gold nanorod substrate immersed in mixtures of water and ethylene glycol. (d) Peak shift *versus* solution refractive index of gold nanorod substrates with various surface coatings of CTAB (green circles), PAA (yellow squares), PAH (orange up-triangles), HEP (pink down-triangles), PDDA (purple diamonds), and PEG (blue right-triangles).

UV-vis absorbance measurement of the polymer-coated gold nanorod substrates in air was carried out to confirm polymer coating by monitoring the longitudinal peak position. The average shifts are listed in Table 3.1. There are blue shifts after the anionic PAA and HEP coatings and red shifts with the cationic PAH and PDDA coatings. Similar plasmon shifts with polyelectrolyte-coated colloidal nanorods have been previously observed and are attributed to differences in hydration of polyelectrolyte layers.[52] After PEGylation, the longitudinal peak of the substrate shifted nearly 30 nm. This shift is likely due to change in refractive index of PEG at the gold nanorod surface because the refractive index of ethylene glycol is greater than that of water.[39]

To estimate analyte binding, it was necessary to measure plasmonic sensitivity to bulk changes in refractive index. Refractive index sensitivity of the plasmon bands decreases as a function of distance from the particle surface. Because the polymers used were varied in composition, the sensitivity of each

substrate was calculated separately. Substrates were immersed in mixtures of water and ethylene glycol ranging from 0 – 75% changing the solution refractive index from 1.33 to 1.41.[39] UV-vis absorbance spectra demonstrated noticeable red-shifts in the longitudinal LSPR maximum with increasing concentration of ethylene glycol. An example of a PEG-coated gold nanorod substrate is shown in Figure 3.3c where the peak shifts from 810 to 823 nm.

The peak shifts relative to the original longitudinal peak maxima in water are plotted against refractive index in Figure 3.3d. The relationship between peak shift and refractive index is approximately linear, and the slope of the line fit to the data points is the refractive index sensitivity in Equation 3.1.[53] The refractive index sensitivities in nm per refractive index unit are listed in Table 3.2 in order from highest to lowest. We note that the refractive index sensitivity value for the CTAB gold nanorods is equivalent to a literature value of 252 nm/RIU for a previously reported gold nanorod sensor,[32] but this was not the highest measured sensitivity. Initial peak shifts for the CTAB substrates are the largest, but at a refractive index of ~1.37, the shifts decrease in magnitude (Figure 3.3d). This non-linearity is likely due to disruption or desorption of the CTAB bilayer by organic ethylene oxide and reduced CTAB concentration has been correlated with a blue shift in the longitudinal plasmon band of gold nanorods.[52] Also, disruption of the CTAB bilayer has been observed to result in decreased sensitivity of CTAB gold nanorod sensors compared to coated gold nanorods.[53] The other gold nanorod coatings followed expected trends in refractive index sensitivity. Since the PAH and PDDA coated nanorods have a PAA layer underneath, their sensitivities are smaller than PAA. The length of a completely extended 5000 MW PEG-SH can be approximated by bond lengths to be ~27 nm.[54] Even though PEG would not completely extend out on a nanoparticle surface, the average chain length is likely greater than two polyelectrolyte layers and results in the lowest refractive index sensitivity.[52]

Table 3.2 Refractive index sensitivity of gold nanorod substrates.

Coating	Refractive index sensitivity (nm/RIU)
PAA	303 ± 11
PAH	285 ± 10
HEP	279 ± 4
PDDA	258 ± 5
CTAB	252 ± 33
PEG	190 ± 6

3.3.3 LPS ATTACHMENT TO GOLD NANOROD SUBSTRATES

Gold nanorod substrates were used to investigate LPS attachment of LPS extracted from *P. aeruginosa*, *S. enterica* and *E. coli*. The LPS had been extracted from the bacteria using phenol. The manufacturers state that there is ≤ 3% protein present after phenol extraction, but RNA can also be present.[41] We determined the nucleic acid content by measuring the absorbance of LPS at 260 nm. The

greatest amount present was in LPS from *E. coli* was ~1.1% and there was <0.2% in LPS from *P. aeruginosa* and *S. enterica*, so nucleic acid was not a large impurity (Table 3.3). Because the impurity in the LPS was so small, the extracted LPS were used as received.

Table 3.3 Quantification of nucleic acid content in 1 mg/mL LPS as measured by absorbance of at 260 and 280 nm.

LPS type	Absorbance at 260 nm	Absorbance at 280 nm	260/280 ratio	Percent absorbance due to nucleic acid	Nucleic acid impurity
P. aeruginosa	0.22	0.17	1.3	10%	0.09%
S. enterica	0.27	0.22	1.3	10%	0.11%
E. coli	1.4	0.94	1.5	20%	1.1%

The gold nanorod substrates were exposed to each type of LPS and binding was monitored *via* LSPR refractometric sensing. The optical setup used in these experiments has been previously described.[40] Water was first injected into the flow cell to acquire an accurate baseline, and then LPS was injected into the flow cell and the peak was monitored for 30 min, under static conditions, to allow for maximum binding. Finally, the substrate was rinsed with water to remove unbound LPS, and the peak was monitored to obtain the final peak position. The data from these sensing experiments are plotted as binding curves of longitudinal peak shift *versus* time. Example binding curves for the six surface coatings and three types of LPS studied are shown in Figure 3.4. In these traces, the LPS addition is shown at the 5 min mark and the rinsing step to remove unbound LPS is at 35 min.

At first, there is an initial red-shift in the longitudinal LSPR maximum due to the change in refractive index from LPS binding, and usually a slight blue-shift occurs after rinsing. When the substrate is rinsed, the unbound or weakly bound LPS are removed, leaving only the strongly bound LPS molecules on the gold nanorods. This binding effect may be analogous to protein binding on gold nanoparticles, resulting in the formation of “hard” and “soft” coronas which is well-documented in the literature.[55] “Hard” corona formation results from macromolecules that have a high affinity for the nanoparticle surface while the “soft” component is dynamic, with rapid exchange between what is bound to the surface and what is in the surrounding medium. Typically, the “soft” corona is easily removed by centrifugation or washing of the nanoparticles, leaving the “hard” corona on the nanoparticle surface.[55] Since LPS molecules are often heterogeneous in size/composition and the O-antigen structure can be highly varied,[26] this may lead to both weak and strong LPS attachment, even within one type of LPS or interactions between LPS molecules that are bound to the gold surface.

Variation in LPS attachment is observed among the different surface coatings on the gold nanorods. For example, smaller red-shifts in the longitudinal LSPR are observed with cationic CTAB, PAA, HEP and PEG nanorods (Figure 3.4a,b,d,f) while larger red-shifts occur with the PAH and PDDA nanorods (Figure 3.4c,e). The smaller LSPR shifts often appear more abrupt. It is possible that these abrupt shifts are only

due to weakly bound LPS or to the change in the solution bulk refractive index because the final peak shifts are small after rinsing. When the initial peak shifts are larger, the LSPR appears to shift more slowly, as if the LPS are continually binding to the surface over time. Cationic PAH and PDDA nanorods demonstrate greater LSPR peak shifts, compared to the anionic PAA and HEP nanorods, likely due to stronger attachment of the anionic LPS. Interestingly, even though CTAB is also cationic, the shifts in the longitudinal LSPR of CTAB NRs are quite small. In fact, during the experiments, there is an initial red-shift after LPS binding, but then the peaks often began to slightly blue-shift. CTAB-coated gold nanorods can be unstable and that CTAB is easily removed from gold nanorod surfaces. It is possible that the LPS molecules are actually pulling the CTAB off the surface instead of binding to the gold nanorods, which would results in a blue shift.[52,53] The neutral PEG nanorods exhibit the smallest peak shifts of all the nanorods coatings studied. PEG is well-known to reduce protein adsorption to nanoparticle surfaces[49] and may also result in decreased LPS attachment.

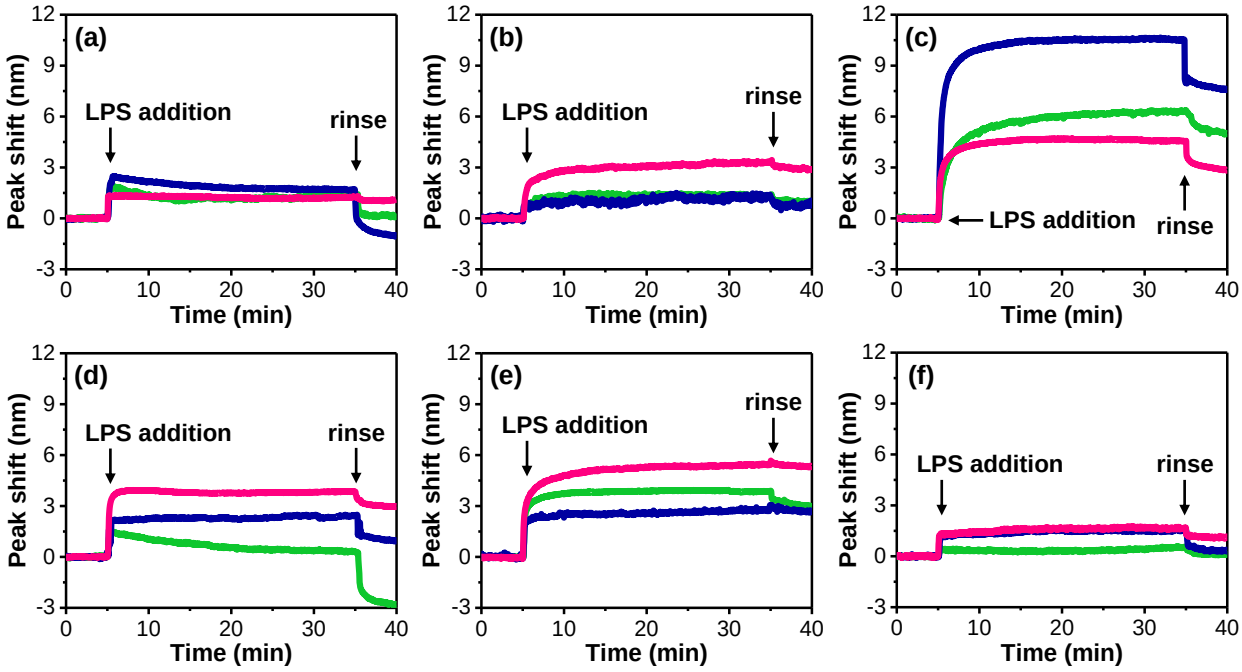

Figure 3.4 Binding of LPS to gold nanorod substrates under static conditions. LPS were injected at 5 min and the substrates were rinsed to remove unbound LPS at 35 min. LSPR peak shift *versus* time for (a) CTAB, (b) PAA, (c) PAH, (d) HEP, (e) PDDA, and (f) PEG coated gold nanorod substrates with LPS from *P. aeruginosa* (green), *S. enterica* (blue), and *E. coli* (pink).

LPS attachment also appears to vary between the LPS bacterial strains. The binding curves and peak shifts (Table 3.4) for *P. aeruginosa* and *S. enterica* LPS appear somewhat similar; however, the LPS from *E. coli* resulted in noticeable red-shifts in the LSPR for all of the nanorod coatings. Potentially, the structures of LPS from *P. aeruginosa* and *S. enterica* are more similar to each other while LPS from *E. coli* is different. Therefore, we might predict that in a natural environment, gold nanoparticles would more likely attach to *E.*

coli than other Gram-negative bacteria. Because each substrate type has a different refractive index sensitivity (Table 3.2), the binding curves alone do not tell the complete story of LPS attachment. The average initial and final longitudinal LSPR peak shifts for the coatings and bacterial strains studied are listed in Table 3.4. These values represent the peak shifts relative to the average LSPR peak position before LPS addition.

Table 3.4 Initial and final longitudinal LSPR shifts due to LPS binding to gold nanorod substrates.

Coating	***P. aeruginosa***		***S. enterica***		***E. coli***	
	Initial shift (nm)	Final shift (nm)	Initial shift (nm)	Final shift (nm)	Initial shift (nm)	Final shift (nm)
CTAB	1.7 ± 0.4	0.3 ± 0.1	2.0 ± 0.5	-2.2 ± 1.6	2.1 ± 0.7	1.1 ± 0.6
PAA	1.2 ± 0.2	1.0 ± 0.0	2.1 ± 1.1	0.7 ± 0.1	3.0 ± 0.3	2.2 ± 0.5
PAH	7.0 ± 1.8	5.7 ± 1.9	8.6 ± 2.5	6.5 ± 1.5	4.0 ± 1.0	2.6 ± 0.9
HEP	1.6 ± 0.1	-2.2 ± 0.8	2.5 ± 0.3	0.8 ± 0.2	4.3 ± 1.0	3.0 ± 0.9
PDDA	7.0 ± 2.9	6.3 ± 3.5	3.4 ± 1.0	3.4 ± 1.3	6.0 ± 1.0	5.7 ± 1.0
PEG	0.8 ± 0.6	0.5 ± 0.4	1.0 ± 0.6	0.1 ± 0.0	1.4 ± 0.3	1.0 ± 0.2

The LSPR shifts were used to estimate the number of LPS bound per gold nanorod. The value for Δn was calculated from Equation 3.1 using the experimentally obtained LSPR shifts and refractive index sensitivities. Coating thickness has been previously calculated for polyelectrolyte layers on gold nanorod surfaces. Therefore, the estimated value for a is 2.9 nm for CTAB nanorods, 3.8 nm for PAA/HEP nanorods, and 7.2 nm for PAH/PDDA nanorods.[52] The thickness of PEG coating is estimated to be 27 nm.[54] For aspect ratio ~3.5 gold nanorods, the value for l is comparable to the diameter of the nanorods,[44] which is 11.6 nm, and l is not altered by coating type/thickness.[56] The adsorbed mass per unit area can be calculated using Equation 3.2 knowing the diameter and refractive index increment. The hydrodynamic diameter of LPS micelles were approximately 50 nm for each LPS strain as measured by dynamic light scattering. The literature value for $\delta n/\delta c$ is 0.15 cm^3/g and the mass of an individual LPS macromolecule is ~15 kDa.[41,57] The surface area of a single nanorod is approximated by a cylinder to be 1750 nm^2, so the exposed portion of a single nanorod (roughly half) is 875 nm^2. This allowed us to estimate the initial and final numbers of LPS per nanorod and the results are shown in Figure 3.5. We note it was not possible to estimate final LPS attachment with CTAB/*S. enterica* and HEP/*P. aeruginosa* due to negative LSPR peak shifts, potentially due to the LPS pulling the adsorbed coating off of the gold surface.

We observe some interesting trends in the number of LPS molecules bound per nanorod. There is a difference in the initial and final number of LPS per nanorod which arises from the difference between the initial and final peak shifts shown in the binding curves (Figure 3.5 and Table 3.4). The initial estimates of binding (Figure 3.5a) show some variation between surface coatings, but the differences between the LPS strains are not so great. The data in Figure 3.5b is more interesting because it represents attachment after removal of unbound/weakly bound LPS. Figure 3.5b reveals that there is some variation in LPS per nanorod

from 6 LPS/nanorod with PEG nanorods and *S. enterica* to 404 LPS/nanorod with PDDA nanorods and *P. aeruginosa*. Since the electromagnetic field decays further away from the surface, and the surface area is limited, it is possible that ~400 LPS/nanorod is the maximum possible number of LPS molecules that can be detected to attach to the surface.

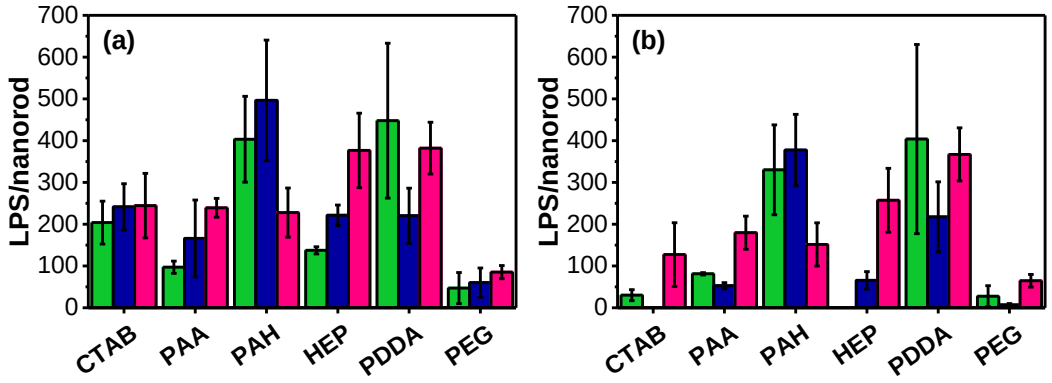

Figure 3.5 Estimation of the (a) initial and (b) final number of LPS molecules bound per nanorod on gold nanorod substrates after exposure to LPS from *P. aeruginosa* (green), *S. enterica* (blue), and *E. coli* (pink).

If the interaction was purely dependent on electrostatics, then CTAB, PAH and PDDA nanorods would always have the greatest amount of LPS bound to the surface and very little would be observed with PAA, HEP and PEG NRs. However, that is not always the case. For example, PAH nanorods exhibit strong interaction with LPS from *P. aeruginosa* and *S. enterica* with >300 LPS/nanorod, but their interaction with *E. coli* LPS is much less (<160 LPS/nanorod). Conversely, LPS attachment to HEP nanorods and LPS from *P. aeruginosa* and *S. enterica* is low, but not with *E. coli* LPS (260 LPS/nanorod). It is interesting to note that there is generally greater attachment of *E. coli* LPS to CTAB, PAA, HEP and PEG gold nanorods than to *P. aeruginosa* and *S. enterica* LPS. Despite the fact that the interactions studied here are non-specific, this result demonstrates that there may be enough variation in the structure of the different types of LPS to have varied attachment to gold nanorods. Therefore, it may be possible to differentiate between bacterial strains using gold nanorod sensors.

3.3.4 LPS ATTACHMENT TO COLLOIDAL GOLD NANORODS

LPS attachment to gold nanorod surfaces and the resulting longitudinal LSPR peak shift may also be dependent on the concentration of LPS. Therefore, colloidal gold nanorods were incubated with varying amounts of LPS (0 – 2000 LPS/nanorod) for each LPS type. The shift of the longitudinal plasmon relative to the original peak position was determined from UV-vis absorbance spectra. Example spectra are shown in Figure 3.6. Plots of peak shift *versus* LPS/nanorod and the ζ-potentials before and after exposure to 2000 LPS/nanorod are shown in Figure 3.7. The shifts observed with the colloidal gold nanorods exhibit different trends compared to the shifts observed with the gold nanorod substrates. There are blue-shifts with HEP, CTAB, PDDA and PAH-coated gold nanorods while the PAA-coated nanorods exhibit noticeable red-shifts,

and there is almost no shift observed in the PEGylated nanorods. In addition, variation between LPS strains is not as apparent. The LSPR shifts observed with the PEG-coated nanorods are minimal because these nanorods are resistant to biomolecule adsorption. The red-shifts with PAA nanorods are likely due to the change in the solution refractive index and as the LPS/nanorod increases, the peak shifts level off at ~6 nm for all three LPS types. It is important to note that the majority of the LSPR shift with colloidal nanorods occurred within the range of 0 – 750 LPS/nanorod which is approximately double the number of LPS/nanorod attached on the gold substrates (Figure 3.5). This number is quite reasonable considering only half of a nanorod is exposed to LPS on a substrate while the full nanorod surface is exposed in solution.

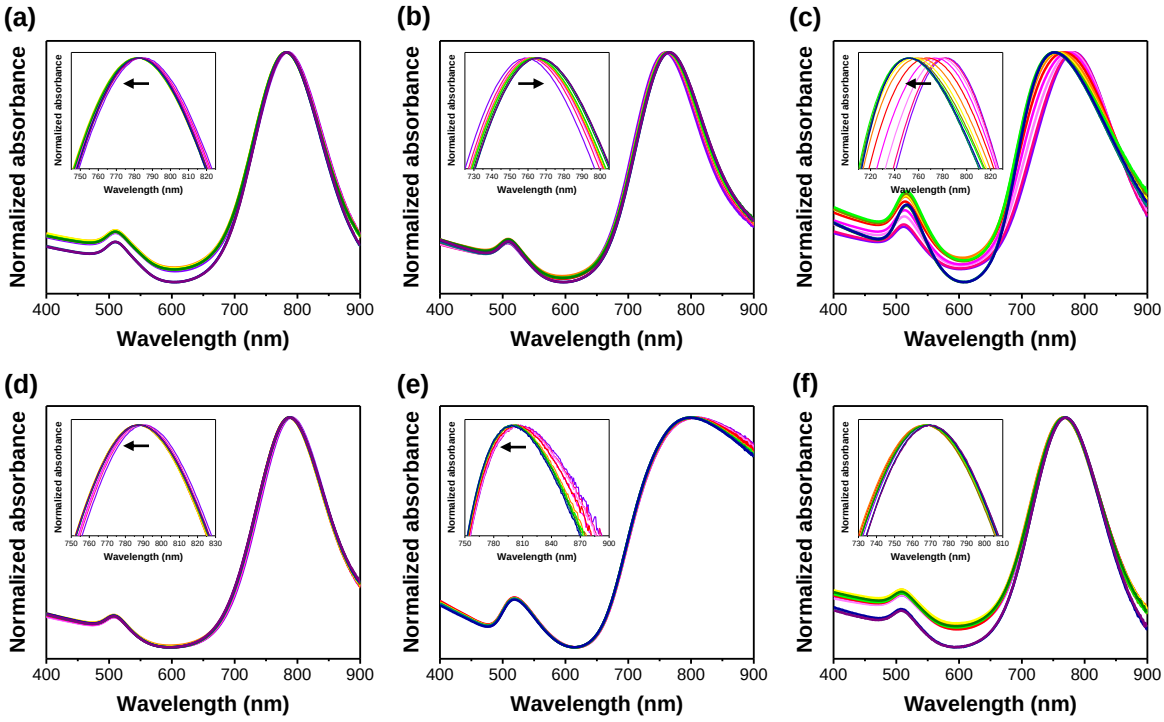

Figure 3.6 UV-vis absorbance spectra of (a) CTAB, (b) PAA, (c) PAH, (d) HEP, (e) PDDA, and (f) PEG coated gold nanorods after incubation with increasing amounts of LPS from *S. enterica* (0 – 2000 LPS/nanorod). Inset spectra show longitudinal peak close up with the arrow indicating shift with increasing LPS/nanorod.

When gold nanorods are on a substrate, they are immobilized and cannot interact with each other, but that is not the case with colloidal particles. The reason for the blue-shifts in the LSPR for the HEP, CTAB, PDDA and PAH-coated nanorods is likely plasmon coupling, not aggregation. Aggregation of gold nanorods causes greater blue-shifts and significant broadening in the longitudinal LSPR, which was not observed in the absorbance spectra (Figure 3.6). The majority of the blue-shifts observed here are less than 10 nm. It is more likely that some of the LPS molecules wrap around multiple nanorods in a side-by-side manner. This would result in plasmon coupling, and a blue-shift in the longitudinal LSPR compared to end-to-end assembly which would result in a red-shift and is less likely to occur considering the length of the LPS

chains.[58] This also fits the trend in the data because there are smaller shifts observed when anionic LPS is exposed to the anionic HEP nanorods than the cationic CTAB, PDDA, and PAH nanorods. In addition, other researchers have also observed plasmon coupling after LPS exposure. Sun *et al.*[30] prepared amine-functionalized gold nanospheres and exposed them to LPS from *E. coli*. UV-vis absorbance measurement revealed that increasing concentration of LPS led a decrease in magnitude of a 525 nm LSPR peak and the production of a new peak at 675 nm. This likely occurred because the LPS wrapped around multiple spheres, causing plasmon coupling and the formation of a new peak at a higher wavelength.

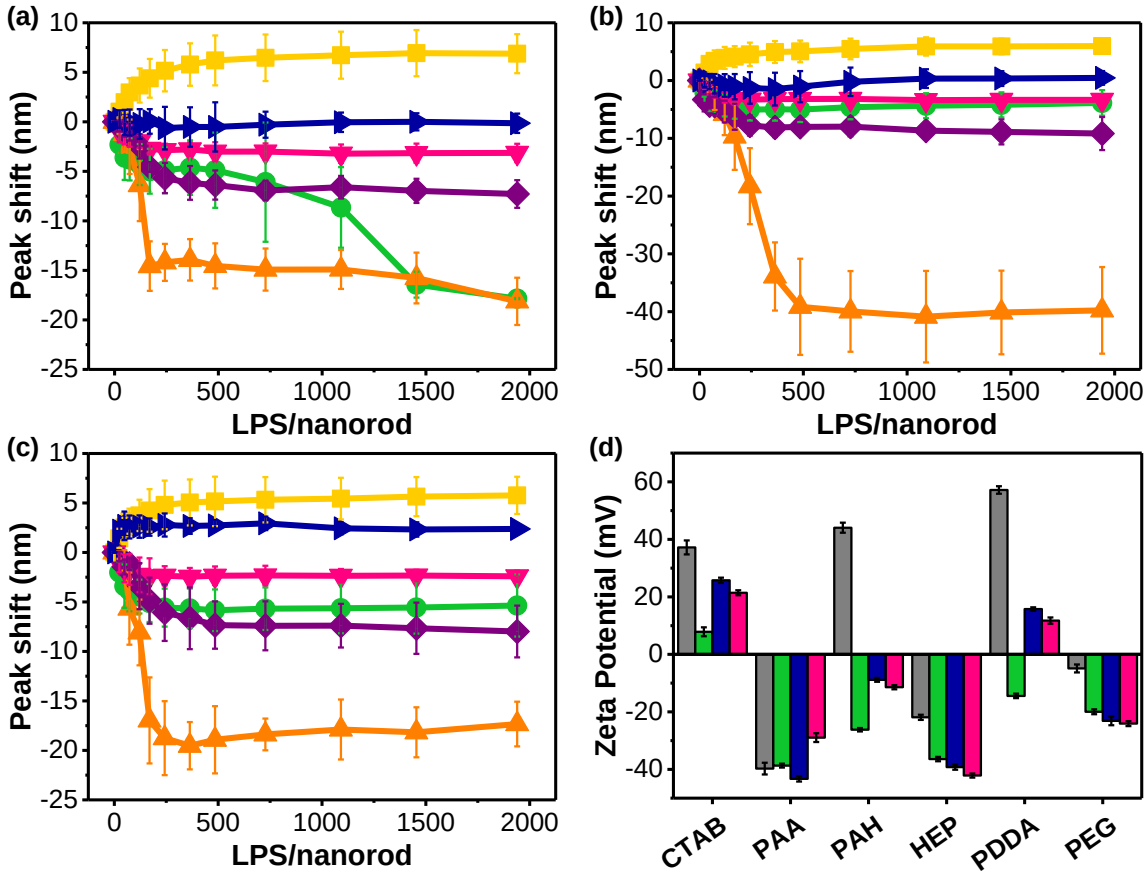

Figure 3.7 Longitudinal LSPR peak shift *versus* LPS/nanorod after 1 h incubation with LPS from (a) *P. aeruginosa*, (b) *S. enterica*, and (c) *E. coli* for colloidal gold nanorods coated with PAA (yellow squares), PEG (blue right-triangles), HEP (pink down-triangles), CTAB (green circles), PDDA (purple diamonds), and PAH (orange up-triangles). (d) Original (grey) and final ζ-potentials of gold nanorods after exposure to 2000 LPS/nanorod with LPS from *P. aeruginosa* (green), *S. enterica* (blue), and *E. coli* (pink). The ζ-potential of free LPS is -5.6 ± 1.3 mV

The notion that the LPS could be wrapping around multiple nanorods also fits the trends observed with ζ-potential (Figure 3.7d). The results show that the ζ-potential of colloidal gold nanorods become more negative after LPS exposure. The change in surface charge for PAH and PDDA-coated gold nanorods is quite dramatic, and indicates significant LPS binding to the nanoparticle surface. The change in ζ-potential of CTAB and PEGylated nanorods is more modest and there is very little change in the surface charge of

anionic PAA and HEP-coated gold nanorods. The actual measured ζ-potential of free LPS is quite small (only -5.6 mV), so the difference in surface charge was not merely due to the presence of LPS in solution. The ζ-potential of Gram-negative bacteria are in the range of -30 to -50 mV.[59] Potentially, the orientation of LPS molecules is altered when they are bound to a surface compared to in solution, which may reduce the measured ζ-potential of LPS on a surface.

The equilibrium association constants (K_a) for LPS attachment to colloidal gold nanorods were calculated using Equation 3.3, following the same method of analysis as Yang *et al*.[60] Plots of relative peak shift ($\Delta\lambda/\Delta\lambda_{max}$) *versus* LPS concentration were fit to a Langmuir adsorption isotherm to determine K_a. An example fit is shown in Figure 3.8. The estimated association constants for CTAB, PAA, PAH, HEP, and PDDA nanorods are listed in Table 3.5 from lowest to highest across the 3 LPS strains. We note that it was not possible to calculate the K_a for PEG nanorods due to variability in the relative plasmon shifts. The binding constants range in magnitude from 10^7-10^{10} M^{-1} which is within the range typically observed with biomolecular adsorption onto gold nanoparticle surfaces.[58] LPS binding varies based on surface coating, with the cationic gold nanorods exhibiting the strongest and the anionic/neutral nanorods exhibiting the weakest association with anionic LPS. The calculated binding constants follow the trend observed with changes in ζ-potential and peak shift and confirm that LPS interaction with gold nanorods is surface chemistry-dependent.

$$\frac{\Delta\lambda}{\Delta\lambda_{max}} = \frac{K_a[LPS]}{1 + K_a[LPS]} \tag{3.3}$$

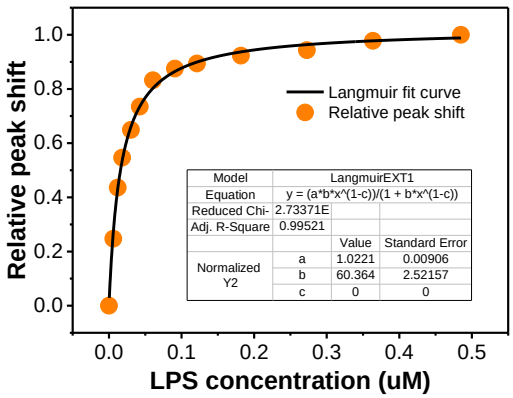

Figure 3.8 Relative peak shift ($\Delta\lambda/\Delta\lambda_{max}$) of colloidal PAA-coated gold nanorods *versus* concentration of LPS from *E. coli*. The data were fit to a Langmuir adsorption isotherm in OriginPro. The inset shows the output from the fit where "b" is the association constant (K_a) in μM^{-1}.

Table 3.5 Average estimated association constants (K_a) for LPS binding to colloidal gold nanorods.

Coating	*P. aeruginosa*	*S. enterica*	*E. coli*
PAA	$3.3 \pm 0.2 \times 10^7$ M^{-1}	$6.1 \pm 0.6 \times 10^7$ M^{-1}	$6.0 \pm 0.3 \times 10^7$ M^{-1}
HEP	$5.7 \pm 0.8 \times 10^7$ M^{-1}	$8.4 \pm 1.8 \times 10^7$ M^{-1}	$1.4 \pm 0.1 \times 10^8$ M^{-1}
CTAB	$1.5 \pm 0.3 \times 10^8$ M^{-1}	$1.1 \pm 0.1 \times 10^8$ M^{-1}	$8.8 \pm 0.8 \times 10^7$ M^{-1}
PDDA	$4.3 \pm 0.7 \times 10^8$ M^{-1}	$1.3 \pm 0.1 \times 10^8$ M^{-1}	$4.4 \pm 2.2 \times 10^8$ M^{-1}
PAH	$2.6 \pm 1.3 \times 10^9$ M^{-1}	$6.9 \pm 6.7 \times 10^9$ M^{-1}	$1.1 \pm 0.3 \times 10^{10}$ M^{-1}

The results presented here reveal interesting implications for applications that may take advantage of interactions between polymers and Gram-negative bacterial surfaces. For example, some researchers have developed antibiofouling substrates of layered polyelectrolytes or polymers which prevent adhesion of bacteria such as *E. coli*,[61] *P. aeruginosa*,[62] *S. aureus*,[63] and *Bacillus subtilis*.[64] Others have coated bacteria such as *S. enterica*, *E. coli*, and *Staphylococcus cohnii*, with PAH, taking advantage of the strong interaction between PAH and LPS. In one report, this increased the potential use of *Salmonella* in cancer therapy and inhibited tumor growth in mice.[65] In another work, PAH-coated bacteria were exposed to anionic metal nanoparticles. The nanoparticle-covered bacteria were used for surface-enhanced Raman spectroscopy, demonstrating single bacterial cell identification.[66] Together, these examples demonstrate how understanding the LPS/nanoparticle/polymer interface may be useful in microbiology applications.

3.4 CONCLUSIONS

We have demonstrated that bacterial LPS interaction with gold nanorod surfaces can be highly varied and is dependent on the gold nanorod surface coating. Gold nanorod colloids and substrates were prepared and coated in various types of polymers. The nanorods were exposed to LPS from *Pseudomonas aeruginosa*, *Salmonella enterica* and *Escherichia coli* and binding was monitored using LSPR sensing. Final LPS attachment ranged from 0 – 400 LPS/nanorod and association constants ranged from 10^7-10^{10} M^{-1}. Both surface charge and surface chemistry were critical to gold nanorod-LPS interactions. A greater amount of LPS bound per nanorod was observed with PAH and PDDA coated gold nanorods and variation in attachment between bacterial strains was also detected. These results demonstrate the complexity of bacteria-nanoparticle interactions and highlight the need for further study of gold nanoparticle interactions with bacterial surface molecules, especially lipopolysaccharides.

3.5 REFERENCES

1. Dreaden, E. C.; Alkilany, A. M.; Huang, X.; Murphy, C. J.; El-Sayed, M. A. The Golden Age: Gold Nanoparticles for Biomedicine. *Chem. Soc. Rev.* **2012**, *41*, 2740-2779.
2. Alkilany, A. M.; Lohse, S. E.; Murphy, C. J. The Gold Standard: Gold Nanoparticle Libraries to Understand the Nano-Bio Interface. *Acc. Chem. Res*. **2013,** *46*, 650-661.
3. Verma, A.; Stellacci, F. Effect of Surface Properties on Nanoparticle-Cell Interactions. *Small* **2010**, *6*, 12-21.

4. Nel, A. E.; Mädler, L.; Velegol, D.; Xia, T.; Hoek, E. M. V.; Somasundaran, P.; Klaessig, F.; Catranova, V.; Thompson, M. Understanding Biophysicochemical Interactions at the Nano-Biointerface. *Nat. Mater.* **2009**, *8,* 543-557.
5. Feng, Z. V.; Gunsolus, I. L.; Qiu, T. A.; Hurley, K. R.; Nyberg, L. H.; Frew, H.; Johnson, K. P.; Vartanian, A. M.; Jacob, L. M.; Lohse, S. E.; Torelli, M. D.; Hamers, R. J.; Murphy, C. J.; Haynes, C. L. Impacts of Gold Nanoparticle Charge and Ligand Type on Surface Binding and Toxicity to Gram-Negative and Gram-Positive Bacteria. *Chem. Sci.* **2015,** *6,* 5186-5196.
6. Chwalibog, A.; Sawosz, E.; Hotowy, A.; Szeliga, J.; Mitura, S.; Mitura, K.; Grodzik, M.; Orlowski, P.; Sokolowska, A. Visualization of Interaction Between Inorganic Nanoparticles and Bacteria or Fungi. *Int. J. Nanomed.* **2010,** *5,* 1085-1094.
7. Zhang, Y.; Peng, H.; Huang, W.; Zhou, Y.; Yan, D. Facile Preparation and Characterization of Highly Antimicrobial Colloid Ag or Au Nanoparticles. *J. Coll. Interface Sci.* **2008,** *325,* 371-376.
8. Zhao, Y.; Tian, Y.; Cui, Y.; Liu, W.; Ma, W.; Jiang, X. Small Molecule-Capped Gold Nanoparticles as Potent Antibacterial Agents That Target Gram-Negative Bacteria*. J. Am. Chem. Soc.* **2010,** *132,* 12349-12356.
9. Li, X.; Robinson, S. M.; Gupta, A.; Saha, K.; Jiang, Z.; Moyano, D. F.; Sahar, A.; Riley, M. A.; Rotello, V. M. Functional Gold Nanoparticles as Potent Antimicrobial Agents Against Multi-Drug-Resistant Bacteria. *ACS Nano* **2014,** *8,* 10682-10686.
10. Hayden, S. C.; Zhao, G.; Saha, K.; Phillips, R. L.; Li, X.; Miranda, O. R.; Rotello, V. M.; El-Sayed, M. A.; Schmidt-Krey, I.; Bunz, U. H. F. Aggregation and Interaction of Cationic Nanoparticles on Bacterial Surfaces. *J. Am. Chem. Soc.* **2012,** *134,* 6920-6923.
11. Bresee, J.; Maier, K. E.; Boncella, A. E.; Melander, C.; Feldheim, D. L. Growth Inhibition of *Staphylococcus aureus* by Mixed Monolayer Gold Nanoparticles. *Small* **2011,** *7,* 2027-2031.
12. Berry, V.; Gole, A.; Kundu, S.; Murphy, C. J.; Saraf, R. F. Deposition of CTAB-Terminated Nanorods on Bacteria to Form Highly Conducting Hybrid Systems. *J. Am. Chem. Soc.* **2005,** *127,* 17600-17601.
13. Gunsolus, I. L. Hu, D.; Mihai, C.; Lohse, S. E.; Lee, C.-S.; Torelli, M. D.; Hamers, R. J.; Murphy, C. J.; Orr, G.; Haynes, C. L. Facile Method to Stain the Bacterial Cell Surface for Super-Resolution Fluorescence Microscopy. *Analyst* **2014,** *139,* 3174-3178.
14. Neu, H. C. The Crisis in Antibiotic Resistance. *Science* **1992,** 257, 1064-1073.
15. Zhu, X.; Radovic-Moreno, A. F.; Wu, J.; Langer, R.; Shi, J. Nanomedicine in the Management of Microbial Infection - Overview and Perspectives. *Nano Today* **2014,** *9,* 478-498.
16. Pissuwan, D.; Cortie, C. H.; Valenzuela, S. M.; Cortie, M. B. Functionalised Gold Nanoparticles for Controlling Pathogenic Bacteria. *Trends Biotechnol*. **2010,** *28*, 207-213.
17. Norman, R. S.; Stone, J. W.; Gole, A.; Murphy, C. J.; Sabo-Atwood, T. L. Targeted Photothermal Lysis of the Pathogenic Bacteria, *Pseudomonas aeruginosa*, with Gold Nanorods. *Nano Lett.* **2008**, *8,* 302-306.
18. Wang, S.; Singh, A. K.; Senapati, D.; Neely, A.; Yu, H.; Ray, P. C. Rapid Colorimetric Identification and Targeted Photothermal Lysis of *Salmonella* Bacteria by Using Bioconjugated Oval-Shaped Gold Nanoparticles. *Chem. - Euro. J*. **2010**, *16*, 5600-5606.
19. Wang, C.; Irudayarah, J. Gold Nanorod Probes for the Detection of Multiple Pathogens. *Small* **2008,** *4*, 2204-2208.
20. Kim, C.-B.; Yi, D. K.; Kim, P. S. S.; Lee, W.; Kim, M. J. Rapid Photothermal Lysis of the Pathogenic Bacteria, *Escherichia coli* Using Synthesis of Gold Nanorods. *J. Nanosci. Nanotechnol.* **2009,** *9,* 2841-2845.
21. Singh, A. K.; Senapati, D.; Wang, S.; Griffin, J.; Neely, A.; Candice, P.; Naylor, K. M.; Varisli, B.; Kalluri, J. R.; Ray, P. C. Gold Nanorod Based Selective Identification of *Escherichia coli* Bacteria Using Two-Photon Rayleigh Scattering Spectroscopy. *ACS Nano* **2009,** *3,* 1906-1912.
22. Kuo, W.-S.; Chang, C.-N.; Chang, Y.-T.; Yeh, C.-S. Antimicrobial Gold Nanorods with Dual-Modality Photodynamic Inactivation and Hyperthermia. *Chem. Commun*. **2009,** *45,* 4853-4855.
23. Huang, W. C.; Tsai, P.-J.; Chen, Y.-C. Multifunctional Fe_3O_4@Au Nanoeggs as Photothermal Agents for Selective Killing of Nosocomial and Antibiotic-Resistant Bacteria. *Small* **2009,** *5,* 51-56.
24. Huang, X.; El-Sayed, I. H.; Qian, W.; El-Sayed, M. A. Cancer Cell Imaging and Photothermal Therapy in the Near-Infrared Region by Using Gold Nanorods. *J. Am. Chem. Soc.* **2006,** *128,* 2115-2120.

25. Le Brun, A. P.; Clifton, L. A.; Halbert, C. E.; Lin, B.; Meron, M.; Holden, P. J.; Lakey, J. H.; Holt, S. A. Structural Characterization of a Model Gram-Negative Bacterial Surface Using Lipopolysaccharides from Rough Strains of *Escherichia coli*. *Biomacromolecules* **2013,** *14,* 2014-2022.
26. Alexander, C.; Rietschel, E. T. Bacterial Lipopolysaccharides and Innate Immunity. *J. Endotoxin Res*. **2001,** *7,* 167-202.
27. Jacobson, K. H.; Gunsolus, I. L.; Kuech, T. R.; Troiano, J. M.; Melby, E. S.; Lohse, S. E.; Hu, D.; Chrisler, W. B.; Murphy, C. J.; Orr, G.; Geiger, F. M.; Haynes, C. L.; Pedersen, J. A. Lipopolysaccharide Density and Structure Govern the Extent and Distance of Nanoparticle Interaction with Actual and Model Bacterial Outer Membranes. *Environ. Sci. Technol.* **2015,** *49,* 10642-10650.
28. Piazza, M.; Colombo, M.; Zanoni, I.; Granucci, F.; Tortora, P.; Weiss, J.; Gioannini, T.; Prosperi, D.; Peri, F. Uniform LPS-Loaded Magnetic Nanoparticles for the Investigation of LPS-TLR4 Signaling. *Angew. Chem., Int. Ed.* **2011,** *50,* 622-626.
29. Oliveira, M. D. L.; Andrade, C. A. S.; Correia, M. T. S.; Coelho, L. C. B. B.; Singh, P. R.; Zeng, X. Impedimetric Biosensor Based on Self-Assembled Hybrid Cysteine-Gold Nanoparticles and CramoLL Lectin for Bacterial Lipopolysaccharide Recognition. *J. Colloid Interface Sci*. **2011,** *362,* 194-201.
30. Sun, J.; Ge, J.; Liu, W.; Wang, X.; Fan, Z.; Zhao, W.; Zhang, H.; Wang, P.; Lee, S.-T. A Facile Assay for Direct Colorimetric Visualization of Lipopolysaccharides at Low Nanomolar Level. *Nano Res*. **2012,** *5,* 486-493.
31. Gao, J.; Lai, Y.; Wu, C.; Zhao, Y. Exploring and Exploiting the Synergy of Non-Covalent Interactions on the Surface of Gold Nanoparticles for Fluorescent Turn-On Sensing of Bacterial Lipopolysaccharide. *Nanoscale* **2013,** *5,* 8242-8248.
32. Marinakos, S. M.; Chen, S.; Chilkoti, A. Plasmonic Detection of a Model Analyte in Serum by a Gold Nanorod Sensor. *Anal. Chem*. **2007**, *79*, 5278-5283.
33. Mayer, K. M.; Lee, S.; Liao, H.; Rostro, B. C.; Fuentes, A.; Scully, P. T.; Nehl, C. L.; Hafner, J. H. A Label-Free Immunoassay Based Upon Localized Surface Plasmon Resonance of Gold Nanorods. *ACS Nano* **2008**, *2,* 687-692.
34. Chen, C.-D.; Cheng, S.-F.; Chau, L.-K.; Wang, C. R. C. Sensing Capability of the Localized Surface Plasmon Resonance of Gold Nanorods. *Biosens. Bioelectron.* **2007,** *22,* 926-932.
35. Abadeer, N. S.; Brennan, M. R.; Wilson, W. L.; Murphy, C. J. Distance and Plasmon Wavelength Dependent Fluorescence of Molecules Bound to Silica-Coated Gold Nanorods. *ACS Nano* **2014,** *8,* 8392-8406.
36. Orendorff, C. J.; Murphy, C. J. Quantitation of Metal Content in the Silver-Assisted Growth of Gold Nanorods. *J. Phys. Chem. B* **2006,** *110,* 3990-3994.
37. Gandra, N.; Portz, C.; Tian, L.; Tang, R.; Xu, B.; Achilefu, S.; Singamaneni, S. Probing Distance-Dependent Plasmon-Enhanced Near-Infrared Fluorescence Using Polyelectrolyte Multilayers as Dielectric Spacers. *Angew. Chem., Int. Ed.* **2014,** *53,* 866-870.
38. Gole, A.; Murphy, C. J. Polyelectrolyte-Coated Gold Nanorods: Synthesis, Characterization and Immobilization. *Chem. Mater.* **2005,** *17,* 1325-1330.
39. Fogg, E. T.; Hixson, A. N.; Thompson, A. R. Densities and Refractive Indexes for Ethylene Glycol-Water Solutions. *Anal. Chem*. **1955,** *27,* 1609-1611.
40. Chen, S.; Svedendahl, M.; Käll, M.; Gunnarsson, L.; Dmitriev, A. Ultrahigh Sensitivity Made Simple: Nanoplasmonic Label-Free Biosensing with an Extremely Low Limit-of-Detection for Bacterial and Cancer Diagnostics. *Nanotechnology* **2009,** *20,* 434015.
41. Lipopolysaccharides. http://www.sigmaaldrich.com/life-science/molecular-biology/molecular-biology-products.html?TablePage=19922916 (accessed September 1, 2015).
42. Chen, S.; Svedendahl. M.; Van Duyne, R. P.; Käll, M. Plasmon-Enhanced Colorimetric ELISA with Single Molecule Sensitivity. *Nano Lett.* **2011,** *11,* 1826-1830.
43. Becker, J.; Trügler, A.; Jakob, A.; Hohenester, U.; Sönnichsen, C. The Optimal Aspect Ratio of Gold Nanorods for Plasmonic Bio-sensing. *Plasmonics* **2010**, *5*, 161-167.
44. Lu, G.; Hou, L.; Zhang, T.; Li, W.; Liu, J.; Perriat, P.; Gong, Q. Anisotropic Plasmonic Sensing of Individual or Coupled Gold Nanorods. *J. Phys. Chem. C* **2011**, *115,* 22877-22885.
45. Refractive index increment dn/dc values. http://www.materials-talks.com/blog/2013/06/18/refractive-index-increment-dndc-values/ (accessed September 1, 2015).

46. Alkilany, A. M.; Nagaria, P. K.; Hexel, C. R.; Shaw, T. J.; Murphy, C. J.; Wyatt, M. D. Cellular Uptake and Cytotoxicity of Gold Nanorods: Molecular Origin of Cytotoxicity and Surface Effects. *Small* **2009,** *5,* 701-708.
47. Wilson, C. G.; Sisco, P. N.; Goldsmith, E. C.; Murphy, C. J. Glycosaminoglycan-Functionalized Gold Nanorods: Interactions with Cardiac Cells and Type I Collagen. *J. Mater. Chem.* **2009,** *19,* 6332-6340.
48. Hauck, T. S.; Ghazani, A. A.; Chan, W. C. Assessing the Effect of Surface Chemistry on Gold Nanorod Uptake, Toxicity, and Gene Expression in Mammalian Cells. *Small* **2008,** *4,* 153-159.
49. Niidome, T.; Yamagata, M.; Okamoto, Y.; Akiyama, Y.; Takahashi, H.; Kawano, T.; Katayama, Y.; Niidome, Y. PEG-Modified Gold Nanorods with a Stealth Character for *In Vivo* Applications. *J. Controlled Release* **2006,** *114,* 343-347.
50. Hu, M.; Noda, S.; Okubo, T.; Yamaguchi, Y.; Komiyama, H. Structure and Morphology of Self-Assembled 3-Mercaptopropyltrimethoxysilane Layers on Silicon Oxide. *Appl. Surf. Sci.* **2001,** *181,* 307-316.
51. Lin, Z.; Cai, J. J.; Scriven, L. E.; Davis, H. T. Spherical-to-Wormlike Micelle Transition in CTAB Solutions. *J. Phys. Chem.* **1994,** *98,* 5984-5993.
52. Huang, J.; Park, J.; Wang, W.; Murphy, C. J.; Cahill, D. G. Ultrafast Thermal Analysis of Surface Functionalized Gold Nanorods in Aqueous Solution. *ACS Nano* **2013,** *7,* 589-597.
53. Wu, C.; Xu, Q-H. Stable and Functionable Mesoporous Silica-Coated Gold Nanorods as Sensitive Localized Surface Plasmon Resonance (LSPR) Nanosensors. *Langmuir* **2009,** *25,* 9441-9446.
54. Cauda, V.; Argyo, C.; Bein, T. Impact of Different PEGylation Patterns on the Long-Term Bio-Stability of Colloidal Mesoporous Silica Nanoparticles. *J. Mater. Chem.* **2010,** *20,* 8693-8699.
55. Lundqvist, M.; Stigler, J.; Elia, G.; Lynch, I.; Cedervall, T.; Dawson, K. A. Nanoparticle Size and Surface Properties Determine the Protein Corona with Possible Implications for Biological Impacts. *Proc. Natl. Acad. Sci. U. S. A.* **2008,** *105,* 14265-14270.
56. Tian, L.; Chen, E.; Gandra, N.; Abbas, A.; Singamaneni, S. Gold Nanorods as Plasmonic Nanotransducers: Distance-Dependent Refractive Index Sensitivity. *Langmuir* **2012,** *28,* 17435-17442.
57. Singh, S.; Papareddy, P.; Mörgelin, M.; Schmidtchen, A.; Malmsten, M. Effects of PEGylation on Membrane and Lipopolysaccharide Interactions of Host Defense Peptides. *Biomacromolecules* **2014,** *15,* 1337-1345.
58. Wang, L.; Zhu, Y.; Xu, L.; Chen, W.; Kuang, H.; Liu, L.; Agarwal, A.; Xu, C.; Kotov, N. A. Side-by-Side and End-to-End Gold Nanorod Assemblies for Environmental Toxin Sensing. *Angew. Chem., Int. Ed.* **2010,** *49,* 5472-5475.
59. Li, B.; Logan, B. E. Bacterial Adhesion to Glass and Metal-Oxide Surfaces. *Colloids Surf., B* **2004,** *36,* 81-90.
60. Yang, J. A.; Johnson, B. J.; Wu, S.; Woods, W. S.; George, J. M.; Murphy, C. J. Study of Wild-Type α-Synuclein Binding and Orientation on Gold Nanoparticles. *Langmuir* **2013,** *29,* 4603-4615.
61. Fu, J.; Ji, J.; Yuan, W.; Shen, J. Construction of Anti-Adhesive and Antibacterial Multilayer Films *via* Layer-by-Layer Assembly of Heparin and Chitosan. *Biomaterials* **2005,** *26,* 6684-6692.
62. Yang, J. M.; Lin, H. T.; Wu, T. H.; Chen, C.-C. Wettability and Antibacterial Assessment of Chitosan Containing Radiation-Induced Graft Nonwoven Fabric of Polypropylene-*g*-Acrylic Acid. *J. Appl. Polym. Sci.* **2003,** *90,* 1331-1336.
63. Fang, B.; Jiang, Y.; Rotello, V. M.; Nüsslein, K.; Santore, M. M. Easy Come Easy Go: Surfaces Containing Immobilized Nanoparticles or Isolated Polycation Chains Facilitate Removal of Captured *Staphylococcus aureus* by Retarding Bacterial Bond Maturation. *ACS Nano* **2014,** *8,* 1180-1190.
64. Lu, J.; Wang, X.; Xiao, C. Preparation and Characterization of Konjac Glucomannan/Poly(diallyldimethylammonium chloride) Antibacterial Blend Films. *Carbohydr. Poly.* **2008**, *73*, 427-437.
65. Lee, C.-H.; Lin, Y.-H.; Hsieh, J.-L.; Chen, M.-C.; Kuo, W.-L. A Polymer Coating Applied to *Salmonella* Prevents the Binding of *Salmonella*-Specific Antibodies. *Int. J. Cancer* **2013,** *132,* 717-725.
66. Kahraman, M.; Zamaleeva, A. I.; Fakhrullin, R. F.; Culha, M. Layer-by-Layer Coating of Bacteria with Noble Metal Nanoparticles for Surface-Enhanced Raman Scattering. *Anal. Bional. Chem.* **2009,** *395,* 2559-2567.

CHAPTER 4:
RECENT PROGRESS IN CANCER THERMAL THERAPY USING GOLD NANOPARTICLES

4.1 INTRODUCTION

In 1852, English scientist Michael Faraday gave a lecture at the Royal Institute in London on the "Experimental Relations of Gold (and Other Metals) to Light." Faraday was the first to recognize gold salts could be reduced to form ruby colored solutions of "finely divided" gold particles.[1] More recently, there has been great interest in the properties of gold nanostructures of various shapes and sizes.[2] The literature is vast, with demonstrating= advancements in synthesis, characterization, and application of gold nanomaterials of various shapes such as spheres,[3] rods,[4] shells,[5] and cages.[6]

Due to their small size, ease of functionalization, and uniquely tunable optical properties, gold nanoparticles are attractive for biomedical use in sensing,[7] cellular imaging,[8] drug delivery,[9] and cancer therapy.[10] These applications may be realized by carefully engineering the size, shape, surface chemistry, and aggregation state of gold nanoparticles.[11] Upon illumination, ~10-200 nm gold nanoparticles can support localized surface plasmon resonances (LSPRs) which are coherent localized oscillations of free conduction band electrons (Figure 4.1). These conduction band electrons are highly polarizable, and when incident light is resonant with the wavelengths of their surface plasmons, the electrons move under the influence of the external field, giving rise to a net charge difference at the nanoparticle boundaries. Incident light can be absorbed/scattered by gold nanoparticles and photon confinement leads to the generation of strong electromagnetic fields at the metal surface, and a wide variety of optical phenomena.[12]

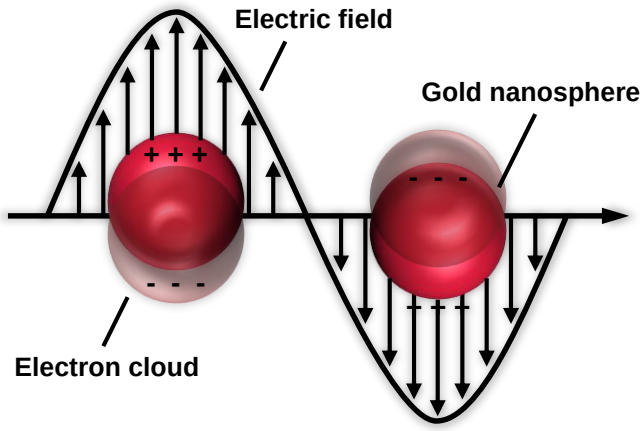

Figure 4.1 Schematic of the localized surface plasmon resonance on gold nanospheres. Upon illumination at resonant wavelengths, conduction band electrons in a gold nanoparticle are delocalized and undergo collective oscillation.

---

* This chapter is reprinted with permission from: Nardine S. Abadeer and Catherine J. Murphy. *J. Phys. Chem. C* **2016,** *118,* Copyright (2016) American Chemical Society.

The mean free path of an electron in gold is around 50 nm; consequently, collisions of conduction band electrons with a gold nanoparticle surface are greatly dependent on nanoparticle diameter. Therefore, the LSPR wavelength (λ_{max}) and extinction cross-section of gold nanoparticle colloids are size and shape dependent.[13] The LSPR is also highly sensitive to the capping agent and surrounding dielectric environment, especially the refractive index at the nanoparticle surface.[14-16] Optical absorbance can therefore be tuned from the visible to the near-infrared (NIR) and has been established both experimentally and theoretically.[17] In anisotropic nanoparticles, the plasmon resonance band may separate into several peaks due to electron oscillation along each axis. For example, in gold nanorods there are two absorbance peaks, one correlated with the shorter transverse axis around 520 nm and one with the longer longitudinal axis. The longitudinal peak is more sensitive to aspect ratio (length/width) and the λ_{max} shifts from 640 to over 800 nm when aspect ratio (AR) is increased from 1.1-4.4. This shift can also be observed in gold nanorod solutions where pink, blue, green and brown colors are clearly visible.[18]

Strong optical absorption and subsequent non-radiative energy dissipation allows for the application of gold nanoparticles in plasmonic photothermal therapy. Link *et al.*[19] described the photothermal heating process in gold nanoparticles, which has been observed using femtosecond transient absorption spectroscopy. NIR laser pulses absorbed by gold nanoparticles excite free electrons in the plasmon band, creating a pulse of hot electrons. The hot electron pulse cools rapidly through electron-phonon interactions by colliding with the gold lattice, heating it to thousands of degrees (depending on laser power) within ~1 ps. Heat is then transferred from the nanoparticle to its surroundings through phonon-phonon interactions on a timescale of ~100 ps, resulting in an increase in temperature of the surrounding medium by tens of degrees. An example of this process in gold nanorods is shown in Figure 4.2.[20]

The electron and the lattice temperatures have been described mathematically (Equations 4.1 and 4.2) using the two-temperature model where C_e and C_l are the electronic and lattice heat capacities, T_e is the electron temperature, T_l is the lattice temperature, g is the electron-phonon coupling constant, κ' is the electronic thermal conductivity describing the heat transport away from the excited laser spot, $LP(z,t)$ is the spatial temporal evolution of the exciting laser pulse.[20] For a more complete physical description on the photothermal process, we direct interested readers to reference 19.

$$C_e(T_e)\frac{\partial T_e}{\partial t} = -g(T_e - T_l) + \nabla \cdot (\kappa' \nabla T_e) + LP(z,t) \tag{4.1}$$

$$C_l \frac{\partial T_1}{\partial t} = g(T_e - T_l) \tag{4.2}$$

It is possible to roughly estimate the change in temperature of a laser-irradiated nanoparticle solution. For example, a 50 mW, 785 nm laser will deliver 60 J of energy after 20 minutes. If the absorbance of 1 mL of gold nanorods is 1 at 785 nm, then light transmittance is 10%, and 90% of that light would

absorbed/scattered by the particles. Given that 97% of extinction is due to absorbance,[17] 52 J would be absorbed. If we assume photothermal conversion efficiency is 100%, then the change in temperature of the water would be ~11°C.

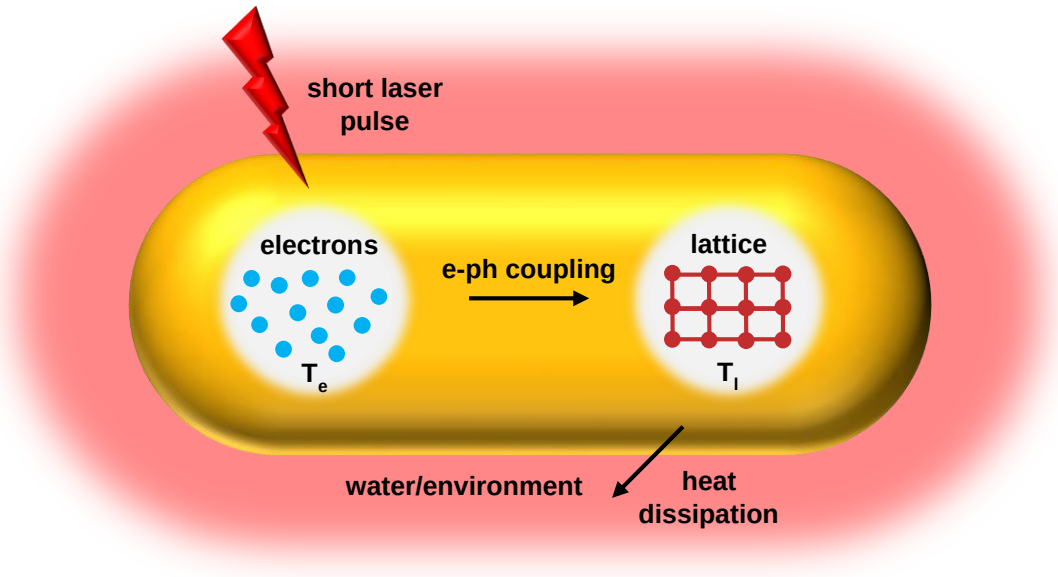

Figure 4.2 Photophysical processes of a gold nanorod excited by a short femtosecond laser pulse. (1) Absorption of photons excites free electrons in the plasmon band. (2) The non-thermal electron distribution relaxes *via* electron-electron scattering. (3) There is electron-phonon coupling and heat transfer from the electrons to the gold lattice. (4) Phonon-phonon interactions leads to heat dissipation from the crystal lattice and the system returns to its starting electron temperature. When a continuous-wave laser source is used, heat generated in the lattice is continuously dissipated into the surrounding environment. Adapted with permission from Reference 20. Copyright (2014) University of Illinois.

Because the photothermal process requires light absorption, nanoparticle extinction influences the resulting change in surrounding temperature. The extinction cross-section of gold nanoparticles in the NIR is 10^8-10^{10} $M^{-1}cm^{-1}$, several orders of magnitude larger than even the strongest absorbing organic chromophores.[21] We note that there can be millions of atoms per gold nanoparticle and extinction is typically reported in molarity, not mass. Absorbance is usually the greater contributor to extinction, and since smaller gold nanoparticles generally have higher absorbance cross-sections than larger nanoparticles (scattering contribution increases with nanoparticle size), they can be more efficient nanoheaters. In addition, the LSPR of gold nanoparticles can be tuned to a desired laser wavelength to maximize light absorption. This is especially useful in regions such as the “water window” where body tissues are more optically transparent (700-1200 nm), making it also possible to heat up gold nanoparticles *in vivo*.[17] Heating efficiency is also dependent on the chosen irradiation conditions, and will be discussed later.[22]

4.2 PHOTOTHERMAL CANCER THERAPY USING GOLD NANOPARTICLES

The application of heat to cancer treatment is not new, and has been used since the early 1900's. In traditional hyperthermia, the region of the body containing the tumor is heated to ~40-45°C, several degrees above physiological temperature (37°C).[23] Heat is generated externally using instruments that produce electromagnetic fields (microwaves or radiowaves), or ultrasound.[24] Traditional hyperthermia has been used, in combination with chemotherapy and/or radiation therapy, for the eradication of a variety of cancer types in several clinical trials.[25,26]

The heat generated from gold nanoparticles can be utilized in cancer therapy to damage/destroy cancerous cells and tissues. The difference between traditional hyperthermia and photothermal therapy is that photothermal heating only occurs in the area directly around the gold nanoparticles, and local temperatures can rise to tens or hundreds of degrees above physiological temperature (on very short time scales). This implies that photothermal heating could be more targeted to tumors rather than healthy tissue to potentially reduce negative side effects of cancer therapies.[27] It is thought that tumor tissue is more hypoxic, acidic, and nutrient-deficient compared to normal tissues.[28] These traits may render some cancer cells more sensitive to heat. However, the overexpression of heat shock proteins has also been observed in some cancers.[29] These proteins may then make cancer cells more resistant than expected to heat-based therapies, so the effects of thermal therapy are not universal in all types of cancer.[30]

The first example of gold nanoparticle-mediated photothermal cancer therapy was reported in 2003 by West, Halas and coworkers.[31] Gold nanoshells consisting of 110 nm silica cores surrounded by 10 nm gold shells were functionalized with the biocompatible polymer polyethylene glycol (PEG) which is often used to minimize nanoparticle aggregation and to increase blood circulation and half-life. These particular nanoshells had a λ_{max} of 820 nm, but LSPRs in gold nanoshells can be tuned from 700-1000 nm by increasing the core-to-shell ratio.[32] SK-BR-3 human breast carcinoma cells were incubated with the gold nanoshells for 1 h and then exposed to laser light (820 nm, 35 W/cm^2, 7 min). Fluorescence imaging of the treated cells revealed damage in the irradiated region (Figure 4.3) including lost cell membrane integrity and cell death, which was not observed in the controls with laser irradiation or gold nanoshells alone. Db17-Prkd c SCID/J mice with 1 cm tumors in their hind legs were treated to demonstrate the potential of the therapy *in vivo*. Gold nanoshells were directly injected into the tumors and NIR irradiation (820 nm, 4 W/cm^2, 6 min) resulted in an average temperature increase in the irradiated tumor spot of 37.4 ± 6.6ºC compared to 9.1 ± 4.7ºC with the laser alone. Histological analysis revealed that there was some thermal damage to tumors including coagulation, and cell shrinkage. Unfortunately, fast diffusion of the nanoshells throughout the tumor and high tissue absorption resulted in only 4-6 mm maximum depth of the damaged areas, demonstrating a limitation of the treatment.[31] The same researchers carried out a study in 2004 demonstrating *in vivo* photothermal destruction of CT26.WT murine colon tumors in the dorsal flanks of BALB/cAnNHsd mice. This time, the tumors were much smaller (5.5 mm) and laser irradiation was carried out 6 h after intraperitoneal injection of the gold nanoshells to allow time for the nanoparticles to accumulate in the tumors. NIR laser irradiation (808 nm, 4 W/cm^2, 3 min) resulted in tumor temperatures of ~50ºC which was significantly higher than the control tumors without nanoshells. 10 days after treatment, the tumors

were gone and all mice remained healthy and tumor-free for 90 days. Conversely, all controls demonstrated significant tumor growth and had a mean survival time of only 10 days. This suggested there was some potential in photothermal cancer therapy using gold nanoparticles.[33]

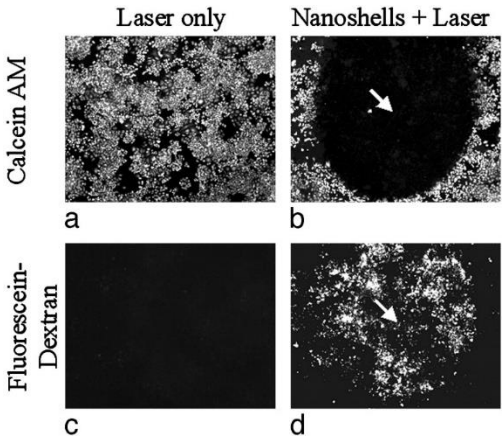

Figure 4.3 Human breast epithelial carcinoma SK-BR-3 cells irradiated in the absence of nanoshells maintained viability, as depicted by (a) calcein fluorescence, and membrane integrity, as indicated by (c) lack of intracellular fluorescein dextran uptake. Cells irradiated with nanoshells possess well defined circular zones of cell death in the (b) calcein AM study and (d) cellular uptake of fluorescein dextran from increased membrane permeability. Adapted from Reference 31. Copyright (2003) National Academy of Sciences, USA.

El-Sayed and coworkers advanced the prospective application of photothermal treatment by using targeted gold nanoparticles.[34] Gold nanospheres (40 nm, λ_{max} = 530 nm) were functionalized with anti-epidermal growth factor receptor (EGFR) monoclonal antibodies which facilitate binding and uptake of nanoparticles by cancer cells that are known to overexpress EGFR.[35] Cells were immersed in nanoparticle solutions for 40 min and subsequent laser irradiation (514 nm, 13-76 W/cm^2, 4 min) resulted in selective killing of HSC-3 and HOC-313 malignant human oral squamous cell carcinoma (Figure 4.4). Interestingly, HSC cell death occurred at laser powers ≥25 W/cm^2 while HOC cells underwent photothermal killing at ≥19 W/cm^2. This was potentially due to greater nanoparticle binding to the surface of the HOC cells. There was some photothermal destruction to benign HaCaT human keratinocytes, but only at laser powers ≥57 W/cm^2 due to the non-specific binding of gold nanoparticles. In addition, there was no cell death observed when cells were exposed to laser light alone, up to 76 W/cm^2 power density.[34] The same researchers later demonstrated photothermal treatment with anti-EGFR gold nanorods (AR 3.9, λ_{max} ~790 nm). Laser irradiation (800 nm, 4 min) of cells incubated with the nanorods demonstrated death of HSC and HOC cells at ≥10 W/cm^2. The greater amount of cell destruction at lower laser density could be attributed to higher nanorod light absorbance and enhanced light penetration in the NIR, and demonstrated that nanoparticle shape may influence heating.[36]

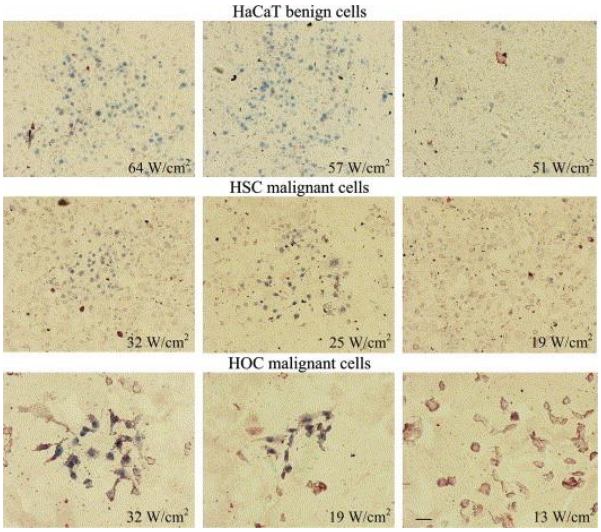

Figure 4.4 HaCaT benign cells (top row). HSC malignant cells (middle row), and HOC malignant cells (bottom row) incubated with gold nanospheres, irradiated at different laser powers, and then stained with trypan blue (indicative of cell death). HaCaT cells were killed at and above 57 W/cm^2. HSC malignant cells were killed at and above 25 W/cm^2 and HOC malignant cells were killed at and above 19 W/cm^2. Scale bar = 60 μM. Adapted with permission from Reference 34. Copyright (2006) Elsevier.

The first demonstrations of gold nanoparticle-mediated photothermal therapy has led to an increase in studies seeking to use gold nanoparticles for photothermal cancer treatment (Figure 4.5). Photothermal cancer therapy with gold nanoparticles is desirable for many reasons. First, with advancements in synthesis, scientists have been able to scale up preparations of gold nanoparticles of various sizes and shapes. The vast majority of these procedures are aqueous, so phase transfer from organic solvents is not an issue.[37,38] This may allow for more widespread application of gold nanoparticles. Second, compared to other metals, gold is more chemically inert, potentially rendering the gold nanoparticle core biocompatible. Studies of short-term gold nanoparticle exposure to various cell types suggest they are non-cytotoxic, and non-immunogenic at clinically relevant concentrations.[39.40] However, surface chemistry-dependent changes in cell function including gene expression,[41] and migration[42] have been reported. We also note that molecules used in nanoparticle synthesis (i.e. surfactants) can be cytotoxic.[43] Therefore the effect of a chosen surface ligand on cell viability and cell behavior is an important consideration before biological exposure. Third, since gold nanoparticles are highly tunable in their size, shape and surface chemistry it may be possible to engineer them for maximum tumor accumulation *in vivo*.[44] Nanoparticles that are 60-400 nm in diameter can extravasate in solid tumors due to the leakiness of tumor vasculature, allowing for a passive form of tumor targeting. This is known as the enhanced permeability and retention (EPR), and is well-documented in the literature.[45,46] Finally, gold nanoparticles can be designed to more actively target tumor sites through modification of their surface chemistry. A wide array of small molecules, proteins, and peptides has been developed to bind to specific receptors on tumor cells with varying degrees of tumor accumulation.[47] Targeting ligands may include antibodies that bind to an overexpressed protein,[48] RNA/DNA aptamers that fold into unique 3-D conformations *via* intermolecular interactions and bind to

target molecules on a cellular surfaces,[49.50] or molecules such as folate to facilitate translocation into cancer cells over-expressing folate receptors *via* receptor-mediated endocytosis.[51] Then, once gold nanoparticles bind to or accumulate in cells/tumors, NIR irradiation can trigger photothermal heating.[34] Nanoparticle LSPR, and irradiation conditions can be designed to maximize heating efficiency.[22] Because irradiation is localized at the tumor site, this may avert unwanted side effects associated with conventional cancer treatments. However, photothermal therapy may also be used in conjunction with other cancer treatments, such as chemotherapy, to enhance tumor destruction.[28]

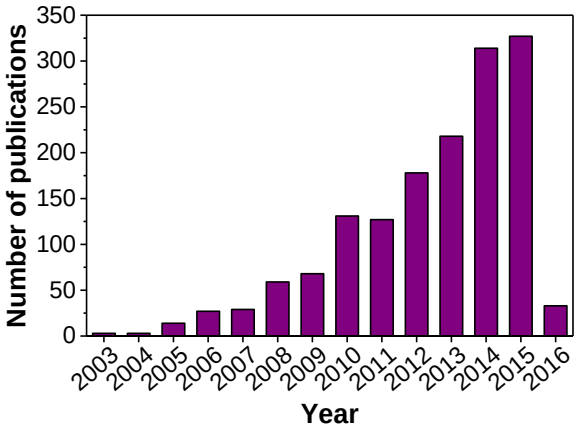

Figure 4.5 The number of SciFinder Scholar references per year since 2003 containing the search terms gold, photothermal, and cancer as of January 27, 2016.

In this review we describe the aspects of gold nanoparticle design which may be important for clinical application of gold nanoparticle heating for cancer therapy.[52] This includes consideration of nanoparticle structure including: composition, size, shape, extinction, surface charge, and targeting ligand. In addition to photothermal heating efficiency, these characteristics can also affect nanoparticle transport across tissue/tumor/cell boundaries, blood half-life, *in vivo* biodistribution and potential toxicity or damage due to long-term exposure. Understanding how design affects biological fate will allow for the conditions of therapy (dose and irradiation) to be optimized for successful cancer treatment. Irradiation conditions such laser type, laser wavelength, spot size, and depth of light penetration also need to be considered for optimized heating. All these factors may influence cancer cell death *in vitro*, and consequently *in vivo* tumor destruction. We focus the majority of our discussion on the progress of gold nanoparticle-mediated thermal therapy since 2010 including: treatment *via* radiofrequency hyperthermia, temperature changes and distribution due to photothermal heating, potential mechanisms of cancer cell death, recent advancements in nanoparticle design for *in vitro* and *in vivo* studies, biodistribution of gold nanoparticles, and the current progression toward application in clinical cancer therapy.

4.3 RADIOFREQUENCY HYPERTHERMIA WITH GOLD NANOPARTICLES

Gold nanoparticles have been reported to heat up the surrounding medium when they are exposed to external capacitively-coupled radiofrequency (RF) electric fields. We note that RF hyperthermia is different from traditional radiofrequency ablation therapy. In traditional RF ablation therapy, heating is accomplished through a probe directly inserted into the tumor, and there are no nanoparticles present. Direct exposure of a tumor to low frequency 350-500 kHz RF fields can aid in destruction of tumor cells in a variety of cancers; however, the application can also cause a significant amount of pain in patients due to thermal injury.[53] In the RF hyperthermia systems described in this review, a 13.56 MHz signal is applied to a sample containing gold nanoparticles which is placed in the space between two electrodes (Figure 4.6). The concept of this treatment is that gold nanoparticles absorb the radiofrequencies and generate heat. Heating through RF hyperthermia may be desirable because RF fields penetrate through non-conducting materials, unlike NIR light, so invasive needles may not be necessary.[54]

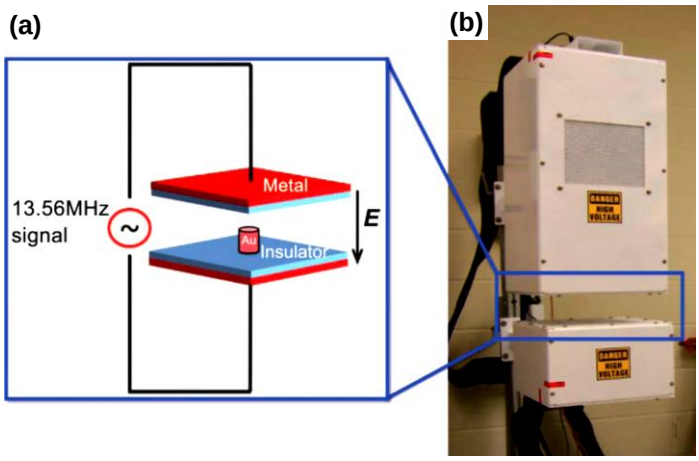

Figure 4.6 (a) Diagram of an RF heating system. A 13.56 MHz signal is applied across two metal electrodes (red) that are coated with an insulating Teflon® layer (blue) which produces a high-voltage RF field (15 kV/m at 600 W generator power) over a variable air gap. Gold nanoparticle suspensions are placed on a platform. (b) Prototype capacitive RF device. The metal chassis (upper white box) contains high voltage matching circuits to produce RF fields between the electrodes. The location of the electrodes within the chassis is highlighted by the blue rectangle. Adapted from Reference 55. Copyright (2009) Springer.

Radiation parameters and gold nanoparticle design may be modified to optimize RF hyperthermia. For example, Moran *et al.*[55] investigated the effects of gold nanosphere size (5-250 nm) or gold concentration (up to 36 ppm) using 10 nm gold nanospheres. RF exposure (13.56 MHz 600 W, 15 kV/m) resulted in temperature increases of up to 50ºC with higher gold concentration and greater heating rates for smaller diameter particles. The authors proposed the change in temperature was due to Joule heating (an electric current through a metal releases heat resistively). In the case of gold, the superior heating efficiency of smaller nanoparticles was credited to their greater resistivity compared to larger/bulk gold.[55] Due to the significant temperature increases reported after RF exposure, researchers have investigated RF fields to heat up gold nanoparticles for cancer therapy.[56] However, there is an ongoing debate and discussion on

the amount of heat which can be generated through RF exposure to gold nanoparticles.[57] The mechanism of this heating process is not well-understood and is debated in the literature. Some researchers have suggested that capacitively coupled RF fields heat gold nanoparticles inductively (Joule heating),[55] or with a combination of magnetic and electrophoretic heating mechanisms.[58] Readers interested in the mechanism are directed to a recent critical review that summarizes mechanisms postulated in the literature.[59]

Researchers have explored RF heating of gold nanoparticles for thermal therapy of cancer *in vitro* in a variety of cancer cell lines. All the following *in vitro* and *in vivo* reports mentioned here are summarized in Table 4.1 Cardinal *et al.*[60] were some of the first to report effective cancer treatment. Citrate gold nanospheres (15 nm) were exposed to HepG2 hepatocarcinoma cells and exposed to RF fields (13.56 MHz, 35 W, 3-7 min). This resulted in 35% cell death after 3 min, 60% cell death after 5 min, and 80% cell death after 7 min.[60] Glazer *et al.*[61] reported that the success of RF heating (13.56 MHz, 200 S, 10-15 kV/m, 5 min) with anti-EGFR functionalized gold nanoparticles (20 nm) was surface chemistry dependent. A 61% decrease in viability of Panc-1 (a pancreatic cancer cell line that overexpresses EGFR) was observed compared to a 6.3% decrease with Cama-1, which did not express EGFR. This suggested that internalization of nanoparticles into cancer cells was critical to successful RF thermal therapy.[61] The aggregation state of gold nanoparticles was investigated in 2012 by Raoof *et al.*[62] They prepared anti-EGFR gold nanospheres (10 nm) to be internalized into endosomes of SNU-449 liver cancer cells. Due to the decrease in endosomal pH to 5.5, intracellular aggregation occurred, which was attributed to removal of the antibody at lower pH. However, the authors were able to prevent nanoparticle aggregation in some cells with the addition of Concanamycin A, which blocked acidification of cell vesicles. RF exposure (13.56 MHz, 600 W, 12.4 kV/m, 9 min) resulted in 40% cell death of aggregated nanoparticles and 55% cell death of non-aggregated nanoparticles. A significant decrease in nanoparticle heating rate and increase in viability of SNU-449 was observed between non-aggregated and aggregated gold nanoparticles. This suggested that nanoparticle aggregation state affected the RF absorption cross-section and cancer therapy outcomes.[62]

Others have reported RF hyperthermia *in vivo.* Curley and coworkers[63] injected nude balb/c mice with Panc-1 or Capan-1 human pancreatic carcinoma cells to form subcutaneous tumors. 10 nm gold nanospheres were functionalized with anti-EGFR or PAM4 antibodies to target EGFR or MUC-1 receptors, respectively on pancreatic cells. No thermal injuries were observed in mice due to RF exposure (13.56 MHz, 600 W, 10 min) because any effects of excess electric current were prevented by attaching conductive tape to the extremities of the mice. Treatment with RF and nanoparticles resulted in a bulk Panc-1 tumor temperature increase of 3ºC above body temperature. After six weeks treatment, tumor growth was significantly impeded with the dual treatment compared to a significant volume increase with untreated mice or nanoparticles/RF exposure alone. Mass spectrometry analysis of organs revealed that there was accumulation of the nanoparticles in the tumor (25.1 ± 6.4 mg), but also the spleen (257.6 ± 7.6 mg), liver (302.7 ± 82.5 mg), kidneys (4.1 ± 0.1 mg), and lungs (4.0 ± 0.3 mg) of mice. Surprisingly, no tissue damage

was reported in those non-tumor regions, even with the substantial accumulation of nanoparticles in the liver and spleen. In the Capan-1 tumors, PAM4 gold nanoparticles and RF exposure seemed to slow growth in the first few weeks, but did not significantly reduce tumor size after 7 weeks. Since PAM4 is more pancreas cancer-specific than anti-EGFR, the reduced effectiveness of PAM4 gold nanoparticles in RF cancer therapy was unexpected. This suggested that the chosen nanoparticle ligand was influential in successful RF therapy.[63]

In 2014, Raoof *et al.*[64] carried out RF hyperthermia in conjunction with chemotherapy *in vivo* using C225 antibody-functionalized gold nanospheres. The gold nanospheres were loaded with the chemotherapeutic gemcitabine to enhance tumor cell destruction. BalbC/Nu mice bearing 0.5 cm subcutaneous hepatocarcinoma tumors, were intraperitoneally injected with 10 nm gold nanospheres (10 mg/kg nanoparticles, 1.2 mg/kg gemcitabine) 24 h prior to RF exposure. Mice were treated two times a week for three weeks with gold nanoparticles/RF exposure (13.56 MHz, 600 W, 10 min). Afterwards, mice treated with the gold nanoparticles alone, or nanoparticles in conjunction with RF exposure experienced a significant reduction in tumor weight compared to untreated tumors or RF exposure alone. There was also a 50% reduction in tumor weight/volume between mice treated with gold nanoparticles alone and gold nanoparticles plus RF exposure. This suggested that gold nanoparticle delivery followed RF exposure may have reduced tumor growth.[64]

There has been one commercial attempt for application of RF-based cancer therapy with gold nanoparticles, which was initiated in 2005.[65] The system employs a patented RF field generator, called the Kanzius machine, (Figure 4.6) and 3–40 nm antibody-functionalized gold nanoparticles, requiring 2–3 RF treatments per week and multiple weeks of treatment.[66] There are no reports of clinical trials on clinicaltrials.gov, but clinical application for cancer therapy was the eventual goal of the organizations involved.[67] The rights to the Kanzius machine technology were recently purchased from AkesoGenX by NeoTherma Oncology.[68] Human clinical trials with the device only (no nanoparticles) are pending approval in Italy during 2016 to determine the effect of RF exposure alone to cancer cells.[69] However, as there is a debate surrounding the effect mechanism of RF hyperthermia with gold nanoparticles, it would be useful to resolve the fundamental scientific questions in order to further cancer therapy with this technology.

A report by D. Li *et al.*[70] investigated RF heating in nanoparticle colloids and their supernatant solutions. Citrate-coated gold nanospheres (5-200 nm) were separated from the other components in solution by centrifugation. Nanoparticle and supernatant samples were exposed to RF fields (13.56 MHz, 25 W, 2.5 kV/m) and heating rates were monitored over time. The results suggested that it was actually the ionic components and impurities in the supernatant which absorbed the majority of RF radiation and led to Joule heating, not the gold nanoparticles.[55,71] A separate investigation by X. Liu *et al.*[72] exposed citrate-coated gold nanospheres (10-30 nm) to stronger RF fields (13.56 MHz, 600 W, 16 kV/m, 10 min), and came to the conclusion that there was very little heat generated by gold nanoparticles after RF exposure. A follow up report by Corr *et al.*[73] carried out a study to evaluate the impact of nanoparticle size and concentration on RF heating (13.56 MHz, 100-950 W, 90 kV/m) using unpurified and purified citrate gold nanospheres (5-50

nm). They acknowledged that while impurities may have contributed to the majority of RF heating observed in many of the previous reports, gold nanoparticles are RF "active" when the diameter is ≤10 nm, and high-power RF electric fields (≥90 kV/m) are used. They also noted that heating is strongly dependent on nanoparticle concentration but did not suggest a new mechanism.[73]

Together, these reports necessitate further investigation on the amount of heat which can be generated using RF exposure to gold nanoparticles. It is quite encouraging that Curley and coworkers have observed a great deal of consistency in temperature changes, and persistent effectiveness in treatment of cancer *in vitro* and *in vivo* using their RF system in conjunction with gold nanoparticles.[74-77] However, it is concerning that there is a paucity of reports by other groups that confirm these findings. The field of RF-mediated thermal therapy with gold nanoparticles could be further advanced if other researchers investigated and reported upon the effects of size, shape and surface chemistry on heat generation and cancer cell death.

Table 4.1 Summary of references using RF heating of gold nanoparticles for cancer therapy.

Reference	Nanoparticle	Dose and exposure	Animal model or cell line	RF conditions	Results
Cardinal[60]	Citrate gold nanospheres, 13 nm	4 nM, 4 h	HepG2	13.56 MHz, 35 W, 3-7 min	35% cell death (3 min), 60% cell death (5 min), 80% cell death (7 min)
Glazer[61]	Anti-EGFR gold nanospheres, 20 nm	50 nM, 3 h	Panc-1 and Cama-1	13.56 MHz, 200 W, 10-15 kV/m, 5min	60.6% Panc-1 cell death, 6.3% Cama-1 cell death
Raoof[62]	aggregated or non-aggregated anti-EGFR gold nanospheres, 10 nm	100 µg/mL, 4 h	SNU-449	13.56 MHz, 600 W, 12.4 kV/m, 9 min	~40% cell death (aggregated) and ~55% cell death (non-aggregated)
Glazer[63]	Anti-EGFR or PAM4 gold nanospheres, 10 nm	10 mg gold/kg, intraperitoneal injection, 36 h	Panc-1and Capan-1 subcutaneous tumors in the right flank of nude balb/c mice	13.56 MHz, 600 W, 10 min	3ºC tumor temp increase and significant reduction in Panc-1 tumor volume, but no significant decrease in Capan-1 tumor volume
Raoof[64]	C225-functionalized gemcitabine gold nanospheres, 10 nm	10 mg/kg, intraperitoneal injection, 24 h	Subcutaneous hepatocarcinoma tumors in balb/c mice	13.56 MHz, 600 W, 10 min	~50% reduction in tumor weight with nanospheres alone, ~75% reduction in tumor weight with nanospheres + RF

4.4 PHYSICAL INVESTIGATIONS INTO PHOTOTHERMAL HEATING WITH GOLD NANOPARTICLES

Due to strong NIR light absorption, the majority of interest in gold nanoparticle cancer therapy is in photothermal therapy, so the amount of heat generated is an area of research interest. H.-C. Huang *et al.*[78] theoretically and experimentally evaluated spatiotemporal changes in temperature from NIR irradiation of PEG-functionalized gold nanorods (λ_{max} = 800 nm). They employed a heat transfer model based on the Pennes' bioheat equation to estimate temperature distributions in 16 mm well plates containing evenly distributed nanorods. Samples were irradiated with a continuous wave (CW) laser (800 nm, spot size 2 mm, 20 W/cm^2, 15 min) and temperature was monitored at different positions using thermocouples. In the first experiment, the optical density of gold nanorods was varied from 0.065-0.50 and higher optical density resulted in greater increases in temperature up to 45ºC.[78] It is reasonable that increased concentration of nanorods would result in stronger light absorption and greater photothermal heating, but there is a limit to this effect in solution. Other researchers have demonstrated increased gold nanorod optical density can decrease light penetration, resulting in restricted depth to photothermal heating.[79] Both the experimental data and model predictions revealed that a steady-state temperature was reached within 20 min after irradiation. When thermocouples were placed 4 mm from the center of the well, and at the edge of the well, there was a difference in radial temperature (Figure 4.7a). This was in agreement with the prediction that the temperature would decrease further from the focused laser spot. NIR laser power also affected heating, and 8-32 W/cm^3 laser energies resulted in steady state temperatures from 36-60ºC. Photothermal heating of PC3-PSMA human prostate cancer cells was carried out. At a gold nanorod optical density of 0.2, increased laser irradiation times from 0-20 min greatly increased temperature (Figure 4.7b), and decreased cell viability (Figure 4.7c). Despite the spatial differences between the middle and edge of the wells, it was still possible to achieve high rates of cancer cell death due to the susceptibility of cancer cells to heating. In addition, there was strong agreement between the heat transfer model and experimental data. This demonstrated that models can be used to successfully predict the effects of nanoparticle concentration, laser power, and irradiation time on photothermal therapy.[78]

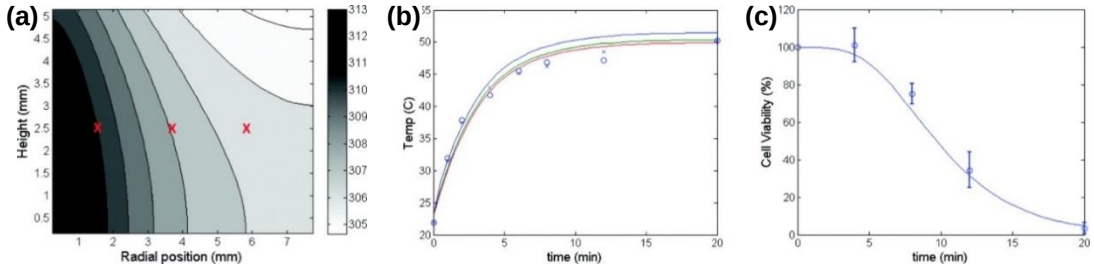

Figure 4.7 (a) Predicted spatiotemporal distribution after NIR irradiation within a well for gold nanorod optical density of 0.45. The temperature is reported in K, and approximate locations of thermocouples are shown by the red X's. (b) Temperature measurements (circles) and model predictions (solid lines) for a gold nanorod solution with 0.2 optical density. (c) PC3 cancer cell viability 24 h after different laser irradiation times (circles) and corresponding predictions (solid line) at 0.2 gold nanorod optical density. Adapted with permission from Reference 78. Copyright (2010) American Chemical Society.

Photothermal conversion efficiency (η) is the ratio of absorption to extinction and is used to describe the efficiency of the light-to-heat conversion. Recent simulation work has demonstrated that there is opportunity to optimize nanoparticle LSPR maximum for greater heating efficiency. Wang and coworkers[80] reported a systematic study of the photothermal conversion efficiency in gold nanorods. Temperature was directly monitored by inserting a thermocouple into an aqueous nanorod dispersion. Gold nanorods coated with the surfactant cetyltrimethylammonium bromide (CTAB) with widths 10-20 nm, lengths 20-65 nm and LSPRs ranging from 520-960 nm were prepared *via* seed-mediated growth. After CW laser irradiation (809 nm, 30 min) a temperature rise of 55ºC to 76ºC was observed when the LSPR was at 810 nm and therefore resonant with laser wavelength (Figure 4.8a). The temperature increase is 5ºC less when the LSPR was 50 nm blue-shifted or red-shifted from the laser wavelength (Figure 4.8b), and can be attributed to the decreased extinction and NIR absorption.[80] Interestingly, no matter the LSPR, all of the traces demonstrated a plateau after ~20 min of irradiation, the same trend observed by H.-C. Huang *et al.*[78]

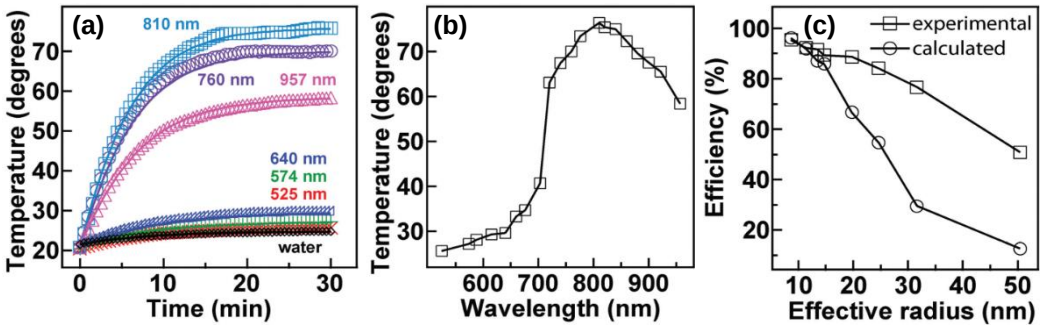

Figure 4.8 (a) Experimental (symbols) and calculated (solid lines) temperature traces for irradiated gold nanorod samples in pure water. The numbers indicate the longitudinal plasmon wavelengths of the nanorods. (b) Dependence of the final temperature on the longitudinal plasmon wavelength. The end temperature is the average of the last 5 points for each trace. (c) Dependence of the experimental and calculated photothermal conversion efficiency on nanoparticle radius. Adapted with permission from reference 80. Copyright (2010) John Wiley and Sons.

Heating efficiency *versus* volume was determined both experimentally and theoretically with gold nanorods and nanobipyramids having the same λ_{max} but different absolute dimensions (Figure 4.8c). Photothermal heating efficiency was experimentally determined to be the highest at 95% with 10x38 nm gold nanorods and lowest at 51% with 77x173 nm nanobipyramids.[80] We note that the maximum experimental photothermal conversion efficiency reported is 97-103% for 20 nm gold nanospheres which absorb at ~530 nm.[81] The authors determined that greater particle size/volume was generally correlated with decreased photothermal conversion efficiency, and this conclusion has been supported by other works.[80,82] The absorbance/scattering ratio is greatest in nanoparticles with smaller radii, so it follows that the nanoparticles with smaller volume were more efficient light converters.[17] However, as extinction is reduced with smaller nanoparticles, this effect may be limited.[83] Interestingly, in the FDTD simulations the photothermal conversion decreased from 96% to 13% so the effect of nanoparticle radius was more pronounced (Figure 4.8c). Potentially, the experimental efficiencies were higher due to scattering and

subsequent reabsorption in solution, which would increase with nanoparticle size. Nonetheless, the trend observed was similar to the experimental data, demonstrating the size effect in photothermal heating.[80]

The absorption cross-section and LSPR peak position are shape-dependent, and may therefore impact light to heat conversion and resulting tumor temperature. Several studies have experimentally investigated photothermal conversion efficiencies of gold nanoparticles of varying shapes and sizes.[84-90] The η values from some of these reports are listed in Table 4.2, and efficiency does vary quite a bit (22 – 100%). We note that these η values were not calculated *in vitro* or *in vivo*, and it is possible that exposure to physiological conditions would change aggregation state and potentially the LSPR of the nanoparticles. Potentially, some of the variation in these reported values is due to the different laser irradiation conditions and nanoparticle dose. However, unlike nanoparticle volume, there is no apparent trend with particle shape. It is difficult to compare efficiencies between studies due to the different experimental conditions; therefore, we cannot make a definitive statement on the optimum shape for heating. Because of this variation, we suggest it may be useful to calculate/estimate the photothermal conversion efficiency of a nanoparticle shape in a physiological environment before considering an application in photothermal therapy.

Table 4.2 Examples of experimentally determined photothermal conversion efficiencies (η), listed from highest to lowest, of gold nanoparticles of various shapes when excited at/near the λ_{max}.

Reference	Nanoparticle	Nanoparticle size	λ_{max}	Laser	η
Richardson[81]	Gold nanospheres	20 nm	-	0.28 W, CW laser, 532 nm	97-103%
Chen[80]	Gold nanorods	10x38 nm	810 nm	CW laser, 809 nm	95%
Huang[84]	Gold bellflowers	145x123x10 nm	~800 nm	1W/cm^2, 808 nm	74%
Zeng[85]	Gold nanocages	Edge length, 45 nm Wall thickness, 5 nm	805-810 nm	0.4 W/cm^2, 808 nm	64%
Ayala-Orozco[90]	Gold nanomatryoshkas	88 nm	783 nm	CW laser, 2 W/cm^2, 810 nm	63%
Cole[88]	Au/Au_2S nanoshells	50 nm	~810 nm	815 nm	59%
Santos[87]	Nanoporous gold disks	400 nm	~1100 nm	CW laser, 0.1 W/mm^2, 700-900 nm	56%
Cole[88]	Gold nanorods	13x44 nm	780 nm	815 nm	55%
Chen[80]	Gold nanobipyramids	77x173 nm	809 nm	CW laser, 809 nm	51%
Pattani[89]	Gold nanorods	7x26 nm	770 nm	2 W/cm^2, 808 nm	50%
Ayala-Orozco[90]	Gold nanoshells	152 nm	796 nm	CW laser, 2 W/cm^2, 810 nm	39%
Huang[86]	Biodegradable gold vesicles	207 nm	800 nm	1 W/cm^2, 808 nm	37%
Cole[88]	Au/SiO_2 nanoshells	154 nm	~815 nm	815 nm	30%
Zeng[85]	Gold hexapods	60 nm	~810 nm	0.4 W/cm^2, 808 nm	30%
Pattani[89]	Gold nanoshells	145 nm	780 nm	2 W/cm^2, 808 nm	25%
Zeng[85]	Gold nanorods	17x56 nm	~810 nm	0.4 W/cm^2, 808 nm	22%

The surface chemistry of gold nanoparticles is usually considered when attempting to increase tumor targeting or blood circulation times, but ligands may also affect thermal conductance. Within short time scales after laser irradiation (< 1000 ps), a change in the transient absorption signal of gold nanoparticles can be observed due an increase in temperature in the immediate surroundings of the nanoparticle. J. Huang *et al.*[91] measured thermal dissipation in gold nanorods using pump-probe transient absorption spectroscopy. Gold nanorods (12x56 nm, AR ~3.9, λ_{max} = 776 nm) were prepared with varied amounts of CTAB or coated with charged polyelectrolytes *via* layer-by-layer addition of negatively and positively charged polymers to investigate the effect of surface coating on photothermal heating. Transient absorption was measured following femtosecond pumping (785 nm, 1.5 mW, <0.5 ps pulses, 80 MHz) of aqueous gold nanorod dispersions. The thermal conductivity could be extracted from the change in transient absorption. Below the critical micelle concentration for CTAB (1 mM), the thermal conductivity of gold nanorods was 0.24 W/mK and decreased to 0.18 W/mK above 1 mM. Interestingly, thermal conductivity actually increased from 0.32 to 0.45 W/mK with multiple layers of poly(acrylic acid) but decreased from 0.58 to 0.53 W/mK with additional layers of polyallylamine hydrochloride. Together, these results suggested that greater water penetration within the CTAB bilayer or polymer layers increased thermal conductivity and heat capacity of gold nanorods and may play a role in photothermal heating efficiency.[91]

Strong laser irradiation can impact the physical dimensions of gold nanoparticles, sometimes resulting in melting and fragmentation. Altering the shape may affect gold nanoparticle optical properties and consequently photothermal heating ability.[92] Ungureanu *et al.*[93] investigated these changes in gold nanorods using pulsed lasers under different irradiation conditions. CTAB gold nanorods (λ_{max} = 713 nm or 810 nm) were irradiated at their transverse and longitudinal LSPRs (700 nm or 810 nm). Exposures were 1 min with a 10 Hz frequency and laser fluence ranged from 1-20 mJ/cm^2 per 6 ns pulse. It was possible to observe the “melting” of nanorods to nanospheres by simply monitoring the absorbance spectrum for a decrease in amplitude of the longitudinal LSPR as a function of time. In both types of gold nanorods the laser fluence threshold for 50% reshaping was 3.5 mJ/cm^2 and 6 mJ/cm^2 for 95% reshaping. The authors also investigated the impact of laser fluence on gold nanorods functionalized with the HER81 monoclonal antibody *via* a PEG linker. At 4.3 mJ/cm^2 there was only a small decrease in the amplitude of longitudinal LSPR, but the LSPR peak completely disappeared at 62 mJ/cm^2. Potentially, the antibody-functionalized gold nanorods were more resistant to reshaping due to higher heat diffusivity of the PEG chains compared to CTAB. HER2 positive SKBR3 human breast carcinoma cells were then incubated with gold nanorods for 24 h (18x10^9 nanorods/mL), but irradiation (700 nm, 20 mJ/cm^2 or 100 mJ/cm^2) did not cause any significant cell death. Instead, the energy of the absorbed laser pulses reshaped the nanoparticle crystals from a rods to a spheres. However, when the cells were irradiated with a 532 nm laser at the same conditions, significant cell death was observed, potentially due to plasmonic coupling and greater stability of the transverse plasmon band. This result revealed that laser settings can be adjusted to maintain nanoparticle optical properties.[93]

Simulated and experimental investigations into the effects of nanoparticle design and irradiation conditions demonstrate that photothermal heating can be quite complicated. Together, these reports suggest that nanoparticle characteristics such as volume, LSPR wavelength, surface ligand, and concentration affect photothermal heating efficiency and subsequent temperature changes. However, heating is also influenced by irradiation conditions including irradiation time, laser power, and laser wavelength. There does not appear to be a "silver bullet" in irradiation conditions for photothermal therapy, so scientists will likely have to investigate and optimize these parameters for maximum heating in any chosen physiological system.

4.5 MECHANISMS OF *IN VITRO* CELL DEATH DUE TO PHOTOTHERMAL TREATMENT

Traditional cancer hyperthermia results in thermal damage and temperatures in the extracellular matrix ranging from 41-48ºC. Cancer cell death from traditional hyperthermia can result from: damage to the cell membrane, denaturation of intracellular proteins, damage/impairment of RNA/DNA synthesis, changes in gene expression, and induction of cell death *via* apoptosis.[94] Heating may also increase susceptibility or sensitize cancer cells to other cancer treatments, including radiation and chemotherapy.[95] The effects of photothermal heating on cancer cells can be similar to traditional hyperthermia. However, as demonstrated by the ongoing debate in the literature between death by apoptosis or necrosis, one singular mechanism may not be sufficient to describe the effects of photothermal therapy with gold nanoparticles.[96] Apoptosis, also called programmed cell death, is characterized by membrane blebbing, nuclear fragmentation and apoptotic body formation. The apoptotic bodies are eventually recognized by the immune system and are removed by phagocytes. Necrosis, originally thought to be a more passive form of cell death, results from toxicity or damage and is characterized by membrane collapse, cell swelling, resulting in rupture and release of the cellular contents.[97] The following reports in this section on observed mechanisms of cell death after photothermal therapy are summarized in Table 4.3.

A report by Tong *et al.*[98] investigated the mechanism of photothermal injury to malignant KB cells *in vitro* using folate-functionalized gold nanorods (length 46.5 nm, AR 3.7, λ_{max} = 765 nm). Cells were incubated with the gold nanorods for 6 h to maximize binding to cellular surfaces or 17 h to ensure intracellular delivery to the perinuclear region. CW laser irradiation (765 nm, 6-60 mW, 81.4 s) was carried out to induce photothermal damage. Interestingly, the cells with internalized gold nanorods required 60 mW laser intensity *versus* only 6 mW for surface-bound nanorods. This demonstrated that nanoparticle location in or on cells was a critical factor in the success of photothermal heating, with the surface-bound gold nanorods being the more effective photothermal transducers. Ethidium bromide staining revealed that cell death was due to membrane cavitation by gold nanorods. Furthermore, actin staining demonstrated disruption of actin filaments by an influx of extracellular Ca^{2+}, resulting in extensive membrane blebbing.[98] Blebbing is the result of disruption of the connections between the cell membrane[99] and cytoskeleton and was proposed to be the cause of cell death *via* apoptosis.[98]

X. Huang *et al.*[100] investigated how targeting gold nanoparticles to specific locations inside cancer cells affected photothermal treatment. Gold nanospheres (30 nm, λ_{max} = 526 nm) were functionalized with an arginine-glycine-aspartate peptide (RGDRGDRGDRGDPGC) to bind alpha v beta 3 integrin receptors and localize in the cytoplasm, or the nuclear localization sequence (GGGPKKKRKVGG) peptide to target the cell nucleus. Human oral squamous cell carcinoma (HSC-3) cells were incubated with the nanoparticles for 24 h, and then irradiated using a CW laser (514 nm, 25 W/cm^2, 5 min) or a nanosecond-pulsed laser (532 nm, 0.3-0.8 mJ, 6-7 ns). The energy threshold to induce cell death with pulsed lasers was 0.3 mJ for nuclear-targeted and 0.8 mJ for cytoplasm-targeted gold nanoparticles. In contrast, the energy threshold for cell death using CW laser irradiation was 210 J for nuclear-targeted and 60 J for cytoplasm-targeted nanoparticles. Potentially, the nanoparticles were distributed more evenly in the cytoplasm but were more aggregated at the nucleus. Non-linear absorption of aggregated gold nanoparticles may have enhanced the heating efficiency of pulsed lasers at the nucleus whereas slower CW laser heating was more effective in the cytoplasm. The researchers then stained the treated cells to determine the pathway of cell death. In nucleus-targeted cells, CW irradiation exhibited signs of early apoptosis, followed by necrosis while pulsed laser irradiation triggered only necrosis due to immediate cell death. In cytoplasm-targeted targeted cells, apoptosis was observed with CW irradiation at energies below 120 J, but necrosis with pulsed lasers or at CW energies higher than 120 J. This demonstrates that the effects of location and heating method are quite complex and may affect cell death mechanisms in photothermal therapy.[100]

J.-L. Li *et al.*[101] also varied laser energy during photothermal heating of gold nanorods. Gold nanorods (AR 4.0, λ_{max} = 795 nm) were functionalized with transferrin to target transferrin receptors which are overexpressed in rapidly dividing cancer cells. Then, the particles were incubated with HeLa cervical cancer cells for 6 h. Cells were irradiated with a femtosecond pulsed scanning laser (800 nm, 13.9-55.6 W/cm^2) and stained with Annexin V-Cy3.18 and propidium iodide to indicate apoptotic or necrotic cell death, respectively. At a laser power of 27.8 W/cm^2, 10 scans were sufficient to induce apoptosis was observed, while 30 scans resulted in necrosis. However, at 13.9 W/cm^2 and 9.5 W/cm^2, cell death was caused only by apoptosis. Increasing power to 55.6 W/cm^2 resulted in necrosis after only 1 scan. This suggested that laser power could be used to influence pathways of cell death.[101]

C.-L. Chen *et al.*[102] monitored cancer cells in real-time to better understand changes in cellular morphology that occur during photothermal heating. Gold nanorods (AR 3.9, λ_{max} = 800 nm) were functionalized with the negatively charged polyelectrolyte polystyrene sulfonate to enhance nanorod biocompatibility. EMT-6 breast cancer cells were incubated with gold nanorods overnight to facilitate cellular uptake into the endosomes or lysosomes. Endocytosis resulted in the uptake of a few hundred to a few thousand nanorods per cell. Irradiation with a femtosecond pulsed laser (790 nm, 0.5 ms) seemed to explode the lysosomes in the cells, but interestingly, cell death was not immediate. Photothermal treatment caused a great amount of cell damage due to the formation of 10 μM cavities, and then led to rupture of the plasma membrane. Subsequent intracellular responses eventually resulted in death of the cells within

4 min of laser irradiation at 185 W/cm^2 and 222 W/cm^2 (Figure 4.9). The authors proposed that cell death was mainly the result of oncosis (Ischemic cell death) due to sudden swelling.[102]

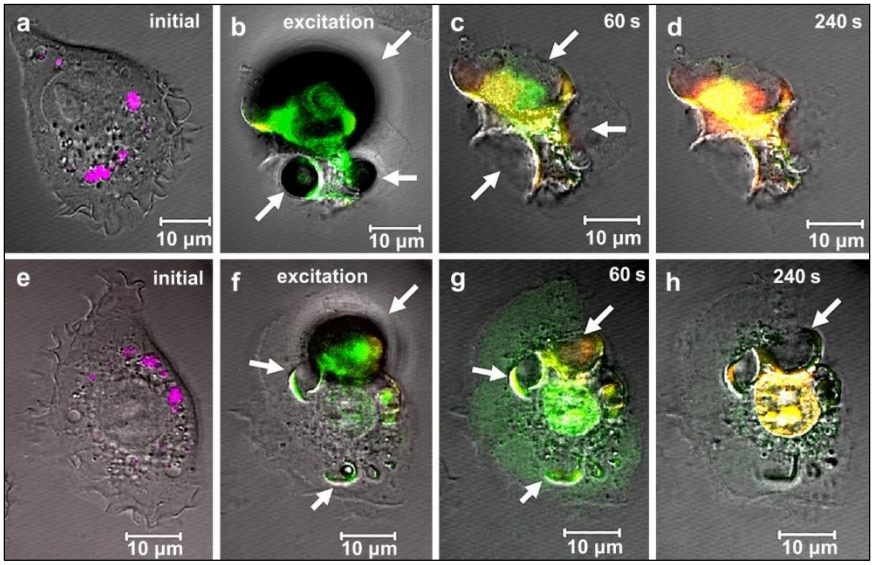

Figure 4.9 Images of EMT-6 tumor cells at various time-points during photothermal heating by polyelectrolyte-coated gold nanorods at (a-d) 222 W/cm^2 or (e-h) 185 W/cm^2 laser power. Location of gold nanorods was observed using two-photon photoluminescence and are indicated by the purple dots, but disappear after irradiation due to gold nanorod "melting". YOPRO-1 (green stain), indicates increased cell membrane permeability and propidium iodide (red stain) is indicative of cell death. Arrows represent the formation of characteristic cavities due to photothermal damage. Adapted with permission from Reference 102. Copyright (2010) Elsevier.

A recent report by Pérez-Hernández *et al.*[103] examined the cellular pathways which lead to apoptotic cell death *via* photothermal heating using triangular gold nanoprisms. The gold nanoprisms (λ_{max} = 1080 nm) were functionalized with glucose to enhance uptake into cell lysosomes *via* carbohydrate receptors. SV40-transformed murine embryonic fibroblasts (MEF cells) were exposed to the nanoprisms overnight and upon CW irradiation (1064 nm, 5 W/cm^2, 10 min) a temperature rise by 13ºC was observed and resulted in 58% cell death. Cells were stained with Annexin V and 7-Aminoactinomycin D, used to recognize apoptosis or necrosis, respectively. Their results suggested that under these experimental conditions, MEF cell death was first driven by apoptosis, and then secondary necrosis, but could also be regulated by irradiation duration and intensity. For example, only apoptosis was observed in cells irradiated for 30 s at 5 W/cm^2, but only necrosis was observed in cells irradiated for 2 min at 30 W/cm^2. Further investigation of apoptotic cell death was carried out by examining biomarkers of cellular pathways. The expression of heat shock proteins was detected using Western blot in photothermally treated cells. In addition, mitochondrial outer membrane permeabilization and activation of the protein caspase-3 indicated that apoptosis was intrinsic/mitochondrial. Apoptosis was initiated by Bid activation *via* lysosomal disruption (Figure 4.10).[103] These authors, and others,[104] suggested that because apoptosis does not cause inflammation, and is a

more efficient and a “cleaner” form of cell death compared to necrosis, photothermal treatments should be designed to trigger apoptosis.

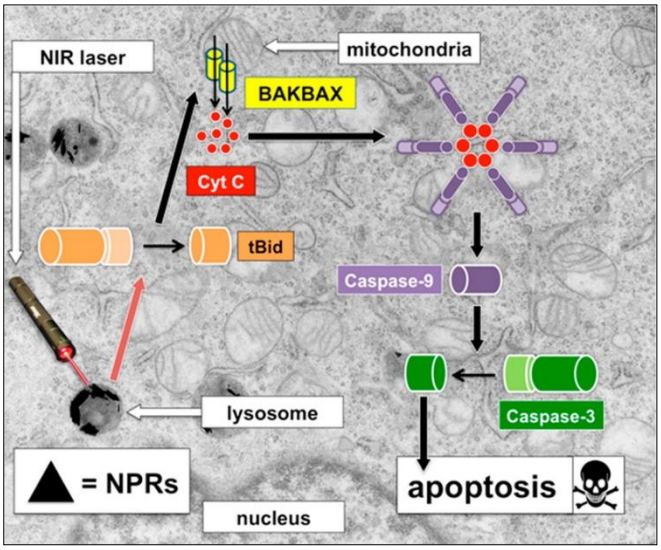

Figure 4.10 Proposed mechanism of apoptosis resulting from laser irradiation of MEF cells incubated with gold nanoprisms. MEF cells were irradiated with an unfocused laser beam for 4 min produce apoptosis *via* activation of Bid. Activation of the pro-apoptotic BH3-only protein Bid leads to oligomerization of Bak and/or Bax in the outer mitochondrial membrane, which forms a pore allowing the release from the intermembrane space of molecules including cytochrome c. This interacts with Apaf-1, dATP and pro-caspase 9, forming a complex termed apoptosome that facilitates the activation of caspase 9 and consequently downstream executioner caspases-3, -6, or -7, which ultimately are responsible for apoptotic cell death. Adapted with permission from Reference 103. Copyright (2015) American Chemical Society.

Due to the great variation in methods of nanoparticle delivery, dosing and irradiation conditions in photothermal treatment, the cellular responses to photothermal therapy seem to also vary. These particular studies demonstrated that photothermal treatment may result in cancer cell death *via* apoptosis or necrosis, but oncosis has also been observed. Higher laser powers, and pulsed lasers appeared to trigger necrosis while lower laser powers and continuous wave lasers resulted in apoptosis. Heating with continuous wave lasers, resulting in apoptosis, is the same mechanism observed in traditional hyperthermia. This may potentially be due to similar changes in temperature near cancer cells, which would be influenced by heating conditions. However, gold nanoparticle location on the surface, in the cytoplasm or at the cell nucleus also influenced photothermal therapy. Further investigations into the effect of irradiation conditions are required to gain a more complete picture of what influences each pathway. One avenue not yet explored is the effects of cancer cell type on the mechanism of death. Differences between death mechanisms in cancer cell types may also be due to the elevation of heat shock proteins, and may greatly affect the success of thermal therapy. If scientists are better able to understand the mechanisms and pathways that lead to cell death in a specific type of cancer, photothermal heating conditions can potentially be tailored to enhance the success of cancer treatment.

Table 4.3 Summary of references investigating the effect of photothermal therapy on the mechanism of cancer cell death.

Reference	Nanoparticle	Dose and exposure	Cell line	NIR conditions	Cell death	Death mechanism
Tong[98]	Folate-functionalized gold nanorods, λ_{max} = 765 nm	0.02 nM, 6 h (surface) or 17 h (internalized)	KB cells	CW laser, 765 nm, 6-60 mW, 81.4 s	6 mW with surface-bound nanorods and 60 mW with internalized nanorods	Apoptosis
X. Huang[100]	Peptide-functionalized gold nanospheres, λ_{max} = 526 nm	0.2 nM, 24 h	HSC-3	CW laser, 514 nm, 25 W/cm^2, 5 min	210 J to cause death with nucleus-targeted nanospheres and 60 J to cause death with cytoplasm targeted nanospheres	Apoptosis and necrosis
X. Huang[100]	-	-	-	Pulsed laser, 532 nm, 0.3 or 0.8 mJ, 6-7 ns	0.3 mJ to cause death with nucleus-targeted nanospheres and 0.8 mJ to cause death with cytoplasm-targeted nanospheres	Necrosis
J.-L. Li[101]	Transferrin-functionalized gold nanorods, λ_{max} = 795 nm	0.5 nM, 6 h	HeLa	Pulsed laser, 800 nm, 13.9-55.6 W/cm^2	Cell death with 10 scans at 27.8 W/cm^2 or 1 scan 55.6 W/cm^2	Apoptosis or necrosis
C.-L. Chen[102]	Polyelectrolyte-functionalized gold nanorods, λ_{max} = 800 nm	A few thousand to a few hundred per cell, overnight	EMT-6	Femtosecond pulsed laser, 790 nm, 0.5 ms	Cell death at 185 W/cm^2	Oncosis
Pérez-Hernández[103]	Glucose-functionalized gold nanoprisms, λ_{max} = 1080 nm	-	MEF	CW laser, 1064 nm, 5 W/cm^2, 10 min	58% cell death	Apoptosis then necrosis

4.6 RECENT NANOPARTICLE DESIGNS FOR *IN VITRO* PHOTOTHERMAL TREATMENT

There has been a great deal of interest in modifying gold nanoparticle surface chemistry for more selective cancer cell targeting and enhanced photothermal destruction. The following reports in this section describing some of recent advancements in gold nanoparticle design for *in vitro* photothermal treatment (Tables 4.4 and 4.5). Van de Broek *et al.*[105] prepared branched gold nanoparticles (60 nm, λ_{max} = 628 nm) functionalized with anti-HER2 and anti-PSA nanobodies. Nanobodies are the small antibody fragments (~15 kDa) that bind antigens, and research has suggested that minimizing domain size increases target affinity. Flow cytometry revealed anti-HER2 nanoparticles were successful in binding to HER2 positive SKOV3 ovarian cancer cells but not to HER2 negative CHO cells. In addition, anti-PSA nanoparticles (negative control) exhibited little non-specific binding to SKOV3 cells. Laser irradiation (690 nm, 38 W/cm^2, 5 min) of SKOV3 cells incubated with anti-HER2 nanoparticles resulted in a 28ºC temperature increase and cell death. Under these same conditions, no death was observed in the negative control.[105] Yuan *et al.*[106] successfully targeted 50 nm gold nanostars to cancer cells using the TAT cell-penetrating peptide (CPP). CPPs are chains of 30 or less amino acids that facilitate transport across cellular membranes and enhance nanoparticle intranuclear cellular delivery *via* macropinocytosis. Enhanced uptake of functionalized gold nanostars into BT549 breast cancer cells was observed compared to bare or PEG-functionalized nanostars (Figure 4.11) within 1 h of exposure. Extremely low pulsed laser irradiation (850 nm, 0.4 W/cm^2, 3 min) of BT549 cells incubated with the TAT gold nanostars was sufficient to cause significant cell death, and no cell damage was observed in the controls. Even lower irradiation (0.2 W/cm^2) resulted in some cell death.[106]

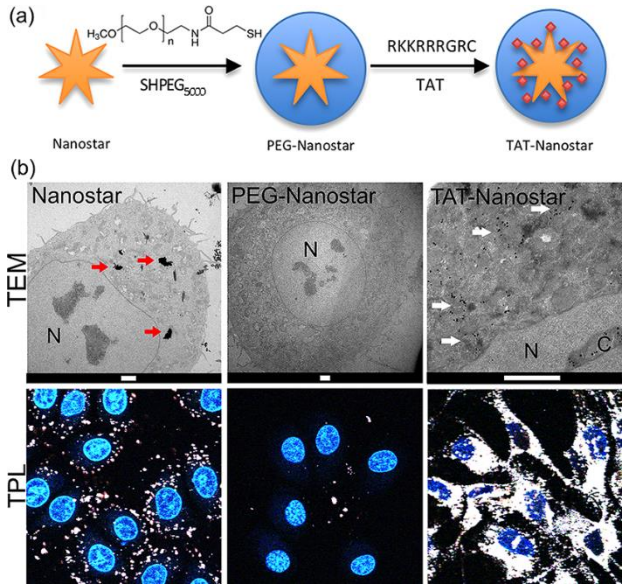

Figure 4.11 (a) Schematic for TAT coating on gold nanostars. Bare nanostars were coated with PEG, then with cysteine-terminated TAT. (b) Transmission electron microscopy images demonstrating cellular uptake of 0.1 nM bare (red arrows), PEG-functionalized (no uptake) and TAT-functionalized (white arrows) gold nanostars into BT549 cells. N = cell nucleus, C = nuclear cleft and scale bars = 2 μm. TPL (two-photon luminescence) images of 125x125 μm^2 area of BT549 cells. White patterns represent locations of gold nanostars. Adapted with permission from Reference 106. Copyright (2012) American Chemical Society.

Ali *et al.*[107] demonstrated enhanced photothermal therapy of two sizes of gold nanorods (3.5x17 nm or 10x47 nm) functionalized with the targeting agent rifampicin. Rifampicin is actually an antibiotic but was observed to enhance internalization of gold nanorods into the endosomes of HSC human squamous carcinoma cells. Photothermal heating of the smaller gold nanorods resulted in ~80% cell death *versus* ~35% without rifampicin. The larger gold nanorods were somewhat less efficient with ~65% cell death with rifampicin and ~20% cell death without it. Nevertheless, rifampicin enhanced photothermal heating. Together, these three studies demonstrate how innovative surface functionalization may be effective in enhancing photothermal therapy *via* targeted uptake of gold nanoparticles into cells.[107]

Researchers have also explored multifunctional nanocomposites containing gold nanoparticles *in vitro* to impart cell imaging or diagnostic functionalities in addition to photothermal treatment. Qian *et al.*[108] reported a preparation of 70-80 nm gold-decorated $NaYF_4$:Yb,Er/$NaYF_4$/silica core/shell/shell nanocomposites for photothermal therapy and imaging *via* upconversion fluorescence. The addition of the silica shell reduced fluorescence emission quenching by the gold shell. The nanocomposites (λ_{max} ~ 500-560 nm) were incubated with SK-N-BE(2)-C human neuroblastoma cells and then irradiated with a CW laser (980 nm, 20W/cm^2, 20 min). Photothermal heating resulted in a temperature increase of 9ºC and 67.5% cancer cell death compared to only a 4ºC increase and 9.4% cell death in silica-gold nanocomposites without the upconverting core. Potentially, heating was enhanced because green emission from the upconverting core was absorbed by the plasmonic particles.[108] Wu *et al.*[109] combined photothermal therapy with surface-enhanced Raman scattering (SERS) for cancer detection. The researchers prepared 100-120 nm gold-silver bimetallic nanoparticles functionalized with the S2.2 aptamer to target MUC1 receptors on MCF-7 breast cancer cells. The nanoparticles were surrounded by a gold shell which prevented potential silver toxicity and the combination of gold and silver in the core enabled SERS of the Raman reporter Rh6G for MCF-7 cell detection. Targeting studies demonstrated enhanced nanoparticle uptake by MCF-7 cells, but little binding to HEPG2 liver cancer cells or MCF-10A breast cancer cells. Subsequent low power laser irradiation (808 nm, 0.06-0.25 W/cm^2, 60 min) of these bimetallic particles resulted in 97% breast cancer cell death.[109] Ke *et al*.[110] prepared 2.3 μm gold-nanoshelled polymeric microcapsules containing ultrasound-responsive poly(lactic) acid. Enhancement of kidney ultrasound contrast imaging in New Zealand white rabbits were observed after injection of the microcapsules. In addition, NIR laser irradiation (808 nm, 4 W/cm^2, 10 min) of HeLa cervical cancer cells incubated with the particles resulted in 80% cell death due to photothermal damage. No cell death was observed after irradiation of cells without the microcapsules, indicating that laser irradiation did not damage cells.[110] Khan *et al.*[111] prepared single-walled carbon nanotubes decorated with gold nanocages for enhanced confocal fluorescence imaging. The hybrid materials were functionalized with the A9 RNA aptamer to target prostate-specific antigen on LNCaP human prostate cancer cells and then exposed to NIR irradiation (1064 nm, 1-2 W/cm^2, 10 min). Photothermal heating resulted in 95% cancer cell death at 2 W/cm^2 for LNCaP cells versus ≤10% cell death in PC-3 or HaCAT which do not over express prostate-specific antigen. Confocal fluorescence imaging showed a

similar selectivity in binding.[111] Together, these examples demonstrate the potential imaging versatility and multifunctionality when other nanostructures are combined with gold to form nanocomposites.

Targeted delivery of chemotherapeutic drugs to tumors using nanoparticles is of widespread interest in the cancer community due to the undesirable side effects of conventional cancer treatments.[112] When drug delivery is combined with photothermal therapy, there is potential to design optically responsive drug release systems and/or to have a synergistic effect on cancer treatment.[9] X. Yang *et al*.[113] used 60 nm mesoporous silica-coated gold nanorods (AR 3.8, λ_{max} ~800 nm) carrying the well-known chemotherapeutic drug doxorubicin (DOX) for light-triggered photothermal chemotherapy. DOX was loaded into the pores, and the silica surface was functionalized with the AS1411 DNA aptamer to target nucleolin receptors on MCF-7 breast cancer cells. Some cytotoxicity (20%) was observed when the DOX-loaded gold nanorods were incubated with the cells, indicating that some DOX leaked out. NIR irradiation (808 nm, 1.2 Wcm^2, 10 min) triggered dehybridization of the DNA aptamers and resulted in greater DOX release. Over 90% of MCF-7 cells were killed by the DOX-gold nanorods, much higher than the 5% with nanorods alone or 40% with DOX alone.[113]

Shi *et al.*[114] designed pH-responsive ligands to trigger DOX release from 50 nm porous gold nanocages. The pores in carboxylate-functionalized, DOX-loaded nanocages were blocked with 10 nm calcium phosphate-coated iron oxide nanoparticles. The calcium phosphate could be dissolved after internalization of the nanocages in an acidic endosome environment, triggering DOX release (Figure 4.12a). DOX release was further enhanced by NIR light (808 nm, 1 W, 5 min) and resulted in 47% cell death *versus* 15% with nanocages alone or 23% with DOX alone (Figure 4.12b).[114]

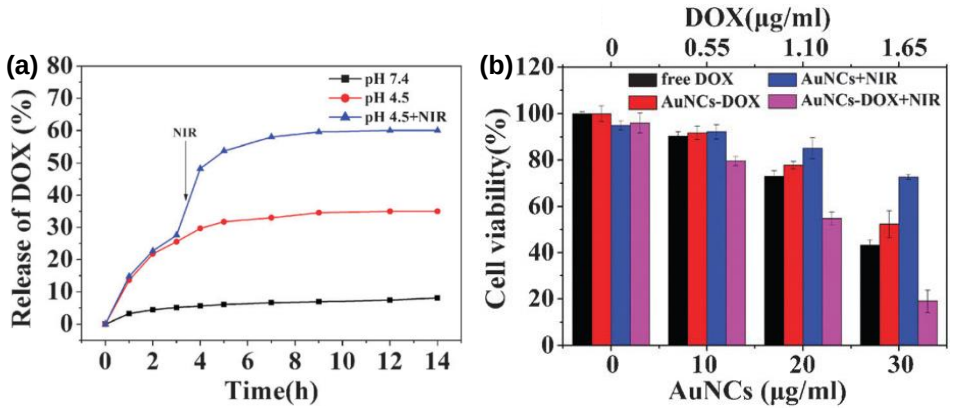

Figure 4.12 (a) Release kinetics of DOX from DOX-loaded gold nanocages in PBS buffer at pH 7.4 and 4.5 with or without 808 nm laser irradiation. (b) MCF-7 cell viability after a 24 h incubation with different concentrations of free DOX, gold nanocages (AuNCs) with NIR irradiation and DOX-loaded AuNCs with or without NIR irradiation. Adapted with permission from Reference 114. Copyright (2012) Royal Society of Chemistry.

Ma *et al.* [115] incorporated gold nanoshells, DOX and magnetic nanoparticles into 272 nm nanomicelles made from cholesteryl succinyl silane. In the presence of a magnetic field, laser photothermal heating (808

nm, 4 W/cm^2, 10 min) triggered micelle collapse and resulted in a 90% reduction in viability of HeLa cells compared to 65% with gold alone or 20% with DOX alone.[115] Each of these reports demonstrate that cancer cell death can be enhanced when photothermal heating is combined with chemotherapy. It is possible that enhanced cell death is due to sensitization of cells after heat treatment, rendering them more susceptible to chemotherapeutics.[28] If this is the case, then combination drug/heat therapy may be useful in cancer treatment.

Other researchers have combined photothermal therapy with photodynamic therapy (PDT) to enhance cancer cell death. Photosensitizers are usually tetrapyrrole structures with absorption peaks 600-800 nm, and are clinically approved for cancer treatment. When oxygen is present, excitation of photosensitizers at their absorbance maxima can result in the generation of reactive oxygen species such as cytotoxic singlet oxygen ($^1O_2$). This often results in cell death *via* apoptosis or necrosis due to damage to nearby cells, and tumor vasculature.[116] L. Gao *et al.*[117] incorporated the photosensitizer hypocrellin into lipid vesicles and used them to coat 45 nm gold nanocages (λ_{max} = 800 nm). Femtosecond pulsed laser irradiation (790 nm, 85.5 pJ/pulse, 300 s) was carried out at the two-photon absorbance maximum for hypocrellin. Combination photothermal/photodynamic therapy resulted in 83% death of HeLa cells *versus* 35% with hypocrellin alone or 45% with gold nanocages alone.[117] Wang *et al.*[118] functionalized gold nanorods (AR 3.3, λ_{max} ~ 750 nm) with an aptamer switch probe linked to the photosensitizer chlorin e6. The aptamer, sgc8, could bind to the protein tyrosine kinase-7 on CCRF-CEM acute lymphoblastic leukemia T-cells. Chlorin e6 has absorbance maxima at 397, 510 and 664 nm. Irradiation with white light (2 h), and then a NIR laser (812 nm, 10 min) resulted in a temperature increase from 25ºC to 55ºC and 60% cell death with chlorin e6-loaded nanorods. This was more effective compared to 20% with chlorin e6 alone or 37% with gold nanorods alone.[118] Kuo *et al.*[119] incorporated the hydrophilic photosensitizer indocyanine green onto anti-EGFR antibody-functionalized 100 nm gold nanospheres. Indocyanine absorbance max is around 800 nm, and could therefore sensitize oxygen by NIR light. Laser irradiation (808 nm, 20 W/cm^2, 2 min) resulted in over 90% cell death of A549 adenocarcinoma cells versus 20% with indocyanine green alone.[119] Together, these examples, the combination of photodynamic therapy with photothermal therapy resulted in greater cell death than with separate treatments.

In vitro photothermal treatment of cancer has progressed in many directions in the last several years. Innovative gold nanoparticle ligands have been developed for more efficient cell targeting, and photothermal therapy has been combined with cell imaging/diagnosis, chemotherapy and photodynamic therapy for more effective cancer treatment. Further investigation with nanoparticle design will likely produce even more avenues for multifunctionality in gold nanoparticle-mediated photothermal therapy. The *in vitro* studies described here used 2D cell culture which is a rapid way to screen potential therapies; however, 2D cultures may not adequately represent *in vivo* cell-cell and cell-matrix interactions. We anticipate that future *in vitro* studies of photothermal therapy will include 3D cell culture such as hydrogels or spheroids. 3D cell culture may be a better way mimic *in vivo* environments and a good next step in evaluating the effectiveness of these photothermal therapies.[120,121]

Table 4.4 Summary of references on the recent advancements in nanoparticle design with targeting agents or imaging agents for *in vitro* photothermal therapy.

Reference	Nanoparticle	Dose and exposure	Cell line	NIR conditions	Results
Van de Broek[105]	Anti-HER2 nanobody-functionalized branched gold nanoparticles, λ_{max} = 628 nm	optical density 1-6, 1 h	SKOV3	CW laser, 690 nm, 38 W/cm^2, 5 min	Optical density 1-2 no cell death, optical density 4-6 induced significant cell death
Yuan[106]	TAT peptide-functionalized gold nanostars	0.3 nM, 4 h	BT549	Pulsed laser, 1 mW, 12.5 pJ/pulse, 0.4 W/cm^2, 3 min	Significant cell death at 0.4 W/cm^2, some cell death at 0.2 W/cm^2
Ali[107]	"Small" and "big" rifampicin-functionalized gold nanorods, λ_{max} ~770 nm	0.1 nM, 0.5-24 h	HSC	CW laser, 808 nm, 2 min	"Small" ~80% cell death with or ~35% cell death without rifampicin and "big" ~65% cell death with or ~20% cell death without rifampicin
Qian[108]	Gold-decorated NaYF4:Yb,Er/NaYF4/silica core/shell/shell upconversion nanocomposites, λ_{max} ~ 500-560 nm	120 µg/mL, 15 min	SK-N-Be(2)-C	CW laser, 980 nm, 20W/cm^2, 20 min	67.5 % cell death with upconverting/silica/gold composite and 9.4% cell death with silica/gold composite
Wu[109]	Aptamer-functionalized gold-silver bimetallic nanoparticles, λ_{max} ~ 580 nm	30 min	MCF-7	CW laser, 808 nm, 0.06-0.25 W/cm$^{2'}$, 60 min	No death at 0.06W/cm^2, 25% cell death at 0.13W/cm^2, 46% cell death at 0.19 W/cm^2, 97% cell death at 0.25W/cm^2
Ke[110]	Gold-nanoshelled polymeric microcapsules λ_{max} ~ 650-900 nm	0.05-0.5 mg/mL	HeLa	CW laser, 808 nm, 4 W/cm^2, 10 min	40% cell death at 0.05 mg/mL, 80% cell death at 0.5 mg/mL
Khan[111]	Aptamer-functionalized single-walled carbon nanotubes decorated with gold nanocages, λ_{max} ~ 800 nm	24 h	LNCaP	CW laser, 1064 nm, 1-2 Wcm^2, 10 min	95% LNCaP cell death at 2 W/cm^2 and ≤10% cell death without aptamer functionalization

Table 4.5 Summary of references on the recent advancements in nanoparticle design with chemotherapeutics or photosensitizers for *in vitro* photothermal therapy.

Reference	Nanoparticle	Conjugated drug or photosensitizer	Dose and exposure	Cell line	NIR conditions	Results
X. Yang[113]	Aptamer-functionalized, mesoporous silica-coated gold nanorods, λ_{max} ~ 800 nm	Doxorubicin, 38 μg/mg nanorods (DOX)	0.05-0.4 mg/mL, 4 h	MCF-7	CW laser, 808 nm, 1.2 W/cm^2, 10 min	Nanorods + DOX = 97% cell death, nanorods alone = 5% cell death, DOX alone = 40% cell death
Shi[114]	Porous gold nanocages with pH-responsive carboxylate ligands	DOX, 1.1 μg/mL	20 μg/mL, 24 h	MCF-7	CW laser, 808 nm, 1 W, 5 min	Nanocages + DOX = 47% cell death, nanocages alone = 15% cell death, DOX alone = 23% cell death
Ma[115]	Nanomicelles containing gold nanoshells and magnetic nanoparticles, λ_{max} ~ 650-900 nm	DOX, 5 μM	0.01-0.2 mg/mL	HeLa	CW laser, 808 nm, 4 W/cm^2, 10 min	Nanomicelles + DOX = 90% cell death, nanomicelles alone = 65%, DOX alone = 20%
L. Gao[117]	Gold nanocages coated with lipid vesicles, λ_{max} = 800 nm	Hypocrellin B, absorbance at 790 nm, 7 μM	35 pM, 6 h	HeLa	Femtosecond pulsed laser, 790 nm, 85.5 pJ/pulse, 300 s	Nanocages + hypocrellin = 82.6% cell death, nanocages alone = 45.5%, hypocrellin alone = 35.4%
Wang[118]	Aptamer-functionalized gold nanorods, λ_{max}~ 750 nm	Chlorin e6 (Ce6), absorbs white light	0.2 nM, 2 h	CCRF-CEM	White light (2 h) then CW laser, 812 nm, 10 min	Gold nanorods + Ce6 = 60% cell death, gold nanorods alone = 37% cell death, Ce6 alone = 20%
Kuo[119]	Anti-EGFR functionalized gold nanospheres	Indocyanine green (ICG), absorbance at 800 nm, 3.7 mM	12 h	A549	CW laser, 808 nm, 20 W/cm^2, 2 min	Gold nanospheres + ICG = 90% cell death, ICG alone = 20% cell death

4.7 RECENT NANOPARTICLE DESIGNS FOR *IN VIVO* PHOTOTHERMAL TREATMENT

In vivo animal studies are commonly the next step after *in vitro* experiments toward advancing gold nanotherapeutics for clinical use. The following reports in this section describing recent advancements in nanoparticle design for *in vivo* photothermal therapy are summarized in Tables 4.6 and 4.7. Recently, researchers have demonstrated combined photothermal therapy and imaging/diagnosis *in vivo* using multifunctional nanocomposites. Jin and coworkers[122] designed 300 nm PEG-coated gold nanoshelled perfluorooctoylbromide nanocapsules for photothermal therapy and bimodal contrast imaging *via* ultrasound and X-ray computed tomography. The authors were able to enhance contrast in U87 human glioblastoma tumor bearing nude mice and photothermal heating (808 nm, 1.3 W/cm^2, 10 min) resulted in a 35ºC temperature increase and decreased tumor volume by 68% after 16 days.[122] Y. Gao *et al.*[123] prepared 150 nm nanomatryoshkas (λ_{max} = 780 nm), multilayered nanoshell structures of alternating layers of gold and silica for SERS. Thermal imaging of MDA-MB-231 breast cancer tumors in mice revealed tumor temperatures increased by 33ºC after NIR irradiation (808 nm, 2 W, 5 min), more than sufficient for tumor destruction. In addition, enhanced Raman signals of the Raman reporter 4-mercaptobenzoic acid in the tumor region demonstrated the potential for SERS for tumor detection.[123] A. Lin *et al.*[124] combined T2 magnetic resonance imaging (MRI) and photothermal heating using 60 nm PEG-functionalized gold nanoshells containing Fe_3O_4/Ag cores (λ_{max} = 800 nm). B16-F10 melanoma tumors were implanted in C57BL/6 mice and could be detected by MRI when the nanoparticles were present. Photothermal treatment (808 nm, 4 W/cm^2, 30 s) resulted in complete elimination of the tumor after 13 days when the nanoshells were injected directly into the tumor. However, treatment only slowed growth when the nanoparticles were injected intravenously.[124] Sun *et al.*[125] successfully radiolabeled 25 nm arginine-glycine-aspartic acid peptide-modified gold nanorods with ^{64}Cu. Radionuclide-based positron emission tomography imaging in U87 human glioblastoma tumor bearing Athymic nude mice revealed that it was possible to determine *in vivo* nanoparticle biodistribution. Tumor temperature increased by 27ºC and tumor size decreased by 50% after photothermal treatment.[125] Together, these examples demonstrate the potential versatility of multifunctional gold nanoparticles for *in vivo* diagnostic imaging and photothermal therapy. Systems such as these may be beneficial for clinical application because therapy can be limited to the detected diseased area, potentially preventing side-effects associated with part or whole-body treatments.

Photothermal chemotherapy of gold-drug nanoconjugates has also been employed *in vivo* to enhance tumor destruction. H. Liu *et al.*[126] prepared 160 nm gold nanoshelled silica nanorattles (λ_{max} ~ 810 nm) containing the chemotherapeutic Docetaxil and then functionalized them with transferrin. Balb/c mice having MCF-7 tumors were treated with the functionalized gold nanoshells and NIR light (808 nm, 2 W/cm^2, 3 min) demonstrated a tumor temperature increase by 15.2ºC. Tumor volume was measured under several treatment conditions but complete tumor regression was only observed in the group treated with NIR light and targeted gold nanoshells containing Docetaxil. This treatment was more effective compared to the drug alone, nanoparticles alone or nanoparticles without transferrin which all exhibited increased tumor volumes (Figure 4.13).[126] Shao *et al.*[127] functionalized 33 nm gold nanospheres (λ_{max} = 535-540 nm) with PEG and

TNF-α. Pulsed laser irradiation (690 nm, 1 J/cm^2, 1 min) resulted in suppression of tumor growth in A/J mice with SCK mammary cancer tumors after 7 days *versus* 3-7 fold volume increases in all of the control groups. The authors also carried out photothermal treatment at the λ_{max} with a 532 nm laser, but observed inflammation in the surrounding tissues, an undesirable side effect.[127] Nam *et al.*[128] designed 10 nm gold nanospheres (λ_{max} = 535-540 nm) with pH-responsive ligands covalently linked to DOX *via* carbodiimide coupling. In the acidic tumor environment DOX release was triggered *via* hydrolysis. Also, the negatively charged surfaces were converted to a mixture of charges, reducing electrostatic repulsion, and resulted in rapid nanoparticle aggregation and a broadening/red-shift in the LSPR to ~650 nm. Laser irradiation (660 nm, 0.5 W/cm^2, 5 min) in nu/nu nude mice having B16-F10 melanoma tumors, demonstrated tumor temperature increases of 15ºC and tumor growth was halted. This was more effective than DOX or nanoparticles alone, which only slowed tumor growth.[128] These examples reveal that combination photothermal chemotherapy treatment can also be synergistic and effective *in vivo* for tumor destruction. Further work to maximize drug conjugation and better control release rates *in vivo* may serve to increase their potential for clinical application.

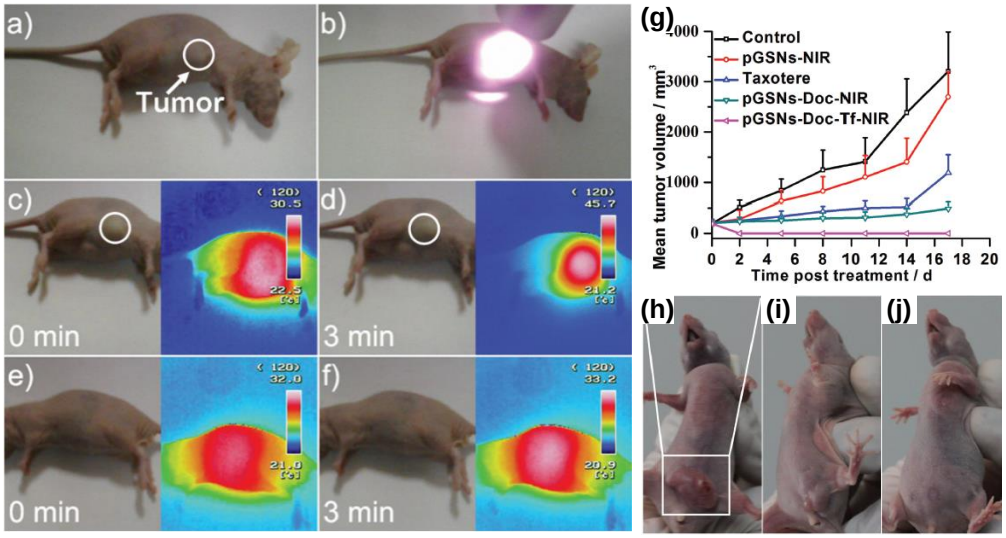

Figure 4.13 (a) Photo of an MCF-7 tumor-bearing balb/c nude mouse and the tumor site is indicated by the arrow. (b) Photo of mouse under 808 nm NIR laser light irradiation. (c-d) Photo and infrared thermal image of the tumor side at 6 h post intravenous injection of gold nanoshelled silica nanorattles before (c) and after (d) NIR laser irradiation at 2 W/cm^2, 3 min. (e-f) Infrared and thermal image of the non-tumor side before (e) and after (f) NIR laser irradiation. The color bars relate the relative temperature values in ºC. (g) *In vivo* antitumor activity of control group (saline), gold nanoshells + NIR, Texotere (Docetaxel), gold nanoshells + Docetaxel + NIR, and transferrin-functionalized gold nanoshells + Docetaxel + NIR. (h-j) Photos of mice with tumors at day 17 representing the (h) control group, (i) gold nanoshells + NIR, (j) and transferrin-functionalized gold nanoshells + Docetaxel + NIR. Adapted with permission from Reference 126. Copyright (2011) John Wiley and Sons.

Combination photothermal photodynamic therapy has been applied to increase tumor destruction *in vivo.* J. Lin *et al.*[129] loaded chlorin e6 into 280 nm plasmonic gold vesicles (λ_{max} ~ 650-800 nm) made from

26 nm self-assembled block copolymer-functionalized gold nanospheres. Athymic nude mice with MDA-MB-435 breast cancer tumors injected with the gold vesicles were laser irradiated (671 nm, 2 W/cm^2, 6 min) resulting in a 10ºC temperature increase. Because chlorin e6 has a peak at 650 nm, this wavelength of laser irradiation could sensitize singlet oxygen. After 14 days, the combined photothermal/photodynamic treatment prevented any tumor growth while the tumors treated with photothermal or photodynamic therapy alone more than doubled in volume.[129] Vijayaraghavan *et al.*[130] synthesized lipid-coated 350 nm gold nanoechinus, nanoparticles with many spiky nanorods sticking out from the surface and a broad absorbance profile. Interestingly, in addition to photothermal therapy, gold nanoechinus are capable of sensitizing singlet oxygen for photodynamic therapy at 915 or 1064 nm laser excitation as measured by phosphorescence emission at 1267 nm. C57BL/6J mice having B16-F10 melanoma tumors were irradiated (808, 915 or 1064 nm, 130 mW/cm^2). Maximum tumor temperature increase was 10ºC at 808 nm and 6ºC at 915 and 1064 nm. However, tumor volume was reduced by 97% at 915 nm and 1064 nm irradiation compared to significant tumor growth at 808 nm. Although irradiation at 915 and 1064 nm did not generate as much photothermal heat, the additional generation of reactive oxygen species significantly increased tumor destruction.[130] Jang *et al.*[131]conjugated the photosensitizer $AlPcS_4$ (absorbance at 675 nm) to RRLAC peptide-functionalized 34 nm gold nanorods (AR 3.7, λ_{max} ~ 800 nm) *via* electrostatic immobilization. Photothermal heating released the bound photosensitizers from gold nanorod surfaces, freeing them for photodynamic therapy. Photothermal therapy (810 nm, 3.82 W/cm^2) followed by photodynamic treatment (670 nm, 331 mW/cm^2) of SCC7 squamous cell carcinoma tumors in balb/c-nu mice resulted in a maximum tumor temperature of 65ºC. Surprisingly, the tumor had disappeared at day 3, but appeared again on day 6 and exhibited growth. After 8 days, tumor volume was 96% compared to the untreated control. However, this treatment was more effective than photothermal or photodynamic treatment alone which had 25% and 79% volume reduction, respectively.[131] Together, these examples demonstrate that photodynamic therapies can be combined with photothermal therapies *in vivo* for enhanced tumor destruction.

There have been many recent *in vivo* investigations into gold nanoparticle-mediated photothermal therapy for cancer treatment. Many researchers have combined photothermal therapy with diagnostic/imaging, chemotherapy and photodynamic therapy using multifunctional nanoparticles. However, researchers may want to consider if the extra effort involved in synthesis and preparation of these nanostructures is worth the benefits of multifunctionality *in vivo*. Some of these studies demonstrated reduced tumor growth while others were successful in complete tumor destruction. The variation in success of photothermal treatments *in vivo* may potentially be due to the disparities in experimental procedures between researchers. There is great variation in types of cancers, animal models, tumor sizes, dosing/irradiation conditions. This may complicate the ability of scientists to evaluate the potential of nanoparticle systems or to optimize treatments due to the cost/effort involved. Further investigation into standardization of modeling methods and optimization of dosing/treatment strategies may aid in furthering *in vivo* photothermal gold nanotherapeutics.

Table 4.6 Summary of references with recent advancements in nanoparticle design with imaging agents for *in vivo* photothermal therapy.

Reference	Nanoparticle	Imaging capability	Dose and exposure	Animal model	NIR conditions	Results
Ke[122]	PEG-functionalized gold nanoshelled nanocapsules, λ_{max} ~ 300-900 nm	Ultrasound and X-ray computed tomography	200 µL of 2 mg/mL, intravenous injection in the tail vein	260 mm^3 U87MG tumors in mice	CW laser, 808 nm, 1.3 W/cm^2, 10 min	35ºC increase in tumor temperature, 67.6% decrease in volume after 16 days
Y. Gao[123]	Nanomatryoshkas, λ_{max} = 780 nm	SERS	100 µL of 4 mg/mL, intravenous injection	MDA-MB-231 tumors in mice	808 nm, 2 W, 5 min	33ºC increase in tumor temperature
A. Lin[124]	PEG-functionalized gold nanoshells with Fe_3O_4/Ag cores, λ_{max} = 800 nm	T2 MRI	10^{12} nanoparticles, intravenous or intratumoral injection	B16-F10 subcutaneous tumors in C57BL/6 mice	808 nm, 4 W/cm^2, 30 s	Complete tumor elimination after 13 days with intratumoral injection, stunted tumor growth with intravenous injection
Sun[125]	Peptide-modified gold nanorods with ^{64}Cu, λ_{max} ~ 780 nm	Radionuclide positron emission tomography	150 µg, intravenous injection, 24 h	U87MG tumor in athymic nude mice	808 nm, 1 W/cm^2, 10 min	27.2ºC increase in tumor temperature, 50% reduction in tumor size

Table 4.7 Summary of references with recent advancements in nanoparticle design with chemotherapeutics or photosensitizers for *in vivo* photothermal therapy.

Reference	Nanoparticle	Conjugated drug or photosensitizer	Dose and exposure	Animal model	NIR conditions	Results
H. Liu[126]	Transferrin-functionalized gold nanoshelled silica nanorattles, λ_{max} ~ 810 nm	Docetaxil	200 µL of 1 mg/mL, intravenous injection, 6h	5x5 mm MCF-7 tumors in balb/c mice	CW laser, 808 nm, 2 W/cm^2, 3 min	15.2º C tumor temperature increase, complete tumor regression after 17 days
Shao[127]	PEG-functionalized gold nanospheres, λ_{max} = 535-540 nm	TNF-α	250 µg/kg, intravenous tail vein injection, 8 h	7-8 mm SCK tumors in the hind limb of A/J mice	Pulsed laser, 5 ns, 100 Hz, 532 nm, 1 J/cm^2, 1 min	Nanospheres + TNF = tumor regression, nanospheres only = 7x, and 690 nm laser = 5x
Nam[128]	Gold nanospheres with pH-responsive ligands, λ_{max} = 520 nm and shifts to ~650 nm at low pH	Doxorubicin, 2.4 mg/kg	100 µL of 1 µM, intravenous tail vein injection, 24 h	5-10 mm subcutaneous B16-F10 tumors in the flank of nu/nu mice	CW laser, 660 nm, 0.5 W/cm^2, 5 min	Tumor temperature increase of 15ºC and halted tumor growth, and DOX or PTT just slowed tumor growth
J. Lin[129]	Plasmonic vesicles containing gold nanospheres, λ_{max} ~ 650-800 nm	Chlorin e6 (Ce6), 18.4 wt.%	50 µL, 368µg/mL, intratumoral injection	60 mm^3 MDA-MB-435 in athymic nude mice	CW laser, 671 nm, 2 W/cm^2, 6 min	Tumor temperature increase 10ºC and prevented tumor growth, and tumor volume with PTT or PDT doubled
Vijayaraghavan[130]	Lipid-coated gold nanoechinus, λ_{max} = 600-1700 nm	-	40 mg/kg, percutaneous injection	B16-F10 tumors in C57BL/6J mice	130 mW/cm^2 at 808 nm, 11 min, or 915 and 1064 nm, for 10 min	97% decrease in tumor volume at 915 and 1064 nm and significant tumor growth at 808 nm
Jang[131]	Peptide-functionalized gold nanorods, λ_{max} ~ 800 nm	$AlPcS_4$, absorbance at 675 nm, 2500/nanorod	1 mg/kg, intravenous injection, 24 h	20 mm^3 SCC7 subcutaneous tumors in balb/c-nu mice	CW laser, 810 nm at 3.82 W/cm^2 then 670 nm at 331 mW/cm^2	Tumor temperatures increased to 65º and tumor volume was 4% of control *versus* 75% with gold nanorods alone or 21% with photosensitizer alone

4.8 *IN VIVO* BIODISTRIBUTION OF GOLD NANOPARTICLES FOR PHOTOTHERMAL THERAPY

A key factor in the success of any nanoparticle-based therapy is the ability to understand and/or control nanoparticle fate *in vivo*.[132] Work by Sonovane *et al.*[133] has previously demonstrated that citrate-capped gold nanoparticles of various sizes (15-200 nm) can bioaccumulate in body tissues. Most of the gold accumulation was in the liver, lungs, spleen, and kidneys, but was also found in the blood, stomach, and pancreas, and particles even penetrated the blood-brain barrier to enter the brain.[133] For photothermal treatment of cancer to be successful, nanoparticles need to accumulate at the tumor site; however, issues of blood half-life, transport, and long-term toxicity/biodistribution are not fully understood. Researchers have therefore explored the individual effects of shape, size, targeting ligand and delivery method as potential avenues to increase gold nanoparticle accumulation in and/or near tumors for photothermal therapy. Tumor uptake of gold nanoparticles in these various studies are summarized in Table 4.8.

Y. Wang *et al.*[134] explored how shape of gold nanoparticles affects their pharmacokinetics. They prepared PEG-functionalized nanohexapods (~ 50 nm, λ_{max} = 805 nm) which are octahedral cores with six arms, nanorods (9x36 nm, λ_{max} = 800 nm), and nanocages (47 nm, λ_{max} = 802 nm). The nanoparticles (100 µL, 4 nM) were injected them intravenously into the rear flanks of athymic Nude-Foxn1nu nude mice having MDA-MB-435 breast cancer tumors (100-300 mm^3). Gold content in various organs was determined by mass spectrometry at 6 h, 24 h and 7 days post-injection (Figure 4.14a-c). The liver and spleen had the highest accumulation after 6 h, but it decreased slightly after 7 days. Interestingly, the blood had some accumulation at 6 h, but after 7 days there was almost no presence of gold, potentially due to renal clearance. Other organs with slight accumulation included the lungs, kidney and heart. After 24 h exposure, 7.2% of nanohexapods, 2.6% of nanocages and 8.4% of nanorods had accumulated in the tumor due to EPR. Photothermal treatment (808 nm, 1.2 W/cm^2, 10 min) resulted in localized heating at the tumor site with temperature increases to 56ºC for nanohexapods, 49ºC for nanocages and 53ºC for nanorods (Figure 4.14d,e). Furthermore, 24 h post-treatment, tumor metabolism was decreased by 90% with nanohexapods and nanorods, 80% with nanocages, and no visible tumors were observed in treated mice, demonstrating successful tumor eradication. This study suggests that shape and morphology of nanostructures influences circulation and biodistribution which would impact the outcome of photothermal treatment on tumors.[134]

Ayala-Orozco *et al*.[135] prepared PEG-functionalized gold nanomatryoshkas (88 nm, λ_{max} = 783 nm) and gold nanoshells (152 nm, λ_{max} ~ 800 nm) to investigate how nanoparticle size affects tumor uptake and photothermal therapy. MDA-MB-231LM2 triple negative breast cancer tumors (1000 mm^3) were grown near the ribcages in Harlan Sprague Dawley athymic nude mice. Nanomatryoshkas and nanoshells (200 µL of 1.5 mg/mL) were injected intravenously into the tail vein and gold biodistribution was determined at various time points post-injection. At 4 h, the highest accumulation of gold was in the spleen and blood, but after 24 h there was very little gold present in the blood. The authors attributed greater tumor accumulation of nanomatryoshkas to their smaller size. Laser irradiation (808 nm, 3 W/cm^2, 5 min) 4 h after injection increased tumor temperature by 25ºC for nanomatryoshkas and 19ºC for nanoshells and 13ºC for laser alone and cancer cell morphology was disrupted.[135] This result suggested that nanoparticle size can also

impact photothermal heating *in vivo*. However, the tumors continued to grow after a few days and photothermal treatment just extended survival, rather than completely removing aggressive tumors.

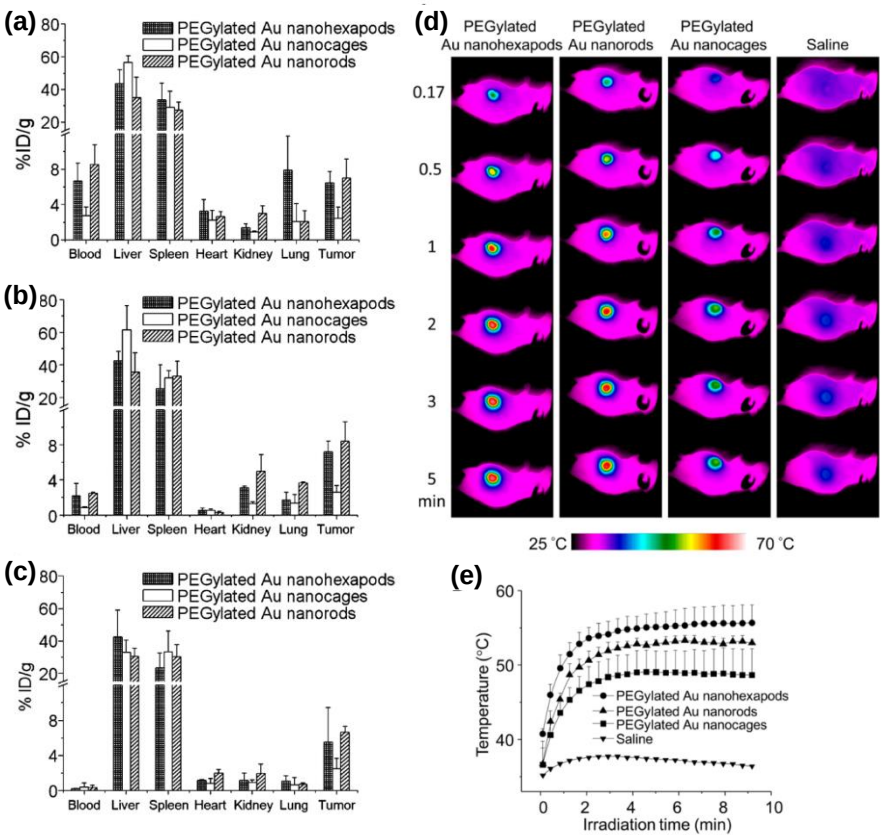

Figure 4.14 *In vivo* biodistribution of PEGylated gold nanohexapods, nanocages and nanorods after they had been intravenously injected into tumor-bearing mice for (a) 6 h, (b) 24 h, and (c) 7 days. (d) Thermographs of tumor-bearing mice receiving photothermal treatment for different periods of time. (e) Plots of average temperature increase within the tumor region as a function of irradiation time. Adapted with permission from Reference 134. Copyright (2013) American Chemical Society.

Puvanakrishnan *et al.*[136] investigated the impact of nanoparticle size and dosing strategy on tumor accumulation using PEGylated gold nanoshells (135 nm, λ_{max} = 810 nm) and smaller gold nanorods (7x24 nm, λ_{max} ~780 nm). The nanoparticles were injected into Swiss *nu/nu* mice, having 8-10 mm subcutaneous tumors of CRL-1555 human epithelial carcinoma. The mice were injected with single or multiple (3 or 5) nanoparticle doses, of the same optical density, at 24 h intervals. Gold accumulation in the tumor and liver was determined using neutron activation analysis for each of the dosing strategies. For a single dose, accumulation in the tumor, by percent of the injected dose, was 12 times for gold nanorods compared to gold nanoshells. As expected, both tumor and liver accumulation of gold nanoshells increased with increasing dose. Interestingly, the gold nanorod accumulation was highest in both the liver and tumor at 3 doses and decreased with 5 doses, but was still greater than a single dose.[136] These results suggested

smaller size nanoparticles, and a multiple dosing strategy may be beneficial to enhance nanoparticle accumulation in tumors prior to photothermal therapy.

In previous sections, we have described methods scientists have used to attach targeting ligands so gold nanoparticles can more specifically bind to tumor cells. A persistent question in the literature is whether the effort involved in active targeting is useful in enhancing accumulation of gold nanoparticles in tumors, and if this increases success of photothermal therapy *in vivo* compared to relying on the EPR effect alone. C. H. J. Choi *et al.*[137] investigated the impact of active targeting by varying the amount of transferrin (0-144/nanoparticle) bound to PEG-functionalized gold nanospheres (50 nm). Many types of cancer cells over express transferrin receptors, so transferrin-functionalized nanoparticles can accumulate in cancer cells *via* receptor-mediated endocytosis. Female A/J mice bearing subcutaneous Neuro2A neuroblastoma tumors were injected with the nanoparticles in the tail vein. Biodistribution after 24 h was determined by mass spectrometric analysis of the digested organs. Despite the differences in transferrin functionalization, nanoparticle accumulation in the liver/spleen were always the highest. Nanoparticle accumulation in the tumors was only 2-3% of the injected dose, and there was little difference in accumulation with the different amounts of transferrin. However, there was higher intracellular accumulation of the transferrin-functionalized nanoparticles in the tumor cells, as determined by transmission electron microscopy. This result suggested the effort to functionalize the nanoparticles with a tumor targeting agent did not effectively increase bulk tumor accumulation but did affect nanoparticle localization within tumor cells.[137]

Other studies which compare active and passive targeting using functionalized gold nanoparticles show similar results. Active functionalization is effective in increasing binding/uptake of gold nanoparticles in cells *in vitro*, but *in vivo* tumor accumulation is usually less than 10% of the intravenous dose.[138,139] One reason for limited tumor uptake is the strong accumulation of nanoparticles by the mononuclear phagocyte system (formerly called the reticulo-endothelial system).[140] Monocytes, dendritic cells and macrophages, which are present in the liver, spleen, and blood, sequester particles larger than ~100 nm. Particles smaller than ~5 nm are rapidly cleared by kidneys. A large percentage of particles ~5-100 nm can also be taken up by macrophages but perhaps not to the same degree as larger particles. Specific targeting ligands are known to prevent macrophage uptake, but PEGylation of nanoparticles is thought to decrease uptake by the mononuclear phagocyte system.[141] This may explain why the vast majority of nanoparticles *in vivo* are found in the liver and spleen, despite differences in nanoparticle design.

Perhaps another reason for limited tumor accumulation is the formation of a protein corona around gold nanoparticles in physiological matrices. Protein binding on nanoparticle surfaces, resulting in the formation of “hard” and “soft” coronas, is well-documented in the literature and a current area of research interest.[142] The ability to understand and protein adsorption to various nanoparticle constructs may allow scientists to better predict and potentially control the “face” which a nanoparticle presents, and therefore its fate in a physiological environment.[143] However, nanoparticle protein coronas also become more complicated *in vivo*. The biomolecular corona may play a role in reducing the effectiveness of targeting agents in binding to tumor cells because proteins may shield an attached ligand, and reduce its targeting functionality.[144]

Therefore, while active tumor targeting can improve nanoparticle intracellular accumulation, the effect on bulk tumor accumulation is marginal at best, and perhaps is not worth the effort involved.[145]

Once nanoparticles travel to the tumor, it is beneficial if they are able to penetrate the tumor center for photothermal heating to result in more effective tumor destruction. J. Chen *et al.*[146] investigated nanoparticle tumor penetration using PEG-functionalized gold nanocages (48 nm, λ_{max} = 800 nm) and Athymic nu/nu mice bearing U87MGwtEGFR human glioblastoma tumors. At 96 h post injection (100 µL, 10 mg/mL) ~6% of the injected dose was in the tumor. After laser irradiation (808 nm, 0.7 W/cm^2, 10 min), tumor temperatures reached 54ºC and tumor metabolic activity was reduced by 70%. The tumors were then dissected to determine spatial nanocage distribution. The edges had more than twice the amount of nanocages as the center, potentially due to the greater presence of blood vessels in the outer areas.[146] Mooney *et al.*[147] used neural stem cells to facilitate delivery of gold nanorods (10x40 nm, λ_{max} = 810 nm) which were functionalized with 11-mercaptoundecyltrimethylammonium bromide into tumors. 5-7 mm MDA-MB-231.Ffluc breast cancer tumors were grown in Charles River Athymic nude mice and were injected with neural stem cell-loaded nanorods or free nanorods. After 3 days, free gold nanorods remained in the tumor core while the neural stem cell-loaded nanorods were evenly distributed throughout the tumor (Figure 4.15). Irradiation (811 nm, 2 W/cm^2, 5 min) resulted in complete tumor ablation but some of tumors regrew. After 100 days, 60% of the mice treated with gold nanorod-loaded neural stem cells and 20% of the mice treated with free nanorods survived while all the mice in the control group were dead by day 30. Potentially, spatially distributed heat generation resulted in more effective thermal destruction by the neural stem cells loaded with gold nanorods.[147]

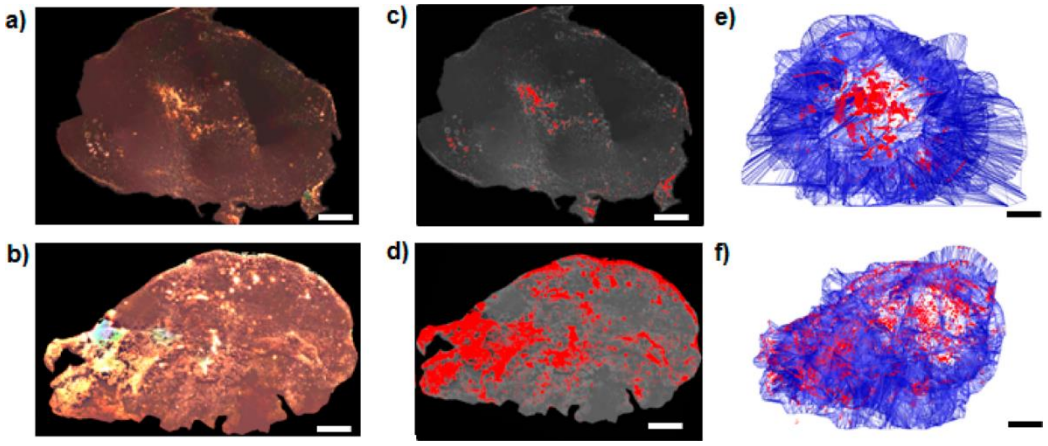

Figure 4.15 Comparison of free gold nanorods and neural stem cell (NSC)-loaded gold nanorod distribution after intratumoral injection. 3 days after nanorod injection, tumors were sectioned and imaged using dark-field microscopy. (a, b) Tiled, flattened, dark-field micrographs of entire cross sections of tumors injected with (a) free nanorods) or (b) NSC nanorods. (c, d) Mapped cross-sections of tumors injected with (c) free nanorods or (b) NSC nanorods. (e, f) 3D projection of all mapped nanorods (red) and tumor (blue) traces generated using Reconstruct software in tumors that received (e) free nanorods or (f) NSC nanorods. Scale bars = 1 mm. Adapted from Reference 147 (not subject to U.S. copyright).

Together, these studies demonstrate that gold nanoparticle design appears to affect biodistribution and therefore the success of gold nanoparticle photothermal therapy *in vivo*. Only one of the *in vivo* studies mentioned here used intratumoral injection, and the majority of researchers injected gold nanoparticles intravenously, relying on the EPR effect to increase tumor accumulation. Shape, size, targeting ligand, and dosing strategy appear to influence whether nanoparticles extravasate into tumors, accumulate in the liver/spleen or are cleared by the kidneys. In addition, nanoparticles location in a tumor is a factor to be considered because nanoparticles which travel into the tumor center are effective in aiding photothermal tumor destruction. However, while the EPR effect is well-known in tumors, it is also not ubiquitous, but also heterogeneous and seems limited because usually less than 10% of intravenously injected nanoparticles actually end up in the tumor. Nanoparticles extravasate into tumors because of the "leakiness" of the vasculature, but pore sizes in tumors may vary depending on cancer type, tumor size, and cancer state (i.e. primary *versus* metastatic). Therefore, we cannot suggest one specific gold nanoparticle design that would be generally successful in accumulating in all tumor types.[148] We direct readers interested in more information on biodistribution to recent reviews on the subject.[45-47,149] In order to increase the effectiveness of photothermal therapies, we suggest researchers continue to explore how design and dosing strategies affect biodistribution and tumor accumulation of gold nanoparticles in a variety of cancers. More *in vivo* studies which investigate the effect of active and passive tumor targeting in conjunction with shape, size, and surface chemistry would be useful in this area.

Table 4.8 Summary of references which analyze gold nanoparticle biodistribution *in vivo*.

Reference	Nanoparticle	Nanoparticle size	Dose and exposure	Animal model	Tumor uptake (% intravenous dose/g)
Y. Wang[134]	PEG gold nanohexapods	core = 25 nm, arms = 16x14 nm	100 µL of 4 nM nanoparticles injected through tail vein	Subcutaneous MDA-MB-435 tumors in right flank athymic mice	6.5% at 6 h, 7.2% at 24 h, ~6% at 7 days
Y. Wang[134]	PEG gold nanorods	9x36 nm	100 µL of 4 nM nanoparticles injected through tail vein	Subcutaneous MDA-MB-435 tumors in right flank athymic mice	7.0% at 6 h, 8.4% at 24 h, ~7% at 7 days
Y. Wang[134]	PEG gold nanocages	Edge length = 47 nm, wall = 5 nm	100 µL of 4 nM nanoparticles injected through tail vein	Subcutaneous MDA-MB-435 tumors in right flank athymic mice	1.2% at 6 h, 2.5% at 24 h, ~2% at 7 days
Ayala-Orozco[135]	PEG gold nanomatryoshkas	88 nm	200 µL of 1.5 mg/mL nanoparticles injected intravenously in the tail vein	MDA-MB-231LM2 tumors near ribcages in Harlan Sprague Dawley athymic nude mice	~2% at 4 h, ~3% at 24 h, ~2% at 72 h
Ayala-Orozco[135]	PEG gold nanoshells	152 nm	200 µL of 1.5 mg/mL nanoparticles injected intravenously in the tail vein	MDA-MB-231LM2 tumors near ribcages in Harlan Sprague Dawley athymic nude mice	~1% at 4 h, ~1.5% at 24 h, ~1% at 72 h
Puvanakrishnan[136]	PEG gold nanoshells	135 nm	1,3, or 5 doses of 7 µL/g at $2.74x10^{8}$ particles/mL	Subcutaneous human epithelial carcinoma in Swiss nu/nu mice	0.12% at 24 h
Puvanakrishnan[136]	PEG gold nanorods	7x24 nm	1, 3, or 5 doses of 7 µL/g at $2.0x10^{11}$ particles/mL	Subcutaneous human epithelial carcinoma in Swiss nu/nu mice	1.35% at 24 h
C. Choi[137]	Transferrin (0-144/particle) and PEG gold nanospheres	50 nm	tail-vein administration of $4.5x10^{11}$ particle	Subcutaneous Neuro2A neuroblastoma in female A/J mice	2–3% at 24 h, independent of Tf, but Tf-dependent, intracellular localization
J. Chen[146]	PEG- gold nanocages	48 nm	100 µL, 10 mg/mL	U87MGwtEGFR human glioblastoma in the left rear flank of Athymic nu/nu mice	6% at 96 h, nanocages were localized at the edges more than the center
Mooney[147]	Gold nanorod-loaded neural stem cells	10x40 nm	12.5 µg intratumoral injection	MDA-MB-231.Ffluc breast cancer in Charles River Athymic nude mice	"free" gold nanorods remained in the tumor core neural stem cell-loaded nanorods were evenly distributed throughout the tumor

4.9 PROGRESSION OF PHOTOTHERMAL THERAPY TO CLINICAL USE

Currently, only one gold nanoparticle photothermal treatment system has progressed to clinical trials. Nanospectra Biosciences, Inc., founded in 2002, is a company focused on commercializing photothermal therapeutics for destruction of solid tumors. AuroLase® Therapy consists of AuroShell® particles which are 150 nm gold nanoshells (λ_{max} = 780-820 nm) and functionalized with a 5,000 molecular weight PEG-thiol. The nanoshells are injected intravenously and PEGylation allows them to circulate in the blood long enough to accumulate in tumors *via* the EPR effect. Then, a fiber optic NIR laser (808 nm) is inserted through the skin into or near the tumor and subsequent irradiation(s) may result in cancer cell death and tumor regression.[150] A fiber optic laser is used because NIR light can only penetrate up to 10 cm in tissue so tumors in deep areas of the body cannot be treated with lasers at/above the skin.[151] The use of a fiber optic laser inserted into the body is a useful solution to the problem of limited penetration depth. This was demonstrated by Schwartz *et al* who used an optical fiber to carry photothermal treatment in a venereal tumor in a canine brain model.[152]

There have been two human clinical trials for photothermal treatment using gold nanoshells. The AuroLase® pilot study began in April 2008 and was completed August 2014. This trial consisted of a single dose nanoparticle treatment for 5 patients with refractory and/or recurrent tumors of the head and neck, who would be observed in the 6 months following treatment. No results have yet been posted.[153] The second clinical trial began in October 2012 and is ongoing with a projected end date of June 2016. This trial is for the treatment of primary and/or metastatic lung tumors, and patients are given a systemic infusion of the gold nanoshells followed by escalating doses of NIR irradiation.[154]

4.10 CONCLUSIONS AND PERSPECTIVES

There has been a great deal of development in the field of gold nanoparticle-mediated cancer therapy *in vitro* and *in vivo* in the last 13 years. The potential of radiofrequency hyperthermia using gold nanoparticles has been investigated and has been demonstrated to be effective under certain conditions, and the treatment may merit further study. Many researchers have also demonstrated effective cancer treatment, at least in the lab, with photothermal therapy. The effects of structure, composition, and surface chemistry of gold nanomaterials have been investigated to better understand photothermal heating efficiency. Researchers have demonstrated enhanced nanoparticle accumulation and cell death in cancer cells and tumors by attaching targeting ligands to gold nanoparticles or by taking advantage of the EPR effect. Photothermal therapy has also been combined with imaging modalities or other methods of cancer treatment including chemotherapy and photodynamic therapy to achieve synergistic cancer treatment *in vitro* and *in vivo*. Recent advancements in nanoparticle design and a better understanding of the effects of photothermal heating demonstrates that there is potential for this therapy in clinical applications. In addition, the continuation of AuroLase® to a second human trial is encouraging. If these clinical trials of AuroLase Therapy demonstrate effective treatment, then maybe other gold nanoparticle treatment systems will follow.

Thus far, scientists have found many ways to destroy cancer cells *in vitro* and *in vivo* in mice, but translation to commercial clinical use has not yet occurred. The following characteristics of a treatment are attractive for photothermal cancer therapy with gold nanoparticles: scalability in production, effective tumor targeting and tumor penetration, effective destruction of cancer, and demonstration of low/no long-term *in vivo* toxicity. One large barrier to application and commercialization may be the lack of nanoparticle model standards to test the effectiveness of photothermal therapy. All the studies described here used gold nanomaterials, but factors such as size, shape, surface coating, injected dose, animal model and cancer model varied and can make comparison between the studies a significant challenge.[155] Also, despite the demonstrations of scaled-up synthesis, nanomaterial synthesis is notorious for being irreproducible, and no two nanoparticle batches are the exact same. Variation in nanoparticle structure/composition may affect tumor targeting ability and penetration along with photothermal heating efficiency. In addition, the toxicity of nanomaterials is not well-understood and could also vary with structure/composition. Therefore, for photothermal cancer therapy to be realized, it would be beneficial if all treatments are standardized or compared to a known reference material, cancer type, and animal model. This way, improvements in targeting and therapy can be correlated with more effective cancer therapy in humans.

Another significant barrier to commercialization of photothermal therapy may be the cost and time involved in preparing and studying nanomaterial treatment systems. Y. Wang *et al.*[134] injected 100 µL of 4 nM PEGylated gold nanoparticles into 5-6 week old Athymic Nude-Foxn1nu nude mice, which they treated using photothermal therapy. If we assume these mice weigh on average of ~17 g,[156] we can extrapolate that the dose required to treat a 75 kg human subject would be 450 mL of 4 nM gold nanoparticles and we can estimate treatment cost. NanoHybrids charges $500 for 1 mL of 120 nM PEGylated gold nanorods with an LSPR at 808 nm.[157,158] Therefore, 15 mL of these PEG functionalized gold nanorods would cost approximately $7500 for a single treatment. It is well known that the costs of cancer treatment can be quite high in the United States.[159] For example, the average cost per patient for chemo/radiation therapy during treatment of pancreatic cancer was $8700 between the years 2000-2007.[160] In 2006 the price of various chemotherapy or radiative treatments of advanced cervical cancer in women was $1997-10705.[161] Given that a single dose of nanoparticles for photothermal therapy approaches the cost of these treatments, the price of photothermal therapy should be evaluated in its ability to eradicate cancer in a cost-effective manner.

Another potential barrier to commercialization is that many of the systems described in the literature are quite complicated in design, and are often referred to as theranostic (therapeutic and diagnostic). The added multifunctionality in active targeting ligands, imaging modalities or photodynamic/chemotherapeutic loads while fundamentally interesting and potentially useful, also may complicate syntheses a great deal. This might translate to a significant added cost and extra time involved in investigating nanotoxicity, gaining clinical approval, and achieving large-scale nanoparticle production and commercialization. Additionally, the added costs are not guaranteed to add to the effectiveness of the treatment due to limited nanoparticle accumulation in tumors. In fact, the nanoparticle constructs, which have been clinically approved for various

treatments/diagnostic tests, are more simple in design – one type of core particle with one surface functional group/ligand.[145] Perhaps it would be better if scientists, clinicians and researchers interested in gaining clinical approval photothermal therapy focus on better synthetic control and characterization of nanomaterials as well as improvement of the pharmacokinetic profiles and photothermal conversion efficiencies of simple nanoparticle systems. We are not yet in the era of personalized medicine.[162] For now, the route to improved patient outcomes may be in working to carry out photothermal therapy using "simple" nanostructures - this is exemplified by the AuroLase treatment, which is simpler in design.

4.11 REFERENCES

1. Faraday, M. Experimental Relations of Gold (and Other Metals) to Light. *Philos. Trans.* **1857,** *147,* 145-181.
2. Eustis, S.; El-Sayed, M. A. Why Gold Nanoparticles are More Precious than Pretty Gold: Noble Metal Surface Plasmon Resonance and its Enhancement of the Radiative and Nonradiative Properties of Nanocrystals of Different Shapes. *Chem. Soc. Rev.* **2006,** *35,* 209-217.
3. Daniel, M.-C.; Astruc, D. Gold Nanoparticles: Assembly, Supramolecular Chemistry, Quantum-Size-Related Properties, and Applications toward Biology, Catalysis, and Nanotechnology. *Chem. Rev.* **2004,** *104,* 293-346.
4. Murphy, C. J.; Sau, T. K.; Gold, A. M.; Orrendorff, C. J.; Gao, J.; Gou, L.; Hunyadi, S. E.; Li, T. Anisotropic Metal Nanoparticles: Synthesis, Assembly, and Optical Applications. *J. Phys. Chem. B* **2005,** *109,* 13857-13870.
5. Bardhan, R.; Lal, S.; Joshi, A.; Halas, N. J. Theranostic Nanoshells: From Probe Design to Imaging and Treatment of Cancer. *Acc. Chem. Res.* **2011,** *44,* 936-946.
6. Skrabalak, S. E.; Chen, J.; Sun, Y.; Lu, X.; Au, L.; Cobley, C. M.; Xia, Y. Gold Nanocages: Synthesis, Properties, and Applications. *Acc. Chem. Res.* **2008,** *41,* 1587-1595.
7. Saha, K.; Agasti, S. S.; Kim, C.; Li, X.; Rotello, V. M. Gold Nanoparticles in Chemical and Biological Sensing. *Chem. Rev.* **2012,** *112,* 2739-2779.
8. Murphy, C. J.; Gole, A. M.; Stone, J. W.; Sisco, P. N.; Alkilany, A. M.; Goldsmith, E. C.; Baxter, S. C. Gold Nanoparticles in Biology: Beyond Toxicity to Cellular Imaging. *Acc. Chem. Res.* **2008,** *41,* 1721-1730.
9. Ghosh, P.; Han, G.; De, M.; Kim, C. K.; Rotello, V. M. Gold Nanoparticles in Delivery Applications. *Adv. Drug Deliv. Rev.* **2008,** *60,* 1307-1315.
10. Jain, S.; Hirst, D. G.; O'Sullivan, J. M. Gold Nanoparticles as Novel Agents for Cancer Therapy. *Br. J. Radiol.* **2012,** *85,* 101-113.
11. Dreaden, E. C.; Alkilany, A. M.; Huang, X.; Murphy, C. J.; El-Sayed, M. A. The Golden Age: Gold Nanoparticles for Biomedicine. *Chem. Soc. Rev.* **2012,** *41,* 2740-2779.
12. Ghosh, S. K.; Pal, T. Interparticle Coupling Effect on the Surface Plasmon Resonance of Gold Nanoparticles: From Theory to Applications. *Chem. Rev.* **2007,** *107,* 4797-4862.
13. Link, S.; El-Sayed, M. A. Size and Temperature Dependence of the Plasmon Absorption of Colloidal Gold Nanoparticles. *J. Phys. Chem. B* **1999,** *103,* 4212-4217.
14. Miller, M. M.; Lazarides, A. A. Sensitivity of Metal Nanoparticle Surface Plasmon Resonance to the Dielectric Environment. *J. Phys. Chem. B* **2005,** *109,* 21556-21565.
15. Mulvaney, P. Surface Plasmon Spectroscopy of Nanosized Metal Particles. *Langmuir* **1996,** *12,* 788-800.
16. Underwood, S.; Mulvaney, P. Effect of the Solution Refractive Index on the Color of Gold Colloids. *Langmuir* 1994, *10,* 3427-3430.
17. Jain, P. K.; Lee, K. S.; El-Sayed, I. H.; El-Sayed, M. A. Calculated Absorption and Scattering Properties of Gold Nanoparticles of Different Size, Shape, and Composition: Applications in Biological Imaging and Biomedicine. *J. Phys. Chem. B* **2006,** *110,* 7238-7248.
18. Abadeer, N. S.; Brennan, M. R.; Wilson, W. L.; Murphy, C. J. Distance and Plasmon Wavelength Dependent Fluorescence of Molecules Bound to Silica-Coated Gold Nanorods. *ACS Nano* **2014,** *8,* 8392-8406.

19. Link, S.; El-Sayed, M. A. Shape and Size Dependence of Radiative, Non-Radiative and Photothermal Properties of Gold Nanocrystals. *Int. Rev. Phys. Chem.* **2000,** *19,* 409-453.
20. Huang, J. Photothermal Properties and Applications of Gold Nanorods. Ph.D. Thesis, University of Illinois, Urbana, IL, 2014.
21. Huang, X.; Jain, P. K.; El-Sayed, I. H.; El-Sayed, M. A. Plasmonic Photothermal Therapy (PPTT) Using Gold Nanoparticles. *Lasers Med. Sci.* **2008,** *23,* 217-228.
22. Link, S.; Burday, C.; Mohamed, M. B.; Nikoobakht, B.; El-Sayed, M. A. Laser Photothermal Melting and Fragmentation of Gold Nanorods: Energy and Laser Pulse-Width Dependence. *J. Phys. Chem. A* **1999,** *103,* 1165-1170.
23. Field, S. B.; Bleehen, N. M. Hyperthermia in the Treatment of Cancer. *Cancer Treat. Rev.* **1979,** *6,* 63-94.
24. Cheung, A. Y.; Neyzari, A. Deep Local Hyperthermia for Cancer Therapy: External Electromagnetic and Ultrasound Techniques. *Cancer Res.* **1984,** *44,* 4736-4744.
25. Zager, T. M.; Oleson, J. R.; Vujaskovic, Z.; Dewhirst, M. W.; Craniunescu, O. I.; Blackwell, K. L.; Prosnitz, L. R.; Jones, E. L. Hyperthermia for Locally Advanced Breast Cancer. *Int. J. Hyperthermia* **2010,** *26,* 618-624.
26. Oleson, J. R.; Samulski, T. V.; Leopold, K. A.; Clegg, S. T.; Dewhirst, M. W.; Dodge, R. K.; George, S. L. Sensitivity of Hyperthermia Trial Outcomes to Temperature and Time: Implications for Thermal Goals of Treatment. *Int. J. Radiat. Oncol., Biol., Phys.* **1993,** *25,* 289-297.
27. Day, E. S.; Morton, J. G.; West, J. L. Nanoparticles for Thermal Cancer Therapy. *J. Biomech. Eng.* **2009,** *131,* 074001.
28. Wust, P.; Hildebrandt, B.; Sreenivasa, G.; Rau, B.; Gellermann, J.; Riess, H.; Felix, R.; Schlag, P. M. Hyperthermia in Combined Treatment of Cancer. *Lancet* **2002,** *3,* 487-497.
29. Ciocca, D. R.; Calderwood, S. K. Heat Shock Proteins in Cancer: Diagnostic, Prognostic, Predictive, and Treatment Implications. *Cell Stress Chaperones* **2005,** *10,* 86-103.
30. Calderwood, S. K.; Ciocca, D. R. Heat Shock Proteins: Stress Proteins with Janus-Like Properties in Cancer. *Int. J. Hyperthermia* **2008,** *24,* 31-39.
31. Hirsch, L. R.; Stafford, R. J.; Bankson, J. A.; Sershen, S. R.; Rivera, B.; Price, R. E.; Hazle, J. D.; Halas, N. J.; West, J. L. Nanoshell-Mediated Near-Infrared Thermal Therapy of Tumors Under Magnetic Resonance Guidance. *Proc. Natl. Acad. Sci. U.S.A.* **2003,** *100,* 13549-13554.
32. Hirsch, L. R.; Gobin, A. M.; Lowery, A. R.; Tam, F.; Drezek, R. A.; Halas, N. J.; West, N. J. Metal Nanoshells. *Ann. Biomed. Eng.* **2006,** *34,* 15-22.
33. O'Neal, D. P.; Hirsch, L. R.; Halas, N. J.; Payne, J. D.; West, J. L. Photo-Thermal Tumor Ablation in Mice Using Near-Infrared-Absorbing Nanoparticles. *Cancer Lett.* **2004,** *209,* 171-176.
34. El-Sayed, I. H.; Huang, X.; El-Sayed, M. A. Selective Laser Photo-Thermal Therapy of Epithelial Carcinoma Using anti-EGFR Antibody Conjugated Gold Nanoparticles. *Cancer Lett.* **2006,** *239,* 129-135.
35. El-Sayed, I. H.; Huang, X.; El-Sayed, M. A. Surface Plasmon Resonance Scattering and Absorption of anti-EGFR Antibody Conjugated Gold Nanoparticles in Cancer Diagnostics: Applications in Oral Cancer. *Nano Lett.* **2005,** *5,* 829-834.
36. Huang, X.; El-Sayed, I. H.; Qian, W.; El-Sayed, M. A. Cancer Cell Imaging and Photothermal Therapy in the Near-Infrared Region by Using Gold Nanorods. *J. Am. Chem. Soc.* **2006,** *128,* 2115-2120.
37. Lohse, S. E.; Eller, J. R.; Sivapalan, S. T.; Plews, M. R.; Murphy, C. J. A Simple Millifluidic Benchtop Reactor System for the High-Throughput Synthesis and Functionalization of Gold Nanoparticles with Different Sizes and Shapes. *ACS Nano* **2013,** *7,* 4135-4150.
38. Cabeza, V. S.; Kuhn, S.; Kulkami, A. A.; Jensen, K. F. Size-Controlled Flow Synthesis of Gold Nanoparticles Using a Segmented Flow Microfluidic Platform. *Langmuir* **2012,** *28,* 7007-7013.
39. Shukla, R.; Bansal, V..; Chaudhary, M.; Basu, A.; Bhonde, R. R.; Sastry, M. Biocompatibility of Gold Nanoparticles and Their Endocytotic Fate Inside the Cellular Compartment: A Microscopic Overview. *Langmuir* **2005,** *21,* 10644-10654.
40. Alkilany, A. M.; Murphy, C. J. Toxicity and Cellular Uptake of Gold Nanoparticles: What We Have Learned so Far? *J. Nanopart. Res.* **2010,** *12,* 2313-2333.
41. Grzincic, E. M.; Yang, J. A.; Drnevich, J.; Falagan-Lotsch, P.; Murphy, C. J. Global Transcriptomic Analysis of Model Human Cell Lines Exposed to Surface-Modified Gold Nanoparticles: The Effect of Surface Chemistry. *Nanoscale* **2015,** *7,* 1349-1362.

42. Yang, J. A.; Phan, H. T.; Vaidya, S.; Murphy, C. J. Nanovacuums: Nanoparticle Uptake and Differential Cellular Migration on a Carpet of Nanoparticles. *Nano Lett.* **2013,** *13,* 2295-2302.
43. Connor, E. E.; Mwamuka J.; Gole, A.; Murphy, C. J.; Wyatt, M. D. Gold Nanoparticles are Taken Up by Human Cells but Do Not Cause Acute Cytotoxicity. *Small* **2005,** *1,* 325-327.
44. Akiyama, Y.; Mori, T.; Katayama, Y.; Niidome, T. The Effects of PEG Grafting Level and Injection Dose on Gold Nanorod Biodistribution in the Tumor-Bearing Mice. *J. Control. Rel.* **2009,** *139,* 81-84.
45. Jain, R. K.; Stylianopoulos, T. Delivering Nanomedicine to Solid Tumors. *Nature Rev. Clin. Oncol.* **2010,** *7,* 653-664.
46. Decuzzi, P.; Godin, B.; Tanaka, T.; Lee, S.-Y.; Chiappini, C.; Liu, X.; Ferrari, M. Size and Shape Effects in the Biodistribution of Intravascularly Injected Particles. *J. Control. Rel.* **2010,** *141,* 320-327.
47. Khlebtsov, N.; Dykman, L. Biodistribution and Toxicity of Engineered Gold Nanoparticles: A Review of *In vitro* and *In vivo* Studies. *Chem. Soc. Rev.* **2011,** *40,* 1647-1671.
48. Popovtzer, R.; Agarwal, A.; Kotov, N. A.; Popovtzer, A.; Balter, J.; Carey, T. E.; Kopelman, R. Targeted Gold Nanoparticles Enable Molecular CT Imaging of Cancer. *Nano Lett.* **2008,** *8,* 4593-4596.
49. Kim, D.; Jeong, Y. Y.; Jon, S. A Drug-Loaded Aptamer-Gold Nanoparticle Bioconjugate for Combined CT Imaging and Therapy of Prostate Cancer. *ACS Nano* **2010,** *4,* 3689-3696.
50. Huang, Y.-F.; Sefah, K.; Bamrungsap, S.; Chang, H.-T.; Tan, W. Selective Photothermal Therapy for Mixed Cancer Cells Using Aptamer-Conjugated Nanorods. *Langmuir* **2008,** *24,* 11860-11865.
51. Tong, L.; Wei, Q.; Wei, A.; Cheng, J.-X. Gold Nanorods as Contrast Agents for Biological Imaging: Optical Properties, Surface Conjugation and Photothermal Effects. *Photochem. Photobiol.* **2009,** *85,* 21-32.
52. Sanhai, W. R.; Sakamoto, J. H.; Canady, R.; Ferrari, M. Seven Challenges for Nanomedicine. *Nature Nanotech.* **2008,** *3,* 242-244.
53. Friedman, M.; Mikityansky, I.; Kam, A.; Libutti, S. K.; Walther, M. M.; Neeman, Z.; Locklin, J. K.; Wood, B. J. Radiofrequency Ablation of Cancer. *Cardiovasc. Intervent. Radiol.* **2004,** *27,* 427-434.
54. Glazer, E. S.; Curley, S. A. Non-Invasive Radiofrequency Ablation of Malignancies Mediated by Quantum Dots, Gold Nanoparticles and Carbon Nanotubes. *Ther. Delivery* **2011,** *2,* 1325-1330.
55. Moran, C. H.; Wainerdi, S. M.; Cherukuri, T. K.; Kittrell, C.; Wiley, B. J.; Nicholas, N. W.; Curley, S. A.; Kanzius, J. S.; Cherukuri, P. Size-Dependent Joule Heating of Gold Nanoparticles Using Capacitively Coupled Radiofrequency Fields. *Nano Res.* **2009,** *2,* 400-405.
56. Kruse, D. E.; Stephens, D. N.; Lindfors, H. A.; Ingham, E. S.; Paoli, E. E.; Ferrara, K. W. A Radio-Frequency Coupling Network for Heating of Citrate-Coated Gold Nanoparticles for Cancer Therapy: Design and Analysis. *IEEE Trans. Biomed. Eng.* **2011,** *58,* 2002-2012.
57. Pearce, J. A.; Cook, J. R. Heating Mechanisms in Gold Nanoparticles at Radio Frequencies. Engineering in Medicine and Biology Society, EMBC, 2011 Annual International Conference of the IEEE 5577-5580.
58. McCoy, R. S.; Choi, S.; Collins, G.; Ackerson, B. J.; Ackerson, C. J. Superatom Paramagnetism Enables Gold Nanocluster Heating in Applied Radiofrequency Fields. *ACS Nano* **2013,** *7,* 2610-2616.
59. Collins, C. B.; McCoy, R. S.; Ackerson, B. J.; Collins, G. J.; Ackerson, C. J. Radiofrequency Heating Pathways for Gold Nanoparticles. *Nanoscale* **2014,** *6,* 8459-8472.
60. Cardinal, J.; Klune, J. R.; Chory, E.; Jeyabalan, G.; Kanzius, J. S.; Nalesnik, M.; Geller, D. A. Non-Invasive Radiofrequency Ablation of Cancer Targeted by Gold Nanoparticles. *Surgery* **2008,** *144,* 125-132.
61. Glazer, E. S.; Curley, S. A. Radiofrequency Field-Induced Thermal Cytotoxicity in Cancer Cells Treated With Fluorescent Nanoparticles *Cancer* **2010,** *116,* 3285-3293.
62. Raoof, M.; Corr, S. J.; Kaluarachchi, W. C.; Massey, K. L.; Briggs, K.; Zhu, C.; Cheney, M. A.; Wilson, L. J.; Curley, S. A. Stability of Antibody-Conjugated Gold Nanoparticles in the Endolysosomal Nanoenvironment: Implications for Non-Invasive Radiofrequency-Based Cancer Therapy. *Nanomedicine* **2012,** *8,* 1096-1105.
63. Glazer, E. S.; Zhu, C.; Massey, K. L.; Thompson, C. S.; Kaluarachchi, W. D.; Hamir, A. N.; Curley, S. A. Noninvasive Radiofrequency Field Destruction of Pancreatic Adenocarcinoma Xenografts Treated with Targeted Gold Nanoparticles. *Clin. Cancer Res.* **2010,** *16,* 5712-5721.

64. Raoof, M.; Corr, S. J.; Zhu, C.; Cisneros, B. T.; Kaluarachchi, W. D.; Phounsavath, S.; Wilson, L. J.; Curley, S. A. Gold Nanoparticles and Radiofrequency in Experimental Models for hepatocellular Carcinoma. *Nanomedicine: Nanotechnology, Biology, and Medicine* **2014,** *10,* 1121-1130.
65. J. S. Kanzius, US Patent Publication Nos. US20050251233 A1, US20050251234 A1, and US20060190063 A1.
66. Houston-Based AkesoGenX Corp. http://bionews-tx.com/news/2014/01/20/houston-based-akesogenx-corp-acquires-rights-to-kanzius-cancer-treatment-technology-will-move-to-commercialize-noninvasive-radio-wave-cancer-treatment/ (accessed January 28, 2016).
67. Kanzius Cancer Research Foundation. http://www.kanziuscancerresearch.org (accessed January 28, 2016).
68. NeoTherma Oncology. http://www.neothermaoncology.com/ (accessed January 28, 2016).
69. Kanzius Cancer Machine Gets its First Human Trial http://www.newsweek.com/2015/07/31/kanzius-cancer-machine-gets-its-first-human-trial-355758.html (accessed January 28, 2016).
70. Li, D.; Jung, Y. S.; Tan, S.; Kim, H. K.; Chory, E.; Geller, D. A. Negligible Absorption of Radiofrequency Radiation by Colloidal Gold Nanoparticles. *J. Colloid Interface Sci.* **2011,** *358,* 47-53.
71. Sassaroli,, E.; Li, K. C. P.; O'Neill, B. E. Radio Frequency Absorption in Gold Nanoparticle Suspensions: A Phenomenological Study. *J. Phys. D: Appl. Phys.* **2012,** *45,* 075303.
72. Liu, X.; Chen, H.-J.; Chen, X..; Parini, C.; Wen, D. Low Frequency Heating of Gold Nanoparticle Dispersions for Non-Invasive Thermal Therapies. *Nanoscale* **2012,** *4,* 3945-3953.
73. Corr, S. J.; Raoof, M.; Mackeyev, Y.; Phounsavath, S.; Cheney, M. A.; Cisneros, B. T.; Shur, M.; Gozin, M.; McNally, P. J.; Wilson, L. J.; Curley, S. A. Citrate-Capped Gold Nanoparticle Electrophoretic Heat Production in Response to a Time-Varying Radio-Frequency Electric Field. *J. Phys. Chem. C* **2012,** *116,* 24380-24389.
74. Bogdanov, A. A.; Gupta, S.; Koshkina, N.; Corr, S. J.; Zhang, S.; Curley, S. A.; Han, G. Gold Nanoparticles Stabilized with MPEG-Grafted Poly(L-lysine): *In Vitro* and *in Vivo* Evaluation of a Potential Theranostic Agent. *Bioconj. Chem.* **2015***, 26,* 39-50.
75. Raoof, M.; Zhu, C.; Kaluarachchi, W. D.; Curley, S. A. Luciferase-Based Protein Denaturation Assay for Quantification of Radiofrequency Field-Induced Targeted Hyperthermia: Developing an Intracellular Thermometer. *Int. J. Hyperthermia* **2012,** *28,* 202-209.
76. Curley, S. A.; Cherukuri, P.; Briggs, K.; Patra, C. R.; Upton, M.; Dolson, E.; Mukherjee, P. Noninvasive Radiofrequency Field-Induced Hyperthermia Cytotoxicity in Human Cancer Cells Using Cetuximab-Targeted Gold Nanoparticles. *J. Exp. Ther. Oncol.* 2008, *7,* 313-326.
77. Gannon, C. J.; Patra, C. R.; Bhattacharya, R.; Mukherjee, P.; Curley, S. A. Intracellular Gold Nanoparticles Enhance Non-Invasive Radiofrequency Thermal Destruction of Human Gastrointestinal Cancer Cells. *J. Nanobiotechnol.* **2008,** *6,* 1-9.
78. Huang, H.-C.; Rege, K.; Heys, J. J. Spatiotemporal Temperature Distribution and Cancer Cell Death in Response to Extracellular Hyperthermia Induced by Gold Nanorods. *ACS Nano* **2010,** *4,* 2892-2900.
79. Jang, B.: Kim, Y. S.; Choi, Y. Effect of Gold Nanorod Concentration on the Depth-Related Temperature Increase During Hyperthermic Ablation. *Small* **2011,** *2,* 265-270.
80. Chen, H.; Shao, L.; Ming, T.; Sun, Z.; Zhao, C.; Yang, B.; Wang, J. Understanding the Photothermal Conversion Efficiency of Gold Nanocrystals. *Small* **2010,** *6,* 2272-2280.
81. Richardson, H. H.; Carlson, M. T.; Tandler, P. J.; Hernandez, P.; Govorov, A. O. Experimental and Theoretical Studies of Light-to-Heat Conversion and Collective Heating Effects in Metal Nanoparticle Solutions. *Nano Lett.* **2009,** *9,* 1139-1146.
82. Jiang, K.; Smith, D. A.; Pinchuk, A. Size-Dependent Photothermal Conversion Efficiencies of Plasmonically Heated Gold Nanoparticles. *J. Phys. Chem. C* **2013,** *117,* 27073-27080.
83. Mackey, M. A.; Ali, M. R. K.; Austin, L. A.; Near, R. D.; El-Sayed, M. A. The Most Effective Gold Nanorod Size for Plasmonic Photothermal Therapy: Theory and *In Vitro* Experiments. *J. Phys. Chem. B* **2014,** *118,* 1319-1326.
84. Huang, P.; Rong, P.; Lin, J.; Li, W.; Yan, x.; Zhang, M. G.; Nie, L.; Niu, G.; Lu, J.; Chen, X. Triphase Interface Synthesis of Plasmonic Gold Bellflowers as Near-Infrared Light Mediated Acoustic Thermal Theranostics. *J. Am. Chem. Soc*. **2014,** *136,* 8307-8313.
85. Zeng, J.; Goldfeld, D.; Xia, Y. A Plasmon-Assisted Optofluidic (PAOF) System for Measuring the Photothermal Conversion Efficiencies of Gold Nanostructures and Controlling an Electrical Switch. *Angew. Chem. Int. Ed.* **2013,** *52,* 4169-4173.

86. Huang, P.; Lin, J.; Li, W.; Rong, P.; Wang, Z.; Wang, S.; Wang, X.; Sun, X.; Aronova, M.; Niu, G.; Leapman, R. D.; Nie, Z.; Chen, X. Biodegradable Gold Nanovesicles with an Ultrastrong Plasmonic Coupling Effect for Photoacoustic Imaging and Photothermal Therapy*. Angew. Chem. Int. Ed.* **2013,** *52,* 13958-13964.
87. Santos, G. M.; Zhao, F.; Zeng, J.; Shih, W.-C. Characterization of Nanoporous Gold Disks for Photothermal Light Harvesting and Light-Gated Molecular Release. *Nanoscale* **2014,** *6,* 5718-5724.
88. Cole, J. R.; Mirin, N. A.; Knight, M. W.; Goodrich, G. P.; Halas, N. J. Photothermal Efficiencies of Nanoshells and Nanorods for Clinical Therapeutic Applications. *J. Phys. Chem C* **2009,** *113,* 12090-12094.
89. Pattani, V. P.; Tunnell, J. W. Nanoparticle-Mediated Photothermal Therapy: A Comparative Study of Heating for Different Particle Types. *Lasers in Surg. and Med.* **2012,** *44,* 675-684.
90. Ayala-Orozco, C.; Urban, C.; Knight, M. W.; Urban, A. S.; Neumann, O.; Bishnoi, S. W.; Mukherjee, S.; Goodman, A. M.; Charron, H.; Mitchell, T.; Shea, M.; Roy, R.; Nanda, S.; Schiff, R.; Halas, N. J.; Josh, A. Au Nanomatryoshkas as Efficient Near-Infrared Photothermal Transducers for Cancer Treatment: Benchmarking Against Nanoshells. *ACS Nano* **2014,** *8,* 6372-6381.
91. Huang, J.; Park, J.; Wang, W.; Murphy, C. J. Cahill, D. G. Ultrafast Thermal Analysis of Surface Functionalized Gold Nanorods in Aqueous Solution. *ACS Nano* **2013,** *7,* 589-597.
92. Link, S.; Burda, C.; Mohamed, M. B.; Nikoobakht, B.; El-Sayed, M. A. Laser Photothermal Melting and Fragmentation of Gold Nanorods: Energy and Laser Pulse-Width Dependence*. J. Phys. Chem. A* **1999,** *103,* 1165-1170.
93. Ungureanu, C.; Kroes, R.; Petersen, W.; Groothuis, T. A. M.; Ungureanu, F.; Janssen, H.; van Leeuwen, F. W. B.; Kooyman, R. P. H.; Manohar, S.; van Leeuwen, T. G. Light Interactions with Gold Nanorods and Cells: Implications for Photothermal Nanotherapeutics. *Nano Lett.* **2011,** *11,* 1887-1894.
94. Hildebrandt, B.; Wust, P.; Ahlers, O.; Dieing, A.; Sreenivasa, G.; Kerner, T.; Felix, R.; Riess, H. The Cellular and Molecular Basis of Hyperthermia. *Critical Rev. Oncol. Hemat.* **2002,** *43,* 33-56.
95. Jaque, D.; Maestro, L. M.; del Rosal, B.; Haro-Gonzaléz, P.; Benayas, A.; Plaza, J. L.; Rodriguez, E. M.; Solé, J. G. Nanoparticles for Photothermal Therapies. *Nanoscale* **2014,** *6,* 9494-9530.
96. Melamed, J. R.; Edelstein, R. S.; Day, E. S. Elucidating the Fundamental Mechanisms of Cell Death Triggered by Photothermal Therapy. *ACS Nano* **2015,** *9,* 6-11
97. Edinger, A. L.; Thompson, C. B. Death by Design: Apoptosis, Necrosis and Autophagy. *Curr. Opin. Cell Biol.* **2004,** *16,* 663-669.
98. Tong, L.; Zhao, Y.; Huff, T. B.; Hansen, M. N.; Wei, A.; Cheng, J.-X. Gold Nanorods Mediate Tumor Cell Death by Compromising Membrane Integrity*. Adv. Mater.* **2007,** *19,* 3136-3141.
99. Coleman, M. L.; Sahai, E. A.; Yeo, M.; Bosch, M.; Dewar, A.; Olson, M. F. Membrane Blebbing During Apoptosis Results from Caspase-Mediated Activation of ROCK I. *Nat. Cell Biol.* **2001,** *3*, 339-345.
100. Huang, X.; Kang, B.; Qian, W.; Mackey, M. A.; Chen, P. C.; Oyelere, A.; El-Sayed, I. H.; El-Sayed, M. A. Comparative, Study of Photothermolysis of Cancer Cells with Nuclear-Targeted or Cytoplasm-Targeted Gold Nanospheres: Continuous Wave or Pulsed Lasers. *J. Biomed. Optics* **2010,** *15,* 058002.
101. Li, J.-L.; Gu, M. Surface Plasmonic Gold Nanorods for Enhanced Two-Photon Microscopic Imaging and Apoptosis Induction of Cancer Cells. *Biomaterials* **2010,** *31,* 9492-9498.
102. Chen, C.-L.; Kuo, L.-R.; Chang, C.-L.; Hwu, Y.-K.; Huang, C.-K.; Lee, S.-Y.; Chen, K.; Lin, S.-J.; Huang, J.-D.; Chen, Y.-Y. *In situ* Real-Time Investigation of Cancer Cell Photothermolysis Mediated by Excited Gold Nanorod Surface Plasmons. *Biomaterials* **2010,** *31,* 4104-4112.
103. Pérez-Hernández, M.; del Pino, P.; Mitchell, S. G.; Moros, M.; Stepien, G.; Pelaz, B.; Parak, W. J.; Gálvez, E. M.; Pardo, J.; de la Fuente, J. M. Dissecting the Molecular Mechanism of Apoptosis during Photothermal Therapy Using Gold Nanoprisms. *ACS Nano* **2015,** *9,* 52-61.
104. Pattani, V. P.; Shah, J.; Atalis, A.; Sharma, A.; Tunnell, J. W. Role of Apoptosis and Necrosis in Cell Death Induced by Nanoparticle-Mediated Photothermal Therapy. *J. Nanopart. Res.* **2015,** *17,* 20.
105. Van de Broek, B.; Devoogdt, N.; D'Hollander, A.; Gijs, H.-L.; Jans, K.; Lagae, L.; Muyldermans, S.; Maes, G.; Borghs, G. Specific Cell Targeting with Nanobody Conjugated Branched Gold Nanoparticles for Photothermal Therapy. *ACS Nano* **2011,** *5,* 4319-4328.

106. Yuan, H.; Fales, A. M.; Vo-Dinh, T. TAT Peptide-Functionalized Gold Nanostars: Enhanced Intracellular Delivery and Efficiently NIR Photothermal Therapy Using Ultralow Irradiance. *J. Am. Chem. Soc.* **2012,** *134,* 11358-11361.
107. Ali, M. R. K.; Panikkanvalappil, S. R.; El-Sayed, M. A. Enhancing the Efficiency of Gold Nanoparticles Treatment of Cancer by Increasing Their Rate of Endocytosis and Cell Accumulation Using Rifampicin. *J. Am. Chem. Soc.* **2014,** *136,* 4464-4467.
108. Qian L. P.; Zhou, L. H.; Too, H.-P.; Chow, G.-M. Gold Decorated $NaYF_4$:Yb,Er/$NaYF_4$/silica (Core/Shell/Shell) Upconversion Nanoparticles for Photothermal Destruction of Be(2)-C Neuroblastoma Cells. *J. Nanopart. Res.* **2011,** *13,* 499-510.
109. Wu, P.; Gao, Y.; Zhang, H.; Cai, C. Aptamer-Guided Silver-Gold Bimetallic Nanostructures with Highly Active Surface-Enhanced Raman Scattering for Specific Detection and Near-Infrared Photothermal Therapy of Human Breast Cancer Cells. *Anal. Chem.* **2012,** *84,* 7692-7699.
110. Ke, H.; Wang, J.; Dai, Z.; Jin, Y.; Qu, E.; Xing, Z.; Guo, C.; Yue, X, Liu, J. Gold-Nanoshelled Microcapsules: A Theranostic Agent for Ultrasound Contrast Imaging and Photothermal Therapy. *Angew. Chem. Int. Ed.* **2011,** *123,* 3073-3077.
111. Khan, S. A.; Kanchanapally, R.; Fan, Z.; Beqa, L.; Sing, A. K.; Senapati, D.; Ray, P. C. A Gold Nanocage-CNT Hybrid for Targeted Imaging and Photothermal Destruction of Cancer Cells. *Chem. Commun.* **2012,** *48,* 6711-6713.
112. Farokhzad, O. C.; Langer, R. Impact of Nanotechnology on Drug Delivery. *ACS Nano* **2009,** *3,* 16-20.
113. Yang, X.; Liu, X.; Liu, Z.; Pu, F.; Ren, J.; Qu, X. Near-Infrared Light-Triggered, Targeted Drug Delivery to Cancer Cells by Aptamer Gated Nanovehicles. *Adv. Mater.* **2012,** *24,* 2890-2895.
114. Shi, P.; Qu, K.; Wang, J.; Li, M..; Ren, J.; Qu, X. pH-Responsive NIR Enhanced Drug Release From Gold Nanocages Possesses High Potency Against Cancer Cells. *Chem. Commun.* **2012,** *48,* 7640-7642.
115. Ma, Y.; Liang, X.; Tong, S.; Bao, G; Ren, Q.; Dai, Z. Gold Nanoshell Nanomicelles for Potential Magnetic Resonance Imaging, Light-Triggered Drug Release, and Photothermal Therapy. *Adv. Funct. Mater.* **2013,** *23,* 815-822.
116. Agostinis, P.; Berg, K.; Cengel, K. A.; Foster, T. H.; Girotti, A. W.; Gollnick, S.. O.; Hahn, S. M.; Hamblin, M. R.; Juzeniene, A.; Kessel, D.; Korbelik, M.; Moan, J.; Mroz, P.; Nowis, D.; Piette, J.; Wilson, B. C. Golab, J. Photodynamic Therapy of Cancer: An Update. *CA- Cancer J. Clin.* **2011,** *61,* 250-281.
117. Gao, L.; Fei, J..; Zhao, J.; Li, H.; Cui, Y.; Li, J. Hypocrellin-Loaded Gold Nanocages with High Two-Photon Efficiency for Photothermal/Photodynamic Cancer Therapy *In Vitro*. *ACS Nano* **2012,** *6,* 8030-8040.
118. Wang, J.; Zhu, G.; You, M.; Song, E.; Shukoor, M. I.; Zhang, K.; Altman, M. B.; Chen, Y.; Zhu, Z.; Huang, C. Z.; Tan, W. Assembly of Aptamer Switch Probes and Photosensitizer on Gold Nanorods for Targeted Photothermal an Photodynamic Cancer Therapy. *ACS Nano* **2012,** *6,* 5070-5077.
119. Kuo, W.-S.; Chang, Y.-T.; Cho, K.-C.; Chiu, K.-C.; Lien, C.-H.; Yeh, C.-S.; Chen, S.-J. Gold Nanomaterials Conjugated with Indocyanine Green for Dual-Modality Photodynamic and Photothermal Therapy. *Biomaterials* **2012,** *33,* 3270-3278.
120. Tibbitt, M. W.: Anseth, K. S. Hydrogels as Extracellular Matrix Mimics for 3D Cell Culture. *Biotech. Bioeng.* **2009,** *103,* 655-663.
121. Lee, J.; Lilly, D.; Doty, C.; Podsiadlo, P.; Kotov, N. A. *In vitro* Toxicity Testing of Nanoparticles in 3D Cell Culture. *Small* **2009,** *10,* 1213-1221.
122. Ke, H.; Yu, X.; Wang, J.; Xing, ,S.; Zhang, Q.; Dai, Z, Tian, J.; Wang, S.; Jin, Y. Gold Nanoshelled Liquid Perfluorocarbon Nanocapsules for Combined Dual Modal Ultrasound/CT Imaging and Photothermal Therapy of Cancer. *Small* **2014,** *10,* 1220-1227.
123. Gao, Y.; Li, Y.; Wang, Y.; Chen, Y.; Gu, J.; Zhao, W.; Ding, J.; Shi, J. Controlled Synthesis of Multilayered Gold Nanoshells for Enhanced Photothermal Therapy and SERS Detection. *Small* **2015,** *11,* 77-83.
124. Lin, A. Y.; Young, J. K.; Nixon, A. V.; Drezek, R. A. Encapsulated Fe_3O_4/Ag Complexed Cores in Hollow Gold Nanoshells for Enhanced Theranostic Magnetic Resonance Imaging and Photothermal Therapy. *Small* **2014,** *10,* 16, 3246-3251.
125. Sun, X.; Huang, X.; Yan, X.; Wang, Y.; Guo, J.; Jacobsen, O, Liu, D.; Szajek, L. P.; Zhu, W.; Niu, G.; Kiesewetter, D. O.; Sun, S.; Chen. X. Chelator-Free ^{64}Cu-Integrated Gold Nanomaterials for Positron

Emission Tomography Imaging Guided Photothermal Cancer Therapy. *ACS Nano* **2014,** *8,* 8438-8446.
126. Liu, H.; Liu, T.; Wu, X.; Li, L.; Tan, L.; Chen, D.; Tang, F. Targeting Gold Nanoshells on Silica Nanorattles: a Drug Cocktail to Fight Breast Tumors *via* a Single Irradiation with Near-Infrared Laser Light. *Adv. Mat.* **2012,** *24,* 755-761.
127. Shao, J.; Griffin, R. J.; Galanzha, E. I.; Kim, J.-W.; Koonce, N.; Webber, J.; Mustafa, T.; Biris, A. S.; Nedosekin, D. A.; Zharov, V. P. Photothermal Nanodrugs: Potential of TNF-Gold Nanospheres for Cancer Theranostics. *Sci. Rep.* **2013,** *3,* 1293
128. Nam, J.; La, W.-G.; Hwang, S.; Ha, Y. S.; Park, N.; Won, N.; Jung, S.; Bhang, S. H.; Ma, Y.-J.; Cho, Y.-M.; Jin, M..; Han, J.; Shin, J.-Y.; Wang, E. K.; Kim, S. G.; Cho, S.-H.; Yoo, J.; Kim, B.-S.; Kim, S. pH-Responsive Assembly of Gold Nanoparticles and "Spatiotemporally Concerted" Drug Release for Synergistic Cancer Therapy. *ACS Nano* **2013**, *7,* 3388-3402.
129. Lin, J.; Wang, S.; Huang, P.; Wang, Z.; Chen, S.; Niu, G.; Li, W.; He, J.; Cui, D.; Lu, G.; Chen, X.; Nie, Z.; Photosensitizer-Loaded Gold Vesicles with Strong Plasmonic Coupling Effect for Imaging-Guided Photothermal/Photodynamic Therapy. *ACS Nano* **2013,** *7,* 5320-5329.
130. Vijayaraghavan, P.; Liu, C.-H.; Vankayala, R.; Chang, C.-S.; Hwang, K. C. Designing Multi-Branched Gold Nanoechinus for NIR Light Dual Modal Photodynamic and Photothermal Therapy in the Second Biological Window. *Adv. Mater.* **2014,** *26,* 6689-6695.
131. Jang, B.; Park, J.-Y.; Tung, C.-H.; Kim, I.-H.; Choi, Y. Gold Nanorod-Photosensitizer Complex for Near Infrared Fluorescence Imaging and Photodynamic/Photothermal Therapy *In vivo*. *ACS Nano* **2011,** *5,* 1086-1094.
132. Li, Y.-F.; Chen, C. Fate and Toxicity of Metallic and Metal-Containing Nanoparticles for Biomedical Applications. *Small* **2011,** *7,* 2965-2980.
133. Sonovane G.; Tomoda, K.; Makino, K. Biodistribution of Colloidal Gold Nanoparticles After Intravenous Administration: Effect of Particle Size. *Colloids Surf., B* **2008,** *66,* 274-280.
134. Wang, Y.; Black, K. C. L.; Luehmann, H.; Li, W.; Zhang, Y.; Cai, X.; Wan, D.; Liu, S.-Y.; Li, M.; Kim, P.; Li, Z.-Y.; Wang, L. V.; Liu, Y.; Xia, Y. Comparison Study of Gold Nanohexapods, Nanorods, and Nanocages for Photothermal Cancer Treatment. *ACS Nano* **2013,** *7,* 2068-2077.
135. Ayala-Orozco, C.; Urban, C.; Bishnoi, S.; Urban, A.; Charron, H.; Mitchell, T.; Shea, M.; Nanda, S.; Schiff, R.; Halas, N.; Joshi, A. Sub-100 nm Gold Nanomatryoshkas Improve Photo-Thermal Therapy Efficacy in Large and Highly Aggressive Triple Negative Breast Tumors. *J. Control. Release* **2014,** *191,* 90-97.
136. Puvanakrishnan, P.; Park, J.; Chatterjee, D.; Krishnan, S.; Tunnell, J. W. In vivo Tumor Targeting of Gold Nanoparticles: Effect of Particle Type and Dosing Strategy. *Int. J. Nanomed.* **2012,** *7,* 1251-1258.
137. Choi, C. H. J.; Alabi, C. A.; Webster, P.; Davis, M. E. Mechanism of Active Targeting in Solid Tumors with Transferrin-Containing Gold Nanoparticles. *Proc. Natl. Acad. Sci. U. S. A.* **2010,** *107,* 1235-1240.
138. Huang, X.; Peng, X.; Wang, Y.; Wang, Y.; Shin, D. M.; El-Sayed, M. A.; Nie, S. A Reexamination of Active and Passive Tumor Targeting by Using-Rod-Shaped Gold Nanocrystals and Covalently Conjugated Peptide Ligands. *ACS Nano* **2010,** *4,* 5887-5896.
139. Chanda, N.; Kattumuri, V.; Shukla, R.; Zambre, A.; Katti, K.; Upendran, A.; Kulkarni, R. R.; Kan, P.; Fent, G. M.; Casteel, S. W.; Smith, C. J.; Boote, E.; Robertson, J. D.; Cutler, C.; Lever, J. R.; Katti, K. V.; Kannan, R. Bombesin Functionalized Gold Nanoparticles Show *In vitro* and *In vivo* Cancer Receptor Specificity. *Proc. Natl. Acad. Sci. U. S. A.* **2010,** *107,* 8760-8765.
140. Kai, M. P.; Brighton, H. E.; Fromen, C. A.; Shen, T. W.; Luft, J. C.; Luft, Y. E.; Keeler, A. W.; Robbins, G. R.; Ting, J. P. Y.; Zamboni, W. C.; Bear, J. E.; DeSimone, J. M. Tumor Presence Induces Global Immune Changes and Enhances Nanoparticle Clearance. *ACS Nano* **2016,** *10,* 861-870.
141. García, K. P.; Zarschler, K.; Barbaro, L.; Barreto, J. A.; O'Malley, W.; Spiccia, L.; Stephan, H.; Graham, B. Zwitterionic-Coated "Stealth" Nanoparticles for Biomedical Applications: Recent Advances in Countering Biomolecular Corona formation and Uptake by the Mononuclear Phagocyte System. *Small,* **2014,** *10,* 2516-2529.
142. Lundqvist, M.; Stigler, J.; Elia, G.; Lynch, I.; Cedervall, T.; Dawson, K. A. Nanoparticle Size and Surface Properties Determine the Protein Corona with Possible Implications for Biological Impacts. *Proc. Natl. Acad. Sci. U. S. A.* **2008,** *105,* 14265-14270.

143. Lin, W.; Insley T.; Tuttle, M. D.; Zhu, L.; Berthold, D. A.; Král, P.; Rienstra, C. M.; Murphy, C. J. Control of Protein Orientation on Gold Nanoparticles. *J. Phys. Chem C* **2015,** *119,* 21035-21043.
144. Walkey C. D.; Chan, W. C. W. Understanding and Controlling the Interaction of Nanomaterials with Proteins in a Physiological Environment. *Chem. Soc. Rev.* **2012,** *41,* 2780-2799.
145. Cheng, Z.; Zaki, A. A.; Hui, J. Z.; Muzykantov, V. R.; Tsourkas, A. Multifunctional Nanoparticles: Cost Versus Benefit of Adding Targeting and Imaging Capabilities. *Science* **2012,** *338,* 903-910.
146. Chen, J.; Glaus, C.; Laforest, R.; Zhang, Q.; Yang, M.; Gidding, M.; Welch, M. J.; Xia, Y. Gold Nanocages as Photothermal Transducers for Cancer Treatment. *Small* **2010,** *6,* 811-817.
147. Mooney, R.; Roma, L.; Zhao, D.; Van Haute, D.; Garcia, E.; Kim, S. U.; Annala, A. J.; Aboody, K. S.; Berlin, J. M. Neural Stem Cell-Mediated Intratumoral Delivery of Gold Nanorods Improves Photothermal Therapy. *ACS Nano* **2014,** *8,* 12450-12460.
148. Prabhakar, U.; Maeda, H.; Jain, R. K.; Sevick-Muraca, E. M.; Zamboni, W.; Farokhzad, O. C.; Barry, S. T.; Gabizon, A.; Piotr, G.; Blakey, D. C. Challenges and Key Considerations of the Enhanced Permeability and Retention Effect for Nanomedicine Drug Delivery in Oncology. *Cancer Res.* **2013,** *73,* 2412-2417.
149. Kumar, A.; Zhang, X.; Liang, X.-J. Gold Nanoparticles: Emerging Paradigm for Targeted Drug Delivery System. *Biotechnol. Adv.* **2013,** *13,* 593-606.
150. Nanospectra. http://www.nanospectra.com/ (accessed January 28, 2016).
151. Weissleder, R. A Clearer Vision for In vivo Imaging. *Nat. Biotechnol.* **2001,** *19,* 316-317.
152. Schwartz, J. A.; Shetty, A. M.; Price, R. E.; Stafford, R. J.; Wang, J. C.; Uthamanthil, R. K.; Pham, K.; McNichols, R. J.; Coleman, C. L.; Payne, J. D. Feasibility Study of Particle-Assisted Laser Ablation of Brain Tumors in Orthotopic Canine Model. *Cancer Res.* **2009,** *69,* 1659-1667.
153. Pilot Study of AuroLase™ Therapy in Refractory and/or Recurrent Tumors of the Head and Neck. https://clinicaltrials.gov/show/NCT00848042 (accessed January 28, 2016).
154. Efficacy Study of AuroLase Therapy in Subjects With Primary and/or Metastatic Lung Tumors. https://clinicaltrials.gov/ct2/show/NCT01679470 (accessed January 28, 2016).
155. Alkilany, A. M.; Lohse S. E.; Murphy, C. J. The Gold Standard: Gold Nanoparticle Libraries To Understand the Nano-Bio Interface. *Acc. Chem. Res.* **2013,** *46,* 650-661.
156. Athymic Nude Mice http://www.simlab.com/products/nudes.html (accessed January 28, 2016).
157. Gold NanoRods. http://nanohybrids.net/products/gold-nanorods-1 (accessed January 28, 2016).
158. Gold NanoRods https://cdn.shopify.com/s/files/1/0259/2325/files/Tech_Specs_NanoHybrids_-_CTAB_stabilized_PEGylated_Gold_NanoRods.pdf?3044871944869406716 (accessed January 28, 2016).
159. Schnipper, L. E.; Davidson, N. E.; Wollins, D. S.; Tyne, C.; Blayney, D. W.; Blum, D.; dicker, A. P.; Ganz, P. A.; Hoverman, J. R.; Langdon, R.; Lyman, G. H.; Meropal, N. J.; Mulvey, T.; Newcomer, L.; peppercorn, J.; Polite, B.; Raghavan, D.; Rossi, G.; Saltz, L.; Schrag, D.; Smith, T. J.; Yu, P. P.; Hudis, C. A.; Schilsky, R. L. American Society of clinical Oncology Statement: A Conceptual Framework to Assess the Value of Cancer Treatment Options. *J. Clin. Oncol.* **2015,** *33, 2563-2577*.
160. O'Neill, C. B.; Atoria, C. L.; O'reilly, E. M.; LaFemina, J.; Henman, M. C.; Elkin, E. B. Costs and Trends in Pancreatic Cancer Treatment. *Cancer* **2012,** *118,* 5132-5139.
161. Smith, B.; Cohn, D. E.; Clements, A.; Tierney, B. J.; Straughn, J. M. Is the Progression Free Survival Advantage of Concurrent Gemcitabine Plus Cisplatin and Radiation Followed by Adjuvant Gemcitabine and Cisplatin in Patients with Advanced Cervical Cancer Worth the Additional Cost? A Cost-Effective Analysis. *Gynecol. Oncol.* **2013,** *130,* 416-420.
162. Shin, S. J.; Beech, J. R.; Kelly, K. A. Targeted Nanoparticles in Imaging: Paving the Way for Personalized Medicine in the Battle Against Cancer. *Integr. Biol.* **2013,** *5,* 29-42.

CHAPTER 5:
PHOTOTHERMAL INACTIVATION OF THE THERMOPHILIC BACTERIUM *GEOBACILLUS STEAROTHERMOPHILUS* USING GOLD NANORODS

5.1 INTRODUCTION

The interface between bacteria and metal nanoparticles is a growing field of research and is interesting for a variety of reasons.[1-3] For example, gold nanoparticles can be prepared *via* microbial synthesis,[4,5] and it is thought that the environmental fate of gold nanomaterials is strongly tied to nanoparticle-bacterial surface interactions.[6-8] Additionally, gold nanoparticles have been used in applications related to microbial sensing or antibacterial treatment. It is possible to detect or quantify pathogens using techniques such as fluorescence spectroscopy,[9] light-scattering,[10-12] colorimetric assays,[13-15] or surface-enhanced Raman spectroscopy.[16-20] Gold nanoparticles have also been used as antibacterial agents with surface coatings that are antimicrobial,[21-23] as delivery agents to carry antibiotic drug payloads,[24-27] or to carry photosensitizers for enhanced photodynamic therapy.[28-31] These applications are possible because of the unique size-dependent optical properties of gold nanomaterials, and they are realized by careful control of nanoparticle size, shape and surface chemistry.[1-3]

Laser photothermal heating is another potential application of gold nanoparticles which might be used to kill bacteria.[2] Photothermal heating is a well-known phenomenon, and occurs because of the strong absorbance of light by gold nanoparticles. Gold nanoparticles absorb light at frequencies which are resonant with their localized surface plasmon resonance (LSPR).[32] The LSPR is the coherent oscillation of conduction band electrons. The LSPR wavelength is dependent upon the size and shape of a plasmonic nanoparticle, and shape can be synthetically controlled, resulting in LSPR tunability from the visible to the near-infrared (NIR). When gold nanoparticles absorb light, the LSPR is excited and the energy absorbed by the crystal lattice can be dissipated as heat *via* electron-phonon and phonon-phonon interactions on picosecond timescales. This can heat up the surrounding medium by tens of degrees and the local temperature rise around a gold nanoparticle can be even greater.[33]

If laser-irradiated gold nanoparticles are bound to or near a cell surface, the heat generated can be great enough to cause cell death. Photothermal therapy using NIR irradiation has been carried out in a variety of cancer cell lines *in vitro* and *in vivo,* and has been used in clinical trials for the treatment of head, neck, and lung cancers.[33] Photothermal heating has also been demonstrated to kill pathogenic bacteria.[2,33,34] In those reports, gold nanoparticles are usually functionalized with a targeting ligand which facilitates particle binding to the bacterial surface. Subsequent laser irradiation of the suspension by continuous or pulsed lasers can result in a significant amount of bacterial cell death or inactivation. Researchers have demonstrated successful killing of a variety of bacterial strains including *Escherichia coli*,[36] *Bacillus subtilis*, *Exiguobacterium*,[37] *Streptococcus*,[38] *Salmonella typhimurium*,[39,40] *Pseudomonas aeruginosa*,[41] and *Staphylococcus aureus*.[31,42,43] The success of systems such as these are promising and exciting as the threat of antibiotic resistant bacteria continues to increase.[44]

To our knowledge, while there have been many demonstrations of photothermal inactivation of various strains of bacterial cells, no researchers have investigated photothermal inactivation of bacterial endospores. Because of their resistance to extreme conditions, bacterial endospores are a useful candidate for laser photothermal heating studies. Sporulation is a process which is triggered in certain strains of Gram-positive bacteria when they encounter conditions which are unfavorable for growth. Bacterial endospores are living structures which exist in a dormant state.[45] They have no metabolism and are highly resistant to extreme environmental conditions such as extreme heat, UV light, or harsh chemicals.[46] This is due to the dehydrated nature of the spore core and the presence of a thick spore coat, cortex and cell wall which reduces access to the spore interior. Endospores can therefore be more antibiotic resistant than their vegetative cell counterparts.[47] However, while spores are not hazardous in their dormant state, this does not render them harmless. An endospore can exist for thousands of years, and when conditions are favorable for growth, a series of signaling events take place, and the spore will germinate to form a new vegetative cell. Spore-forming bacteria such as *Bacillus anthracis*, *Bacillus cereus*, and *Clostridium botulinum* have been implicated in terrorist attacks and foodborne illnesses, and might pose a threat to public health.[45-47] Therefore, it is worth investigating alternative methods which can be used to inactivate bacterial endospores.

In this report we investigate the application of gold nanorods in photothermal inactivation of endospores and vegetative cells of the thermophilic, Gram-positive spore-forming bacterium *Geobacillus stearothermophilus*. *G. stearothermophilus* is a non-pathogenic, biosafety level 1 organism, and its spores are known to be resistant to sterilization by heat, plasma, microwaves, steam or chemical agents.[48-51] Additionally, *G. stearothermophilus* endospores are a standard biological indicator to test steam-based sterilization methods so they serve as an excellent model organism for photothermal studies.[52] In this study, we compare the effect of photothermal heating on *G. stearothermophilus* using gold nanorods having four different cationic, anionic and neutrally charged polymer coatings. Gold nanorods having different surface chemistries are prepared and characterized. The nanorods are incubated with spores and vegetative cells, and then are irradiated with a continuous wave 785 nm laser diode. Inactivation of *G. stearothermophilus* is measured by a colony counting technique. The interaction between the nanorods and spore surfaces is investigated by scanning electron microscopy to determine if there is any change in endospore morphology after nanorod exposure or photothermal treatment. Additionally, photothermal treatment of vegetative cells is compared to heating in a water bath.

5.2 MATERIALS AND METHODS

5.2.1 MATERIALS

Cetyltrimethylammonium bromide (CTAB, ≥99.0%), hydrogen tetrachloroaurate trihydrate ($HAuCl_4 \cdot 3H_2O$, ≥99.9%), sodium borohydride ($NaBH_4$, ≥99%), silver nitrate ($AgNO_3$, ≥99.0%), poly(acrylic acid sodium salt) (PAA, MW ~15,000, 35 wt.% in H_2O), polyallylamine hydrochloride (PAH, MW ~15,000) polydiallyldimethyl ammonium chloride (PDDA, MW ~200,000-350,000), phosphate buffered saline (10X

PBS), and Tween80 were purchased from Sigma-Aldrich. Methoxyl polyethylene glycol thiol (PEG-SH, 5000 g/mol) was purchased from Nanocs. L (+)-ascorbic acid (99%) was purchased from Acros Organics. Butterfield's buffer and Petrifilm Aerobic Count Plates were purchased from Nelson-Jameson. *Geobacillus stearothermophilus* (ATCC 7953, ~10^6 CFU/0.1 mL) vegetative cells were purchased from ATCC and endospores were purchased from NAMSA. All solutions and experiments used deionized water (18 MΩ) from a Milli-Q Millipore water purification system. All chemicals and materials were used as received.

5.2.2 SYNTHESIS AND FUNCTIONALIZATION OF GOLD NANORODS

Gold nanorods were synthesized following the seed-mediated growth procedure described in a previous report.[53] The addition of $AgNO_3$ to the growth solution promotes gold nanorod formation and allows for the control of gold nanorod aspect ratio. Silver concentration was therefore adjusted so the longitudinal absorbance band maximum of the gold nanorods would overlap with the 785 nm laser for more efficient photothermal heating.

After synthesis, the gold nanorods were purified *via* centrifugation at 11,500 rcf for 20 min. The CTAB-coated gold nanorods were functionalized with PAA, PAH, PDDA, or PEG to reduce toxicity and to enhance their stability against aggregation. First, 10 mL of 1 nM CTAB gold nanorod were centrifuged a second time at 11,500 rcf for 20 min to remove any excess CTAB. The polyelectrolytes PAA, PAH, and PDDA were wrapped around the gold nanorods by following a layer-by-layer deposition technique.[54,55] The supernatant was removed and the pellet was resuspended in 10 mL of deionized water. Then, 2 mL of a polyelectrolyte solution (10 mg/mL polyelectrolyte solution and 1 mM NaCl) and 1 mL of 10 mM NaCl was added to the gold nanorod solution. The solutions were mixed *via* vortex, and then left overnight (12 h) to allow for maximum wrapping. The wrapped gold nanorods were centrifuged at 10,000 rcf for 20 min to remove excess polyelectrolyte, and then were resuspended in deionized water. For PAA coating, one layer of the negatively charged polyelectrolyte was wrapped around the positively charged CTAB gold nanorods. For positively charged polyelectrolyte coating, the CTAB gold nanorod were first wrapped in PAA, and then wrapped in the PAH or PDDA following the same technique. CTAB gold nanorods were also functionalized with PEG following a ligand exchange technique.[56] A solution of PEG-SH (2 mg/mL) was added dropwise to a pellet of concentrated gold nanorods and the solution was mixed for 24 h. The gold nanorods were purified *via* centrifugation at 10,000 rcf for 20 min. After functionalization, all of the coated gold nanorods were diluted to 3 nM with deionized water.

Functionalized gold nanorods were characterized to determine LSPR peak position, nanorod concentration, absolute dimensions, hydrodynamic size, and surface charge. UV-vis absorbance measurement of gold nanorods was carried out on a Cary 5000 UV-vis spectrophotometer (Agilent, USA). Gold nanorod concentration was determined using known extinction coefficients, which were determined in a previous report.[57] Transmission electron microscopy (TEM) images were obtained on a JEOL 2100 cryo TEM (JEOL, Japan). ImageJ analysis of TEM images (100 particles) was carried out to determine the

average dimensions and aspect ratio of the gold nanorods. Dynamic light scattering and ζ-potential measurements were carried out on a ZetaPals zeta-potential analyzer (Brookhaven, USA).

5.2.3 LASER PHOTOTHERMAL HEATING EXPERIMENTS

Functionalized gold nanorods were used in laser photothermal heating experiments with vegetative cells and endospores of the bacterium *G. stearothermophilus.* 20 µL of 3 nM gold nanorods were incubated with 10 µL of vegetative cells or spores which were ~10^6 CFU (colony-forming units) per 0.1 mL for at least 10 min. The cells were vortexed prior to incubation to ensure consistency between experiments. The solutions were irradiated with a laser for 25 minutes (785 nm, 50 mW, continuous wave (CW)). Parallel samples of a control of deionized water with cells, and a control of nanorods and cells without laser exposure were also prepared to determine the effect of nanorod exposure. Laser irradiation of cells with deionized water was carried out to control for laser exposure. Also, the effect of heat on vegetative cells was demonstrated by heating them in a water bath at 50°C, 60°C or 69°C for 25 min. Growth or inactivation of *G. stearothermophilus* was determined by colony counting. All experiments were carried out in triplicate. Additionally, scanning electron microscopy (SEM) imaging of spores alone, incubated with nanorods, and treated by photothermal heating were carried out on a Hitachi 4700 SEM. Spore samples dropcast on glass slides were sputter-coated in Au/Pd for 30 s prior to imaging. ImageJ analysis of SEM images (150 endospores) was carried out to determine the average lengths and widths of the spores.

5.2.4 QUANTIFICATION OF INACTIVATION OF *GEOBACILLUS STEAROTHERMOPHILUS*

After treatment, growth or inactivation of *G. stearothermophilus* was determined by serial dilution and colony counting (Scheme 5.1). The 30 µL samples containing cells/endospores and nanorods/deionized water were quantitatively transferred to a 10 mL solution of sterile PBS solution containing 0.1% Tween80 (called 1XPBST). The presence of the surfactant Tween 80 is used to break up any clumps of *G. stearothermophilus*.[58] Serial 10-fold dilutions of the suspension were carried out by transferring 1 mL to tubes containing 9 mL of Butterfield's buffer, and the solutions were vortexed to ensure homogenous mixing.[59] Then, 1 mL aliquots of each dilution concentration (up to 10^{-4} of the original concentration) was spread onto a Petrifilm plate.[60] The plates were incubated at 55°C overnight (~18 h) to allow enough time for growth of *G. stearothermophilus*.[61] Colonies appeared as red dots on the plates after growth. Colonies were counted visually, and the number of CFU after treatment was determined based on the dilution volume which had been used.

5.3 RESULTS AND DISCUSSION

There have been several studies which investigate gold nanoparticle interactions with vegetative cells and spores in a range of bacterial strains. Gold nanoparticles have been designed to bind to bacterial surfaces by several methods. Active targeting to proteins on a bacterial cell wall is possible by covalent attachment of specific antibodies to a nanoparticle surface.[62-64] Additionally, specific binding can be

achieved by modifying nanoparticles with sugar moieties such as mannose and galactose. This allows nanoparticles to bind to a bacterial surface *via* carbohydrate-protein interactions.[65-67] Non-specific nanoparticle attachment is also possible by exploiting electrostatic interactions between a nanoparticle and the negatively charged bacterial surface.[68] Researchers have demonstrated that self-assembly of various types of cationic gold nanoparticles on many species of bacterial cells is possible by electrostatic attachment in a variety of applications.[69-74] These studies demonstrate that gold nanoparticles can attach to bacterial cell walls, but they do not observe uptake of nanoparticles into bacterial cells. Even though nanoparticles are likely not internalized by bacteria, nanoparticle exposure can still result in cytotoxicity. This has been observed by concentration-dependent changes in viability, cell morphology and gene expression of bacteria after nanoparticle exposure in a variety of report.[75-79] Therefore, it is important to consider the impact of nanoparticle exposure on bacteria when investigating photothermal treatment.

In this report we work to expand the range of photothermal therapy to investigate inactivation of vegetative cells and spores of *G. stearothermophilus* using polymer-functionalized gold nanorods. Gold nanorods were prepared following the well-known, seed-mediated, silver-assisted growth procedure. The longitudinal LSPR in gold nanorods can be controlled by changing the aspect ratio, making it possible for them to absorb laser light at 785 nm.[53] The UV-vis spectrum of the as-synthesized gold nanorods (Figure 5.1) shows a longitudinal LSPR maximum at 790 nm. ImageJ analysis of TEM images of the gold nanorods revealed that they are aspect ratio 3.6 and are 43 ± 5 nm in length and 12 ± 2 nm in width.

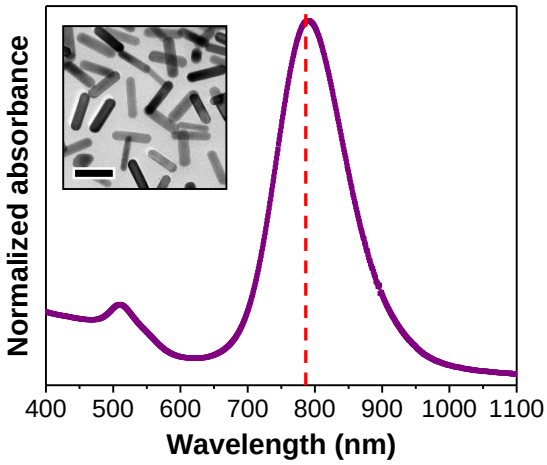

Figure 5.1 UV-vis absorbance spectrum of CTAB gold nanorods. The red line represents the wavelength of the continuous wave laser used in photothermal heating experiments. Inset is a TEM image of aspect ratio 3.6 gold nanorods which are 43 ± 5 nm in length and 12 ± 2 nm in width. Scale bar = 50 nm.

Gold nanorods prepared by this method are coated in the surfactant cetyltrimethylammonium bromide (CTAB). In addition to being more prone to aggregation in physiological environments, CTAB gold nanorods can be cytotoxic due to the presence of free CTAB which desorbs from the gold surface. However, cytotoxicity and aggregation issues can be reduced by coating positively charged CTAB nanorods with

polyelectrolytes *via* layer-by-layer sequential wrapping of anionic and cationic polymers, or by functionalizing gold nanorods with a thiolated polyethylene glycol (PEG) *via* ligand exchange (Figure 5.2).[56,80]

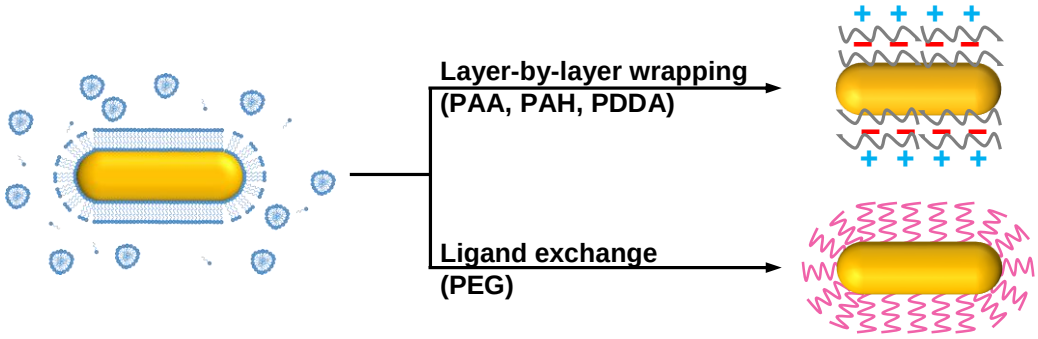

Figure 5.2 Routes to modification of CTAB gold nanorods. Sequential wrapping of polyanions and polycations is possible using layer-by-layer chemistry. PEG-SH can displace CTAB *via* Au-S chemistry.

It has been previously demonstrated that bacterial endospores can be encapsulated by multilayer polyelectrolyte shells using layer-by-layer assembly. *Balkundi et al.*[81] coated *Bacillus subtilis* endospores with 20-100 nm shells using cationic polylysine, polyallylamine hydrochloride (PAH) or polydiallyldimethyl ammonium chloride (PDDA), and anionic sodium polystyrene sulfonate or polyglutamic acid. This was possible because a spore surface is negatively charged, so cationic polyelectrolytes could adsorb to the surface by electrostatic attachment. We chose to use negatively charged polyacrylic acid (PAA), and positively charged PAH and PDDA for polyelectrolyte coating and neutral PEG on gold nanorods (Table 5.1) to investigate the impact of electrostatic interactions on gold nanorod attachment to bacterial surfaces.

Table 5.1 Characterization data for gold nanorods from UV-vis, DLS and ζ-potential measurements.

Surface coating	Abbreviation	LSPR	Hydrodynamic diameter	ζ-potential
Cetyltrimethylammonium bromide	CTAB	790 nm	15.5 ± 0.6 nm	19 ± 1 mV
Polyacrylic acid	PAA	770 nm	32.0 ± 0.3 nm	-26 ± 1 mV
Polyallylamine hydrochloride	PAH	787 nm	47 ± 1 nm	49 ± 2 mV
Polydiallyldimethyl ammonium chloride	PDDA	826 nm	98 ± 1 nm	62 ± 1 mV
Methoxyl polyethylene glycol thiol	PEG	785 nm	10.0 ± 0.1 nm	-2 ± 5 mV

After functionalization with PAA, PAH, PDDA, or PEG, gold nanorods were characterized by UV-vis absorbance, dynamic light scattering (DLS), and ζ-potential measurements. The data from these analyses techniques are shown in Table 5.1. UV-vis measurements revealed small shifts in the longitudinal LSPR

peak position relative to the original CTAB gold nanorods. These shifts are typically observed with polymer coating and may be due to a change in the refractive index or hydration at the nanorod surface.[1,82] Changes in the hydrodynamic diameter and ζ-potential of gold nanorods after coating were also observed after polymer coating. These differences are evidence that the polymer coatings effectively altered material characteristics.

Laser photothermal heating experiments and colony counting was carried out following the procedure outlined in Scheme 5.1. The gold nanorods were incubated with spores and vegetative cells of *G. stearothermophilus* with ~10^5 cells or spores and 10^{10} nanorods for at least 10 min. Then, the nanorod/bacterial suspension was irradiated using a 50 mW, continuous wave, 785 nm laser diode for 25 min. Control samples included spores/cells alone in deionized water, spores/cells exposed to the nanorods without the laser, and spores/cells exposed to the laser without nanorods present. This made it possible to compare the individual effects of laser irradiation and gold nanorod exposure on growth of vegetative cells and spores. Some condensation formed after laser irradiation with the gold nanorods present, which was not observed when gold nanorods were not present (Figure 5.3). The condensation indicates that heating did occur, and was due to irradiation of the gold nanorods at a wavelength resonant with the longitudinal LSPR maximum. After treatment, the amount of inactivation of *G. stearothermophilus* spores was measured by a colony counting, serial dilution technique. It is not possible to calculate viability using live/dead cell stains, so spore inactivation is usually quantified by counting the number of colony forming units (CFU). The CFU were calculated for each treatment condition from plates which had been incubated at 55°C. This is within the optimum temperature range (55-60°C) for *G. stearothermophilus* germination and growth.[61]

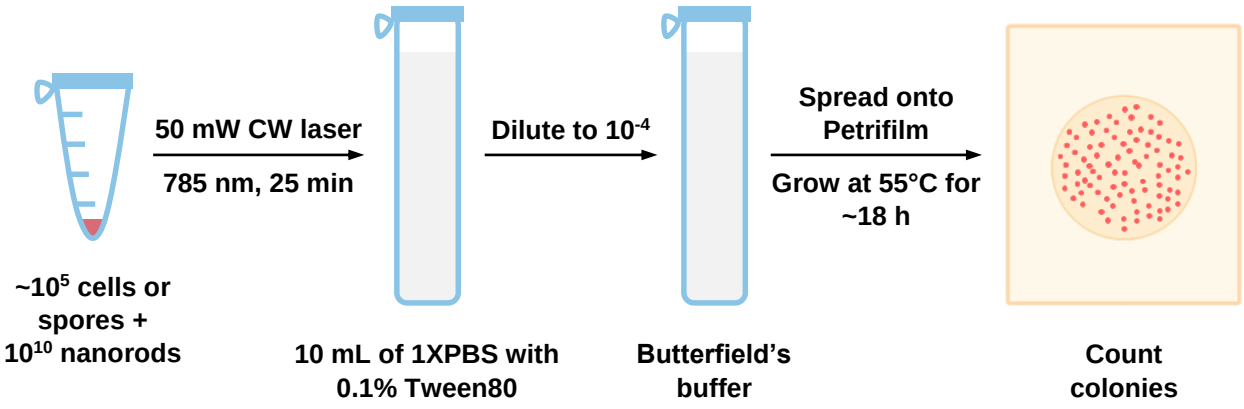

Scheme 5.1 Experimental procedure for photothermal treatment. Gold nanorods were incubated with spores or vegetative cells of *Geobacillus stearothermophilus* in an Eppendorf tube for 10 min. The spores/cells were then exposed to a 785 nm continuous wave (CW) laser (50 mW) for 25 min. The treated spores/cells were transferred to a 1XPBST solution and then serially diluted in Butterfield's buffer. Aliquots (1 mL) of the diluted spores/cells were spread onto Petrifilm and incubated for ~20 h at 55°C before counting colonies. Control samples included spores/cells in deionized water, spores/cells in deionized water with laser exposure, nanorods and cells without laser exposure, and cells in deionized water heated up to 69°C in a water bath.

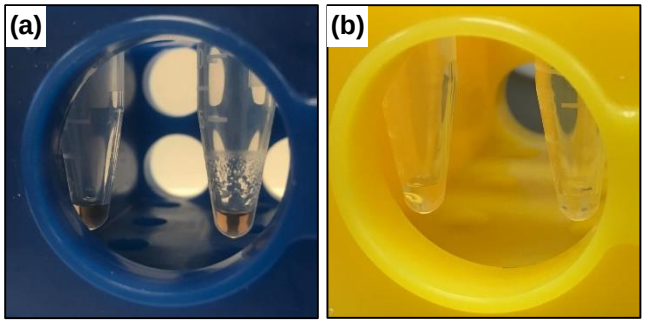

Figure 5.3 Photographs of Eppendorf tubes containing (a) spores and gold nanorods or (b) spores alone both (left) before and (right) after laser irradiation at 785 nm. Laser irradiation of gold nanorods heated the solution as demonstrated by the condensation which appeared after irradiation.

The effects of the various treatment conditions on colony formation of endospores are shown in Figure 5.4, and the results are quite interesting. Laser irradiation did not significantly alter colony growth compared to untreated spores; however, there were significant reductions in colony formation after gold nanorod exposure for all four types of polymer coatings. The greatest decrease in CFU by 13% was due to exposure to PDDA nanorods, followed by an 11% decrease with PAH nanorods, 6% with PEG nanorods, and 5% with PAA nanorods. It has been observed that exposure to nanomolar concentrations of polymer-coated gold nanorods can decrease eukaryotic cell viability by around ~10%, and these results are consistent with that report.[80] This suggests that there may have been some surface chemistry-dependent interaction between gold nanorods and spores which inactivated the spores and prevented germination.

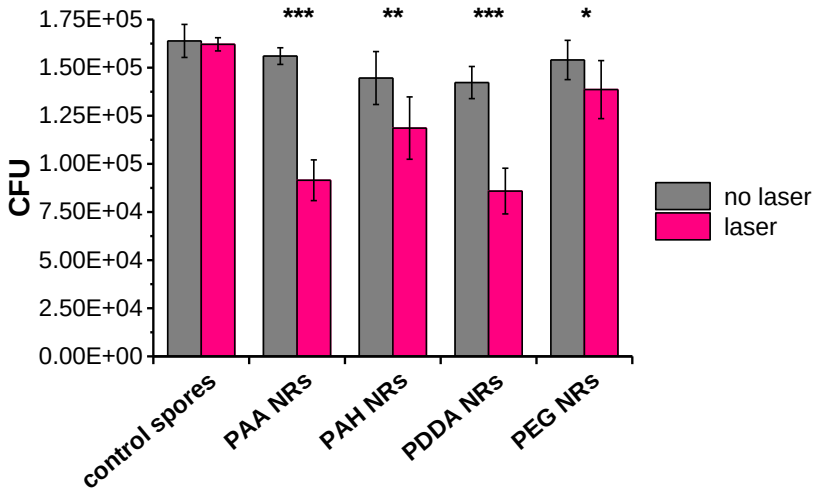

Figure 5.4 Effect of laser irradiation, nanorod (NR) exposure and photothermal heating on growth of *G. stearothermophilus* spores as determined by colony counting. Values for colony forming units (CFU) are calculated from four separate experiments (***** $p < 0.1$, ****** $p < 0.05$, ******* $p < 0.01$).

Photothermal heating of spores incubated with all four types of polymer-coated gold nanorods also resulted in significantly decreased CFU. The greatest decrease was 48% for PDDA nanorods, followed by a 44% decrease with PAA nanorods, 28% with PAH nanorods, and 15% with PEG nanorods compared to the untreated control. *G. stearothermophilus* spores are known to be resistant to heating, and exposure of spores to temperatures at or above 100°C is required for inactivation.[50,51] A previous report of laser irradiation under similar irradiation conditions has suggested that laser photothermal heating resulted in solution temperatures of 30-40°C, far below inactivation temperatures.[54] Though condensation formed above the suspension (Figure 5.3a) it did not appear that the solutions were boiling. Therefore, we propose that while the solution temperature may not have been high enough to inactivate the spores, the local temperatures around the nanorods may have been higher, and resulted in spore inactivation and the decreased CFU after laser irradiation. If there were differences in interactions and attachment of the polymer-coated gold nanorods to the spore surfaces, this may account for the observed differences CFU.

Spores were examined using scanning electron microscopy (SEM) to investigate differences in how the gold nanorods attach to the spore surfaces. SEM images of untreated spores are shown in Figure 5.5. They are football-shaped structures and the surfaces appear smooth. The endospores are aspect ratio 1.9 and approximately 1.6 μm long and 0.9 μm wide. SEM images of spores exposed to gold nanorods and treated by photothermal heating are shown in Figure 5.6. There are areas on the spores where bright spots are present – these are likely gold nanorods, because these are not present in untreated spores. It appears that PAA, PAH, and PDDA gold nanorods can attach to the surfaces of the spores while PEG nanorods appear to have very little interaction with the spores. PEG is known to increase biocompatibility and reduce nonspecific adsorption of gold nanorods *in vivo*.[56] Therefore, it is not expected that there is little interaction with the spore surface, and this can be correlated with the smallest reduction in CFU after photothermal treatment (Figure 5.4). Attachment of PAH and PDDA nanorods to spores is expected because cationic gold nanorods might bind to the anionic spore surface electrostatically. However, anionic PAA nanorods also appear to attach, but perhaps not as much as PAH and PDDA. This suggests that electrostatic interactions may not have been the only factor which influenced gold nanorod attachment to spores.

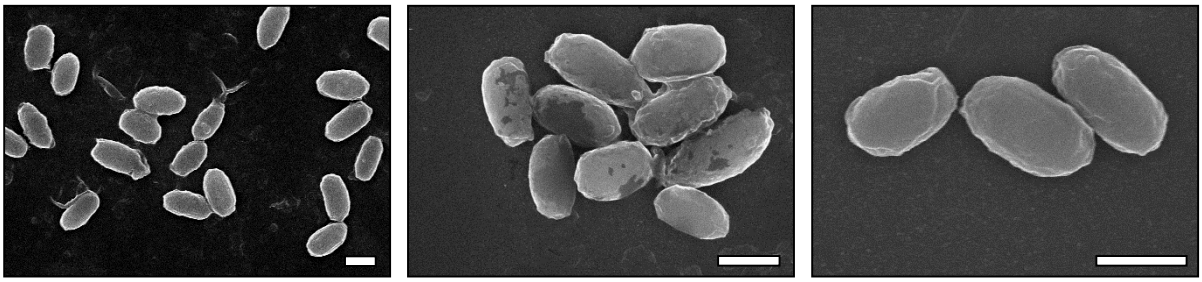

Figure 5.5 Example SEM images of *G. stearothermophilus* spores. Scale bars = 1 μm.

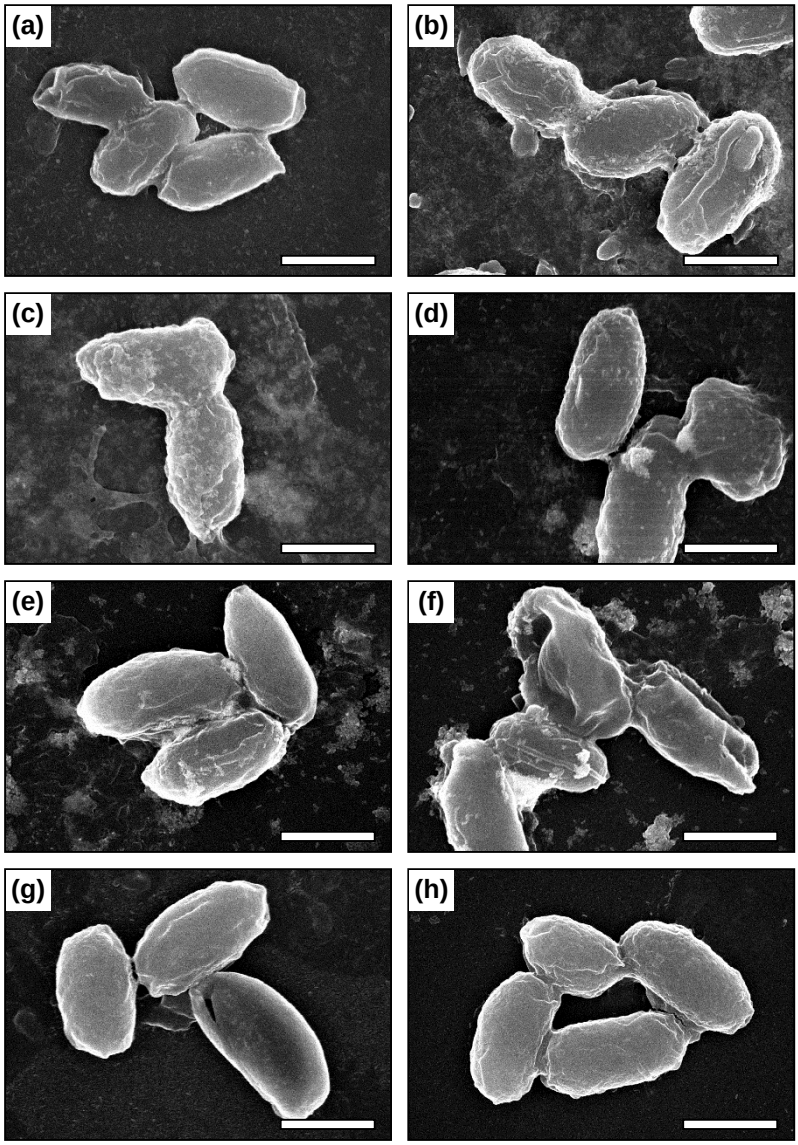

Figure 5.6 Example SEM images of *G. stearothermophilus* spores incubated with (a, b) PAA, (c, d) PAH, (e, f) PDDA, and (g, h) PEG gold nanorods, (a, c, e, g) before and (b, d, f, g) after photothermal treatment. Scale bars = 1 µm.

SEM was also used to observe any changes in morphology which could be correlated with reductions in CFU due to nanorod exposure and/or photothermal treatment. Balkundi *et al.*[81] observed that coating *G. stearothermophilus* spores with polymers reduced permeability and decreased germination rates. It is possible that nanorods coating the spore surfaces had the same effect on germination rates and therefore CFU. After photothermal treatment, some of the spores appear to fuse together or break open which might be a sign of physical damage. However, it is difficult to correlate these observed changes in morphology with reductions in CFU.

A previous report found that the absolute dimensions of *G. stearothermophilus* spores changed after plasma sterilization, and this was quantified by SEM image analysis.[49] Therefore, ImageJ analysis of the

length and width of spores was carried out to determine if there were any quantifiable change in dimensions after nanorod exposure and/or photothermal treatment. Morphology was quantified by aspect ratio (length/width) and area per spore (π*[length]*[width]*0.25) and the results are shown in Table 5.2. There are small changes in the lengths and widths of the spores which resulted in decreased aspect ratio and increased area per spore compared to the untreated control. These results seem to somewhat correlate with the observed changes in CFU after nanorod exposure or photothermal heating (Figure 5.4). The greatest decrease in aspect ratio and increase in area was observed in spores with photothermal treatment using PDDA nanorods. Therefore, photothermal heating using gold nanorods may be causing physical changes to spores, which could be causing spore inactivation and/or preventing spore germination. Sterilization is usually counted by log scale reductions in CFU. While we do observe reductions in CFU and small changes in morphology, these changes are not as great as the effects from other more commonly-studied sterilization techniques, like plasma exposure.[49]

Table 5.2 Average dimensions, aspect ratio and area of *G. stearothermophilus* spores which are untreated, exposed to gold nanorods (NRs) and treated by photothermal heating.

Treatment condition	Length	Width	Aspect ratio	Area per spore
Control spores	1.60 ± 0.21 μm	0.85 ± 0.09 μm	1.90 ± 0.06	1.06 μm^2
PAA NRs	1.61 ± 0.22 μm	0.85 ± 0.11 μm	1.90 ± 0.01	1.07 μm^2
PAA NRs + laser	1.61 ± 0.19 μm	0.86 ± 0.09 μm	1.87 ± 0.02	1.08 μm^2
PAH NRs	1.60 ± 0.19 μm	0.86 ± 0.09 μm	1.87 ± 0.04	1.08 μm^2
PAH NRs + laser	1.59 ± 0.22 μm	0.86 ± 0.12 μm	1.85 ± 0.01	1.08 μm^2
PDDA NRs	1.61 ± 0.22 μm	0.87 ± 0.12 μm	1.85 ± 0.01	1.09 μm^2
PDDA NRs + laser	1.62 ± 0.23 μm	0.89 ± 0.12 μm	1.81 ± 0.02	1.13 μm^2
PEG NRs	1.60 ± 0.23 μm	0.85 ± 0.08 μm	1.88 ± 0.09	1.07 μm^2
PEG NRs + laser	1.61 ± 0.25 μm	0.86 ± 0.09 μm	1.87 ± 0.10	1.08 μm^2

Vegetative cells of *G. stearothermophilus* were exposed to the same treatment conditions in order to determine the effect of photothermal heating on cell type. The effects of the various treatment conditions on colony formation of vegetative cells are shown in Figure 5.7. Again, laser irradiation alone did not significantly alter colony growth but there was no reduction in CFU from exposure to PAA or PEG nanorods. The only significant reduction in CFU was a 78% decrease with PDDA nanorods, but there was also a 12% decrease in CFU with PAH nanorods. Photothermal heating of vegetative cells incubated with all four types of nanorods also significantly decreased CFU. The greatest decrease was 91% with PDDA nanorods, followed by a 51% decrease with PAH nanorods, 21% with PEG nanorods and 17% with PAA nanorods compared to the untreated control. It appears that the positively charged surface coatings have a greater impact on growth and inactivation of vegetative cells. While these results are slightly different than the

changes in CFU observed with spores, again, it seems there are surface chemistry-dependent interactions between gold nanorods and bacterial surfaces which might influence the impact of photothermal heating.

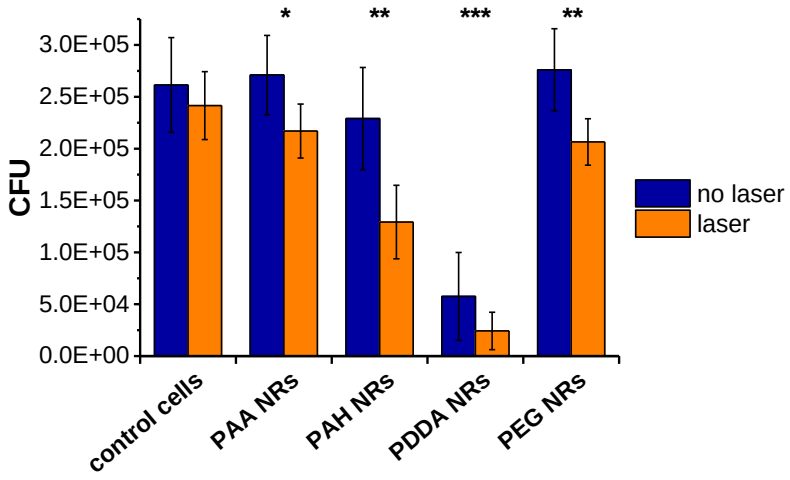

Figure 5.7 Effect of laser irradiation, nanorod (NR) exposure and photothermal heating on growth of *G. stearothermophilus* vegetative cells as determined by colony counting. Values for colony forming units (CFU) are calculated from four separate experiments (***** $p < 0.1$, ****** $p < 0.05$, ******* $p < 0.01$).

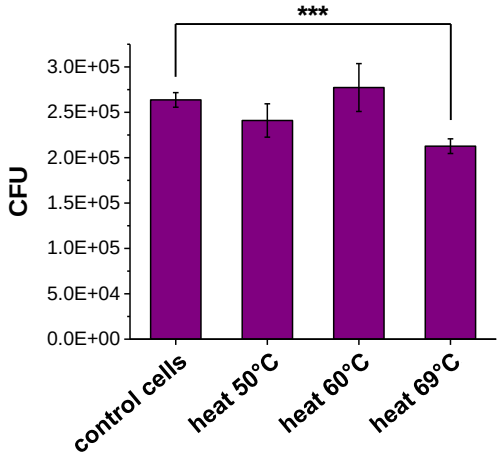

Figure 5.8 Effect of heating in a water bath on growth of *G. stearothermophilus* vegetative cells as determined by colony counting. Values for colony forming units (CFU) are calculated from three separate experiments (******* $p < 0.01$).

Vegetative cells are thought to be more susceptible to heat than spores because they do not have the thick spore coat. Therefore, the effect of heat on vegetative cell growth was examined by heating the cells in a water bath at temperatures of 50, 60 and 69°C, and the results are shown in Figure 5.8. Heating at 50°C or 60°C did significantly alter colony growth, which is expected since those temperatures are within the range for vegetative cell growth. However, there was a 19% decrease in growth at 69°C. It is possible

that there was a similar increase in solution temperature after photothermal heating, which caused cell inactivation. However, because there were differences in CFU with gold nanorod coating type, the effect of surface chemistry and gold nanorod attachment to cells should not be ignored.

5.4 CONCLUSIONS

Here, we have investigated the impact of photothermal heating on endospores and vegetative cells of the Gram-negative bacterium *Geobacillus stearothermophilus*. Gold nanorods with an LSPR ~785 nm were prepared and characterized. The nanorods were coated with four different neutral or charged polymers (PAA, PAH, PDDA, and PEG) to investigate the impact of electrostatic interactions on cell attachment and inactivation. The effects of gold nanorod exposure and photothermal heating using a 785 nm laser on colony growth of spores and vegetative cells revealed greater reductions in CFU with positively charged nanorods. Additionally, spore morphology was examined before and after treatment. There were changes in morphology observed as increasing area per spore and decreased spore aspect ratio which were somewhat correlated with inactivation. These results demonstrate that while it is possible to use photothermal heating with gold nanorods to inactivate heat-resistant bacterial endospores, the effects of photothermal heating on spores is not as great as traditional sterilization methods. However, further work with gold nanorods which are specifically targeted to cell surfaces may enhance photothermal effects.

5.5 REFERENCES

1. Abadeer, N. S.; Fülöp, G.; Chen, S.; Käll, M.; Murphy, C. J. Interactions of Bacterial Lipopolysaccharides with Gold Nanorod Surfaces Investigated by Refractometric Sensing. *ACS Appl. Mater. Interfaces* **2015,** *7,* 24915-24925.
2. Pissuwan, D.; Cortie, C. H.; Valenzuela, S. M.; Cortie, M. B. Functionalised Gold Nanoparticles for Controlling Pathogenic Bacteria. *Trends Biotechnol.* **2010,** *28,* 207-213.
3. Zhu, X.; Radovic-Moreno, A. F.; Wu, J.; Langer, R.; Shi, J. Nanomedicine in the Management of Microbial Infection - Overview and Perspectives. *Nano Today* **2014,** *9,* 478-498.
4. Husseiny, M. I.; El-Aziz, M. A.; Badr, Y.; Mahmoud, M. A. Biosynthesis of Gold Nanoparticles using *Pseudomonas aeruginosa*. *Spectrochim. Acta, Part A* **2007,** *67,* 1003-1006.
5. Fayaz, A. M.; Girilal, M.; Rahman, M.; Venkatesan, R.; Kalaichelvan, P. T. Biosynthesis of Silver and Gold Nanoparticles using Thermophilic Bacterium *Geobacillus stearothermophilus*. *Process Biochem.* **2011,** *46,* 1958-1962.
6. Shah, V.; Belozerova, I. Influence of Metal Nanoparticles on the Soil Microbial Community and Germination of Lettuce Seeds. *Water, Air, Soil Pollut.* **2009,** *197,* 143-148.
7. Burns, J. M.; Pennington, P. L.; Sisco, P. N.; Frey, R.; Kashiwada, S.; Fulton, M. H.; Scott, G. I.; Decho, A. W.; Murphy, C. J.; Shaw, T. J.; Ferry, J. L. Surface Charge Controls the Fate of Au Nanorods in Saline Estuaries. *Environ. Sci. Technol.* **2013,** *47,* 12844−12851.
8. von Moos, N.; Slaveykova, V. I. Oxidative Stress Induced by Inorganic Nanoparticles in Bacteria and Aquatic Microalgae – State of the Art and Knowledge Gaps. *Nanotoxicology* **2014,** *6,* 605-630.
9. Gültekin, A.; Ersöz, A.; Hür, D.; Sariözlü, N. Y.; Denizli, A.; Say, R. Gold Nanoparticles having Dipicolinic Acid Imprinted Nanoshell for *Bacillus cereus* Spores Recognition. *Appl. Surf. Sci.* **2009,** *256,* 142-148.
10. Chang, Y.-C.; Yang, C.-Y.; Sun, R.-L.; Cheng, Y.-F.; Kao, W.-C.; Yag, P.-C. Rapid Single Cell Detection of *Staphylococcus aureus* by Aptamer-Conjugated Gold Nanoparticles. *Sci. Rep.* **2013,** *3,* 1863.
11. Storhoff, J. J.; Marla, S. S.; Bao, P.; Hagenow, S.; Mehta, H.; Lucas, A.; Garimella, V.; Patno, T.; Buckingham, W.; Cork, W.; Müller, U. R. Gold Nanoparticle-Based Detection of Genomic DNA

Targets on Microarrays using a Novel Optical Detection System. *Biosens. Bioelectron.* **2004,** *19,* 875-883.
12. Singh, A. K.; Senapati, D.; Wang, S.; Griffin, J.; Neely, A.; Candice, P.; Naylor, K. M.; Varisli, B.; Kalluri, J. R.; Ray, P. C. Gold Nanorod Based Selective Identification of *Escherichia coli* Bacteria Using Two-Photon Rayleigh Scattering Spectroscopy. *ACS Nano* **2009,** *3,* 1906-1912.
13. Khan, S. A.; Singh, A. K.; Senapati, D.; Fan, Z.; Ray, P. C. Targeted Highly Sensitive Detection of Multi-Drug Resistant *Salmonella* DT104 using Gold Nanoparticles. *Chem. Commun.* **2011,** *47,* 9444–9446.
14. Liandris, E.; Gazouli, M.; Andreadou, M.; Čomor, M.; Abazovic, N.; Sechi, L. A.; Ikonomopoulos, J. Direct Detection of Unamplified DNA from Pathogenic *Mycobacteria* using DNA-Derivatized Gold Nanoparticles. *J. Microbiol. Methods* **2009,** *78,* 260-264.
15. Su, H.; Ma, Q.; Shang, K.; Liu, T.; Yin, H.; Ai, S. Gold Nanoparticles as Colorimetric Sensor: A Case Study on *E. coli* O157:H7 as a Model for Gram-Negative Bacteria. *Sens. Actuators, B* **2012,** *161,* 298-303.
16. Cheng, H.-W.; Huan, S.-Y.; Wu, H.-L.; Shen, G.-L.; Yu, R. Q. Surface-Enhanced Raman Spectroscopic Detection of a Bacteria Biomarker Using Gold Nanoparticle Immobilized Substrates. *Anal. Chem.* **2009,** *81,* 9902–9912.
17. Çulha, M.; Adigüzel, A.; Yazici, M. M.; Kahraman, M.; Şahin, F.; Güllüce, M. Characterization of Thermophilic Bacteria Using Surface-Enhanced Raman Scattering. *Appl. Spectrosc.* **2008,** *62,* 1226-1232.
18. Kotanen, C. N.; Martinez, L.; Alvarez, R.; Simecek, J. W. Surface Enhanced Raman Scattering Spectroscopy for Detection and Identification of Microbial Pathogens Isolated from Human Serum. *Sens. Bio-Sens. Res.* **2016,** *8,* 20-26.
19. Cheng, H.-W.; Chen, Y.-Y.; Lin, X.-X.; Huan, S.-Y.; Wu, H.-L.; Shn, G.-L.; Yu, R.-Q. Surface-Enhanced Raman Spectroscopic Detection of *Bacillus subtilis* Spores using Gold Nanoparticle Based Substrates. *Ana. Chim. Acta* **2011,** *707*, 155-163.
20. Daniels, J. K.; Caldwell, T. P.; Christensen, K. A.; Chumanov, G. Monitoring the Kinetics of *Bacillus subtilis* Endospore Germination *via* Surface-Enhanced Raman Scattering Spectroscopy. *Anal. Chem.* **2006,** *78,* 1724-1729.
21. Zhao, y.; Tian, Y.; Cui, Y.; Liu, W.; Ma, W.; Jiang, X. Small Molecule-Capped Gold Nanoparticles as Potent Antibacterial Agents that Target Gram-Negative Bacteria. *J. Am. Chem. Soc.* **2010,** *132,* 12349-12356.
22. Goodman, C. M.; McCusker, C. D.; Yilmaz, T.; Rotello, V. M. Toxicity of Gold Nanoparticles Functionalized with Cationic and Anionic Side Chains. *Bioconjugate Chem.* **2004,** *15,* 897-900 897.
23. Bresee, J.; Maier, K. E.; Boncella, A. E.; Melander, C.; Feldheim, D. L. Growth Inhibition of *Staphylococcus aureus* by Mixed Monolayer Gold Nanoparticles. *Small* **2011,** *7,* 2027-2031.
24. Zawrah, M. F.; Abd El-Moez, S. I. Antimicrobial Activities of Gold Nanoparticles against Major Foodborne Pathogens. *Life Sci. J.* **2011,** *8,* 37-44.
25. Burygin, G. L.; Khlebtsov, B. N.; Shantrokha, A. N.; Dykman, L. A.; Bogatyrev, V. A.; Khlebtsov, N. G. On the Enhanced Antibacterial Activity of Antibiotics Mixed with Gold Nanoparticles. *Nanoscale Res. Lett.* **2009,** *4,* 794-801.
26. Gu, H.; Ho, P. L.; Tong, E.; Wang, L.; Xu, B. Presenting Vancomycin on Nanoparticles to Enhance Antimicrobial Activities. *Nano Lett.* **2003,** *3,* 1261-1263.
27. Rosemary, M. J.; MacLaren, I.; Pradeep, T. Investigations of the Antibacterial Properties of Ciprofloxacin@SiO_2. *Langmuir* **2006,** *22,* 10125-10129.
28. Perni, S.; Piccirillo, C.; Pratten, J.; Prokopovich, P.; Chrzanowski, W.; Parkin, I. P.; Wilson, M. The Antimicrobial Properties of Light-Activated Polymers Containing Methylene Blue and Gold Nanoparticles. *Biomaterials* **2009,** *30,* 89-93.
29. Perni, S.; PIccirillo, C.; Kafizas, A.; Uppal, M.; Pratten, J.; Wilson, M.; Parkin, I. P. Antibacterial Activity of Light-Activated Silicone Containing Methylene Blue and Gold Nanoparticles of Different Sizes. *J. Clust. Sci.* **2010,** *21,* 427-438.
30. Gil-Tomás, J.; Tubby, S.; Parkin, I. P.; Narband, N.; Dekker, L.; Nair, S. P.; Wilson, M.; Street, C. Lethal Photosensitisation of *Staphylococcus aureus* using a Toluidine Blue O–Tiopronin–Gold Nanoparticle Conjugate. *J. Mater. Chem.* **2007,** *17,* 3739-3746.
31. Kuo, W.-S.; Chang, C.-N.; Chang, Y.-T.; Yeh, C.-S. Antimicrobial Gold Nanorods with Dual-Modality Photodynamic Inactivation and Hyperthermia. *Chem. Commun.* **2009,** *45,* 4853-4855.

32. Huang, X.; Jain, P. K.; El-Sayed, I. H.; El-Sayed, M. A. Plasmonic Photothermal Therapy (PPTT) using Gold Nanoparticles. *Lasers Med. Sci.* **2008,** *23,* 217-228.
33. Abadeer, N. S.; Murphy, C. J. Recent Progress in Cancer Thermal Therapy Using Gold Nanoparticles. *J. Phys. Chem. C* **2016,** *120,* 4691−4716.
34. Huang, W.-C.; Tsai, P.-J.; Chen, Y.-C. Functional Gold Nanoparticles as Photothermal Agents for Selective-Killing of Pathogenic Bacteria. *Nanomedicine* **2007,** *2,* 777-787.
35. Huang, W.-C.; Tsai, P.-J.; Chen, Y.-C. Multifunctional Fe3O4@Au Nanoeggs as Photothermal Agents for Selective Killing of Nosocomial and Antibiotic-Resistant Bacteria. *Small* **2009,** *5,* 51-56.
36. Kim, C.-B.; Yi, D.-K.; Kim, P. S. S.; Lee, W.; Kim, M. J. Rapid Photothermal Lysis of the Pathogenic Bacteria, *Escherichia coli* using Synthesis of Gold Nanorods. *J. Nanosci. Nanotech.* **2009,** *9,* 2841-2845.
37. Santos, G. M.; de Santi Ferrara, F. I.; Zhao, F.; Rodrigues, D. F.; Shih, W.-C. Photothermal Inactivation of Heat-Resistant Bacteria on Nanoporous Gold Disk Arrays. *Opt. Mater. Express* **2016,** *6,* 1217-1229.
38. Castillo-Martínez, J. C.; Martínez-Castañon, G. A.; Martínez-Gutierrez, F.; Zavalo-Alonso, N. V.; Patiño-Marín, N.; Niño-Martinez, N.; Zaragoza-Magaña, V.; Cabral-Romero, C. Antibacterial and Antibiofilm Activities of the Photothermal Therapy Using Gold Nanorods against Seven Different Bacterial Strains. *J. Nanomater.* **2015,** *2015,* 883671.
39. Wang, S.; Sing, A. K.; Senapati, D.; Neely, A.; Yu, H.; Ray, P. C. Rapid Colorimetric Identification and Targeted Photothermal Lysis of *Salmonella* Bacteria by using Bioconjugated Oval-Shaped Gold Nanoparticles. *Chem. Eur. J.* **2010,** *16,* 5600-5606.
40. Khan, S. A.; Singh, A. K.; Senapati, D.; Fan, Z.; Ray, P. C. Bio-Conjugated Popcorn Shaped Gold Nanoparticles for Targeted Photothermal Killing of Multiple Drug Resistant *Salmonella* DT104. *J. Mater. Chem.* **2011,** *21,* 17705-17709.
41. Norman, R. S.; Stone, J. W.; Gole, A.; Murphy, C. J.; Sabo-Attwood, T. L. Targeted Photothermal Lysis of the Pathogenic Bacteria, *Pseudomonas aeruginosa*, with Gold Nanorods. *Nano Lett.* **2008,** *8,* 302-306.
42. Zharov, V. P.; Mercer, K. E.; Galitovskaya, E. N.; Smeltzer, M. S. Photothermal Nanotherapeutics and Nanodiagnostics for Selective Killing of Bacteria Targeted with Gold Nanoparticles. *Biophys. J.* **2006,** *90,* 619-627.
43. Millenbaugh, N. J.; Baskin, J. B.; DeSilva, M. N.; Elliott, W. R.; Glickman, R. D. Photothermal Killing of *Staphylococcus aureus* using Antibody-Targeted Gold Nanoparticles. *Int. J. Nanomed.* **2015,** *10,* 1953-1960.
44. Neu, H. C. The Crisis in Antibiotic Resistance. *Science* **1992,** *257,* 1064-1073.
45. Atrih, A.; Foster, S. J. Bacterial Endospores the Ultimate Survivors. *Int. Dairy J.* **2002,** *12,* 217-223.
46. Horneck, G.; Bücker, H.; Reitz, G. Long-Term Survival of Bacterial Spores in Space. *Adv. Space Res.* **1994,** *14,* 41-45.
47. Friedline, A. W.; Zachariah, M. M.; Middaugh, A. N.; Garimella, R.; Vaishampayan, P. A.; Rice, C. V. Sterilization Resistance of Bacterial Spores Explained with Water Chemistry. *J. Phys. Chem. B* **2015,** *119,* 14033-14044.
48. Iciek, J.; Blaszczyk, I.; Papiewska, A. The Effect of Organic Acid Type on Thermal Inactivation of *Geobacillus stearothermophilus* Spores. *J. Food Eng.* **2008,** *87,* 16-20.
49. Kylián, O.; Sasaki, T.; Rossi, F. Plasma Sterilization of *Geobacillus stearothermophilus* by O_2:N_2 Inductively Coupled Plasma. *Eur. Phys. J. Appl. Phys.* **2006,** *34,* 139-142.
50. Patazca, E.; Koutchma, T.; Ramaswamy, H. S. Inactivation Kinetics of *Geobacillus stearothermophilus* Spores in Water using High-pressure Processing at Elevated Temperatures. *J. Food Sci.* **2006,** *71,* M110-M116.
51. Somavat, R.; Mohamed, H. M. H.; Chung, Y.-K.; Yousef, A. E.; Sastry, S. K. Accelerated Inactivation of *Geobacillus stearothermophilus* Spores by Ohmic Heating. *J Food Eng.* **2012,** *108,* 69-76.
52. Guizelini, B. P.; Vandenberghe, L. P. S.; Sella, S. R. B. R.; Soccol, C. R. Study of the Influence of Sporulation Conditions on Heat Resistance of *Geobacillus stearothermophilus* used in the Development of Biological Indicators for Steam Sterilization. *Arch. Microbiol.* **2012,** *194,* 991-999.
53. Abadeer, N. S.; Brennan, M. R.; Wilson, W. L.; Murphy, C. J. Distance and Plasmon Wavelength Dependent Fluorescence of Molecules Bound to Silica-Coated Gold Nanorods. *ACS Nano* **2014,** *8,* 8392-8406.

54. Huang, J.; Jackson, K. S.; Murphy, C. J. Polyelectrolyte Wrapping Layers Control Rates of Photothermal Molecular Release from Gold Nanorods. *Nano Lett.* **2012,** *12,* 2982−2987.
55. Gole, A.; Murphy, C. J. Polyelectrolyte-Coated Gold Nanorods: Synthesis, Characterization and Immobilization. *Chem. Mater.* **2005,** *17,* 1325-1330.
56. Niidome, T.; Yamagata, M.; Okamoto, Y.; Akiyama, Y.; Takahashi, H.; Kawano, T.; Katayama, Y.; Niidome, Y. PEG-Modified Gold Nanorods with a Stealth Character for *In vivo* Applications. *J. Controlled Release* **2006,** *114,* 343-347.
57. Orendorff, C. J.; Murphy, C. J. Quantitation of Metal Content in the Silver-Assisted Growth of Gold Nanorods. *J. Phys. Chem. B* **2006,** *110,* 3990-3994.
58. Silva, S. M. D.; Filliben, J. J.; Morrow, J. B. Parameters Affecting Spore Recovery from Wipes Used in Biological Surface Sampling. *Applied Environ. Microbiol.* **2011,** *77,* 2374-2380.
59. Luftman, H. S.; Regits, M. A. *B. atrophaeus* and *G. stearothermophilus* Biological Indicators for Chlorine Dioxide Gas Decontamination. *Appl. Biosaf.* **2008,** *13,* 143-157.
60. Smith, L. B.; Fox, T. L.; Busta, F. F. Comparison of a Dry Medium Culture Plate (Petrifilm SM Plates) Method to the Aerobic Plate Count Method for Enumeration of Mesophilic Aerobic Colony-Forming Units in Fresh Ground Beef. *J. Food Prot.* **1985,** *48,* 1044-1045.
61. Rogers, J. V.; Sabourin, C. L. K.; Choi, Y. W.; Richter, W. R.; Rudnicki, D. C.; Riggs, K. B.; Taylor, M. L.; Chang, J. Decontamination Assessment of *Bacillus anthracis*, *Bacillus subtilis*, and *Geobacillus stearothermophilus* Spores on Indoor Surfaces using a Hydrogen Peroxide Gas Generator. *J. Appl. Microbiol.* **2005,** *99,* 739-748.
62. Navarre, W. W.; Schneewind, O. Surface Proteins of Gram-Positive Bacteria and Mechanisms of Their Targeting to the Cell Wall Envelope. *Microbiol. Mol. Biol. Rev.* **1999,** *63,* 174-229.
63. Ho, K.-C.; Tsai, P.-J.; Lin, Y.-S.; Chen, Y.-C. Using Biofunctionalized Nanoparticles to Probe Pathogenic Bacteria. *Anal. Chem.* **2004,** *76,* 7162-7168.
64. Wang, C.; Irudayaraj, J. Gold Nanorod Probes for the Detection of Multiple Pathogens. *Small* **2008,** *4,* 2204-2208.
65. Lin, C.-C.; Yeh, Y.-C.; Yang, C.-Y.; Chen, C.-L.; Chen, G.-F.; Chen, C.-C.; Wu, Y.-C. Selective Binding of Mannose-Encapsulated Gold Nanoparticles to Type 1 Pili in *Escherichia coli*. *J. Am. Chem. Soc.* **2002,** *124,* 3508-3509.
66. Luo, P. G.; Wang, H.; Gu, L.; Lu, F.; Lin, Y.; Christensen, K. A.; Yang, S.-T.; Sun, Y.-P. Selective Interactions of Sugar-Functionalized Single-Walled Carbon Nanotubes with *Bacillus* Spores. *ACS Nano* **2009,** *3,* 3909-3916.
67. Wang, H.; Gu, L.; Lin, Y.; Lu, F.; Meziani, M. J.; Luo, P. G.; Wang, W.; Cao, L.; Sun, Y.-P. Unique Aggregation of Anthrax (Bacillus anthracis) Spores by Sugar-Coated Single-Walled Carbon Nanotubes. *J. Am. Chem. Soc.* **2006,** *128,* 13364-13365.
68. van Loosdrecht, M. C. M.; Lyklema, J.; Norde, W.; Zehnder, A. J. B. Bacterial Adhesion: A Physicochemical Approach. *Microb. Ecol.* **1989,** *17,* 1-5.
69. Berry, V.; Saraf, R. F. Self-Assembly of Nanoparticles on Live Bacterium: An Avenue to Fabricate Electronic Devices. *Angew. Chem., Int. Ed.* **2005,** *44,* 6668-6673.
70. Berry, V.; Gole, A.; Kundu, S.; Murphy, C. J.; Saraf, R. F. Deposition of CTAB-Terminated Nanorods on Bacteria to Form Highly Conducting Hybrid Systems. *J. Am. Chem. Soc.* **2005,** *127,* 17600-17601.
71. Hayden, S. C.; Zhao, G.; Saha, K.; Phillips, R. L.; Li, X.; Miranda, O. R.; Rotello, V. M.; El-Sayed, M. A.; Schmidt-Krey, I.; Bunz, U. H. F. Aggregation and Interaction of Cationic Nanoparticles on Bacterial Surfaces. *J. Am. Chem. Soc.* **2012,** *134,* 6920−6923.
72. Kinoshita, T.; Kiso, K.; Le, D. Q.; Shigi, H.; Nagaoka, T. Light-Scattering Characteristics of Metal Nanoparticles on a Single Bacterial Cell. *Anal. Sci.* **2016,** *32,* 301-305.
73. Chwalibog, A.; Sawosz, E; Hotowy, A.; Szeliga, J.; Mitura, S.; Mitura, K.; Grodzik, M.; Orlowski, P.; Sokolowska, A. Visualization of Interaction Between Inorganic Nanoparticles and Bacteria or Fungi. *Int. J. Nanomed.* **2010,** *5,* 1085-1094.
74. Jacobson, K. H.; Gunsolus, I. L.; Kuech, T. R.; Troiano, J. M.; Melby, E. S.; Lohse, S. E.; Hu, D.; Chrisler, W. B.; Murphy, C. J.; Orr, G.; Geiger, F. M.; Haynes, C. L.; Pedersen, J. A. Lipopolysaccharide Density and Structure Govern the Extent and Distance of Nanoparticle Interaction with Actual and Model Bacterial Outer Membranes. *Environ. Sci. Technol.* **2015,** *49,* 10642−10650.

75. Feng, Z. V.; Gunsolus, I. L.; Qiu, T. A.; Hurley, K. R.; Nyberg, L. H.; Frew, H.; Johnson, K. P.; Vartanian, A. M.; Jacob, L. M.; Lohse, S. E.; Torelli, M. D.; Hamers, R. J.; Murphy, C. J.; Haynes, C. L. Impacts of Gold Nanoparticle Charge and Ligand Type on Surface Binding and Toxicity to Gram-Negative and Gram-Positive Bacteria. *Chem. Sci.* **2015,** *6,* 5186-5196.
76. Cui, Y.; Zhao, Y.; Tian, Y.; Zhang, W.; Lü, X.; Jiang, X. The Molecular Mechanism of Action of Bactericidal Gold Nanoparticles on *Escherichia coli*. *Biomaterials* **2012,** *33,* 2327-2333.
77. Li, S.; Robinson, S. M.; Gupta, A.; Saha, K.; Jiang, Z.; Moyano, D. F.; Sahar, A.; Riley, M. A.; Rotello, V. M. Functional Gold Nanoparticles as Potent Antimicrobial Agents against Multi-Drug-Resistant Bacteria. *ACS Nano* **2014,** *8,* 10682-10686.
78. Wang, S.; Lawson, R.; Ray, P. C.; Yu, H. Toxic Effects of Gold Nanoparticles on *Salmonella typhimurium* Bacteria. *Toxicol. Ind. Health* **2011,** *27,* 547-554.
79. Zhang, Y.; Peng, H.; Huang, W.; Zhou, Y.; Yan, D. Facile Preparation and Characterization of Highly Antimicrobial Colloid Ag or Au Nanoparticles. *J. Colloid Interface Sci.* **2008,** *325,* 371-376.
80. Alkilany, A. M.; Nagaria, P.; Hexel, C. R.; Shaw, T. J.; Murphy, C. J.; Wyatt, M. D. Cellular Uptake and Cytotoxicity of Gold Nanorods: Molecular Origin of Cytotoxicity and Surface Effects. *Small* **2009,** *5,* 701-708.
81. Balkundi, S. S.; Veerabadran, N. G.; Eby, D. M.; Johnson, G. R.; Lvov, Y. M. Encapsulation of Bacterial Spores in Nanoorganized Polyelectrolyte Shells. *Langmuir* **2009,** *25,* 14011-14016.
82. Huang, J.; Park, J.; Wang, W.; Murphy, C. J.; Cahill, D. G. Ultrafast Thermal Analysis of Surface Functionalized Gold Nanorods in Aqueous Solution. *ACS Nano* **2013,** *7,* 589-597.

CHAPTER 6:
ENHANCED OPTICAL STABILITY OF MESOPOROUS SILICA-COATED GOLD NANORODS

6.1 INTRODUCTION

Gold nanorods have unique optoelectronic properties due to the presence of a localized surface plasmon resonance (LSPR). When excited at resonant frequencies, conduction band electrons in gold oscillate along the transverse and longitudinal axes. This results in strong absorbance of light, and the observance of transverse and longitudinal LSPR peaks which can be tuned from the visible to the near-infrared (NIR). Light absorbance, resonant scattering and the production of strong electromagnetic fields are a few of the optical phenomena which occur at a gold nanorod surface.[1] These optical properties can be useful in a variety of nano-enabled applications.[2,3] For example, refractometric sensing is possible by monitoring LSPR peak position of gold nanorods after binding of a target analyte.[4] In photothermal therapy, gold nanorods can be targeted to cancer cells, and dissipation of absorbed laser light energy as heat can cause cancer cell death.[5] Additionally, molecular signals from fluorophores or Raman-active molecules can be enhanced near a gold nanorod surface.[6,7] Optical applications such as these are possible because of the exquisite ability researchers have to control size and shape of gold nanomaterials.[8]

For optical applications to be realized, it is critical that gold nanorods maintain their morphology and optical properties, in non-ideal conditions. Gold nanorods are synthesized in the presence of the surfactant cetyltrimethylammonium bromide (CTAB); however CTAB gold nanorods have been observed to quickly aggregate in physiological environments, or in non-aqueous media.[9,10] Surface functionalization strategies by ligand exchange and polyelectrolyte wrapping can be employed to reduce this sort of aggregation which results from a destabilized surface.[11,12] The physical dimensions of gold nanorods can also be significantly altered when they are exposed to high intensity radiation from pulsed lasers. For example, Link *et al.*[13] monitored the power-dependent shape transformation of CTAB gold nanorods (λ_{max} = 800 nm). Gold nanorods were exposed to high energy femtosecond laser pulses (100 fs, 800 nm, 1 kHz) or nanosecond laser pulses (7 ns, 800 nm, 10 Hz). UV-vis absorbance measurements demonstrated a decrease in the magnitude of the longitudinal LSPR over time. Analysis by transmission electron microscopy revealed that gold nanorods “melted” and became spheres under femtosecond laser pulses, and fragmented into smaller particles under nanosecond pulses. This resulted in drastic modification of gold nanorod optical properties.

This sort of shape transformation occurs because of electron dynamics within a gold nanorod. Absorbed NIR laser pulses excite free electrons in the plasmon band, called electron thermalization, which cool *via* electron-phonon interactions. The gold nanorod lattice is heated, and heat is transferred from the nanoparticle to its surroundings through phonon-phonon interactions on a timescale of ~100 ps.[14] This can heat up the surrounding medium by tens of degrees and is often used in photothermal heating applications.[5] However, when the energy deposition rate is faster than the rate of energy dissipation by phonon-phonon interactions, such as with femtosecond pulsed lasers, the electronic temperature can become higher than

the melting temperature of bulk gold. This results in reshaping (700K) and/or melting (1337K) of gold nanostructures, in a process called surface melting (Figure 6.1).[15]

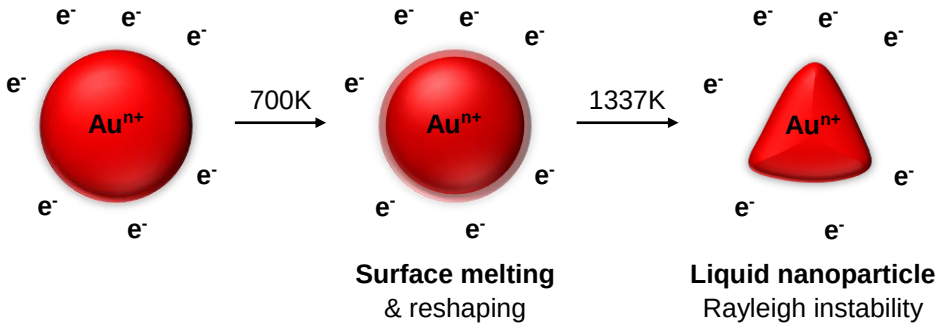

Figure 6.1 Proposed femtosecond laser-induced reshaping process of gold nanospheres (3-10 ps). Fast energy absorption heats the nanoparticles above the melting temperature, and induces reshaping and melting. Adapted from Reference 15. Copyright (2016) American Chemical Society.

The process of reshaping of gold nanomaterials is dependent on a variety of factors. Of course laser parameters such as pulse length, pulse width, pulse energy and laser wavelength can affect the final morphology of the irradiated particles. However, nanoparticle material characteristics such as shape, size, crystal structure, metal composition, and surface coating are also important. These nanoparticle features can modify electron dynamics, alter melting and evaporation threshold temperatures, and change how energy is dissipated from the particle surface.[15,16] Thermal heating has also been observed by researchers to result in surface melting, and can produce changes in gold nanorod morphology. Petrova *et al.*[17] found that heating gold nanorods at temperatures from 100-250°C resulted in reshaping of the nanorods to spheres in timescales of hours to days. Mohamed *et al.*[18] proposed that this reshaping was due to the decomposition and instability of the gold nanorod surface after thermal heating.

It is possible to better preserve optical properties of gold nanorods by altering surface characteristics. Researchers have shown that it is possible to reduce these aforementioned changes in gold nanorod morphology, which are induced by laser irradiation or thermal heating, by coating gold nanorods with shells of mesoporous silica.[19-27] To our knowledge, no researchers have investigated how functionalization of silica-coated gold nanorods with organic silanes may preserve optical properties against heat or laser irradiation. Here, we prepare a library of mesoporous silica-coated gold nanorods functionalized with four different commercially available silanes. We investigate gold nanorod optical properties and morphology by transmission electron microscopy and UV-vis absorbance after heating to 150°C. Additionally, CTAB, silica-coated and amine-functionalized silica-coated gold nanorods are exposed to charging from exposure to high energy electron beams, or irradiation with femtosecond pulsed lasers. We demonstrate that changes in morphology and optical properties are reduced compared to silica-coated or CTAB gold nanorods. These results suggest this is a useful method to modify gold nanorod surface chemistry to better preserve gold nanorod optical properties in gold nanorod-enabled optical applications.

6.2 MATERIALS AND METHODS

6.2.1 MATERIALS

Cetyltrimethylammonium bromide (CTAB), gold tetrachloroaurate ($HAuCl_4 \cdot 3H_2O$), sodium borohydride ($NaBH_4$), silver nitrate ($AgNO_3$), ascorbic acid, sodium hydroxide (NaOH), tetraethylorthosilicate (TEOS), methanol (MeOH), ethanol (EtOH), dimethyl sulfoxide (DMSO), 3-aminopropytrimethoxy silane (APTMS), 3-mercaptopropytrimethoxy silane (MPTMS), and 3-chloropropyltrimethoxy silane (CPTMS) were purchased from Sigma-Aldrich (USA). 2-[methoxy(polyethyleneoxy)$_{9\text{-}12}$propyl] trimethoxysilane (PEG-silane) was purchased from Gelest. Unless otherwise noted, solutions were made in 18 MΩ Nanopure deionized water. All chemicals were used as received.

6.2.2 SYNTHESIS, SILICA COATING AND SILANE FUNCTIONALIZATION, OF GOLD NANORODS

Five-hundred milliliter batches of CTAB gold nanorods were prepared following a previously published protocol.[6] Briefly, gold seeds were prepared by reduction of $HAuCl_4$ with $NaBH_4$ in the presence of CTAB. The seeds were aged at least 1 h before addition to a growth solution containing CTAB, $AgNO_3$ and $HAuCl_4$ which had been reduced by ascorbic acid. The gold nanorod solutions were aged 12 h before purification by centrifugation (11,500 g, 15 min), and the supernatant was removed. The pellets were combined and redispersed in 50 mL of deionized water for long-term storage at room temperature (25°C).

Silica coating was carried out by a modified Stöber process.[6,28] Individual aliquots (15 samples of 1 mL) of CTAB gold nanorods were diluted to ~ 1 nM with deionized water to 10 mL volumes, and the nanorods were centrifuged a second time (11,200 g, 20 min) to remove excess CTAB. The supernatant was removed, and the 15 samples were combined into three, 50 mL centrifuge tubes. Then, 400 µL of 0.1 M CTAB was added to each tube, and the solutions were diluted to 50 mL with deionized water. CTAB was allowed to equilibrate on the surface overnight (~12 h) by mixing on a Stovall Belly Dancer lab shaker. Then, 200 µL of 0.1 M NaOH was added to each tube and the solutions were mixed for 30 min. Next, 450 µL of 20% TEOS in MeOH (freshly made) was added and the solutions were mixed for 20 h. After coating, nanorods were purified by centrifugation (8000 g, 20 min) and were separated into 15 tubes, and each sample was diluted to 10 mL with EtOH.

Silane-functionalization was carried out by adding equimolar amounts of an organic silane to silica-coated gold nanorods in EtOH. APTMS (50 µL), MPTMS (53 µL), CPTMS (52 µL) or PEG-silane (175 µL) was added to the solutions and they were mixed for 48 h at room temperature. The functionalized gold nanorods were purified by centrifugation (8000 g, 20 min) and were resuspended in DMSO and diluted to a final concentration of 1 nM. Three separate samples were prepared for each type of silane. Additionally, three samples of regular silica-coated gold nanorods were suspended in DMSO.

6.2.3 CHARACTERIZATION OF GOLD NANORODS

UV-vis absorbance measurements of gold nanorods in water, EtOH and DMSO were carried out on a Cary 5000 UV-vis spectrometer (Agilent, USA) to determine LSPR wavelength and gold nanorod

concentration. Extinction coefficients of gold nanorod solutions were known from a previous report.[29] Transmission electron microscopy (TEM) images were obtained on a JEOL 2100 cryo-TEM (JEOL, Japan). ImageJ analysis of TEM images (100-300 particles per sample) was used to determine average length, width, aspect ratio (length/width) of gold nanorods and thickness of silica shells. We note thickness of silica shells was measured from the sides, not the ends. Prior to analysis by TEM, gold nanorod solutions in water or EtOH were dropcast onto lacey Formvar copper TEM grids (Ted Pella). Dynamic light scattering (DLS) and ζ-potential measurements of CTAB, silica-coated, and silane-functionalized gold nanorods in deionized water were carried out using a ZetaPALS analyzer (Brookhaven, USA). Prior to analysis by TEM, DLS and ζ-potential, 0.5 mL of gold nanorods in DMSO were centrifuged (8000 g, 20 min) and resuspended in 1.5 mL of deionized water.

6.2.4 THERMAL HEATING OF GOLD NANORODS

Thermal stability measurements were carried out in triplicate on CTAB gold nanorods in water and silica-coated and silane functionalized gold nanorods in DMSO with help from Andrei Andreev. Aliquots (3 mL) of gold nanorods were transferred to glass vials and loosely capped. The vials were heated at 50, 75, 100, 125 and 150°C for 2 h intervals. After each cycle of heating, the solutions were allowed to cool to room temperature before analysis. 100 µL aliquots of each sample were then diluted in 1 mL of water or DMSO, and the absorbance spectrum was measured. After the final heating cycle at 150°C, aliquots of gold nanorods in DMSO were centrifuged and resuspended in deionized water for TEM analysis.

6.2.5 EXPOSURE OF GOLD NANORODS TO CHARGING FROM AN ELECTRON BEAM

Imaging of CTAB, silica-coated and silane-functionalized gold nanorods was typically carried out on a JEOL 2100-cryo TEM with a 200 kV electron beam. An image of the gold nanorods was quickly captured at 100K magnification. Then the electron beam was focused to a spot of ~ 200 nm diameter for 30 s. Another image was captured after the exposure to the focused electron beam.

6.2.6 EXPOSURE OF GOLD NANORODS TO FEMTOSECOND PULSED LASER IRRADIATION

Gold nanorods were exposed to femtosecond laser pulses. The laser system used was a Spitfire Ace laser system (Spectra-Physics) in the Materials Research Laboratory Laser & Spectroscopy Facility with assistance from Julio Soares. A Nd:YLF Q-switched laser (532 nm, 14 mJ, 1 kHz repetition rate) seeds the regenerative amplifier producing high energy pulses (120 fs, 2.5 mJ, 800 nm) with a power of 1.9 W. Gold nanorod samples (200 µL, ~1 nM) in a quartz cuvette were exposed to the laser for 10 min. UV-vis absorbance and TEM analysis before and after exposure was carried out to examine the effect of high energy radiation on morphology and optical properties.

6.3 RESULTS AND DISCUSSION

6.3.1 PREPARATION AND CHARACTERIZATION OF GOLD NANORODS

Due to their high surface area-to-volume ratio, gold nanorods have a high surface energy and are therefore susceptible to material deformation by pulsed lasers,[13,15] thermal heating,[17-19] or charging by electrons.[30,31] For any optical application to be effective, gold nanorods must maintain their morphology and retain their unique optical properties in high energy conditions. Silica coating is generally a useful modification technique to stabilize a gold nanorod surface.[6,32] An inorganic mesoporous silica shell can increase the stability of gold nanorods against aggregation in organic solvents while also preserving gold nanorod optical properties.[6,19-27] A silica surface is also quite versatile because the reactive silanols can be modified with other silane-functionalized ligands, or to carry payloads for light-controlled drug release. [6,33,34]

Many researchers have investigated how a porous silica matrix or mesoporous silica shells can stabilize gold nanorods against thermal heating to temperatures up to 700°C, or high energy laser irradiation. Here we further investigate the stability of mesoporous silica-coated gold nanorods which are functionalized with four different commercially available silanes: 3-aminopropyltrimethoxy silane (APTMS), 3-mercaptopropyltrimethoxy silane (MPTMS), 3-chloropropyltrimethoxysilane (CPTMS), or 2-[methoxy(polyethyleneoxy)$_{9-12}$propyl] trimethoxysilane (PEG-silane). The chemical structures of these silanes are shown in Figure 6.2.

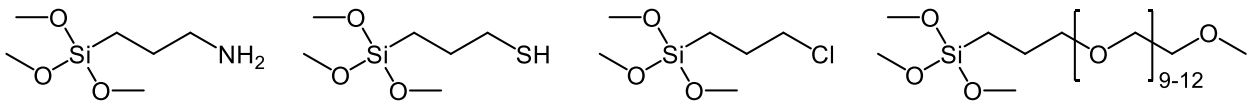

APTMS **MPTMS** **CPTMS** **PEG-silane**

Figure 6.2 Chemical structures of silanes used for surface functionalization of mesoporous silica-coated gold nanorods. 3-aminopropyltrimethoxy silane (APTMS), 3-mercaptopropyltrimethoxy silane (MPTMS), 3-chloropropyltrimethoxysilane (CPTMS), and 2-[methoxy(polyethyleneoxy)$_{9-12}$propyl]trimethoxy silane (PEG-silane).

Silica coating and silane functionalization was carried out following the procedure outlined in Scheme 6.1 Cetyltrimethylammonium bromide (CTAB)-capped nanorods were prepared following the well-known seed-mediated, silver-assisted synthesis.[35,36] The nanorods were aspect ratio 3.5 and approximately 45 ± 6 nm in length and 13 ± 2 nm in width with a longitudinal LSPR at 770 nm. As-synthesized nanorods were purified by two rounds of centrifugation to remove excess reactants. For silica coating to be successful, it is important for CTAB concentration to be in the 0.1 – 2 mM range. Silica coating was carried out by the hydrolysis and condensation of the silica precursor TEOS at pH 10.6 and a CTAB concentration of 0.8 nM. At this CTAB concentration mesoporous silica shells are produced which are ~22 nm thick.[6] After silica coating, the gold nanorods were purified by centrifugation and redispersed in EtOH for silane functionalization. The functionalized gold nanorods were purified by centrifugation and resuspended in dimethyl sulfoxide (DMSO) and diluted to a final concentration of ~1 nM for all studies.

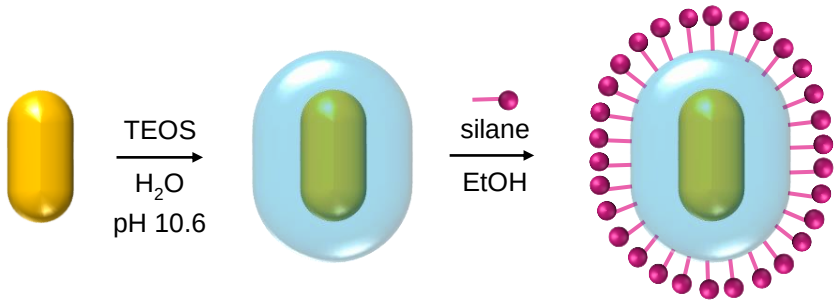

Scheme 6.1 Process for silica coating and surface functionalization of CTAB gold nanorods. Gold nanorods were coated in mesoporous silica by hydrolysis and condensation of the silica precursor tetraethylorthosilicate (TEOS) at pH 10.6 and CTAB concentration of 0.8 mM. After coating, silica-coated gold nanorods purified by centrifugation and were redispersed in EtOH. The nanorods were functionalized with various silanes (Figure 6.2) at room temperature for 48 h. Silica-coated and silane-functionalized gold nanorods were purified by centrifugation and redispersed in DMSO for all stability studies.

CTAB, silica-coated and silane-functionalized gold nanorods dispersed in water were characterized by UV-vis absorbance, dynamic light scattering, and ζ-potential measurements to ensure functionalization was successful, and that there was no aggregation of gold nanorods. The data from these measurements are summarized in Table 6.1. The longitudinal LSPR peak shifted after silica coating and silane functionalization. It is known that longitudinal LSPR in gold nanorods is highly sensitive to the refractive index at the surface, so small shifts in the peak position are an indication of a changed environment at/near the nanorod surface. Since silica has a higher refractive index than water, a red-shift in the absorbance is expected after silica coating.[4] Additionally, we note that there was no evidence of aggregation of nanorods in the UV-vis spectra (not shown) because there was no broadening in the longitudinal LSPR peaks. After silica coating and silane functionalization the hydrodynamic diameter was increased, as measured by dynamic light scattering. Also, ζ-potential measurements demonstrated that silica coating of positively charged CTAB gold nanorods resulted in a negatively charged surface. Silane functionalized gold nanorods had increased ζ-potentials compared to the silica-coated gold nanorods. Together, these characterization data suggest that silica coating and silane-functionalization was successful.

Table 6.1 Characterization data for CTAB, silica and silane-functionalized gold nanorods in water.

Sample	Longitudinal peak	Hydrodynamic diameter	ζ-potential
CTAB	770 nm	18.2 ± 0.2 nm	31 ± 2 mV
silica	774 nm	44.0 ± 0.7 nm	-34 ± 4 mV
APTMS	762 nm	153 ± 38 nm	4 ± 1 mV
MPTMS	790 nm	55.8 ± 0.4 nm	-17 ± 1 mV
CPTMS	785 nm	53.5 ± 0.2 nm	-18 ± 2 mV
PEG-silane	784 nm	44.8 ± 0.3 nm	0.2 ± 2.6 mV

6.3.2 EFFECT OF THERMAL HEATING ON GOLD NANORODS

Gold nanorods were heated in an oven at 50, 75, 100, 125 then 150°C for 2 h intervals to examine the thermal stability of the various surface coatings. The boiling point of DMSO is 189°C so silica-coated and silane-functionalized gold nanorods remained dispersed in solution, even at the highest temperature. We note that the CTAB gold nanorods in water evaporated at/above 100°C, but dried samples could be redispersed in water by sonication. Photographs of the gold nanorod solutions before and after heating are shown in Figure 6.3. There is a noticeable color change of the gold nanorod solutions which is an indication of changes in gold nanorod optical properties. Before heating the solutions were brown, which is typical of nanorods with a longitudinal plasmon ~780 nm. After heating the solution of CTAB gold nanorods turned purple while silica-coated, and CPTMS and PEG-functionalized gold nanorod solutions turned green. The APTMS and MPTMS-functionalized nanorod solutions appeared more brownish/gray. These differences in color suggested that the surface coating can alter how gold nanorods respond to heat.

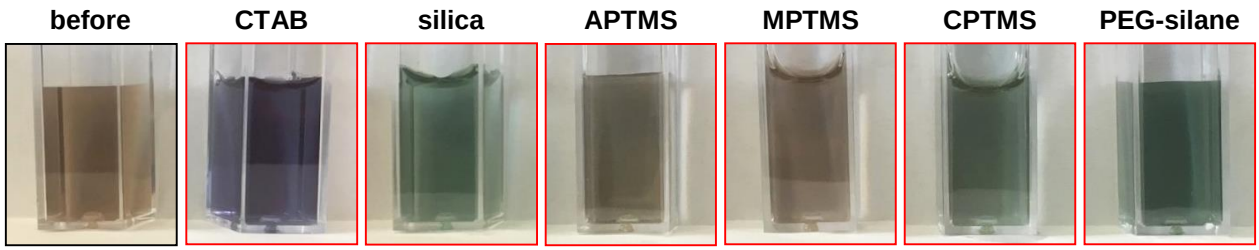

Figure 6.3 Photographs of solutions of CTAB, silica-coated, and silane-functionalized gold nanorods before (black outline) and after (red outlines) heating to 150°C.

UV-vis absorbance measurement of gold nanorods was carried out to monitor the change in optical properties after each interval of heating. Plots of peak shift *versus* temperature for each type of surface coating are shown in Figure 6.4a. Shifts represent the peak shift in the longitudinal LSPR relative to the original peak position of the nanorods before heating. Example UV-vis absorbance spectra of silica-coated gold nanorods in DMSO before heating, and after each heating interval are shown in Figure 6.4b. There are noticeable blue-shifts in the longitudinal LSPR of the silica-coated gold nanorods after heating which indicates that thermal heating can significantly alter optical properties. However, the peak shift observed in the silica-coated gold nanorods (73 nm) was not as great as the CTAB gold nanorods (149 nm). This result confirms the conclusions from previous reports that a mesoporous silica coating can improve the stability of gold nanorod optical properties. However, Figure 6.4a also demonstrates that functionalization of the silica coating with an organic silane can further improve thermal stability. Peak shifts were reduced for all of the silane-functionalized silica-coated gold nanorods. However, it is interesting to note that there were differences in peak shifts between the silanes. After heating to 150°C, the blue shift observed in APTMS-functionalized nanorods was only 7 nm, followed by MPTMS (19 nm), CPTMS (50 nm) and PEG-silane (55 nm). This indicates that silane functionalization of mesoporous silica coatings can further preserve gold nanorod optical properties, but the chosen silane does seem to matter.

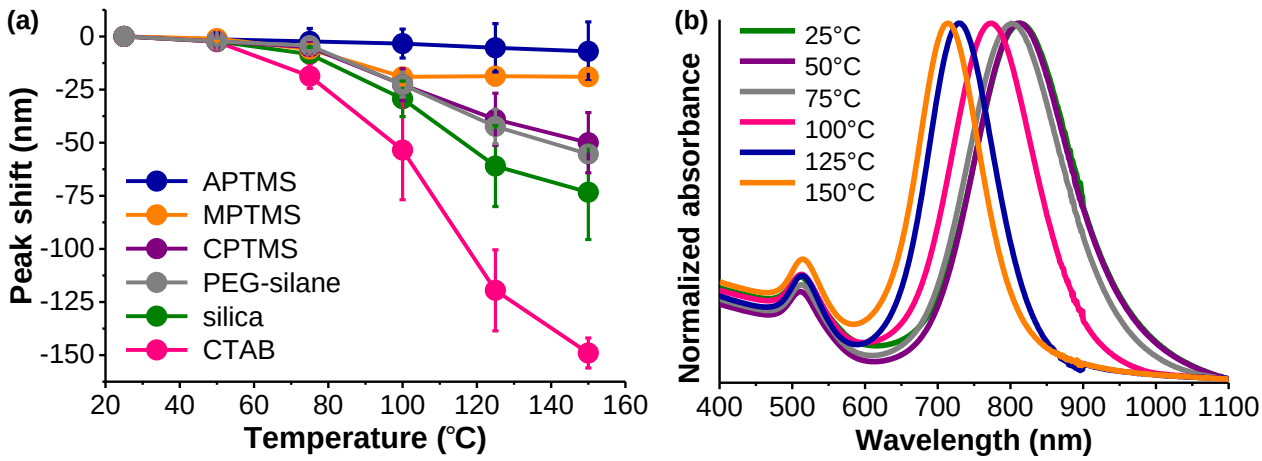

Figure 6.4 (a) Temperature *versus* peak shift of the longitudinal LSPR of gold nanorods relative to the original peak position after heating in an oven at 50, 75, 100, 125 and 150°C for 2 h intervals. Shifts are from CTAB gold nanorods in water, and silica-coated, and silane-functionalized gold nanorods in DMSO. (b) Example UV-vis spectra of silica-coated gold nanorods in DMSO at room temperature (25°C) and after heating in an oven at 50, 75, 100, 125 and 150°C for 2 h intervals.

The morphology of gold nanorods before and after heating to 150°C was examined using transmission electron microscopy (TEM). Example TEM images of CTAB, silica coated and APTMS-functionalized gold nanorods before and after heating are shown in Figure 6.5. After heating, CTAB gold nanorods became more spherical and some large aggregates formed (Figure 6.5d). This obvious shape change did not occur in silica-coated (Figure 6.5e) or APTMS-functionalized (Figure 6.5f) gold nanorods which were more stable (Figure 6.4a). However, it did appear as if the silica-coated gold nanorods became shorter after heating. Analysis of the TEM images was carried out using ImageJ to determine if there was a change in aspect ratio of the gold nanorods or in silica shell thickness.

The results of the analysis for CTAB, silica-coated and silane-functionalized gold nanorods are shown in Table 6.2. The nanorods with the greatest peak shifts (Figure 6.4a) also had the greatest decreases in aspect ratio. The decreases in aspect ratio occurred because the nanorods got shorter but wider after heating (length and width data are not shown). The presence of a shell reduced that change. It is also interesting to note that there was a slight increase in silica shell thickness for the silica-coated gold nanorods and most of the silane-functionalized gold nanorods after heating. We note that silica shell thickness was measured from the sides of the gold nanorods, not the ends. Therefore, it is likely that the shortening and widening in the nanorods also resulted in shortening and widening of the silica shell.

Heating causes gold nanorod morphology to become more rounded/spherical, a result of decreased surface energy. Other researchers have suggested that the silica shell is flexible, but does not typically deform at these temperatures, and a change in shape of the silica shell is due mechanical stress is exerted on the shell by deforming gold nanorods.[19] It is possible that silane functionalization further stabilized the shell, which reduced surface energy, and therefore less gold nanorod deformation was observed. An alternative explanation is that the thermal conductivity of gold nanorods was enhanced by surface coating.[37]

Silica coated gold nanorods can more efficiently transfer heat to the surroundings, so material deformation is reduced.[26] If there were differences in thermal conductivity of the organic silanes on the surface, this may have impacted thermal conductivity of the silica shell. However, regardless of the mechanism, it is apparent that morphology is better preserved by silica coating and functionalization, and this results in better preserved optical properties of gold nanorods.

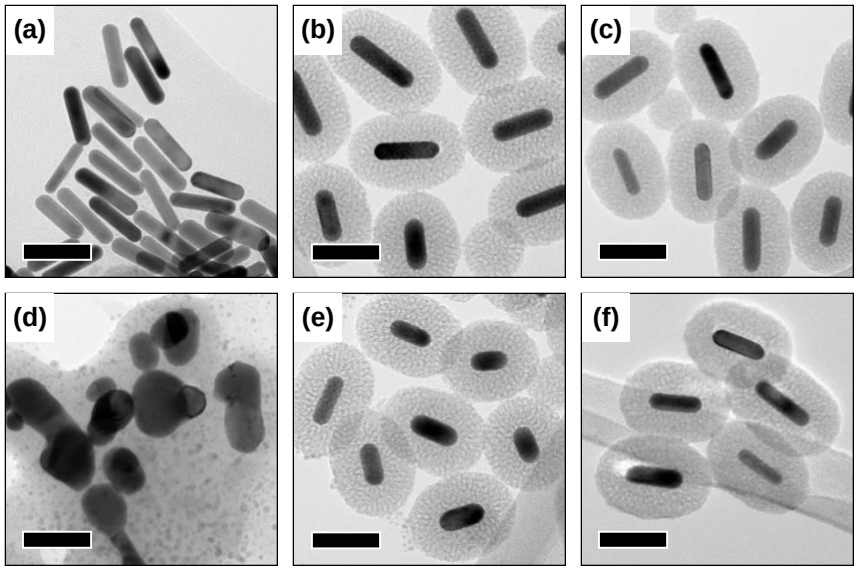

Figure 6.5 Example TEM images of (a, d) CTAB, (b, e) silica-coated, and (c, f) APTMS-functionalized gold nanorods (a-c) before and (d-e) after heating in an oven to 150°C.

Table 6.2 Aspect ratio and silica shell thickness of CTAB, silica-coated, and silane-functionalized gold nanorods before and after heating in an oven to 150°C.

Sample	Aspect ratio	Aspect ratio (heated to 150°C)	Shell thickness	Shell thickness (heated to 150°C)
CTAB	3.57 ± 0.02	1.55 ± 0.01	-	-
silica	3.35 ± 0.08	2.41 ± 0.10	21.6 ± 1.5	22.2 ± 1.3
APTMS	3.52 ± 0.14	3.42 ± 0.04	22.2 ± 1.2	23.0 ± 1.3
MPTMS	3.45 ± 0.07	3.24 ± 0.01	21.6 ± 1.2	21.9 ± 1.2
CPTMS	3.44 ± 0.22	2.95 ± 0.19	21.9 ± 1.5	22.3 ± 1.4
PEG-silane	3.44 ± 0.13	2.83 ± 0.10	21.7 ± 1.3	21.7 ± 1.3

6.3.3 EFFECT OF CHARGING BY AN ELECTRON BEAM ON GOLD NANORODS

It has been observed that gold nanorods can deform when they undergo charging from electrons. The longitudinal LSPR is especially sensitive to surface perturbation by electron injection because the electron density within a particle is altered. This was demonstrated by blue-shifts in the absorbance spectrum after the introduction of the reducing agent $NaBH_4$ or by an applied potential into a solution of gold nanorods.[30,31]

Electron beams can also be used to pattern gold nanostructures, and may therefore be a powerful tool to perturb the gold nanorod structure.[38,39]

During TEM imaging of gold nanorods an electron beam is usually spread over a portion of the sample hundreds of nanometers or microns in diameter. To further investigate the stability of gold nanorods, TEM grids of gold nanorod samples were exposed to charging from a focused electron beam (200 kV, 150 pa/cm^2, 30 s). By focusing the electron beam to a smaller area (200 nm) it was possible to introduce enough electrons to the sample to generate noticeable changes in gold nanorod morphology. TEM images of CTAB, silica-coated and APTMS-functionalized gold nanorods before and after charging from an electron beam are shown in Figure 6.6. The CTAB gold nanorods appear to fuse together after the exposure (Figure 6.6d). This fusion was not observed in the silica-coated (Figure 6.6e) or APTMS-functionalized (Figure 6.6f) gold nanorods which seemed protected by the silica shells. However, it did appear that the silica shells became thinner and less porous after exposure to the focused electron beam.

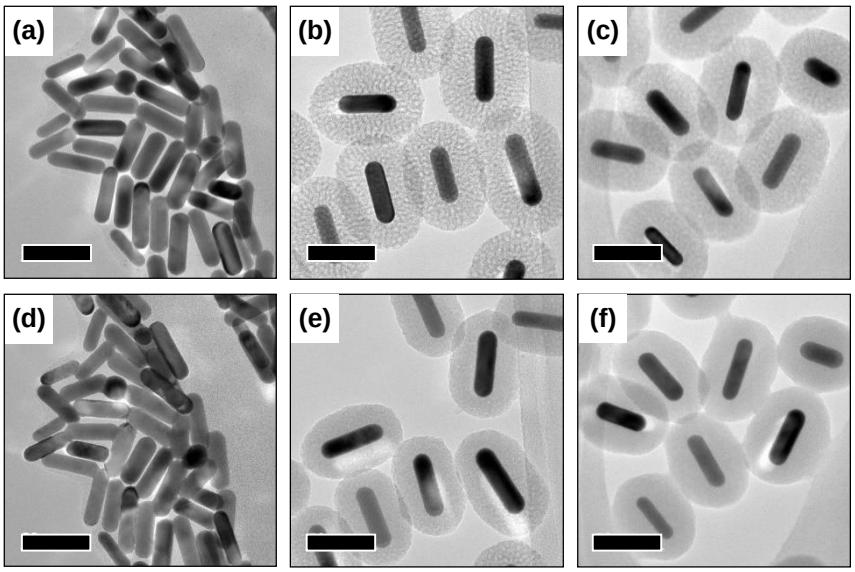

Figure 6.6 Example TEM images of (a, d) CTAB, (b, e) silica-coated, and (c, f) APTMS-functionalized gold nanorods (a-c) directly before and (d-e) after exposure to an electron beam (200 kV, 150 pA/cm^2, 30 s). Scale bars = 50 nm.

Analysis of the TEM images was carried out to determine if there was a change in aspect ratio or silica shell thickness after dosing gold nanorods with electrons, and the results are shown in Table 6.3. There is a decrease in aspect ratio observed with the CTAB gold nanorods which resulted from a decrease in length and increase in width of the nanorods (length and width are not shown). As described by the above references,[30,31] this deformation this is likely due to perturbation of the LSPR by electron injection. However, there was no significant change in dimensions or aspect ratio with the silica-coated or APTMS-functionalized gold nanorods. This demonstrates that silica coating and functionalization may enhance the stability of gold nanorods in highly charged environments. Interestingly though, there was a measurable

decrease in silica shell thickness after electron exposure. The TEM images of the shells appear as if porosity was lost due to the shells annealing (Figure 6.6e,f). Annealing of mesoporous silica, resulting in complete loss of porosity, has been observed to occur at high temperatures due to complete hydrolysis and condensation silanol groups.[40,41] It is possible that the collapse in pore structure resulted in annealing, further strengthening the silica shell and prevented deformation of the gold nanorods.

Table 6.3 Aspect ratio and shell thickness of CTAB, silica-coated, and APTMS-functionalized gold nanorods before and after exposure to an electron beam (200 kV, 150 pA/cm^2, 30 s).

Sample	Aspect ratio	Aspect ratio (electron beam)	Shell thickness	Shell thickness (electron beam)
CTAB	3.37 ± 0.12	3.12 ± 0.10	-	-
silica	3.45 ± 0.08	3.43 ± 0.01	24.1 ± 1.1 nm	19.9 ± 2.3 nm
APTMS	3.39 ± 0.03	3.41 ± 0.01	22.8 ± 1.4 nm	20.1 ± 1.4 nm

6.3.4 EFFECT OF FEMTOSECOND PULSED LASER IRRADIATION ON GOLD NANORODS

Exposure of gold nanorods to irradiation from femtosecond pulsed lasers is a common method to heat up gold nanorods in photothermal therapy applications.[5] However, if gold nanorods are quickly deformed by high energy pulses, this limits their effectiveness in photothermal heating.[42] Surface melting occurs because rates of energy absorption are higher than thermal dissipation. However, if a gold nanorod surface coating has lower thermal resistance,[20] or enhanced rigidity,[21] it may be possible to reduce the effects of laser-induced deformation. Gold nanorods were exposed to femtosecond pulsed laser irradiation to determine if silica coating and silane functionalization could prevent/reduce changes in gold nanorod morphology. The laser used was 800 nm, so there was strong overlap with the longitudinal LSPR of the gold nanorods (Figure 6.7). Solutions of CTAB, silica-coated and APTMS-functionalized gold nanorods were exposed to the laser for 10 min (120 fs pulse width, 1 kHz repetition rate, 2.5 mJ/cm^2).

UV-vis absorbance spectra before and after laser irradiation are shown in Figure 6.7. The longitudinal peak in the spectrum of the CTAB gold nanorods shifts to ~650 nm and is smaller in magnitude compared to the transverse peak. This is an indication of a significant change in morphology. The silica-coated gold nanorods also are blue shifted, and the longitudinal peak is larger in magnitude compared to the transverse peak. This indicates that there was a change in morphology and optical properties in silica-coated nanorods, but it was not as great as the CTAB gold nanorods. Interestingly, laser irradiation of APTMS-functionalized gold nanorods displayed a longitudinal peak ~720 nm, but there was a noticeable decrease in magnitude of the peak and significant broadening, which is suggestive of aggregation. These spectra show that femtosecond laser irradiation of gold nanorods can result in surface chemistry-dependent changes in optical properties. In the case of silica coating and APTMS functionalization, the shift in the longitudinal LSPR was not as great as in CTAB gold nanorods. Therefore, silica coating and silane functionalization can reduce, the changes in gold nanorod optical properties after pulsed laser irradiation.

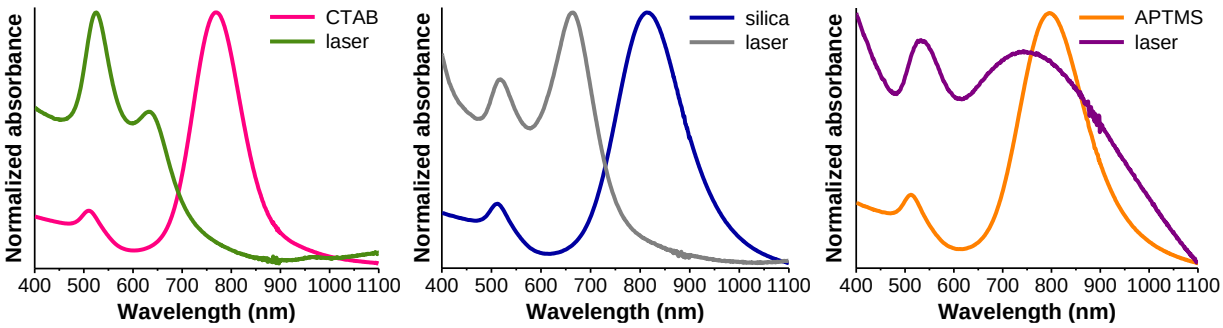

Figure 6.7 UV-vis absorbance spectra of CTAB, silica-coated and APTMS-functionalized gold nanorods before and after exposure to femtosecond pulsed laser irradiation (800 nm, 1 kHz, 120 fs, 1.9 W, 10 min).

TEM images of the gold nanorods before and after laser irradiation are shown in Figure 6.8. CTAB gold nanorods (Figure 6.8a) appear to become large spheres after irradiation or large agglomerated structures (Figure 6.8d,g). The silica-coated gold nanorods (Figure 6.8b) appear to form dimers, spheres, and aspheroidal structures inside the shells. However, no aggregates of gold nanorods are present after laser irradiation, likely due to the silica shell. Additionally, there are small dark particles around/near the rods. Formation of dimers appears to occur because of a loss of gold at the nanorod sides/middle regions. The most likely explanation for the presence of these small particles is that pieces of nanorods, which were produced by laser irradiation, escaped through the pores in the silica shell. The APTMS-functionalized gold nanorods (Figure 6.8c) also form dimer structures after irradiation, but it appears that there are many bowtie-shaped particles present (Figure 6.8f,i). The bowties may be an intermediate structure which nanorods take before forming dimers. Again, small particles of what may be gold are apparent on the silica surfaces. TEM images of CTAB, silica-coated and APTMS-functionalized gold nanorods, were analyzed to determine the shape composition after laser irradiation. The results of the analysis are shown in Figure 6.9. The shapes that were present were nanorods, aspheroids, bowties, dimers, spheres and aggregates. The CTAB gold nanorods formed ~50% spheres after laser irradiation, followed by aggregates, aspheroids and nanorods. There were few bowties and no dimers present. Silica-coated gold nanorods formed mostly into aspheroids and dimers after laser irradiation. Interestingly, the most common structure found in TEM images of the laser-irradiated APTMS-functionalized gold nanorods was bowties. These differences in shape composition suggest that the gold nanorod surface coating had an impact on thermal dissipation and melting. This could have resulted in different shapes of gold nanostructures forming after laser irradiation.

The results of shape transformation in this work are different from previous reports which describe femtosecond pulsed laser irradiation of mesoporous silica-coated gold nanorods.[20,21,25] In those reports the nanorods ends are shortened which results in a gap in the silica shell at the ends, or the nanorods become shorter and wider. Only one other report has observed the formation of nanodumbbells. They suggest that melting started at the ends of the rods and stopped at the sides before complete transformation to a sphere. However, this only occurred in a small population of the nanorods.[43] We observe no such gap and the shape change to aspheroids/bowties/dimers appears to occur as loss of gold at the nanorod sides.

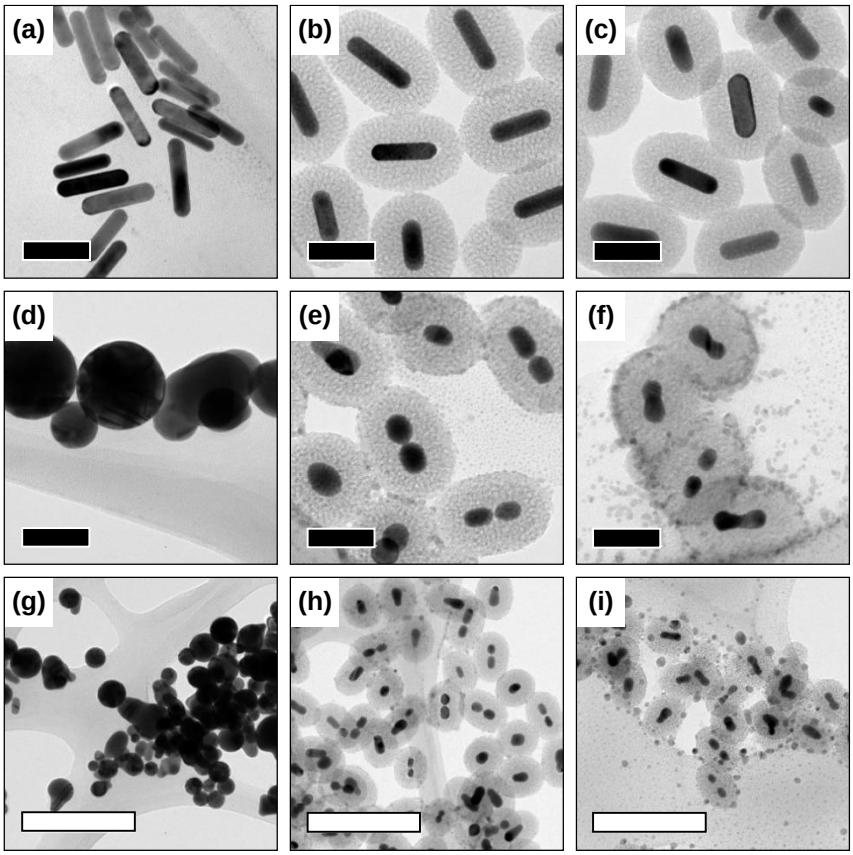

Figure 6.8 Example TEM images of (a, d, g) CTAB, (b, e, h) silica-coated, and (c, f, i) APTMS-functionalized gold nanorods (a-c) before and (d-i) after exposure to femtosecond pulsed laser irradiation (800 nm, 1 kHz repetition rate, 120 fs pulse width, 2.5 J/cm^2 pulse energy, 10 min). Black scale bars = 50 nm. White scale bars = 200 nm.

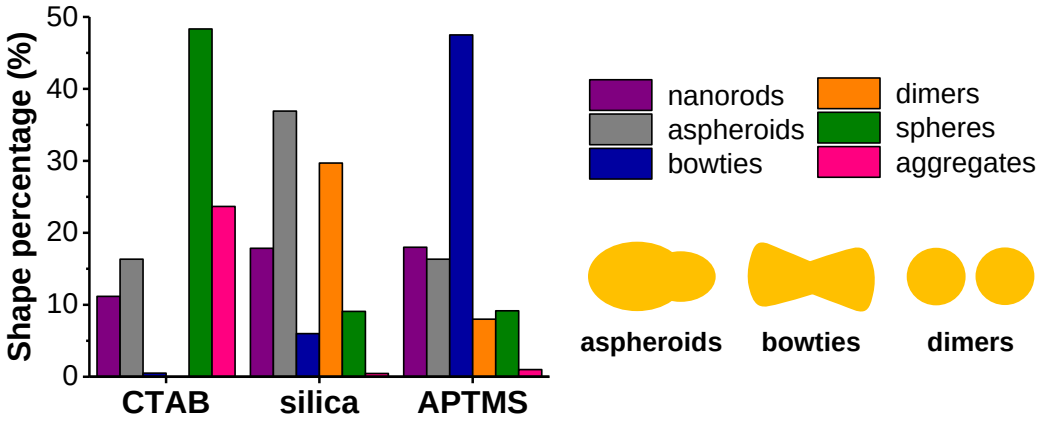

Figure 6.9 Shape distribution of CTAB, silica-coated, and APTMS-functionalized gold nanorods after exposure to femtosecond pulsed laser irradiation (800 nm, 1 kHz repetition rate, 120 fs pulse width, 2.5 mJ/cm^2 pulse energy, 10 min).

It is known that there are differences in melting behavior of the crystal faces on gold, and some crystal faces in gold nanorods could more stable than others.[44-46] El-Sayed and coworkers, have previously

investigated melting in multiple twinned gold nanorods which are icosahedral and consist of 20 tetrahedra with {111} facets. They determined that femtosecond laser-irradiation induced defects, which converted {110} facets into the more stable {100} and {111} facets, to minimize surface energy. They concluded that surface melting begins with formation of defects followed by surface reconstruction and atomic diffusion.[47] This is different from thermal melting of gold nanorods, where the melting starts at the surface and causes different shape changes in gold nanorods (Figure 6.5). If laser-induced deformation is influenced by the crystal facets present on the gold nanorods, which can be different depending on the synthesis technique, then this might explain the morphological changes observed here.[48,49] If the deformation is driven by differences in surface energy, the less stable crystal faces would be deformed before the more stable faces. If silica coating and silane functionalization reduces surface energy of the crystal faces, then this might have resulted in less deformation of the gold nanorod structures and different changes in optical properties.

6.4 CONCLUSIONS AND FUTURE WORK

In this work we have examined how inorganic silica coating and silane functionalization of gold nanorods may better preserve their optical properties after energy input by a variety of methods. Thermal heating in an oven and charging due to electron beam exposure caused shortening and widening of gold nanorods, and also resulted in decreased in aspect ratio. However, these changes in morphology and optical properties were greatly reduced by silica coating and functionalization. Pulsed laser irradiation also altered gold nanorod optical properties, and interesting changes in gold nanorod morphology were observed. Together, these results suggest that silica coating and silane functionalization improve the shape stability of gold nanorods and therefore may help to preserve the optical properties, especially compared to CTAB gold nanorods. The two possible reasons for these observations are that there are changes in heat diffusion rates or reductions in surface energy by silica coating and functionalization. Investigation of heat transfer dynamics in these gold nanorods by pump-probe IR spectroscopy may reveal the mechanism of how nanorod morphology is preserved. In the future, parameters such as silica shell thickness, silane amount, laser power and exposure time would be useful to further optimize gold nanorod optical stability.

6.5 REFERENCES

1. Chen, H.; Shao, L.; Li, Q.; Wang, J. Gold Nanorods and their Plasmonic Properties. *Chem. Soc. Rev.* **2013,** *42,* 2679-2724.
2. Burrows, N. D.; Vartanian, A. M.; Abadeer, N. S.; Grzincic, E. M.; Jacob, L. M.; Lin, W.; Li, J.; Dennison, J. M.; Hinman, J. G.; Murphy, C. J. Anisotropic Nanoparticles and Anisotropic Surface Chemistry. *J. Phys. Chem. Lett.* **2016,** *7,* 632−641
3. Pérez-Juste, J.; Pastoriza-Santos, I.; Liz-Marzán, L. M.; Mulvaney, P. Gold Nanorods: Synthesis, Characterization and Applications. *Coord. Chem. Rev.* **2005,** *249,* 1870-1901.
4. Abadeer, N. S.; Fülöp, G.; Chen, S.; Käll, M.; Murphy, C. J. Interactions of Bacterial Lipopolysaccharides with Gold Nanorod Surfaces Investigated by Refractometric Sensing. *ACS Appl. Mater. Interfaces* **2015,** *7,* 24915-24925.
5. Abadeer, N. S.; Murphy, C. J. Recent Progress in Cancer Thermal Therapy using Gold Nanoparticles. *J. Phys. Chem. C* **2016,** *120,* 4691-4716.

6. Abadeer, N. S.; Brennan, M. R.; Wilson, W. L.; Murphy, C. J. Distance and Plasmon Wavelength Dependent Fluorescence of Molecules Bound to Silica-Coated Gold Nanorods. *ACS Nano* **2014,** *8,* 8392-8406.
7. Sivapalan, S. T.; DeVetter, B. M.; Yang, T. K.; van Dijk, T.; Schulmerich, M. V.; Carney, P. S.; Bhargava, R.; Murphy, C. J. Off-Resonance Surface-Enhanced Raman Spectroscopy from Gold Nanorod Suspensions as a Function of Aspect Ratio: Not What We Thought. *ACS Nano* **2013,** *7,* 2099-2105.
8. Huang, X.; Neretina, S.; El-Sayed, M. A. Gold Nanorods: From Synthesis and Properties to Biological and Biomedical Applications. *Adv. Mater.* **2009,** *21,* 4880-4910.
9. Nikoobakht, B.; El-Sayed, M. A. Evidence for Bilayer Assembly of Cationic Surfactants on the Surface of Gold Nanorods. *Langmuir* **2001,** *17,* 6368-6374.
10. Murphy, C. J.; Thompson, L. B.; Alkilany, A. M.; Sisco, P. N.; Boulos, S. N.; Sivapalan, S.; Yang, J. A.; Chernak, D. J.; Huang, J. The Many Faces of Gold Nanorods. *J. Phys. Chem. Lett.* **2010**, *1*, 2867-2875.
11. Niidome, T.; Yamagata, M.; Okamoto, Y.; Akiyama, Y.; Takahashi, H.; Kawano, T.; Katayama, Y.; Niidome, Y. PEG-Modified Gold Nanorods with a Stealth Character for *In vivo* Applications. *J. Controlled Release* **2006,** *114,* 343-347.
12. Gole, A.; Murphy, C. J. Polyelectrolyte-Coated Gold Nanorods: Synthesis, Characterization and Immobilization. *Chem. Mater.* **2005,** *17,* 1325-1330.
13. Link, S.; Burday, C.; Mohamed, M. B.; Nikoobakht, B.; El-Sayed, M. A. Laser Photothermal Melting and Fragmentation of Gold Nanorods: Energy and Laser Pulse-Width Dependence. *J. Phys. Chem. A* **1999,** *103,* 1165-1170.
14. Link, S.; El-Sayed, M. A. Shape and Size Dependence of Radiative, Non-Radiative and Photothermal Properties of Gold Nanocrystals. *Int. Rev. Phys. Chem.* **2000,** *19,* 409-453.
15. González-Rubio, G.; Guerrero-Martínez, A.; Liz-Marzán, L. M. Reshaping, Fragmentation, and Assembly of Gold Nanoparticles Assisted by Pulse Lasers. *Acc. Chem. Res.* **2016,** *49,* 678-686.
16. Falamas, A.; Tosa, N.; Tosa, V. Dynamics of Laser Excited Colloidal Gold Nanoparticles Functionalized with Cysteine Derivatives. *J. Quant. Spectrosc. Radiat. Transfer* **2015,** *162,* 207-212.
17. Petrova, H.; Perez Juste, J.; Pastoriza-Santos, I.; Hartland, G. V.; Liz-Marzán, L. M.; Mulvaney, P. On the Temperature Stability of Gold Nanorods: Comparison Between Thermal and Ultrafast Laser-Induced Heating. *Phys. Chem. Chem. Phys.* **2006,** *8,* 814-821.
18. Mohamed, M. B.; Ismail, K. Z.; Link, S.; EL-Sayed, M. A. Thermal Reshaping of Gold Nanorods in Micelles. *J. Phys. Chem. B* **1998,** *102,* 9370-9374.
19. Gergely-Fülöp, E.; Zámbo, D.; Deák, A. Thermal Stability of Mesoporous Silica-Coated Gold Nanorods with Different Aspect Ratios. *Mater. Chem. Phys.* **2014,** *148,* 909-913.
20. Nguyen, S. C.; Zhang, Q.; Manthiram, K.; Ye, X.; Lomont, J. P.; Harris, C. B.; Weller, H.; Alivisatos, A. P. Study of Heat Transfer Dynamics from Gold Nanorods to the Environment via Time-Resolved Infrared Spectroscopy. *ACS Nano* **2016,** *10,* 2144-2151.
21. Albrecht, W.; Deng, T.-S.; Goris, B.; van Huis, M. A.; Bals, S.; van Blaaderen, A. Single Particle Deformation Analysis of Silica-Coated Gold Nanorods before and after Femtosecond Laser Pulse Excitation. *Nano Lett.* **2016,** *16,* 1818-1825.
22. Wu, Z.; Zeng, Q.; Wang, H. Structural Controls of AuNR@mSiO_2: Tuning of the SPR, and Manipulation of the Silica Shell Thickness and Structure. *J. Mater. Chem. C* **2016,** *4,* 2614-2620.
23. Gautier, C.; Cunningham, A.; Si-Ahmed, L.; Rober, G.; Bürgi, T. Pigments Based on Silica-Coated Gold Nanorods: Synthesis, Colouring Strength, Functionalisation, Extrusion, Thermal Stability and Colour Evolution. *Gold Bull.* **2010,** *43,* 94-104.
24. Deng, T.-S.; van der Hoeven, J. E. S.; Yalcin, A. O.; Zandbergen, H. W.; van Huis, M. A.; van Blaaderen, A. Oxidative Etching and Metal Overgrowth of Gold Nanorods within Mesoporous Silica Shells. *Chem. Mater.* **2015,** *27,* 7196-7203.
25. Chen, L.-C.; Wei, C.-W.; Souris, J. S.; Cheng, S.-H.; Chen, C.-T.; Yang, C.-S.; Li, P.-C.; Lo, L.-W. Enhanced Photoacoustic Stability of Gold Nanorods by Silica Matrix Confinement. *J. Biomed. Optics* **2010,** *15,* 016010.
26. Chen, Y.-S.; Frey, W.; Kim, S.; Homan, K.; Kruizinga, P.; Sokolov, K.; Emelianov, S. Enhanced Thermal Stability of Silica-Coated Gold Nanorods for Photoacoustic Imaging and Image-Guided Therapy. *Opt. Express* **2010,** *18,* 8867-8878.

27. Bore, M. T.; Pham, H. N.; Switzer, E. E.; Ward, T. L.; Fukuoka, A.; Datye, A. K. The Role of Pore Size and Structure on the Thermal Stability of Gold Nanoparticles within Mesoporous Silica. *J. Phys. Chem. B* **2005,** *109,* 2873-2880
28. Gorelikov, I.; Matsuura, N. Single-Step Coating of Mesoporous Silica on Cetyltrimethyl Ammonium Bromide- Capped Nanoparticles. *Nano Lett.* **2008,** *8,* 369–373.
29. Orendorff, C. J.; Murphy, C. J. Quantitation of Metal Content in the Silver-Assisted Growth of Gold Nanorods. *J. Phys. Chem. B* **2006,** *110,* 3990–3994.
30. Mulvaney, P.; Pérez-Juste, J; Giersig, M.; Liz-Marzán, L. M.; Pecharromán, C. Drastic Surface Plasmon Mode Shifts in Gold Nanorods Due to Electron Charging. *Plasmonics* **2006,** *1,* 61-66.
31. Novo, C.; Funston, A. M.; Gooding, A. K.; Mulvaney, P. Electrochemical Charging of Single Gold Nanorods *J. Am. Chem. Soc.* **2009,** *131,* 14664–14666.
32. Wu, W.-C.; Tracy, J. B. Large-Scale Silica Overcoating of Gold Nanorods with Tunable Shell Thicknesses. *Chem. Mater.* **2015**, *27,* 2888-2894.
33. Lin, Y.-S.; Abadeer, N.; Hurley, K. R.; Haynes, C. L. Ultrastable, Redispersible, Small, and Highly Organomodified Mesoporous Silica Nanotherapeutics. *J. Am. Chem. Soc.* **2011**, *133,* 20444-20457.
34. Liu, J.; Detrembleur, C.; De Pauw-Gillet, M.-C.; Mornet, S.; Jérôme, C.; Duguet, E. Gold Nanorods Coated with Mesoporous Silica Shell as Drug Delivery System for Remote Near Infrared Light-Activated Release and Potential Phototherapy. *Small* **2015**, *11,* 2323-2332.
35. Nikoobakht, B.; El-Sayed, M. A. Preparation and Growth Mechanism of Gold Nanorods (NRS) Using Seed-Mediated Growth Method. *Chem. Mater.* **2003,** *15,* 1957-1962.
36. Gole, A.; Murphy, C. J. Seed-Mediated Synthesis of Gold Nanorods: Role of the Size and Nature of the Seed. *Chem. Mater.* **2004,** *16,* 3633-3640.
37. Huang, J.; Park, J.; Wang, W.; Murphy, C. J.; Cahill, D. G. Ultrafast Thermal Analysis of Surface Functionalized Gold Nanorods in Aqueous Solution. *ACS Nano* **2013,** *7,* 589-597.
38. Koh, A. L.; Fernández-Domínguez, A. I.; McComb, D. W.; Maier, S. A.; Yang, J. K. W. High-Resolution Mapping of Electron-Beam-Excited Plasmon Modes in Lithographically Defined Gold Nanostructures. Nano Lett. *Nano Lett.* **2011,** *11,* 1323–1330.
39. Near, R.; Tabor, C.; Duan, J.; Pachter, R.; El-Sayed, M. A. Pronounced Effects of Anisotropy on Plasmonic Properties of Nanorings Fabricated by Electron Beam Lithography. *Nano Lett.* **2012,** *12,* 2158−2164.
40. Gu, G.; Ong, P. P.; Chu, O. C. Thermal Stability of Mesoporous Silica Molecular Sieve. *J. Phys. Chem. Solids* **1999,** *60,* 943-947.
41. Broyer, M.; Valange, S.; bellat, J. P.; Bertrand, O.; Weber, G.; Gabelica, Z. Influence of Aging, Thermal, Hydrothermal, and Mechanical Treatments on the Porosity of MCM-41 Mesoporous Silica. *Langmuir* **2002,** *18,* 5083-5091.
42. Ungureanu, C.; Kroes, R.; Petersen, W.; Groothuis, T. A. M.; Ungureanu, F.; Janssen, H.; van Leeuwen, F. W. B.; Kooyman, R. P. H.; Manohar, S.; van Leeuwen, T. G. Light Interactions with Gold Nanorods and Cells: Implications for Photothermal Nanotherapeutics. *Nano Lett.* **2011,** *11,* 1887-1894.
43. Chon, J. W. M.; Bullen, C.; Ziljstra, P.; Gu, M. Spectral Encoding on Gold Nanorods Doped in a Silica Sol–Gel Matrix and Its Application to High-Density Optical Data Storage. *Adv. Funct. Mater.* **2007,** *17,* 875–880.
44. Mochrie, S. G. J.; Zehner, D. M.; Ocko, B. M.; Gibbs, D. Structure and Phases of the Au(001) Surface: X-Ray Scattering Measurements. *Phys. Rev. Lett.* **1990,** *64,* 2925-2928.
45. Hoss, A.; Nold, M.; von Blanckenhagen, P.; Meyer, O. Roughening and Melting of Au(110) Surfaces. *Phys. Rev. B* **1992,** *45,* 8714-8720.
46. Carnevali, P.; Ercolessi, F.; Tosatti, E. Melting and Nonmelting Behavior of the Au(111) Surface. *Phys. Rev. B* **1987,** *36,* 6701-6704.
47. Link, S.; Wang, Z. L.; El-Sayed, M. A. How Does a Gold Nanorod Melt? *J. Phys. Chem. B* **2000,** *104,* 7867-7870.
48. Katz-Boon, H.; Rossouw, C. J.; Weyland, M.; Funston, A. M.; Mulvaney, P.; Etheridge, J. Three-Dimensional Morphology and Crystallography of Gold Nanorods. *Nano Lett.* **2011,** *11,* 273–278.
49. Wang, Z. L.; Mohamed, M. B.; Link, S.; El-Sayed, M. A. Crystallographic Facets and Shapes of Gold Nanorods of Different Aspect Ratios. *Surf. Sci.* **1999,** *440,* L809-L814.

CHAPTER 7:
ENGINEERED NANOMATERIALS IN THE ENVIRONMENT: STABILITY AND RETENTION AT MODEL ENVIRONMENTAL INTERFACES AS A FUNCTION OF NANOMATERIAL SURFACE CHEMISTRY

7.1 INTRODUCTION

The prevalence of engineered nanomaterials in commercial products continues to increase.[1,2] Over the past two decades billions of dollars has been invested in research and development of nanomaterial-enabled consumer products in areas such as skin care, sporting goods, industrial catalysis, antimicrobials, and cancer therapeutics.[3-7] As nanomaterials are produced in ever greater quantities to meet demand, and proliferate in consumer products, it is inevitable that engineered nanomaterials will be released into the environment. Recent legislation in the United States has banned the use of plastic microbeads (<5 mm) in personal care products due to issues of waterway contamination.[8] There has been no such regulation in the use of engineered nanomaterials due to their still unknown environmental fate and effects.[9] In order to appropriately regulate nanomaterial-enabled industries and to accurately estimate the environmental risk functionalized nanomaterials pose, it is necessary to investigate the connection between nanomaterial properties and their fate and transport within environmental systems.[10,11]

Functionalized nanomaterials represent a unique class of environmental contaminants. They exist in a size regime (~1-200 nm) that is much closer to the colloidal materials which make up naturally occurring sediment rather than the typical molecular-scale contaminants.[12] It is also challenging to predict how chemical properties of engineered nanomaterials can be successfully related to the risk these materials may pose to environmental and human health. Inside a chemistry laboratory engineered nanomaterials may possess a well-defined structure, with known shape, dimensions, and surface chemistry. However, once nanomaterials have entered the environment, size, shape, or surface chemistry may be significantly altered. This may lead to unpredicted behavior, because the interactions of nanomaterials with biological and environmental systems are strongly influenced by material properties. In order to develop an accurate risk assessment profile for engineered nanomaterials released into the environment, it is essential that we develop an initial understanding of nanomaterial fate within different environmental matrices. This includes investigation into how long they retain their original size, shape, and surface chemistry, and how mobility can be connected to structure and properties.[13,14]

The behavior of functionalized gold nanoparticles within different environmental matrices is of particular interest for three significant reasons. First, because gold nanoparticles are relatively stable against oxidation, easy to track and characterize, and gold occurs at an extremely low background level in most environmental samples, gold nanoparticles are ideal probes for investigating the fate and transport of

[*] This chapter was written with major contribution of writing/data from Samuel E. Lohse, and prepared in collaboration with Michael Zoloty, Jason C. White, Lee A. Newman, and Catherine J. Murphy.

nanoparticles in the environment. Second, the size, shape, and surface chemistry of gold nanoparticles can be controlled in exquisite detail.[15-19] Therefore, the fate and transport of gold nanoparticles in the environment can be closely correlated with material properties. Finally, because gold nanoparticles are being investigated for use in applications such as biomedical imaging and cancer therapy,[7] we can expect a marked increase in the prevalence of gold nanoparticles in the environment in the coming years. As a result, it is imperative to examine the environmental behavior of gold nanoparticles in common environmental matrices such as soil and water in detail.

To date, there have been several studies investigating the environmental fate of gold nanomaterials. However, many of these studies are limited by using only one type of nanoparticle, or they investigate fate in only one environmental medium. Additionally, interactions of nanoparticles with natural organic matter is not considered.[20,21] In order to gain a better understanding of the implications of nanomaterial exposure to the environment, it is necessary to consider variation in nanomaterial characteristics, as well as the chosen environmental medium.

Here, we examine the stability of a library of functionalized gold nanoparticles in simulated groundwater, as well as the mobility of functionalized gold nanoparticles in two types of soils and alginate as a function of gold nanoparticle shape and surface chemistry. We also investigate how the physiochemical properties of the gold nanoparticles change as a result of groundwater, alginate, or soil exposure. Two types of soil samples were used in these studies: a sample of residential soil and a sample of agricultural soil. The polysaccharide alginate is secreted by organisms such as brown algae, seaweed, and bacteria such as *Pseudomonas aeruginosa,* and *Azotobacter vinelandii* during formation of bacterial biofilms.[22-25] Thus, alginate is a useful matrix to investigate interactions between nanomaterials and natural organic matter.

We prepare a library of functionalized gold nanoparticles containing spherical citrate (Cit) and cetyltrimethylammonium bromide (CTAB gold nanoparticles, and CTAB, sodium polyacrylate (PAA), polyallylamine hydrochloride (PAH) gold nanorods. We find that gold nanoparticles functionalized with positively-charged ligands (CTAB, PAH) are immobilized following exposure to soil and alginate columns, but negatively-charged gold nanoparticles (Cit, PAA) were highly mobile, being quickly eluted from the columns. We also find that CTAB spherical gold nanoparticles may undergo aggregation following incubation in simulated ground water and soil, but the type of soil appears to have a minimal effect on nanoparticle mobility.

7.2. MATERIALS AND METHODS

7.2.1 MATERIALS

Gold tetrachloroaurate trihydrate ($HAuCl_4 \cdot 3H_2O$), sodium borohydride ($NaBH_4$), ascorbic acid ($C_6H_8O_6$), sodium polyacrylate (PAA, 30 wt.% solution, 15,000 g/mol), polyallylamine hydrochloride (PAH, 15,000 g/mol), alginic acid (sodium salt), and silver nitrate ($AgNO_3$) were obtained from Aldrich. Hexadecyltrimethylammonium bromide (CTAB), L-ascorbic acid, sodium chloride (NaCl), and trisodium citrate (Cit, $Na_3C_6H_5O_7$) were obtained from Sigma. Calcium chloride dihydrate ($CaCl_2 \cdot 2H_2O$) and

magnesium chloride hexahydrate ($MgCl_2 \cdot 6H_2O$) were obtained from Fisher. Sodium chloride was obtained from EMD Millipore. Deionized water (18.2 MΩ) was prepared using a Barnstead NANOPURE water filtration system. Unless otherwise noted, all nanomaterial syntheses and subsequent experiments were carried out using deionized Nanopure water. Transmission electron microscopy (TEM) grids, SiO on copper mesh (PELCO) were used for transmission electron microscopy. Standard laboratory chromatography sand was obtained from Aldrich. Unless otherwise noted, all materials were used as received.

7.2.2 SYNTHESIS AND CHARACTERIZATION OF FUNCTIONALIZED GOLD NANOPARTICLES

Gold nanoparticles were synthesized and functionalized according to previously reported methods. Citrate-stabilized spherical gold nanoparticles (6 nm) were synthesized using the Turkevich method, and purified by centrifugation and washing (8000 rpm, 15 min).[26-28] 15 nm CTAB-stabilized spherical gold nanoparticles were synthesized using our previously reported seeded growth approach, and were purified by centrifugation and washing (2 cycles, 6000 rpm, 11 min).[29] CTAB-stabilized gold nanorods were prepared using a silver-assisted seeded growth procedure, and were purified by centrifugation and washing (2 cycles, 11000 rcf, 10 min).[30,31] CTAB gold nanorods were then functionalized with either sodium polyacrylate (PAA) or polyallylamine hydrochloride (PAH) using an established layer-by-layer polyelectrolyte wrapping method.[32] The polyelectrolyte-coated gold nanorods (PAA and PAH) were purified by centrifugation and washing (2 cycles, 4500 rcf, 25 min). Functionalized gold nanoparticles were then redispersed in Nanopure deionized water. Diagrams and TEM images of the functionalized gold nanoparticle probes used in these studies are shown in Figure 7.1.

Gold nanoparticles were characterized using a combination of UV-vis absorbance spectroscopy (Varian Cary 500 UV-VIS-NIR Spectrophotometer), transmission electron microscopy (JEOL 2100 Cryo-TEM), and dynamic light scattering/ζ-potential (Brookhaven ZetaPALS). For TEM analysis, dilute nanoparticle solutions were dropcast onto TEM grids and allowed to dry for three hours. Dynamic light scattering (DLS) and ζ-potential data for the as-synthesized gold nanoparticles were obtained from solutions dispersed in Nanopure deionized water (pH = 5.8) at a concentration of 1 nM for gold nanorods and 5 nM for spherical gold nanoparticles. Nanoparticle concentrations in the majority of these studies were determined using absorbance spectroscopy measurements, according to previously reported methods.[33,34]

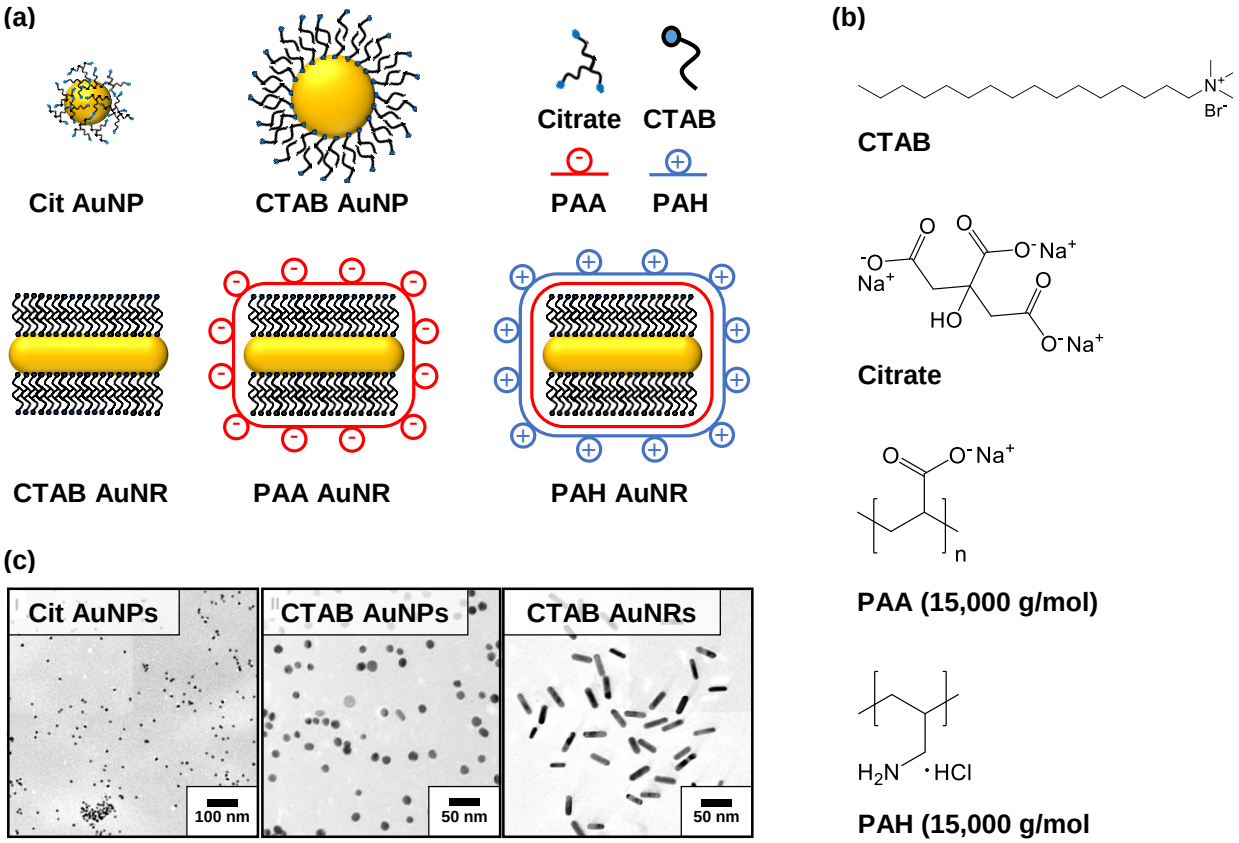

Figure 7.1 The functionalized gold nanoparticles used in this study. (a) Diagrams of the gold nanoparticles (AuNPs) and ligands used for functionalization. (b) Chemical structures of nanoparticle ligands. (c) TEM images of 6 nm Cit AuNPs, 15 nm CTAB AuNPs, and aspect ratio 3.5 CTAB gold nanorods (AuNRs).

7.2.3 SOIL SAMPLE CHARACTERIZATION

Two distinct soil samples were used in these studies: an agricultural soil sample from Lockwood Farms, and a Chlordane residential soil sample. These soil samples were obtained from the Connecticut Agricultural Experiment Station (New Haven, CT). Prior to use in the nanoparticle retention experiments, the soil samples were hand ground with an *aqua regia*-cleaned, oven-dried mortar and pestle for 5 min, and mixed with sand on a 1:5 soil: sand (w/w) basis. Soil characterization data is provided in Table 7.1.

Table 7.1 Summary of soil sample physical properties and chemical characteristics.

Soil property	Lockwood Farms soil	Chlordane residential soil
Moisture content (w:w)	1.1 %	1.5 %
pH	6.2	5.9
Organic matter (w:w)	2.5 %	4.4 %
Surface area	4.6 m^2/g	7.9 m^2/g
Cumulative surface area	18.9 m^2/g	15.2 m^2/g
Cumulative porosity	0.0056 cm^3/g	0.0048 cm^3/g

7.2.4 GOLD NANOPARTICLE STABILITY IN SIMULATED ENVIRONMENTAL CONDITIONS

The stability of the gold nanoparticles against aggregation was investigated under three different environmental conditions: incubation in simulated groundwater (5 ppm $CaCl_2/MgCl_2$), simulated groundwater in the presence of alginic acid (2 ppm), and immersion in an aqueous slurry of soil (1 g of soil in 5 mL of Nanopure deionized water). To probe the stability of the gold nanoparticles in these media, 1 mL of a 5 nM gold nanoparticle solution was added to 4 mL of the chosen environmental medium (for spherical gold nanoparticles), or 1 mL of a 5 nM solution was added to 4 mL (for gold nanorods). The aggregation state of the gold nanoparticles was monitored by a combination of UV-vis absorbance spectroscopy and DLS. The stability of the nanoparticles was monitored over a 48 or 72 h period.

7.2.5 GOLD NANOPARTICLE RETENTION IN SOIL AND ALGINATE COLUMNS

The retention of functionalized gold nanoparticles in the soil samples and alginate hydrogels was studied by constructing columns which were similar to chromatography columns described by Tripathy *et al*.[35] The columns contained two different layers or either soil:sand (1:5 w:w) or an alginate hydrogel and sand. Liquid alginate was made in 2 wt.% and the solution was stirred overnight. Alginate hydrogels were formed by adding 3 mL of 0.1 M $CaCl_2$ to 15 mL of liquid alginate.[23,36] The gels were allowed to sit for 15 min for crosslinking, and then were rinsed with water before being placed in the columns. Images of the alginate and hydrogels are shown in Figure 7.2.

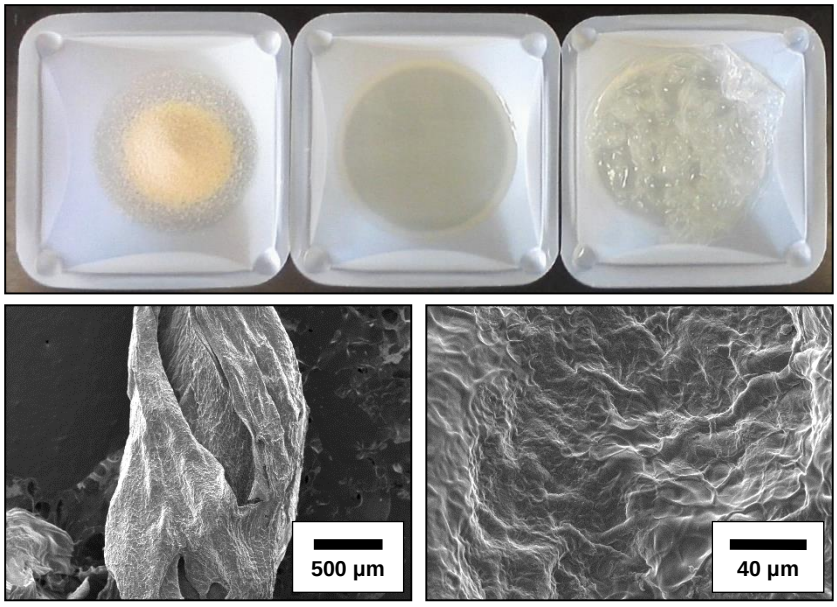

Figure 7.2 Alginate hydrogel formed from alginic acid. From left to right: (top left) alginic acid powder, (top middle) dissolved liquid alginate, and (top right) alginate hydrogel formed by the addition of $CaCl_2 \cdot 2H_2O$. Scanning electron microscopy images are of an alginate hydrogel.

Schematics of the soil and alginate columns used in retention experiments are shown in Scheme 7.1. For soil column retention experiments, 2 mL of a 5 nM spherical gold nanoparticle solution (or 2 mL of 1

nM gold nanorod solution) was added to the column, and allowed to settle into the soil for 20 min, prior to elution. The functionalized gold nanoparticles were eluted using either Nanopure deionized water or simulated groundwater (5 ppm $CaCl_2/MgCl_2$), in separate experiments. The percent of gold nanoparticles retained in the columns was determined by UV-vis absorbance spectroscopy if the gold nanoparticles showed no signs of aggregation after elution. For alginate column retention experiments, the column was hydrated with Nanopure deionized water. Then, 2 mL 0.5 nM were loaded into the column. The gold nanoparticles were allowed to diffuse through until they were at the top of the sand layer, then 30 mL of Nanopure deionized water was added above the sand. Two fractions of eluent (15 mL) were collected. Another 10 mL of water was added above the sand and a 13 mL fraction was collected. UV-Vis absorbance of each of the fractions was used to determine the percent of gold nanoparticles that were transported through the column.

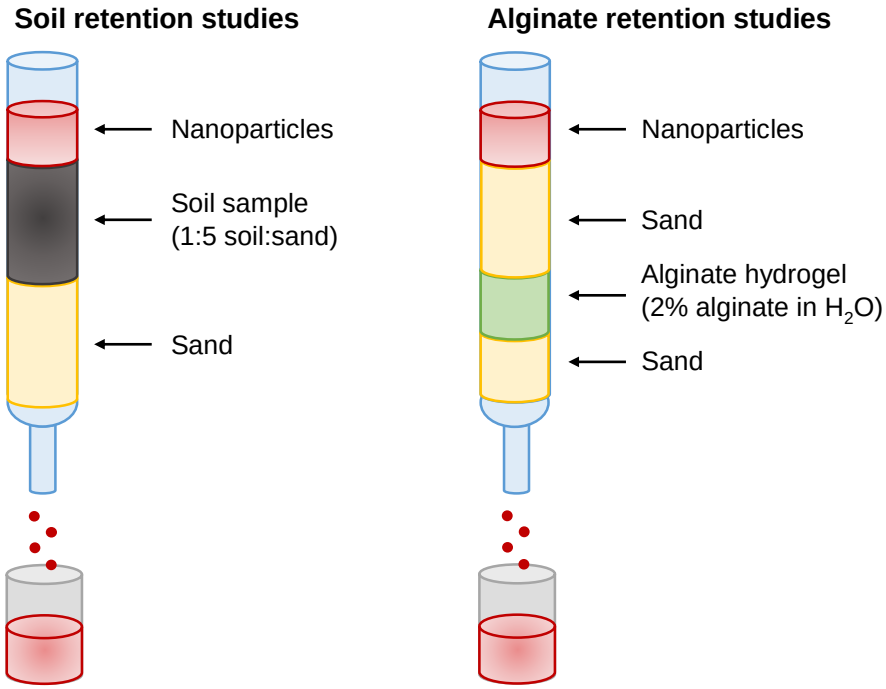

Scheme 7.1 Basic experimental setup for retention studies. Schematics of the soil and alginate columns used in retention studies. Nanoparticles were eluted through columns containing soil/sand or sand/alginate.

7.3 RESULTS AND DISCUSSION

7.3.1 PREPARATION AND CHARACTERIZATION OF THE GOLD NANOPARTICLE LIBRARY

We prepared a library of functionalized gold nanoparticles that possessed various sizes, shapes and surface chemistries, and used these probes to investigate the stability of the nanoparticles against aggregation in soil and groundwater. The library contained spherical gold nanoparticles protected with labile ligands of different charges and surface chemistries: 6 nm citrate gold nanoparticles (Cit AuNPs) and 15 nm CTAB gold nanoparticles (CTAB AuNPs). In addition, the library contained gold nanorods (aspect ratio

3.5) coated with CTAB, PAA, and PAH (CTAB AuNRs, PAA AuNRs and PAH AuNRs). This provided gold nanorods with both positive and negative surface charges, and coated with both labile (monomeric) and non-labile (electrostatically adsorbed polymers) capping agents. The nanoparticles were characterized using UV-vis, TEM, ζ-potential and DLS (Figure 7.1, Table 7.2). The citrate and CTAB capping agents are considered to be relatively labile, since the capping agents are bound to the gold nanoparticle surface as individual monomers, which are electrostatically adsorbed to the AuNP surface (although some studies have shown that the citrate capping agents can act as chelates, making the citrate less likely to desorb than if it were truly bound as a monomer).[37] In contrast, the gold nanorods coated with PAA and PAH, are protected by multiple layers of electrostatically adsorbed polymers. The lability of citrate and CTAB with respect to the gold nanoparticle surface (and compared to polymer-coated gold nanoparticles) in biological media has previously been reported on a number of occasions.[38-42]

Table 7.2 UV-vis, ζ-potential, TEM, and DLS data characterization data for functionalized AuNPs in water prior to environmental exposure.

NP Sample	λ_{max}	Size	ζ-potential	D_H
Cit AuNPs	521 nm	6.2 ± 1.3 nm	-63 ± 7 mV	23 ± 5 nm
CTAB AuNPs	516 nm	14.7 ± 3.2 nm	15 ± 5 mV	48 ± 5 nm
CTAB AuNRs	512 nm, 785 nm	50 nm x 12 nm	23 ± 5 mV	36 ± 25 nm
PAA AuNRs	510 nm, 745 nm	50 nm x 12 nm	-66 ± 8 mV	190 ± 25 nm
PAH AuNRs	516 nm, 739 nm	50 nm x 12 nm	70 ± 5 mV	83 ± 11 nm

Unlike other engineered nanoparticles, the core of gold nanoparticles has been shown to be resistant to oxidation (or dissolution) in most biological and environmental media; however, gold nanoparticles may still aggregate in sufficiently high ionic strength solutions.[43,44] Therefore, this study is primarily focused on investigating the stability of gold nanoparticles against aggregation. We investigated the changes in morphology and aggregation state of the functionalized gold nanoparticles under three environmentally relevant conditions: (1) dispersion in simulated groundwater, (2) dispersion in simulated groundwater containing natural organic matter (in this case, alginic acid), and (3) incubation in agricultural and residential soil samples. The changes in nanoparticle physiochemical properties were assessed using a combination of TEM, UV-vis absorbance spectroscopy, and DLS/ζ-potential analysis. Having developed a basic picture of gold nanoparticle transformation under different environmentally relevant conditions, we sought to examine the mobility of these gold nanoparticles in columns containing alginate, or agricultural and residential soils as a function of nanoparticle surface chemistry.

7.3.2 GOLD NANOPARTICLE STABILITY IN SIMULATED GROUNDWATER

In order to understand how the physiochemical properties of gold nanoparticles change when they are dispersed in simulated groundwater, the functionalized gold nanoparticles were dispersed in a simulated

groundwater solution (5 ppm $CaCl_2/MgCl_2$). The final gold nanoparticles concentration in the samples was 5 nM for the gold nanoparticles, and 1 nM for the gold nanorods after dilution in the simulated groundwater. The aggregation state of the particles was monitored for a 48 h incubation period **(**Figure 7.3). Both UV-vis absorbance spectroscopy and DLS measurements indicated that the Cit AuNPs and CTAB AuNPs completely aggregated within several hours of being dispersed in groundwater. This aggregation is evidenced by a loss of the surface plasmon absorbance peaks in the visible and/or near-infrared regions of the absorbance spectra and a rapid increase in the hydrodynamic diameter (D_h) in the DLS analysis (Table 7.3). This aggregation appears to be irreversible, as the aggregated Cit AuNPs and CTAB AuNPs could not be fully resuspended by sonicating the solution. TEM images of the resulting aggregates were also obtained (Figure 7.3). While electron microscopy does not provide an accurate picture of the size or morphology of the aggregates in solution (due to drying effects and other artifacts), TEM imaging may provide some supplementary insight into the morphology of the aggregated gold nanoparticles. It is interesting to note that the TEM images of the spherical gold nanoparticles, which are stabilized by relatively labile, monomeric capping agents, show that the gold nanoparticles might have fused during the aggregation process, forming what appear to be extended networks of larger particles or amorphous nanostructures (Figure 7.3a,b). The formation of such large, permanently aggregated structures would be consistent with the fact that the aggregates of the Cit AuNPs and CTAB AuNPs cannot be visibly redispersed by extensive sonication of these solutions. Similar irreversible aggregation of Cit AuNPs and AgNPs in moderately hard water has been reported.[45,46]

In contrast to the spherical gold nanoparticles, while the CTAB AuNRs and PAA AuNRs show some loss of stability in simulated groundwater, the aggregation was less rapid as evidenced by UV-vis and DLS (Figure 7.3). The PAH AuNRs show little evidence of aggregation, as the UV-vis spectra of these rods remains essentially unperturbed after 48 h. Additionally, the hydrodynamic diameter of the nanorods show relatively minor increases over the 48 h incubation period, when compared to the spherical Cit and CTAB AuNPs (Table 7.3). The AuNRs investigated do not show any significant evidence of aggregation (either by UV-vis or DLS) until nearly 24 h of incubation time. Aggregation is slow in these samples for both the polyelectrolyte-coated rods (which are stabilized by multiple electrostatic interactions with the gold nanorod surface) and for the CTAB AuNRs (labile ligand). In these cases, TEM analysis of the aggregated rod samples indicated that the while the gold may have aggregated, they do not show the same morphology changes as the spherical gold nanoparticles, and the plasmon absorbance bands could be restored.

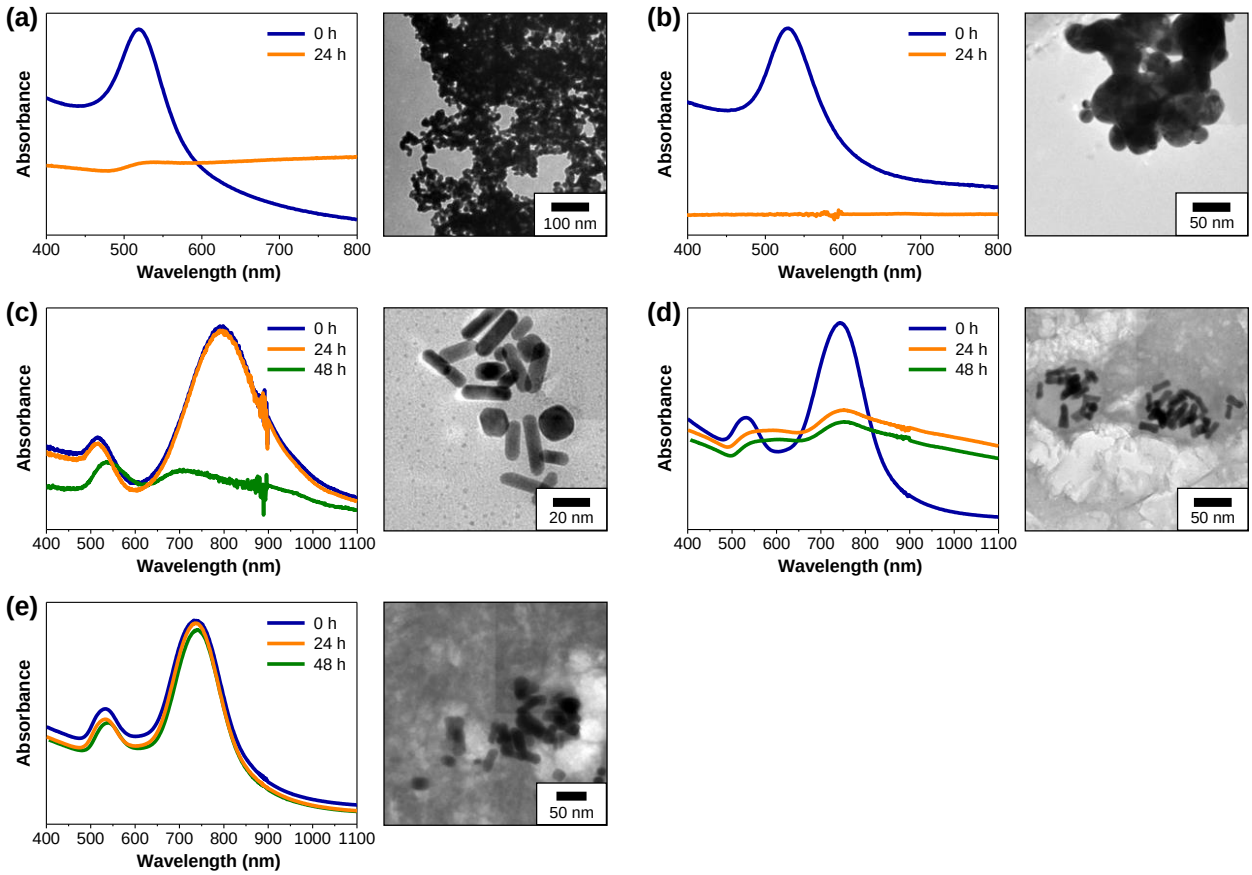

Figure 7.3 UV-vis absorbance spectra and TEM images of functionalized AuNPs exposed to simulated groundwater (5 ppm $CaCl_2/MgCl_2$) after 0, 24, or 48 h. (a) 6 nm Cit AuNPs, (b) 15 nm CTAB AuNPs, (c) CTAB AuNRs, (d) PAA AuNRs, and (e) PAH AuNRs.

Table 7.3 Physiochemical characterization data for AuNPs after incubation in simulated ground water (5 ppm $CaCl_2/MgCl_2$) for 48 h.

AuNP sample	D_H (nm)	ζ-potential (mV)
Cit AuNPs	-	-20 ± 2
CTAB AuNPs	5720 ± 560	-3 ± 4
CTAB AuNRs	394 ± 22	1 ± 7
PAA AuNRs	194 ± 3	-53 ± 4
PAH AuNRs	24 ± 1	46 ± 5

These observations indicate that functionalized gold nanoparticles, which are generally considered to be relatively stable against oxidation,[16,43,44] are susceptible to physiochemical transformations. These transformations may substantially alter their size and shape, due to aggregation, likely coupled with capping agents being released from the nanoparticle surface. This result demonstrates that stability of the nanomaterials in environmental media likely depends not only on the core material, but also on the surface

chemistry. In this case, it is not only the surface charge that influences nanoparticle solubility, but also the chemical nature of the interaction between the capping agent and the nanomaterial surface.

7.3.3 GOLD NANOPARTICLE STABILITY IN SIMULATED GROUNDWATER WITH ALGINIC ACID

In addition to dissolved ions, most natural water sources contain some source of natural organic matter (NOM), whether it be algae, humic acid, or some other material. It has previously been shown that the presence of NOM in natural waters can have a stabilizing effects which reduce aggregation of functionalized nanoparticles, depending on the pH and ionic strength of the solution.[47,48] This is because NOM may adsorb to the surface of the nanoparticle, stabilizing the nanoparticles against aggregation, or because NOM may surround the nanoparticles, linking them together in larger heteroaggregate structures.[49]

Accordingly, we explored whether the addition of a small amount of NOM, in the form of alginic acid, might mediate gold nanoparticle aggregation following gold nanoparticle dispersion in the simulated groundwater. The polysaccharide alginate is secreted by many types of organisms; thus, alginate is a useful matrix to investigate interactions between nanomaterials and NOM. gold nanoparticles were dispersed in simulated groundwater containing a small amount of alginic acid (1 ppm). Changes in gold nanoparticle physiochemical properties were monitored over the course of 72 h. The incubation period in these trials was extended because the gold nanoparticles were observed to aggregate very slowly in the presence of the alginic acid. In the presence of alginic acid, UV-vis absorbance spectroscopy indicated that the rate of gold nanoparticle aggregation may be significantly reduced (Figure 7.4). This was indicated by the fact that the absorbance spectra of all the gold nanoparticles remained relatively unperturbed when alginic acid was present in the water. Only the Cit AuNPs showed any evidence of aggregation as indicated by a noticeable, but minor red shift and broadening of the plasmon absorbance. The UV-vis absorbance spectra alone do not provide a complete picture of the aggregation state of the gold nanoparticles. The spectra may not be perturbed if gold nanoparticles form heteroaggregates with the alginate if the particles are within the aggregate at sufficient distances apart so that the plasmons of the individual gold nanoparticles do not couple. In order to form a better picture of the aggregation states of the gold nanoparticles in the presence of alginate, the alginate-gold nanoparticle complexes were also characterized by DLS, ζ-potential analysis, and TEM imaging (Figure 7.4 and Table 7.4)

Dynamic light scattering of the gold nanoparticle-alginate complexes shows that the hydrodynamic diameter of the gold nanoparticles noticeably increases in the presence of alginate; however, the diameters are generally smaller than gold nanoparticles which aggregated in simulated groundwater in the absence of alginate (Table 7.3). Regardless of the initial gold nanoparticle surface charge, the ζ-potentials of all the nanoparticles were altered following immersion in the solution, and became largely negative, similar to the ζ-potential of the alginate itself. This suggests that gold nanoparticles do adsorb alginate from the aqueous solution. In many cases, the gold nanoparticle hydrodynamic diameter increases, without the corresponding absorbance spectra being perturbed following alginate incubation. This supports the proposition that at some of the gold nanoparticles investigated here form heteroaggregates with the alginate polymer, but the

nature of this heteroaggregation process is not clear. Alginic acid monomers can cross-link to form polymers in aqueous solutions of Ca^{2+}.[50] It is possible that alginate monomers adsorb to the gold nanoparticle surfaces first, and then alginate-coated gold nanoparticles are cross-linked by alginate polymerization, or that alginate polymerization occurs first, and then the gold nanoparticles aggregate with the alginate.

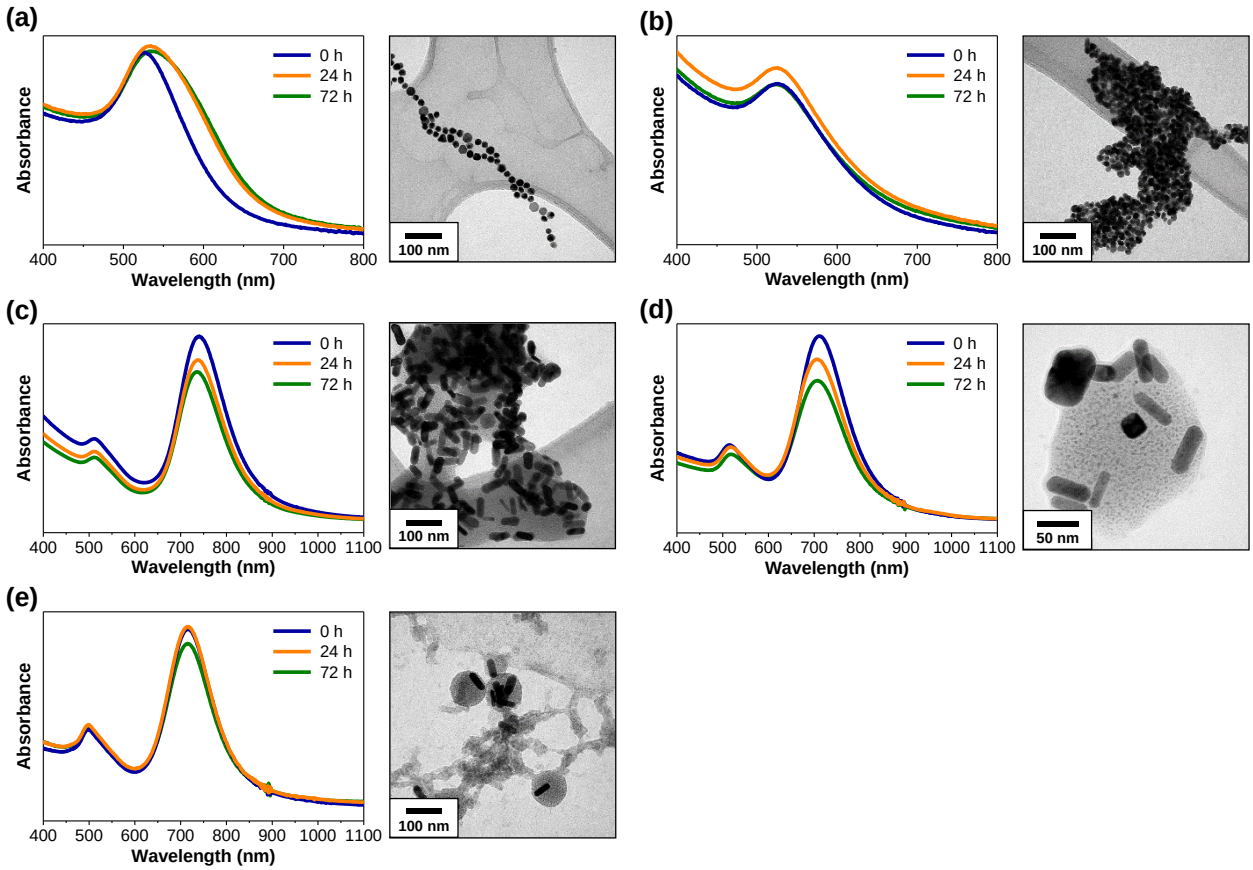

Figure 7.4 UV-vis absorbance spectra and TEM images of functionalized AuNPs exposed to simulated groundwater (5.0 ppm $CaCl_2/MgCl_2$) in the presence of alginate after 0, 24, or 72 h. (a) 6 nm Cit AuNPs, (b) 15 nm CTAB AuNPs, (c) CTAB AuNRs, (d) PAA AuNRs, and (e) PAH AuNRs.

Table 7.4 Physiochemical characterization data for purified AuNPs after incubation in simulated ground water (5 ppm $CaCl_2/MgCl_2$) containing 2 ppm aqueous alginic acid for 7 days.

AuNP sample	D_h (nm)	ζ-Potential (mV)
Cit AuNPs	110 ± 3	-43 ± 1
CTAB AuNPs	249 ± 7	-31 ± 2
CTAB AuNRs	229 ± 26	30 ± 2
PAA AuNRs	69 ± 2	-31 ± 2
PAH AuNRs	30 ± 0.8	40 ± 1
Alginic acid	5040 ± 2440	-59 ± 6

To further investigate the structure of these gold nanoparticle-alginate species, TEM imaging of the gold nanoparticles following alginate incubation was carried out (Figure 7.4). In many of these images, a thin semi-transparent film can be seen around extensive chains of gold nanoparticles on the TEM grids, which would be consistent with both of the proposed explanations. Unfortunately, TEM of dried samples does not provide direct information as to the structure of the gold nanoparticle-alginate aggregates in solution, since drying effects during sample preparation will strongly influence the appearance of the gold nanoparticles on a grid surface. However, all the data taken together indicate that the gold nanoparticles adsorb and/or adsorb to the alginate polymer, mediating the surface charge and aggregation state of the gold nanoparticles in the simulated groundwater. Thus, the alginate acts as a stabilizer, preventing the rapid aggregation observed when the gold nanoparticles are dispersed in simulated groundwater alone. Additionally, it appears that in the presence of alginate, gold nanoparticles exist in simulated groundwater as some type of heteroaggregate with alginate, regardless of the initial surface chemistry.

The formation of gold nanoparticle-NOM heteroaggregates in simulated groundwater would have significant implications for gold nanoparticle stability and transport within the environment. While the alginate appears to improve the stability of the AuNPs against aggregation in groundwater, this stability appears to be the result of heteroaggregation with alginate polymers, which means that gold nanoparticles, regardless of their initial surface charge, most likely are transported through the environment as large aggregates with natural organic matter. This transformation would greatly effect nanoparticle environmental fate because these gold nanoparticles are no longer the well-defined nanostructures synthesized in the lab. It has been previously shown that the majority (60%) of CTAB AuNRs exposed to an environmental system accumulate in biofilms.[51] In addition to bacteria, it is known that a biofilm matrix contains water, DNA, proteins, and NOM, such as the polysaccharide alginate.[24] Potentially, the formation of NOM-gold nanorod heteroaggregates was what drove accumulation of gold nanorods in biofilms. Therefore, we might expect that regardless of core composition, shape and surface chemistry, nanoparticle environmental fate is closely tied to interactions with NOM.

7.3.4 GOLD NANOPARTICLE ADSORPTION TO SOIL COLLOIDS

The stability of the gold nanoparticles were examined in the chosen soil samples (Lockwood Farms and Chlordane residential). In order to isolate the influence of the soil samples alone on gold nanoparticle stability, gold nanoparticle samples were dispersed in Nanopure deionized water and then mixed with the soil samples briefly at vortex. The soil slurry was allowed to settle out, and the supernatant was examined by UV-vis, TEM, DLS, and ζ-potential analyses. Exposure to either soil sample did not induce significant aggregation among the different types of gold nanoparticles, as evidenced by the UV-vis absorbance spectra. However, the gold nanoparticles stabilized with positively-charged ligands (CTAB and PAH) were strongly adsorbed to both soil types tested, as evidenced by the significant decrease in the intensity of the surface plasmon absorbance following soil incubation for the 15 nm CTAB AuNPs, the CTAB AuNRs, and the PAH AuNRs. TEM analysis of the dropcast supernatants further supports this observation, as the

positively-charged AuNPs were found to be closely associated with colloidal materials present in the soil samples, while “free” Cit AuNPs and PAA AuNRs were much more common in their respective supernatants, and were not found to be closely associated with the soil colloids. The UV-vis and TEM data from these experiments using Lockwood Farm soil is shown in Figure 7.5, and the corresponding data for the Chlordane residential soil are quite similar (the data are not shown).

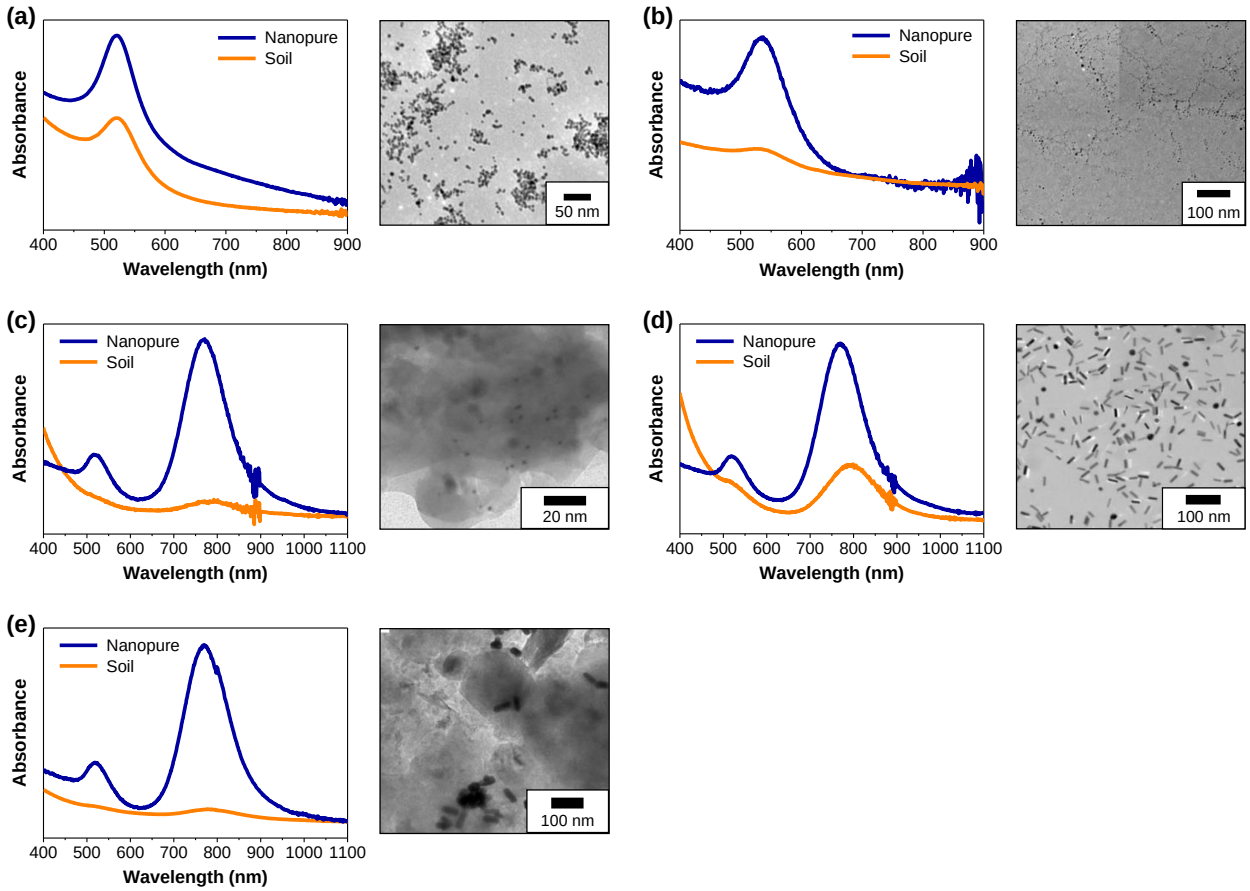

Figure 7.5 UV-Vis absorbance spectra and TEM images of functionalized AuNPs incubated in a slurry of Lockwood Farms soil for 2 h. (a) 6 nm Cit AuNPs, (b) 15 nm CTAB AuNPs, (c) CTAB AuNRs, (d) PAA AuNRs, and (e) PAH AuNRs.

Interestingly, small spherical particles (~ 2 nm) were seen to be prevalent in the TEM images of the 15 nm CTAB AuNPs and the CTAB AuNRs. Smaller nanoparticles were also found, although in smaller amounts, in the TEM images of the CTAB AuNPs and CTAB AuNRs prior to incubation with the soil samples. As gold nanoparticles and gold nanorods were prepared by seeded growth syntheses, and seeds are 1-3 nm,[52] these small particles are likely gold nanoparticle seeds that were not sufficiently removed during purification. These small gold nanoparticles are seen both as free nanoparticles and associated with soil colloids in the TEM images of the soil incubation samples. It should be noted that the optical absorbance of gold nanoparticles of this size are so weak, that their presence in the supernatant may not be easily

detected in the supernatants of the soil incubation samples. Accordingly, it is worth considering that these seed gold nanoparticles may have significantly different fate and transport properties than larger gold nanoparticles with the same surface chemistry, and when examining the environmental fate and transport of gold nanoparticles prepared by seeded growth methods, the presence of these potential impurities should be considered and accounted for.

Combining the data from all of these stability studies, we can develop a much clearer picture of gold nanoparticle physiochemical properties in the environment. Functionalized gold nanoparticles are typically considered to be "stable" under environmental conditions (particularly compared to silver NPs or metal oxide nanoparticles which can oxidize or sulfidize under environmental conditions). However, we find that gold nanoparticles stabilized with labile ligands are indeed susceptible to aggregation in simulated groundwater, quickly giving rise to large aggregates, rather than individual gold nanoparticles. This is an important consideration, as the majority of previous studies that have examined gold nanoparticle fate and transport in mesocosms or uptake into plants have used Cit AuNPs or CTAB AuNPs.[51-55] The rapid aggregation of these gold nanoparticles may have a significant impact on how the gold nanoparticles partition in the environment, or how they biomagnify within the food chain. This rapid aggregation may also have significant consequences for gold nanoparticles that are used in ecotoxicity studies using typical indicator organisms (e.g., Daphnia or zebrafish).[45,56,57]

7.3.5 GOLD NANOPARTICLE RETENTION IN SOIL AND ALGINATE COLUMNS

Transport and retention of gold nanoparticles, through columns containing various types of environmental media, has been demonstrated to be a useful method to examine nanoparticle fate in the environment.[35,58-60] Therefore, having investigated how the physicochemical properties of gold nanoparticles are altered following environmental exposure, we sought to understand how the physiochemical properties of gold nanoparticles might influence their retention in columns of soil and alginate. Schematics of these setups are in Scheme 7.1. Soil columns were set up, in which the gold nanoparticles were briefly allowed to incubate at the top of the soil for 20 minute incubation. The gold nanoparticles were then eluted with Nanopure deionized water, in order to observe how the gold nanoparticles interacted with the soil in the absence of aggregation. UV-vis absorbance spectroscopy was used to quantify the amount of gold nanoparticles that had eluted from a given soil column, and the amount of AuNPs retained in the soil column was determined by subtraction. It almost immediately became evident that the positively-charged gold nanoparticles were strongly retained in columns prepared from either soil sample type. In fact, in the Lockwood Farms soil column, none of the positively-charged gold nanoparticles (CTAB AuNPs, CTAB AuNRs, and PAH AuNRs) could be eluted from the soil column (Figure 7.6a) In contrast, the Cit AuNPs, and the PAA AuNRs were eluted almost immediately from the soil columns. The same general trend was observed in the Chlordane residential soil columns (Figure 7.6b), except that the positively-charged gold nanoparticles were not quantitatively retained by this soil type. It is likely that the positively-charged gold nanoparticle s are strongly retained in these soil types mirrors the strong affinity for

the soil samples that was observed in the soil incubation studies. There is strong interaction between the positively charged gold nanoparticles and the silicates and aluminates present in the soil (although NOM may also play a role in this regard).

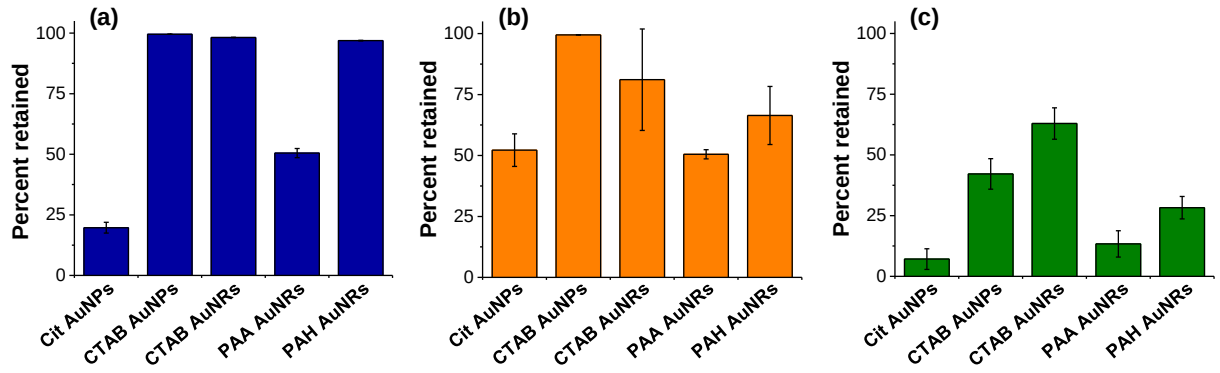

Figure 7.6 Percent of gold nanoparticles retained in (a) Lockwood Farms soil columns, (b) Chlordane residential soil columns, and (c) alginate columns. The eluent was Nanopure deionized water and gold nanoparticle concentration of eluted fractions was determined by UV-vis absorbance spectroscopy.

Similar transport experiments through columns containing alginate hydrogels were carried out. The amount of gold nanoparticles retained by these columns were calculated by subtracting the amount in the samples eluted from the column from the initial known amount added to the columns using UV-vis absorbance spectroscopy. The results from the transport experiments are shown in Figure 7.6c. Generally, gold nanoparticle retention in alginate was lower than in the soil columns; however, the trends with shape and surface chemistry are similar. As expected, the positively charged CTAB AuNPs, CTAB AuNRs, and PAH AuNRs exhibit greater retention than the negatively charged Cit AuNPs or PAA AuNRs. This result demonstrates that the surface charge on gold nanoparticles can influence interactions with an environmental matrix (in this case, negatively charged alginate). However, there were also differences in retention by shape/size and surface coating. For example, the CTAB AuNPs were not as strongly retained in the columns as the CTAB AuNRs. Interestingly, the PAH AuNRs had reduced retention compared to both the CTAB AuNPs and the CTAB AuNRs. These differences suggest that many nanomaterial characteristics (e.g. size, shape, and surface chemistry) can greatly influence the fate of gold nanoparticles in the environment.

7.4 CONCLUSIONS

The increased prevalence of nanomaterials in a range of applications will inevitably lead to nanomaterial contamination of soil and groundwater. It has been shown that nanomaterials' physiochemical properties such as size, shape, and surface chemistry ultimately control the majority of their interactions with biological and environmental systems. The precise manner in which nanoparticle properties may change in response to environmental exposure; however, is not well-understood. Gold nanoparticles are excellent model probes to assess the fate of functionalized nanoparticles in environmental media, because

their size, shape, and surface chemistry can be exquisitely controlled, and their transformation in and progress through complex matrices can be closely monitored using simple instrumental techniques.

Here we investigated how gold nanoparticle shape and surface chemistry influenced their stability and transport within environmental systems. A library of spherical and rod-shaped gold nanoparticles was prepared with different surface chemistries using a polyelectrolyte layer-by-layer coating strategy. Nanoparticle stability against aggregation in simulated groundwater was investigated using UV-vis absorbance spectroscopy and dynamic light scattering. Even though gold nanomaterials are relatively stable against oxidation, gold nanoparticle surface chemistry had a strong influence on stability against aggregation in simulated groundwater. The stability of the gold nanoparticle probes depended on both the surface charge imparted by the capping agent, and the nature of the interaction between the gold nanoparticle surface and the capping agent. Gold nanoparticles protected with relatively labile capping agents, like cetyltrimethylammonium bromide or citrate are more susceptible to irreversible aggregation in groundwater than polyelectrolyte-coated gold nanorods. However, in the presence of alginate, the gold nanoparticles formed heteroaggregates with the alginate polymers, regardless of the initial gold nanoparticle surface coating. The charge and capping agent interaction also exerts a strong influence on functionalized gold nanoparticle retention in these columns. Negatively-charged gold nanoparticles were only weakly retained in soil and alginate, and hence, are potentially much more mobile in environmental matrices than nanoparticles carrying positive surface charges. Together, these data suggest that the environmental fate of nanoparticles is strongly influenced by their surface chemistry, as well as their core material and size.

7.5 REFERENCES

1. Stark, W. J.; Stoessel, P. R.; Wohlleben, W.; Hafner, A. Industrial Applications of Nanoparticles. *Chem. Soc. Rev.* **2015,** *44,* 5793-5805.
2. Benn, T. M.; Westerhoff, P. Nanoparticle Silver Released into Water from Commercially Available Sock Fabrics*. Environ. Sci. Technol.* **2008,** *42,* 4133-4139.
3. Shäfer-Korting, M.; Mehnert, W.; Korting, H.-C. Lipid Nanoparticles for Improved Topical Application of Drugs for Skin Diseases. *Adv. Drug Delivery Rev.* **2007,** *59,* 427-443.
4. Smith, A. Does it Have a Sporting Chance? *Chem. Int.* **2006,** *28,* 8-9.
5. Bell, A. T. The Impact of Nanoscience on Industrial Catalysis. *Science* **2003,** *299,* 1688-1691.
6. Rai, M.; Yadav, A.; Gade, A. Silver Nanoparticles as a New Generation of Antimicrobials. *Biotechnol. Adv.* **2009,** *27,* 76-83.
7. Brannon-Peppas, L; Blanchette, J. O. Nanoparticles and Targeted Systems for Cancer Therapy. *Adv. Drug Delivery Rev.* **2012,** *64,* 206-212.
8. Rochman, C. M.; Kross, S. M.; Armstrong, J. B.; Bogan, M. T.; Darling, E. S.; Green, S. J.; Smyth, A. R.; Veríssimo, D. Scientific Evidence Supports a Ban on Microbeads. *Environ. Sci. Technol.* **2015,** *49,* 10759-10761.
9. Rudd, J. Regulating the Impacts of Engineered Nanoparticles under TSCA: Shifting Authority from Industry to Government. *J. Envtl. L.* **2008,** *33,* 215-282.
10. Wiesner, M. R.; Lowry, G. V.; Jones, K. L. Hochella, M. f.; Di Giulio R. T.; Casman, E.; Bernhardt, E. S. Decreasing Uncertainties in Assessing Environmental Exposure, Risk, and Ecological Implications of Nanomaterials. *Environ. Sci. Technol.* **2009,** *43,* 6458-6462.
11. Godwin, H. A.; Chopra, K.; Bradley, K. A.; Cohen, Y.; Harthorn, B. H.; Hoek, E. M. V.; Holden, P.; Keller, A. A.; Lenihan, H. S.; Nisbet, R. M.; Nel, A. E. The University of California Center for the Environmental Implications of Nanotechnology. *Environ. Sci. Technol.* **2009,** *43,* 6453-6457.

12. Gimbert, L. J.; Haygarth, P. M.; Beckett, R.; Worsfold, P. J. Comparison of Centrifugation and Filtration Techniques for the Size Fractionation of Colloidal Material in Soil Suspensions Using Sedimentation Field-Flow Fractionation. *Environ. Sci. Technol.* **2005,** *39,* 1731-1735.
13. Dale, A. L.; Casman, E. A.; Lowry, G. V.; Lead, J. R.; Viparelli, E.; Baalousha, M. Modeling Nanomaterial Environmental Fate in Aquatic Systems. *Environ. Sci. Technol.* **2015,** *49,* 2587-2593.
14. Lowry, G. V.; Gregory, K. B.; Apte, S. C.; Lead, J. R. Transformations of Nanomaterials in the Environment. *Environ. Sci. Technol.* **2012,** *46,* 6893-6899.
15. Pina, C. D.; Falletta, E.; Prati, L.; Rossi, M. Selective Oxidation Using Gold. *Chem. Soc. Rev.* **2008,** *37,* 2077-2095.
16. Philip, D. Synthesis and Spectroscopic Characterization of Gold Nanoparticles. *Spectrochim. Acta, Part A* **2008,** *71,* 80-85.
17. Ebrahimzadeh, H.; Tavassoli, N.; Amini, M. M.; Fazaeli, Y.; Abedi, H. Determination of Very Low Levels of Gold and Palladium in Wastewater and Soil Samples by Atomic Absorption after Preconcentration on modified MCM-48 and MCM-41 Silica. *Talanta* **2010,** *81,* 1183-1188.
18. Grzelczak, M.; Pérez-Juste, J.; Mulvaney, P.; Liz-Marzán, L. Shape Control in Gold Nanoparticle Synthesis. *Chem. Soc. Rev.* **2008,** *37,* 1783-1791.
19. Mout, R.; Moyano, D. F.; Rana, S.; Rotello, V. M. Surface Functionalization of Nanoparticles for Nanomedicine. *Chem. Soc. Rev.* **2012,** *41,* 2539-2544.
20. Christian, P.; Von der Kammer, F.; Baalousha, M.; Hofmann, T. Nanoparticles: Structure, Properties, Preparation and Behaviour in Environmental Media. *Ecotoxicology* **2008,** *17,* 326-343.
21. Klaine, S. J.; Alvarez, P. J. J; Batley, G. E.; Fernandes, T. F.; Handy, R. D.; Lyon, D. Y.; Mahendra, S.; McLaughlin, M. J.; Lead, J. R. Nanomaterials in the Environment: Behavior, Fate, Bioavailability, and Effects. *Environ. Toxicol. Chem.* **2008,** *27,* 1825-1851.
22. Davis, T. A.; Volesky, B.; Mucci, A. A Review of the Biochemistry of Heavy Metal Biosorption by Brown Algae. *Water Res.* **2003,** *37,* 4311-4330.
23. Gacesa, P. Alginates. *Carbohydr. Polym.* **1988,** *8,* 161-182.
24. Flemming, H.-C.; Wingender, J. The Biofilm Matrix. *Nat. Rev. Microbiol.* **2010,** *8,* 623-633.
25. Clementi, F.; Crudele, M. A.; Parente, E.; Mancini, M.; Moresi, M. Production and Characterisation of Alginate from *Azotobacter vinelandii*. *J. Sci. Food Agric.* **1999,** *79,* 602-610.
26. Turkevich, J. Colloidal Gold. Part II. *Gold Bull.* **1985,** *18,* 125-131.
27. Kimling, J.; Maier, M.; Okenve, B.; Kotaidis, V.; Ballot, H.; Plech, A. Turkevich Method for Gold Nanoparticle Synthesis Revisited. *J. Phys. Chem. B* **2006,** *110,* 15700-15707.
28. Wuithschick, M.; Birnbaum, A.; Witte, S.; Sztucki, M.; Vainio, U.; Pinna, N.; Rademann, K.; Emmerling, F.; Kraehnert, R.; Polte, J. Turkevich in New Robes: Key Questions Answered for the Most Common Gold Nanoparticle Synthesis. *ACS Nano* **2015,** *9,* 7052-7071.
29. Jana, N. R.; Gearheart, L.; Murphy, C. J. Seeding Growth for Size Control of 5-40 nm Diameter Gold Nanoparticles. *Langmuir* **2001,** *17,* 6782-6786.
30. Sau, T. K.; Murphy, C. J. Room Temperature, High-Yield Synthesis of Multiple Shapes of Gold Nanoparticles in Aqueous Solution. *J. Am. Chem. Soc.* **2004,** *126,* 8648-8649.
31. Sau, T. K.; Murphy, C. J. Seeded High Yield Synthesis of Short Au Nanorods in Aqueous Solution. *Langmuir* **2004,** *20,* 6414-6420.
32. Gole, A.; Murphy, C. J. Polyelectrolyte-Coated Gold Nanorods: Synthesis, Characterization and Immobilization. *Chem. Mater.* **2005,** *17,* 1325-1330.
33. Orendorff, C. J.; Murphy, C. J. Quantitation of Metal Content in the Silver-Assisted Growth of Gold Nanorods. *J. Phys. Chem. B* **2006,** *110,* 3990-3994.
34. Khlebtsov, N. G. Determination of Size and Concentration of Gold Nanoparticles from Extinction Spectra. *Anal. Chem.* **2008,** *80,* 6629-6625.
35. Tripathi, S.; Champagne, D.; Tufenkji, N. Transport Behavior of Selected Nanoparticles with Different Surface Coatings in Granular Porous Media Coated with *Pseudomonas aeruginosa* Biofilm. *Environ. Sci. Technol.* **2012,** *46,* 6942-649.
36. Lee, K. Y.; Rowley, J. A.; Eiselt, P.; Moy, E. M.; Bouhadir, K. H.; Mooney, D. J. Controlling Mechanical and Swelling Properties of Alginate Hydrogels Independently by Cross-Linker Type and Cross-Linking Density. *Macromolecules* **2000,** *33,* 4291-4294.
37. Park, J.-W.; Shumaker-Parry, J. S. Strong Resistance of Citrate Anions on Metal Nanoparticles to Desorption under Thiol Functionalization. *ACS Nano* **2015,** *9,* 1665-1682.

38. Leonov, A. P.; Zheng, J.; Clogston, J. D.; Stern, S. T.; Patri, A. K.; Wei, A. Detoxification of Gold Nanorods by Treatment with Polystyrenesulfonate. *ACS Nano* **2008,** *2,* 2481-2488.
39. Huang, J.; Jackson, K. S.; Murphy, C. J. Polyelectrolyte Wrapping Layers Control Rates of Photothermal Molecular Release from Gold Nanorods. *Nano Lett.* **2012,** *12,* 2982-2987.
40. Hicks, J. F.; Seok-Shon, Y.; Murray, R. W.; Layer-by-Layer Growth of Polymer/Nanoparticle Films Containing Monolayer-Protected Gold Clusters. *Langmuir* **2002,** *18,* 2288-2294.
41. Zhou, J.; Pishko, M. V.; Lutkenhaus, J. L. Thermoresponsive Layer-by-Layer Assemblies for Nanoparticle-Based Drug Delivery. *Langmuir* **2014,** *30,* 5903-5910.
42. Artyukhin, A. B.; Bakajin, O.; Stroeve, P.; Noy, A. Layer-by-Layer Electrostatic Self-Assembly of Polyelectrolyte Nanoshells on Individual Carbon Nanotube Templates. *Langmuir* **2004,** *20,* 1442-1448.
43. Alkilany, A. M.; Lohse, S. E.; Murphy, C. J. The Gold Standard: Gold Nanoparticle Libraries to Understand the Nano-Bio Interface. *Acc. Chem. Res.* **2013,** *46,* 650-661.
44. Burns, C.; Spendel, W. U.; Puckett, S.; Pacey, G. E. Solution Ionic Strength Effect on Gold Nanoparticle Solution Color Transition. *Talanta* **2006,** *69,* 873-876.
45. Lee, B.-T.; Ranville, J. F. The Effect of Hardness on the Stability of Citrate-Stabilized Gold Nanoparticles and their Uptake by *Daphnia magna*. *J. Hazard. Mater.* **2012,** *213,* 434-439.
46. Chinnapongse, S. L.; MacCuspie, R. I.; Hackley, V. A. Persistence of Singly Dispersed Silver Nanoparticles in Natural Freshwaters, Synthetic Seawater, and Simulated Estuarine Waters. *Sci. Total Environ.* **2011,** *409,* 2443-2450.
47. Louie, S. M.; Tilton, R. D.; Lowry, G. V. Effects of Molecular Weight Distribution and Chemical Properties of Natural Organic Matter on Gold Nanoparticle Aggregation. *Environ. Sci. Technol.* **2013,** *47,* 4245-4254.
48. Dahdal, Y. N.; Pipich, V.; Rapaport, H.; Oren, Y.: Kasher, O. R.; Schwahn, D. Small-Angle Neutron Scattering Studies of Alginate as Biomineralizing Agent and Scale Initiator. *Polymer* **2016,** *85,* 77-88.
49. Stankus, D. P.; Lohse, S. E.; Hutchison, J. E.; Nason, J. A. Interactions Between Natural Organic Matter and Gold Nanoparticles Stabilized with Different Organic Capping Agents. *Environ. Sci. Technol.* **2011,** *45,* 3238-3244.
50. Becker, T. A.; Kipe, D. R.; Brandon, T. Calcium Alginate Gel: A Biocompatible and Mechanically Stable Polymer for Endovascular Embolization. *J. Biomed. Mater. Res*. **2001**, *54*, 76-86.
51. Ferry, J. L.; Craig, P.; Hexel, C.; Sisco, P.; Frey, R.; Pennington, P. L.; Fulton, M. H.; Scott, G.; Decho. A. W.; Kashiwada, S.; Murphy, C. J.; Shaw, T. J. Transfer of Gold Nanoparticles from the Water Column to the Estuarine Food Web. *Nature Nanotech.* **2009,** *4,* 441-444.
52. Walsh, M. J.; Barrow, S. J.; Tong, W.; Funston, A. M.; Etheridge, J. Symmetry Breaking and Silver in Gold Nanorod Growth. *ACS Nano* **2015,** *9,* 715-724.
53. Glenn, J. B.; Klaine, S. J. Abiotic and Biotic Factors That Influence the Bioavailability of Gold Nanoparticles to Aquatic Macrophytes. *Environ. Sci. Technol.* **2013,** *47,* 10223-10230.
54. Smith, B. M.; Pike, D. J.; Kelly, M. O.; Nason, J. A. Quantification of Heteroaggregation Between Citrate-Stabilized Gold Nanoparticles and Hematite Colloids. *Environ. Sci. Technol.* **2015,** *49,* 12789-12797.
55. Burns, J. M.; Pennington, P. L.; Sisco, P. N.; Frey, R.; Kashiwada, S.; Fulton, M. H.; Scott, G. I.; Decho, A. W.; Murphy, C. J.; Shaw, T. J.; Ferry, J. L. *Environ. Sci. Technol.* **2013,** *47,* 12844-12851.
56. Dominguez, G. A.; Lohse, S. E.; Torelli, M. D.; Murphy, C. J.; Hamers, R. J.; Orr, G.; Klaper, R. D. Effects of Charge and Surface Ligand Properties of Nanoparticles on Oxidative Stress and Gene Expression Within the Gut of *Daphnia Magna*. *Aquat. Toxicol.* **2015,** *162,* 1-9.
57. Bar-Ilan, O.; Albrecht, R. M.; Fako, V. E.; Furgeson, D. Y. Toxicity Assessments of Multisized Gold and Silver Nanoparticles in Zebrafish Embryos. *Small* **2009,** *5,* 1897-1910.
58. Darlington, T. K.; Neigh, A. M.; Spencer, M. T.; Nguyen, O. T.; Oldenburg, S. J. Nanoparticle Characteristics Affecting Environmental Fate and Transport Through Soil. *Environ. Toxicol. Chem.* **2009,** *28,* 1191-1199.
59. Lin, D.; Tian, X.; Wu, F.; Xing, B. Fate and Transport of Engineered Nanomaterials in the Environment. *J. Environmental Qual.* **2010,** *39,* 1896-1908.
60. Nabiul Afrooz, A. R. M.; Das, D.; Murphy, C. J.; Vikesland, P.; Saleh, N. B. Co-transport of Gold Nanospheres with Single-Walled Carbon Nanotubes in Saturated Porous Media. *Water Res.* **2016,** *99,* 7-15.